Abstract

First search for eV-scale sterile neutrinos and precision measurement of the ^{235}U antineutrino spectrum with the PROSPECT experiment

Danielle Norcini

2019

Since the first observation of their existence, reactors have played an important role in our understanding of neutrinos. Recent observations of the electron antineutrino flux and energy spectrum at low-enriched uranium (LEU) reactors disagree with model predictions. The flux deficit, known as the Reactor Antineutrino Anomaly, may indicate new physics in the form of a beyond-the-Standard Model, eV-scale sterile neutrino. This new type of matter would have a profound impact on fundamental physics and cosmology. The spectral deviations may be attributed to an incomplete understanding of antineutrino emission from fissile material. However, the insufficiencies in the nuclear models and the specific isotopic contributions are not yet clear.

PROSPECT is a newly constructed experiment designed to unambiguously search for eV-scale sterile neutrino oscillations and to precisely measure the antineutrino emission from ^{235}U fission. Located at the Oak Ridge National Laboratory, antineutrinos are observed at distances of 7-9 m from the the 85 $\mathrm{MW_{th}}$ highly-enriched uranium (HEU) High Flux Isotope Reactor (HFIR). PROSPECT uses inverse beta decay to identify antineutrino events in a harsh, near-surface background environment. To overcome this challenge, PROSPECT developed a novel, compact ^{6}Li-loaded scintillator detector with efficient neutron tagging and particle identification capabilities. These features, combined with event topology reconstruction made possible by optical segmentation, allow an unprecedented level of background suppression to observe antineutrinos with high energy resolution.

This thesis details the detector design, instrumentation development, and construction of the PROSPECT experiment at the Yale Wright Laboratory between 2014–2018. The detector calibration, event reconstruction, and performance are also discussed. With 33 (28) days of reactor-on(-off) data at HFIR, the first search for eV-scale sterile neutrinos is presented. No sterile neutrino oscillations are observed within the sensitive parameter space (Δm^2_{41}, $\sin^2 2\theta_{14}$) and PROSPECT excludes the best-fit sterile neutrino hypothesis to the Reactor Antineutrino Anomaly at 2.2σ confidence level. With a slightly larger data set containing >31,000 antineutrino candidates, PROSPECT has produced the world-leading measurement of the ^{235}U spectrum with a signal-to-background ratio of 1.7 and $5\%/\sqrt{E(\mathrm{MeV})}$ energy resolution. The experimental data disagrees with the leading Huber HEU reactor antineutrino spectrum model. PROSPECT disfavors ^{235}U as the sole isotope responsible for the spectral deviations observed by LEU experiments at 2.1σ confidence level.

First search for eV-scale sterile neutrinos and precision measurement of the ^{235}U antineutrino spectrum with the PROSPECT experiment

A Dissertation
Presented to the Faculty of the Graduate School
of
Yale University
in Candidacy for the Degree of
Doctor of Philosophy

by
Danielle Norcini

Dissertation Director: Karsten M. Heeger

December 2019

Contents

List of Figures

List of Tables

Acknowledgements

It definitely takes a village.

My village, those who directly contributed to the work in this thesis and those who provided the emotional support needed, spans a great physical distance. Some members of this community I see everyday at home in the Yale Wright Lab, and others only so often, across New England, Philadelphia, and all the way west to Alaska. No matter where, I am so thankful for the scientific and personal courage you all have given over the last six years. At times when it seemed like there was a never-ending chain of hurdles, you all united to carry me over them. And so, whatever has been accomplished in this work, is because of you and for you.

To my advisor Karsten Heeger, for seeing in me what I could not see in myself. You welcomed me into your group during a very confusing time, in both my scientific and professional life, and gave me the tools I needed to develop a unique expertise and big picture vision. Throughout this project you trusted me with grand responsibilities, in the process teaching me how to create opportunties and become a leader. What I admire most about you is your eagerness to build communities inside and outside of research, and I am so thankful for your support (and involvement in) YPPDO, TACO, Women in Physics, and various teaching endeavors. I am most appreciative for the scientific, professional, and personal guidance received from my thesis committee at Yale. To Sarah Demers for being there from the very beginning as both a brilliant role model and confidante during the good and bad times; I will never tell you to

stop talking while at lunch! To Keith Baker for his enduring optimism and genuine excitement about this thesis project and my growth. To Reina Maruyama for always making me feel like her peer through candid conversations about research, academia, and home life. A special thank you to Kam-Biu Luk at UC Berkeley for serving as the external reader of this thesis and providing invaluable, detailed feedback.

I have also had the privilege of being surrounded by mentors on a daily basis. To James Nikkel for his passion, creativity, and shear ability to tell it like it is. You have taught me so many things, but most importantly how to not take oneself too seriously and to only do the things you love. To Tom Langford for always being there for me (literally, as we shared an office) and inspiring an excitement about detectors in me. I have learned from you how to be a scientist and how to represent myself as a scientist. To Pranava Teja Surukuchi who became a fast friend and my most prized PROSPECT colleague. You were there for me through all of the doubts, fears, and complaints. Through your stunning example, you have shown me that anything is possible with enough will and investment (including 5k obstacle course race). And to Myron Campbell at the University of Michigan who believed in my potential as a lost undergraduate and prepared me to take on the challenges at Yale.

To the entire PROSPECT collaboration for making this project possible and exciting, even when we thought time was against us. I would like to thank Nathaniel Bowden for investing a great deal of energy into my scientific development. You are a true mentor inside and outside of the lab, and I am lucky to have spent so many hours with you (and your hipster San Francisco radio stations) in the cleanroom. To Jim Napolitano for providing invaluable research and teaching guidance with great enthusiasm, but most especially for his unwavering belief in me and advice to expand my scientific interests. To Pieter Mumm for the always direct, honest feedback and your PMT housing cleaning skills. To Bryce Littlejohn for always sharing creative ideas on how to extract more physics from analyses, while also treating me an equal.

Construction was fast, because we were so good at our jobs, but I am so happy to have had the privilege to build a real life neutrino detector with an amazing crew: Don, James W., James N., Xianava (Xianyi+Pranava), Danielle B., Jeremy G., Ben, Frank, Jeff, Henry B., the Toms (Tom H., Tom B., Tom W., and Tom L.), and all of the collaborators who came to Yale for PMT housing assembly shifts. From this list, I am unspeakably appreciative to have co-led this operation with James Wilhelmi, who helped me calm down when all I wanted to do was scream, but also joined in the yelling when necessary. And to the forever PROSPECTer Karin Gilje, who taught me how to be both patient and unapologetic in science. It was a pleasure to be under your mentorship, but even better to have you now as a life-long friend.

Figure: **(left)** Leaving our mark on PROSPECT. **(right)** After finishing the inner detector, the most blurry photograph from construction showing the most joy.

To my colleagues at the Wright Lab, who truly got me through each day, during the

highs and lows. Without doubt, my officemates in EAL 100 have had a great impact on this work and my development as a scientist, but also provided the camaraderie to make graduate school fun (even Will). Thanks to Jeremy Gaison and Ben Foust for always allowing me barge into their office to ramble about various dilemmas and providing support within the PROSPECT Yale group. I am especially grateful to Jay Hyun Jo who has not only helped me through every stage of this process, but also has become a trusted friend who I can be open about my experiences with. To Estella Barbosa de Souza for being the co-creator of YPPDO and always being there to listen with a big smile. Although they have moved on from Yale, Ke Han and Kyungeun Lim both offered incredible guidance in my early days, always challenging me to go further but never leaving me to fall. To Paula Farnsworth: we simply get each other and I am so grateful for our unbounded, down-to-earth conversations. To Kimberly Tighe for having a contagious excitement towards everything, including PROSPECT, but especially for treating me like one of her own. To Lil Vinston for teaching me about penny fights and putting your own happiness first - Happy Birthday Lil! I am also thankful to have shared many lunches in the breakroom and days in the Vault with Jeff Ashenfelter, Frank Lopez, and Tom Hurteau. I have learned many things from you, including how to lift large loads (crane, forklift, or otherwise), how to really plan the time needed for a given task, but most of all how enjoy the moments of accomplishment in any project. Although only discussed in the appendix of this thesis, I have very much enjoyed working with Sid Cahn on TACO, amongst other things. Despite the Ludacris blasting from your lab to my office, I am amazed by your pure joy in physics and how you can make so many jokes in which I understand no references. To Ágnes Moscy for the total inspiration she has provided as a scientist, artist, and person. You have taught me how (although I am still learning to implement) to take ownership both outwardly and inwardly for my work. And to Rick Casten for, no matter where in the world he is, always being my

greatest cheerleader and source of, sometimes very deep, wisdom.

To my best friends I have grown with at Yale: Prash Kharel, Stephen Albright, and Shantanu Mundhada, who I am lucky to have shared this experience with. Thank you for sometimes forcing me to stop working and live a little. To those friends who I have known way too long, Addison Weinstein, Sammy Tartar, and Peter Scorzetti. Thanks for sticking by me, even as we have all moved, evolved, and changed. To my friends Field Rogers and Nikita Dutta, who I met when they were undergraduates in our lab, but have since given me all kinds of strength and direction through our group conversations and weekend visits. I am eternally grateful for the friendship with my greatest ally and hero, Emma Ideal. You gave me the bravery to stand up for myself when no one else would and are the absolute reason that I did not quit.

Figure: Puppy Kip enjoying her visit to **(left)** Bradley Point Park and **(right)** EAL 100 in the Wright Lab with Uncle Jay.

To the Norcini-DeSiderio-Patchen clan, most especially my parents Paul and Diane, my Aunt Re and Uncle Chal, Uncle Bruce, and my "networking coach" Uncle Ed, despite the constant phone calls asking when I would be getting a real job. You have not only provided me the resources and opportunities necessary to get here, but

also made it great fun. I am also thankful to my little sister Amanda who never fails to make me laugh, mostly at the expense of our mom. And of course, I am most indebted to my partner Mike for always reminding me to look at the bright side (and to exercise). It is the greatest happiness to share life, and our doggy Kip, with you. In the spirit of Meursault, in a quite different context, "But he stopped me and wanted to know how I pictured this other life. Then I shouted at him, 'One where I could remember this life!' [...]."

Finally, to Dr. Kombo, Mary, Kathleen, Robert, Greg, Dominique, Leslie, and all of the wonderful people at the Yale Eye Center: you saved my sight and helped my family get through a very trying time, and for that I am forever grateful. This thesis would literally not have been possible without you.

Chapter 1

Introduction to neutrinos

1.1 History of beta decay

The radioactive decay of unstable atoms was first observed in 1896 by Becquerel, who discovered shadows on photographic plates after exposure to uranium salts [1]. Rutherford studied the absorption properties of these uranium-rays, and found that such radiation consists of two components with different absorption lengths: easily absorbed α-radiation and more penetrating β-radiation [2]. While it took a number of years to identify α-rays as positively-charged helium nuclei, β-rays were quickly associated with cathode-rays, also known as electrons, discovered by Thomson in 1897 [3].

It was known that β-rays originated from the atom, but it was not understood whether these rays were emitted monoenergetically for a particular isotope, as is the case for α-rays. Meitner and Hahn were the first to approach this question, hypothesizing that the emission of β-rays from radioactive atoms were uniform in velocity, i.e. energy. The group observed a line spectrum on their detector's photographic plates [4], supporting the theory. However, the photographs also revealed additional weak lines that could not be explained by monoenergetic emission of β-rays for a

particular isotope. This observation was rationalized by concluding that the fleeing electrons were originally at the same energy, but a secondary process caused a variation in velocity, creating spectral lines. However, this result came into tension with Chadwick's 1914 measurement, using a Geiger point counter to count each β-ray. Instead of a spectrum consisting of distinct energy values, he found the spectrum to be smooth and continuous across a wide range with a few lines superimposed [5]. Chadwick's result was confirmed in 1927 by Ellis and Wooster with a calorimetry measurement averaging $34400 \pm 10\%$ eV/decay for radium-E (^{210}Bi) [6], well below the endpoint energy of $\sim$100,000 eV. The measured spectrum is shown in Figure 1.1.

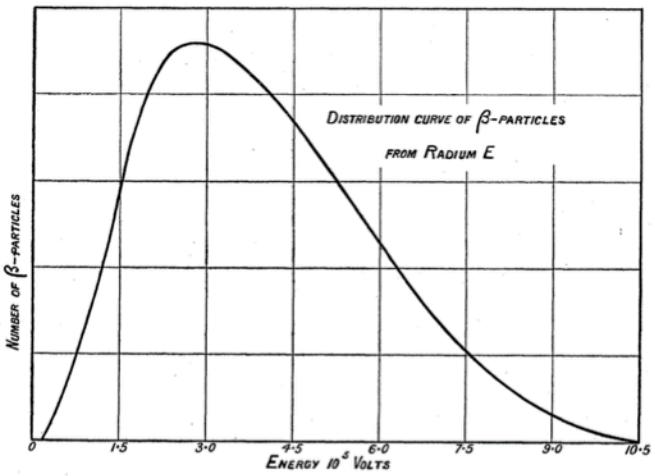

Figure 1.1: Radium-E (^{210}Bi) β spectrum measured by Ellis and Wooster in 1927 [6].

This did not settle the debate on beta decay. A continuous spectrum implied troubling consequences, namely the non-conservation of energy, as well as problems with total angular momentum conservation and the fact that the radius of the nucleus was measured to be too large to solely consist of protons and electrons. There were two main interpretations of these issues. The first was established by Bohr, who upheld that energy and momentum conservation is only valid in statistical processes. Unable to accept that these symmetries so fundamental to classical physics were

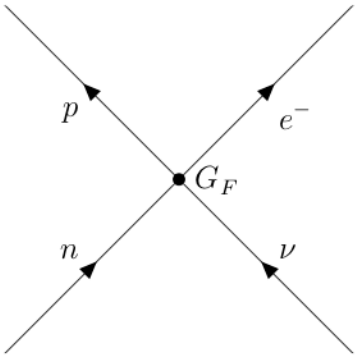

Figure 1.2: Beta decay variant, $n+\nu \rightarrow p+e^-$, where time runs along the vertical axis. The transition amplitude is described by all four fermion wave functions overlapping at a single space-time point (four-point function). This allows for the $n \rightarrow p$ and $\nu \rightarrow e^-$ transitions, driven by the weak coupling strength G_F.

fleeting, Pauli, conjured up an even bolder hypothesis. In his letter to Meitner and others in Tübingen, beginning with "Dear radioactive ladies and gentlemen..." [7], Pauli described a relatively simple solution to the beta decay problem; there exists a new, electrically neutral particle, called the *neutronen*, that carries away the excess energy and spin of the emitted electron in beta decay. The 3-body kinematics between the recoiling nucleus, electron, and the additional particle with a mass comparable to the electron and a spin of 1/2 allows for energy and angular momentum to remain constant. However, Pauli also postulated that these *neutronens*, which would also be contained inside the nucleus, are as penetrating as γ-rays and due to their neutrality, are undetectable.

In 1932, Chadwick discovered a new neutral particle [8] taking the name of neutron, although it was too massive to be considered Pauli's postulated particle, which was renamed the *neutrino* by Fermi. Borrowing ideas from the newly invented Quantum Electrodynamics (QED) field theory, Fermi created a powerful, elegant theory of weak beta decay. It describes how a light, neutral neutrino is emitted in conjunction with an electron by a nucleus containing neutrons in transition to protons [9]. The comparably weaker coupling strength is achieved by the Fermi constant G_F, the analog of the fine structure constant in QED, as illustrated in Figure 1.2.

Fermi's theory allows the shape of the β spectrum to be predicted. Figure 1.3 illustrates how the mass of the neutrino affects the endpoint energy. Previous measurements led Fermi to conclude that the neutrino is either massless or has a very small rest mass in comparison to the electron. The weak theory legitimized Pauli's neutrino as the solution to the thirty year beta decay debate.

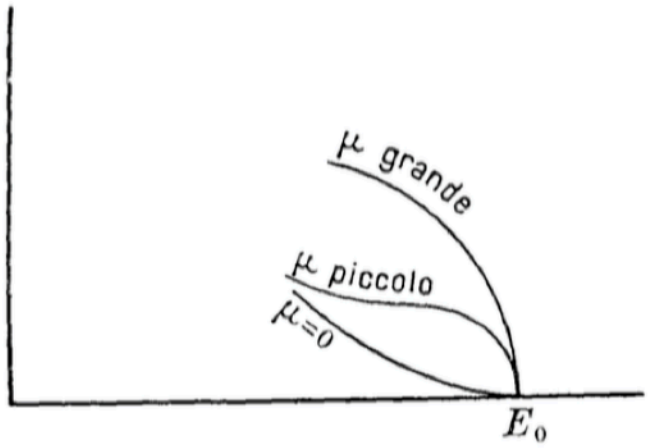

Figure 1.3: Calculation of the β decay endpoint energy for various neutrino masses by Fermi in 1934 [9]. μ *grande* corresponds to a large neutrino mass, μ *piccolo* to a small mass, and $\mu = 0$ to a zero mass.

1.2 Discovery of the neutrino

The next step was to verify that the neutrino exists in nature. Traditionally, charged particles are detected via their electromagnetic interactions with surrounding targets or detector materials. But, for the ultra-penetrating, neutral neutrino, it was not clear whether there would be any mechanism to detect its presence. Bethe and Peierls predicted a possible detection process, essentially running the beta decay process backwards,

$$\overline{\nu}_e + p \rightarrow \beta^+ + n. \tag{1.1}$$

Here, Equation 1.1 is written in the current convention, where neutrinos ν are differentiated by their antiparticle partners, antineutrinos $\overline{\nu}$. Furthermore, three types or flavors of neutrinos are now known, e.g. the electron antineutrino, $\overline{\nu}_e$, as described below.

This inverse beta decay (IBD) interaction was calculated to have an incredibly small cross section of $\mathcal{O}(10^{-44}\,\mathrm{cm}^2)$ [10]. Although deemed impossible to detect, Cowan and Reines designed an experiment to utilize the distinct IBD signature to capture neutrinos emitted by unstable fission products that undergo beta decay within a nuclear reactor. The first attempt, Project Poltergeist, consisted of a 300 L cylindrical tank of cadmium propionate-doped liquid scintillator surrounded by 90 photomultipler tubes (PMTs). The detector was surrounded by lead and boron-loaded paraffin to shield from cosmic-ray neutrons and other particles ejected by the Hanford reactor 11 m away, located in Washington. The backgrounds were still large, although they claimed a small difference in count rate between the reactor-on and -off periods, indicating an excess of events, i.e. neutrinos [11]. To confirm this excess, the team moved to a more powerful reactor at the Savannah River site in South Carolina and built a larger detector 12 m underground to shield from cosmogenic backgrounds, as shown in Figure 1.4. In 1960, Cowan, Reines, and their team observed a cross section of $(1.2^{+0.7}_{-0.4})\times10^{-43}\,\mathrm{cm}^2$ and rate of 3.0 counts/hour, in agreement with the predictions. This measurement confirmed the existence of neutrinos [12]. The techniques employed here, including the use of the IBD coincidence circuit, scintillating target material, and using the Earth as shielding, continue to be the mainstays of modern reactor neutrino experiments.

The discovery of the neutrino, technically the electron antineutrino ($\overline{\nu}_e$), at the Savannah River reactor opened the door to study neutrinos from a variety of sources, including the Sun, the atmosphere, and particle accelerators. In 1959, Pontecorvo first predicted that ν_e and ν_μ were different particles [13]. Accelerator experiments proved

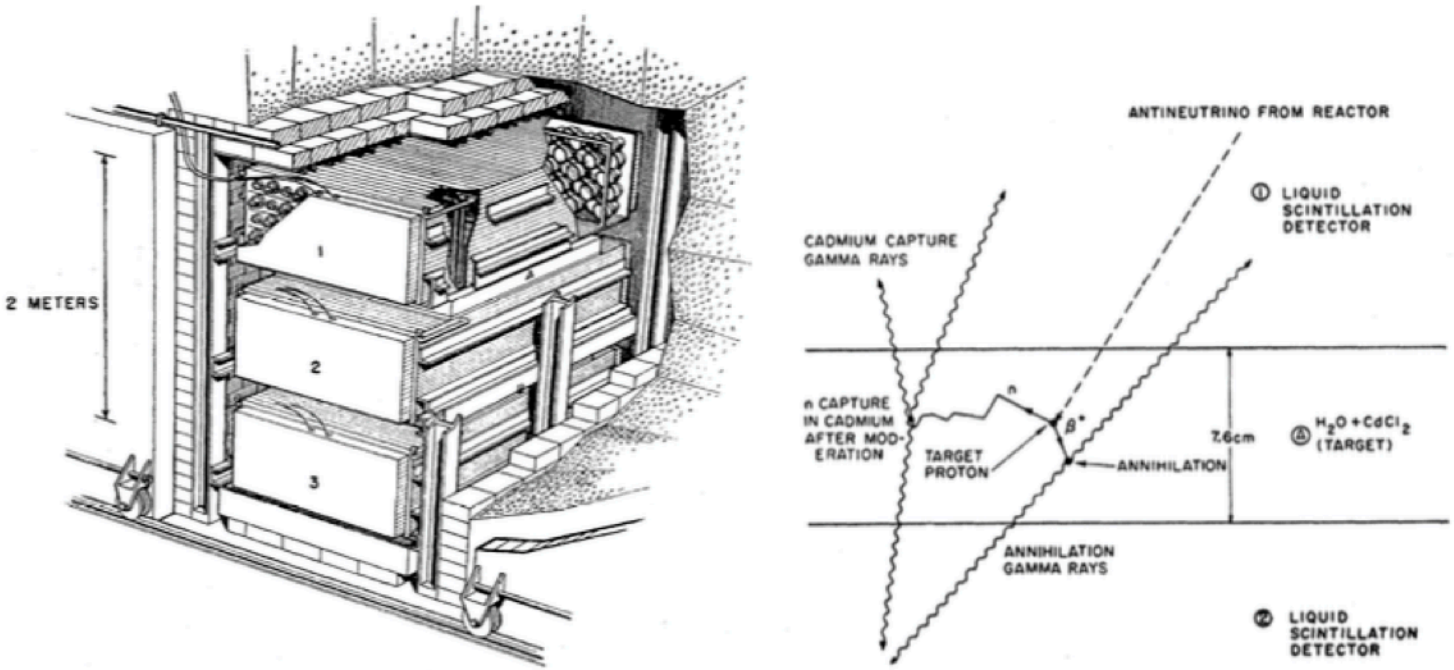

Figure 1.4: **(left)** Schematic of the detector used by Cowan and Reines at the Savannah River reactor. The detector consisted of three layers each with 1400 L liquid scintillator and 110 PMTs (labelled I, II, III) sandwiched between two layers of 200 L cadmium chloride-doped water (labelled A, B). Here, water is used as the target material and the liquid scintillator as the detection medium. Surrounding earth, steel, lead, and polyethylene were used as shielding. **(right)** Illustration of the IBD detection mechanism within the detector [12].

this theory correct, with the addition of a third particle, through the discovery of the muon (ν_μ) and tau (ν_τ) neutrinos in 1962 and 2000, respectively [14, 15]. The three neutral neutrinos and their antiparticles were added to the Standard Model of particle physics, a theoretical framework that describes the unification of the electromagnetic, weak, and strong interactions, as massless, chargeless leptons.

1.3 Massless neutrinos in the Standard Model

The Standard Model is a quantum field theory that describes the interactions and dynamics of the elementary particles through the strong, weak, and electromagnetic interactions. In this model, neutrinos are classified as neutral, spin-1/2 fermions serving as the weak isospin partners to the charged electron, muon, and tau leptons:

$$\begin{pmatrix} \nu_e \\ e^- \end{pmatrix}, \begin{pmatrix} \nu_\mu \\ \mu^- \end{pmatrix}, \begin{pmatrix} \nu_\tau \\ \tau^- \end{pmatrix} \tag{1.2}$$

Analogous 3-generation doublets are constructed from the lepton antiparticles. In general, the Dirac equation represents the equation of motion for spin 1/2 fermions,

$$(i\gamma^\mu \partial_\mu - m)\psi = 0, \tag{1.3}$$

where γ^μ is the set of 4×4 gamma matrices, ∂_μ the momentum operator ($\hat{p_\mu} \rightarrow i\partial_\mu$), m the mass of the particle, and ψ a 4-component spinor. This energy-momentum conservation equation is compatible with the Klein-Gordon equation for spin 0 particles, the relativistic version of the time-dependent Schrödinger wave equation. It ensures positive probability densities and takes into account intrinsic particle spin. Through algebraic manipulations, a continuity equation can be obtained where the fermion current is conserved. In a Feynman diagram, this is represented by the balanced flow of particles (antiparticles) in and out of vertices.

In the case of the charged leptons ($l^{\pm}$), ψ represents the 4 possible solutions or degrees of freedom:

$$\psi = \begin{pmatrix} l_R^- \\ l_L^- \\ l_R^+ \\ l_L^+ \end{pmatrix}, \tag{1.4}$$

where R represents right-handed spin-projected helicity[1] states and L the left-handed states. However, in the basic electroweak theory contained in the Standard Model [16–18], parity (mirror symmetry) is maximally violated under weak interactions. Wu showed this in 1957 through experiments of beta decay using spin-aligned ^{60}Co nuclei, resulting in the detection of electrons preferentially in one direction [19]. Yang and Lee produced a theory to explain the observations, where the chirality of the emitted neutrinos are always left-handed, while antineutrinos are right-handed, no matter the frame of reference. However, this requires that "[...] the mass of the neutrino must be zero, and its wave function need only have two components instead of the usual four" [20]:

$$\psi = \begin{pmatrix} \nu_L \\ \overline{\nu}_{R\cdot} \end{pmatrix}. \tag{1.5}$$

Thus, neutrinos have zero mass in the Standard Model, as the mass terms in the Lagrangian (Dirac mass terms) require a coupling between the left- and right-handed chiral partners.[2]

Parity non-conservation is built into the weak interaction theory through vector-axial (V-A) couplings, as compared to the vector coupling in QED. In the Lagrangian,

[1] Helicity is the projection of a particle's spin along the direction of motion, $\frac{2|\vec{s}\cdot\vec{p}|}{|\vec{p}|}$.

[2] Chirality is the Lorentz invariant form of helcity. Chirality and helicity are the same for massless particles. Neutrinos are approximately massless so these terms are being used casually and interchangeably here.

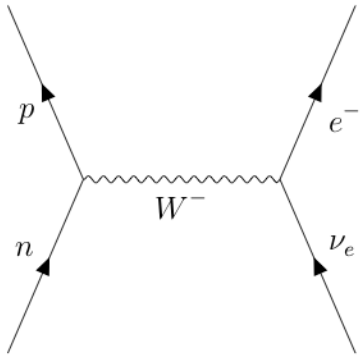

Figure 1.5: Mediation of beta decay variant with the W^- gauge boson propagator.

the weak charged-current (CC) takes the form

$$j^{CC}_{weak} = \frac{g_w}{2\sqrt{2}}\overline{\psi}\gamma^\mu(1-\gamma^5)\psi, \tag{1.6}$$

where g_w is the weak coupling constant with value 0.65. The γ^μ term represents the vector component that can flip parity and the $\gamma^u\gamma^5$ the axial (psuedo-vector) component that does not change under parity. The relative strengths of each are comparable, giving maximal parity violation. Total lepton and lepton family (generation) number are conserved.

Fermi's theory of beta decay is altered by expanding the point-like interaction through the mediation of a heavy gauge boson, $W^\pm$, as seen in the charged-current interaction in Figure 1.5.

Through the transition amplitude in the low-energy limit, the Fermi coupling G_F can then be related to the V-A theory constants,

$$\frac{G_F}{\sqrt{2}} = \frac{g_w^2}{8M_W}, \tag{1.7}$$

where M_W is the mass of the W boson, with value $80.376\,\mathrm{GeV/c^2}$ [21]. The heavy mass of the W limits the distance range where the weak interaction is relevent, unlike the infinte range of the electromagnetic force mediated by the photon. The neutral Z^0 boson also weakly couples to the fermions, but cannot change weak isospin states

(neutral-current interactions).

The Standard Model is now complete with the discovery of the mass-creating Higgs boson by the ATLAS [22] and CMS [23] experiments at the LHC in 2012. The model includes 3 massless neutrinos that only interact through the left-handed weak interaction. Collider experiments at the LEP electron-positron accelerator have confirmed that three generations of light neutrinos exist, through measurements of the width of the Z boson mass peak [24]. Thus far, the predictions of the Standard have been experimetally upheld in all sectors, from the leptons, quarks, and gauge bosons. Despite its extreme success, the Standard Model is not a full representation of the physical world, as it has been shown through solar and atmospheric oscillation experiments that neutrinos have mass.

1.4 Solar and atmospheric neutrino anomalies

The study of solar neutrinos began with a lack of understanding of the nuclear reactions that fuel the Sun. It was thought that the Sun burns primarily by the so-called proton-proton (pp) chain reaction, involving the conversion of light hydrogen nuclei into heavier helium along with the release of 26 MeV from the difference in binding energy. As an intermediate step deuteron is formed and through the weak charged-current interaction, an electron neutrino is emitted by necessity. This process is rare, due to the fact that the initial protons must overcome a Coulomb repulsion via quantum tunnelling, even at the high temperature and density of the Sun. Nonetheless, roughly 10 billion neutrinos with mean energy of 0.26 MeV reach a square centimeter of Earth every second.

Davis built an experiment to detect these solar neutrinos, an endeavor that lasted over 25 years consisting of many experimental attempts and theoretical calculations performed by Bahcall. The technique, first introduced by Pontecorvo in 1945 [25],

involved using 390,000 L of C_2Cl_4 (chlorine-37, 24% abundance) shielded by layers of rock underground at the Homestake Gold Mine in South Dakota and waiting for neutrinos to interact via the radiochemical reactions:

$$\nu_e + {}^{37}Cl \rightarrow {}^{37}Ar + e^- \xrightarrow{t_{1/2}=35\,days} atomic\ e^- + {}^{37}Ar \rightarrow {}^{37}Cl + Auger\ e^-. \quad (1.8)$$

This reaction requires the neutrinos to interact with an energy of greater than 0.81 MeV. Neutrinos coming from the pp chain are below this threshold, with a maximum energy of 0.42 MeV. Heavier, hotter stars can produce higher energy neutrinos, up to 15 MeV, through the production of ^{8}B. The probability of this temperature-dependent process is extremely small, as the proton must undergo tunnelling to pass through the Coulomb barrier of the very positively-charged ^{7}Be nucleus. Davis and Bahcall persisted, with first results in 1968 consisting of an observed upper limit of 3 SNU[3] [26] and a prediction of 7.5±3 SNU on the flux of all above-threshold solar neutrinos (i.e. ^{7}Be, ^{8}B, pep, CNO, hep) [27].

The Homestake experiment continued until 1998, with all measurements indicating that only 1/3 of the expected neutrinos were being detected (see Figure 1.6); the final value for the observed rate was 2.6±0.2 SNU [28] with a standard solar model theoretical prediction of 8.5±1.8 SNU [29]. This discrepancy became known as the "solar neutrino problem".

The results were met with skepticism as the non-real time extraction of radioactive gas and the counting individual chlorine atoms was technically challenging. Measurements in 1985 by the Japanese water Cherenkov experiment, Kamiokande-II, confirmed the observation. The 4.5 kton detector outfitted with PMTs under 1 km of mountain was built to observe the quintessential Grand Unified Theory (GUT)

[3]SNU represents "solar neutrino units" and is defined as the neutrino flux producing 10^{-36} captures per target atom per second.

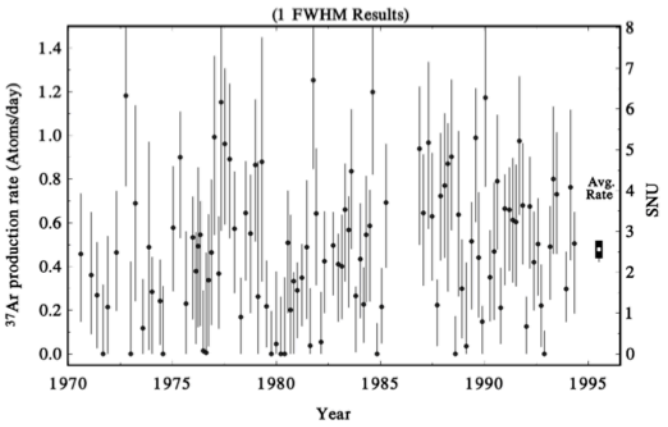

Figure 1.6: A total of 108 events were detected by the Homestake experiment over 25 years of operation [28].

interaction of proton decay,

$$p^+ \rightarrow e^+ + \pi^0. \tag{1.9}$$

Detecting ^{8}B solar electron neutrinos[4] with Kamiokande was also possible and favorable, as neutrino-electron elastic scattering within water retains direction and energy information, possibly revealing the source of the incident neutrinos.[5] In 1989, Kamiokande-II reported the observation of ^{8}B solar neutrinos [30] using the angular distribution of the electron signals as proof. The measured flux ratio to the standard solar model prediction was $0.46\pm0.13(\text{stat.})\pm0.08(\text{syst.})$, in agreement with the Homestake result. The doubts surrounding the radiochemical detector were subdued, but the evidence from Kamiokande-II could not reconcile the disagreement between the models and experiments.

Solar neutrinos were not the only neutrinos from the sky raising questions. Cosmic rays, composed largely of high-energy protons originating from outside the solar sys-

[4]Lower energy solar neutrinos cannot be detected in water due to the velocity (energy) threshold of Cherenkov light, $\beta > \frac{1}{n} \sim 0.75$, where $\beta = \frac{v}{c}$.

[5]All neutrino types can scatter from electrons, however at energies in the ∼MeV range, the ν_e interactions dominate with a substantially larger cross section.

tem, interact with the air nuclei at high altitudes in the atmosphere as they impinge on Earth. These interactions stimulate the production of π and K mesons, which decay into unstable muons and further disintegrate into electrons and positrons. As weak processes, ν_μ ($\overline{\nu}_\mu$) and $\nu_e(\overline{\nu}_e)$ are also generated, with energies in the GeV to TeV region.[6] For each charged pion decay, 2 muon neutrinos (ν_μ+$\overline{\nu}_\mu$) and one electron neutrino (ν_e, $\overline{\nu}_e$) are produced and thus a flux ratio of

$$\frac{\mu}{e} = \frac{\nu_\mu + \overline{\nu}_\mu}{(\nu_e, \overline{\nu}_e)} = 2, \tag{1.10}$$

should be observed as a function of energy. The zenith angle of the neutrino flux entrance and exit should also be related at these energies, $\theta_{in} = \pi - \theta_{out}$, corresponding to an up-down symmetry as cosmic rays approach the atmosphere uniformly.[7]

Kamiokande-II conducted an analysis on atmospheric neutrinos, as they are a significant background for the proton decay signal. In 1988, the collaboration reported the number of ν_μ and $\overline{\nu}_\mu$events observed in the Cherenkov detector to be 85±9.2 (stat.) and 93±9.6 (stat.), respectively [31]. The electron-like events agreed with the predictions from Monte Carlo (MC), while the muon-like events showed a deficit when compared to the models on the order of 40%. Another water Cherenkov experiment, IMB-3 [32], also measured a small flux ratio, along with a steel calorimeter experiment, Soudan-2 [33].[8] This discrepancy became known as the "atmospheric neutrino anomaly".

[6]The flux decreases as $E^{-2.7}$ in this energy range.

[7]For lower energy cosmic rays (< 10 GeV), the particles' trajectories can be influenced by Earth's geomagnetic field and the flux will not exhibit up-down symmetry.

[8]The calorimeter experiments Fréjus [34] and NUSEX [35], with very limited statistics, did not observe any deviation between the observed fraction of muon-like to electron-like events and MC.

1.5 Discovery of neutrino oscillation

Increasing amounts of corroborating empirical evidence suggested that both the solar and atmospheric anomalies were not due to experimental or theoretical errors. The only plausible solution, and the least favored, was that the physics was incorrect. Decades earlier, Pontecorvo had theorized about some properties that electrically neutral neutrinos could exhibit. Namely, whether neutrinos created of a certain flavor could quantum mechanically "mix" or oscillate into a different flavors. Though the concept was not new, as it had been created to solve the τ-θ puzzle of kaon decay, it could be applied to neutrinos as electric charge and total lepton number would remain conserved. Quarks also undergo mixing through the weak interaction [36], where the transition within a generation is more probable than between families. The transmutation between the weak and mass eigenstates is parametrized by the Cabibbo-Kobayashi-Maskawa (CKM) matrix. Although there was clear motivation and precedent for particle mixing, the large deficit observed by the solar and atmospheric neutrino experiments could not be produced with the degree of mixing exhibited by the quark sector. Furthermore, for neutrino oscillations to be realized in nature, flavor (weak) eigenstates need to exist as a linear superposition of mass eigenstates, requiring the neutrinos to have mass.

More statistics were needed to understand the missing number of neutrinos. The 50 kton Super-Kamiokande detector, was built to collect atmospheric neutrino events faster than any other experiment. In 1998, the collaboration announced they had obtained evidence for atmospheric neutrino oscillations from the measurements of a smaller $(\frac{\mu}{e})_{data}/(\frac{\mu}{e})_{MC}$ flux ratio as compared to predictions for sub- and multi-GeV energies and zenith angle distributions showing a deficit in the upward flux at 6σ [37]. No discrepancy was observed in the electron-like events, suggesting that electron-neutrinos are immune to oscillations at path lengths on the order of the Earth's diameter and that muon neutrinos had to be oscillating into the third

neutrino type, ν_τ.

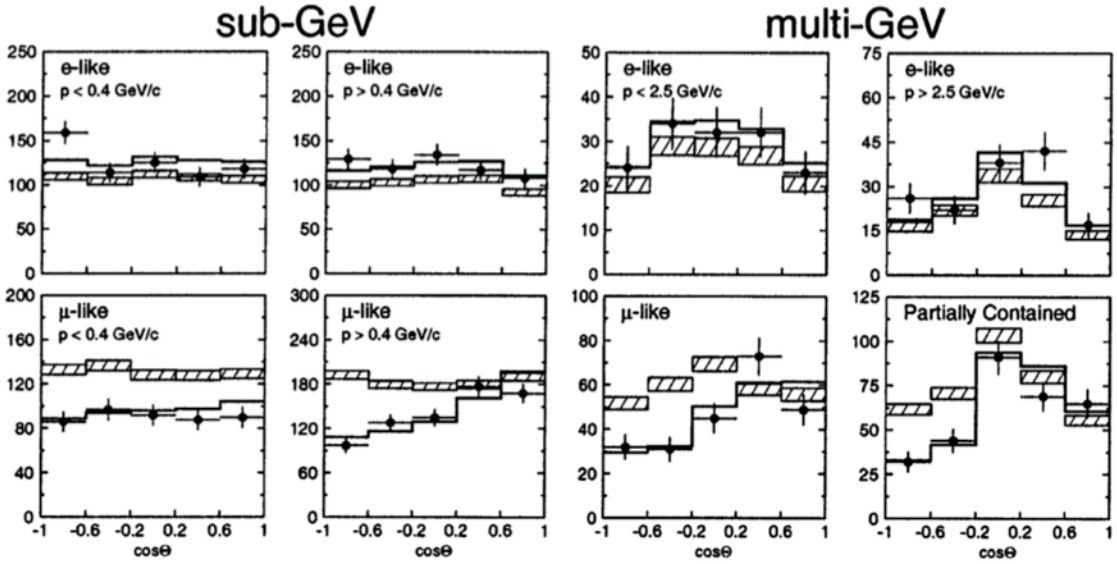

Figure 1.7: Super-Kamiokande event distributions reported in $\cos\theta_{sun}$ for **(left)** sub-GeV and **(right)** multi-GeV events. Upward-going events have $\cos\theta$ = -1 and downward-going have $\cos\theta = 1$. The hatched regions represent the MC prediction for no neutrino oscillations. The bold line shows the expectation for $\nu_\mu \leftrightarrow \nu_\tau$ oscillations.

The results from Super-Kamiokande were convincing to solve the atmospheric neutrino problem, but a claim to the discovery of neutrino oscillations could not be made without detecting all neutrino types. The Sudbury Neutrino Observatory (SNO) was constructed in a Canadian nickel mine to understand the solar neutrino problem. The 1000 ton detector used similar technology to that of Super-Kamiokande, with the exception of heavy water (D_2O) as a target. SNO was sensitive to the same electron-elastic scattering as Super-Kamiokande, but the deuterium in the water allowed for charged-current and neutral-current interactions. Because of the threshold to generate heavy leptons, only ν_e can participate in the charged-current process, whereas all neutrino types can initiate neutral-current reactions. In 2001, SNO solved the solar neutrino problem with a ^{8}B flux measurement of $5.44\pm0.99\times10^6\,\mathrm{cm^2 s^{-1}}$, in agreement with the standard solar models [38]. Furthermore, the results from SNO are regarded as the first direct demonstration of neutrino flavor change, implying

that neutrinos have mass.[9] The puzzle of the solar and atmospheric anomalies lead to the groundbreaking discovery of neutrino oscillations and the leaders of the Super-Kamiokande and SNO collaborations were jointly awarded the 2015 Nobel Prize in Physics "for the discovery of neutrino oscillations, which shows that neutrinos have mass".

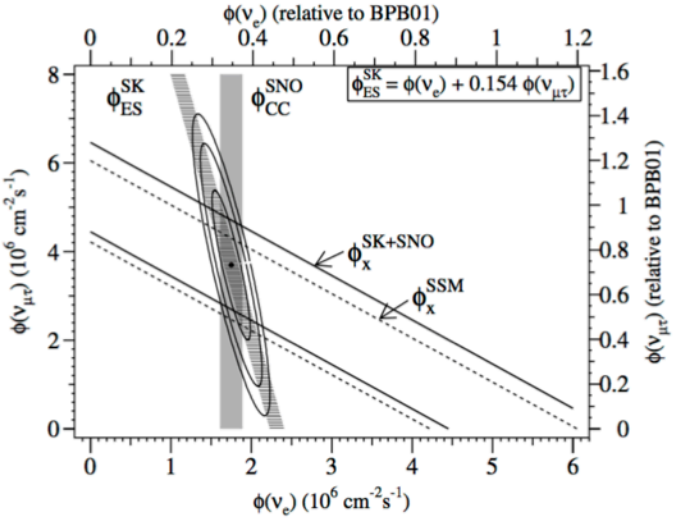

Figure 1.8: Combined $\nu_{\mu,\tau}$ flux versus ν_e flux for boron-8 solar neutrinos from SNO and Super-Kamiokande [38].

The Kamioka Liquid Scintillator Antineutrino Detector (KamLAND) observed the first antineutrino oscillations in 2005 at an average distance of ∼200 km from the nuclear power reactors in Japan, illustrating that antiparticles also mix [39]. Figure 1.9**(left)** shows the beautiful oscillation pattern highlighting the multiple minima and maxima mapped by KamLAND. As will be detailed in Chapter 2, reactors provide a powerful, plentiful source of antineutrinos providing the statistics to make precision measurements. KamLAND used this feature to make detailed measurements of the reactor neutrino energy spectrum further, allowing heavy constraints on the mass difference between the neutrino states participating in the solar anomaly

[9]The flavor change observed by SNO includes modifications from the Mikheyev-Smirnov-Wolfenstein (MSW) effect, altering the general vacuum oscillation probability as neutrinos travel through electron-rich matter, like the sun.

(Δm^2_{21}), confirming the "large mixing angle" solution to the solar neutrino problem. Figure 1.9**(right)** summarizes those constraints with respect to the SNO solar measurements.[10] Furthermore, KamLAND paved the way for precision neutrino science at reactors with large, multi-ton liquid scintillator detectors.

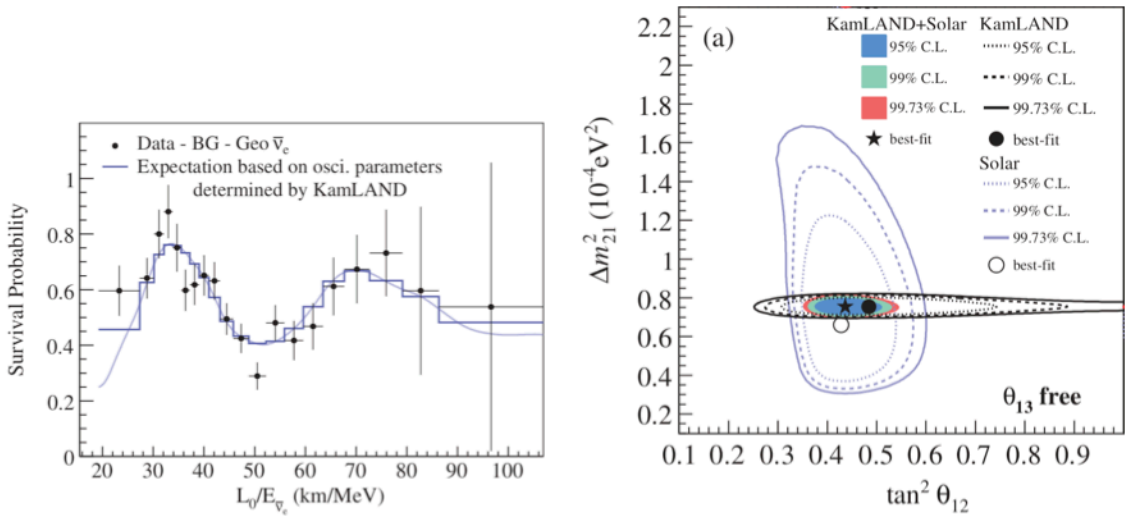

Figure 1.9: **(left)** $\overline{\nu}_e$ survival probability as a function of L/E measured by the KamLAND experiment. This was the first demonstration of antineutrino oscillations [41]. **(right)** Allowed regions of solar mixing parameters with contraints from KamLAND and SNO solar data. The shaded region shows the combined analysis, heavily constraining Δm^2_{21} through KamLAND's spectral distortion measurements [42].

1.6 Massive neutrino theories

Despite its extreme success, the Standard Model is not sufficient to explain our full understanding of the Universe, including neutrinos with mass. Extensions to the Standard Model that incorporate massive neutrinos must include a weak Lagrangian with a mass term. Generally, this is achieved through the Dirac mass term,

$$\mathcal{L}_D = -m(\overline{\psi}_L\psi_R + \overline{\psi}_R\psi_L). \tag{1.11}$$

[10] KamLAND was also the first experiment to measure geoneutrinos originating from nuclear fission of uranium and thorium isotopes in the Earth's mantle [40].

It is clear from this expression that a non-zero Dirac mass requires both left- and right-handed chiral states. To satisfy gauge invariance, the Higgs field is introduced through a Yukawa coupling, providing the particle mass. Constructing a neutrino mass can be achieved in this framework, rewriting the Lagrangian as

$$\mathcal{L}_D^{\nu} = -m_D \overline{\nu}_R \nu_L + h.c. \tag{1.12}$$

A distinct, right-handed *sterile* neutrino is required to exist as a weak isospin singlet, and thus not interact through any force besides gravity, evading detection. However, a very small Yukawa coupling is required to generate the very small neutrino mass indicated by experimental upper bounds, in tension with the more massive charged leptons and quarks.

It is possible to make a right-handed state from a left-handed state through charge conjugation for neutral particles [43]. The charged conjugated spinor takes the form

$$\psi^c = \hat{C}\overline{\psi}^T, \tag{1.13}$$

where $\hat{C}$ is the charge conjugation operator (converts particle into antiparticle) and $\overline{\psi}^T$ is the complex conjugate spinor. Applied to a left-handed chiral state, a right-handed state is obtained:

$$\psi_R = \hat{C}\overline{\psi}_L^T. \tag{1.14}$$

The spinor, known as the Majorana field, can then be written as

$$\psi = \psi_L + \psi_R = \psi_L + \hat{C}\overline{\psi}^T = \psi_L + \psi_L^c, \tag{1.15}$$

implying that $\psi^c = \psi$, i.e. that the particle and antiparticle states are identical. In the case of the neutrino, the Majorana mass term can be expressed in the Lagrangian

as

$$\mathcal{L}_M^\nu = -\frac{1}{2} m_M \overline{\nu}_L^c \nu_L + h.c., \tag{1.16}$$

coupling the neutrino and antineutrino components. But, as the neutrino and antineutrino are the same particle, this theory inherently violates total lepton number conservation.

It is not possible to form such a Majorana mass term with the left-handed neutrinos in the Standard Model.[11] However, Majorana neutrinos can still be considered if a right-handed sterile neutrino exists, as introduced to create the Dirac mass term. Thus, a general Lagrangian can be constructed from both Dirac and Majorana, including left- and right-handed, charged conjugated fields:

$$\mathcal{L}_{mass}^\nu \sim \begin{pmatrix} \overline{\nu}_L^c & \overline{\nu}_R^c \end{pmatrix} \begin{pmatrix} m_L & m_D \\ m_D & m_R \end{pmatrix} \begin{pmatrix} \nu_L \\ \nu_R^c \end{pmatrix} + h.c., \tag{1.17}$$

where m_D is the Dirac mass, m_L the left-handed Majorana mass, and m_R the right-handed Majorana mass. The mass matrix with off-diagonal terms indicates that the chiral fields ν_L and ν_R are not mass eigenstates and do not correspond to a physical particle with definite mass. The observable masses can be obtained by diagonalizing the matrix for eigenstates ν_1 and ν_2. Forcing $m_L = 0$ as prescribed by the Standard Model and taking the limit where $m_R >> m_D$ with m_D on the order of the quark and charged lepton masses, the mass terms simplify to

$$m_1 = \frac{m_D^2}{m_R},\ m_2 = m_R(1 + \frac{m_D^2}{m_R^2}) \approx m_R. \tag{1.18}$$

With these reasonable assumptions, m_1 is very small, representing the mass of the left-handed light Majorana neutrino while m_2 is the very large mass of the mostly

[11] This would require extra Higgs fields with different weak isospin and hypercharge quantum numbers.

heavy right-handed sterile neutrino. This is known as the see-saw mechanism, as the existence of a GUT-scale heavy partner of $\mathcal{O}(10^{15}\,\text{eV})$ can produce the very small mass ($\lesssim$ meV) of the known active neutrinos [44, 45].

1.7 Quantum mechanical description of oscillations

Created with or annihilated to produce a charged lepton, left-handed neutrinos interact via the weak force in flavor (weak) eigenstates, i.e. ν_e, ν_μ, ν_τ, and the antineutrino states. Analogous to the quark model and the CKM matrix, the three neutrino flavor states do not have a one-to-one correspondance to the eigenstates with definite mass (ν_i), resulting in mixing or oscillations. Although the Standard Model does not include massive neutrinos, such a process can be described by a unitary transformation[12] within the charged-current (CC) weak Lagrangian where the weak states are linear combinations of the left-handed components of the 3 massive neutrino fields:

$$\mathcal{L}^{CC}_{weak} = \frac{-g}{2\sqrt{2}} \sum_{\alpha,i} [\bar{l}_\alpha \gamma^\mu (1-\gamma_5) U_{\alpha i} \nu_i W^-_\mu + \overline{\nu}_i \gamma^\mu (1-\gamma_5) U^*_{\alpha i} l_\alpha W^+_\mu], \tag{1.19}$$

where U is the 3×3 unitary mixing or Pontecorvo-Maki-Nakagawa-Sakata (PMNS) matrix,

$$\begin{pmatrix} \nu_e \\ \nu_\mu \\ \nu_\tau \end{pmatrix} = \begin{pmatrix} U_{e1} & U_{e2} & U_{e3} \\ U_{\mu 1} & U_{\nu 2} & U_{\mu 3} \\ U_{\tau 1} & U_{\tau 2} & U_{\tau 3} \end{pmatrix} \begin{pmatrix} \nu_1 \\ \nu_2 \\ \nu_3 \end{pmatrix}. \tag{1.20}$$

Under charge, parity, and time reversal (CPT) symmetry, the PMNS matrix is identical for antineutrinos. A neutrino of specific flavor is thus a mixed state or coherent

[12] The assumption that $UU^\dagger = \mathbb{1}$ is valid in the case of three neutrino flavors with Dirac masses. The unitarity condition is not required for the case of more than three generations or Majorana neutrinos, as the three light neutrinos would be mixed with other light or heavy degrees of freedom.

superposition of neutrino states with different masses[13], e.g. in the case of the electron neutrino,

$$|\nu_e\rangle = U_{e1}\,|\nu_1\rangle + U_{e2}\,|\nu_2\rangle + U_{e3}\,|\nu_3\rangle\,. \tag{1.21}$$

The PMNS matrix can be parameterized by three mixing angles θ_{12}, θ_{23}, θ_{13} and one CP violating phase δ_{CP} if ν_i is Dirac as

$$\begin{aligned} U &= \begin{pmatrix} 1 & 0 & 0 \\ 0 & c_{23} & s_{23} \\ 0 & -s_{23} & c_{23} \end{pmatrix} \begin{pmatrix} c_{13} & 0 & s_{13}e^{-i\delta_{CP}} \\ 0 & 1 & 0 \\ -s_{13}e^{i\delta_{CP}} & 0 & c_{13} \end{pmatrix} \begin{pmatrix} c_{12} & s_{12} & 0 \\ -s_{12} & c_{12} & 0 \\ 0 & 0 & 1 \end{pmatrix} \\ &= \begin{pmatrix} c_{12}c_{13} & s_{12}c_{13} & s_{13}e^{-i\delta_{CP}} \\ -s_{12}c_{23} - c_{12}s_{23}s_{13}e^{i\delta_{CP}} & c_{12}c_{23} - s_{12}s_{23}s_{13}e^{i\delta_{CP}} & s_{23}c_{13} \\ s_{12}s_{23} - c_{12}c_{23}s_{13}e^{i\delta_{CP}} & -c_{12}s_{23} - s_{12}c_{23}s_{13}e^{i\delta_{CP}} & c_{23}c_{13} \end{pmatrix} \end{aligned} \tag{1.22}$$

where s_{ij} represents $\sin\theta_{ij}$ and c_{ij} represents $\cos\theta_{ij}$. If ν_i are Majorana in nature, two additional CP phases, α_{21}, α_{31} are required.

The mixing parameters must be determined experimentally. A convenient quantity to consider is the probability for a neutrino of one flavor to oscillate into another. For simplicity, the oscillation probability can be derived assuming two neutrino flavors in vacuum.[14] In this scenario, a flavor state $|\nu_\alpha\rangle$ can be written as a coherent

[13]The reason for this is that the neutrino masses are too small to be experimentally resolved and it is unknown which mass state the neutrino was produced in. Thus, the neutrino stemming from the weak vertex is a coherent superposition of mass states ν_i. Otherwise, if the mass state was known, it could be followed along its trajectory and the mixing would no longer be probabilistic.

[14]This approximation is valid for many applications due to the small value of θ_{13} and the large difference between mixing angles, e.g. $\nu_\mu \leftrightarrow \nu_\tau$ oscillations with little contribution from ν_e and solar oscillations. Reactor neutrino experiments with baselines <100 km can also be considered in the two neutrino case, which is applies to this thesis.

superposition of mass eigenstates $|\nu_k\rangle$,

$$|\nu_\alpha\rangle = \sum_{k=1,2} U_{\alpha k} |\nu_k\rangle \,, \tag{1.23}$$

where U is the two-dimensional rotation matrix with mixing angle θ. Propagating the initial neutrino wave function as a free particle using the time-dependent Schrödinger equation and assuming a neutrino with energy E_ν and mass m as an ultra-relativistic particle ($E_\nu \gg m$) one arrives to the following oscillation probability expression:

$$P(\nu_\beta \to \nu_\alpha) = \sin^2(2\theta) \sin^2\left(\frac{\Delta m^2 L}{4E_\nu}\right), \tag{1.24}$$

where $\Delta m^2 = m_1^2 - m_2^2$ and $E = E_1 = E_2$. Appearance experiments rely on this formula to determine the amount of ν_α in a neutrino beam that has changed into ν_β. The probability for detecting the original flavor neutrino at some distance L, the survival probability, is then

$$P(\nu_\alpha \to \nu_\alpha) = 1 - P(\nu_\beta \to \nu_\alpha) = 1 - \sin^2(2\theta) \sin^2\left(\frac{\Delta m^2 L}{4E_\nu}\right). \tag{1.25}$$

Disappearance experiments begin with a known flux of ν_α neutrinos and observe how this flux disappears with distance from the source, or baseline. If neutrinos are massless, i.e. $\Delta m_{ij}^2 = 0$, it is evident from Equations 1.24 and 1.25 that the oscillation probability vanishes, contrary to empirical evidence.[15]

The oscillation probability can be understood heuristically by considering the creation of a neutrino with definite flavor and a linear combination of mass states, each of slightly different mass. As the neutrino travels towards a detector at a distance L from the source, the states of definite mass propgate at different phases, reaching the detector with a relative phase difference compared to the original neutrino state.

[15]It should be noted that the oscillation or change of neutrino flavor cannot be accounted for by neutrino interactions with matter. However, interactions with electrons can enhance oscillations by altering the effective mass of propagating neutrinos (MSW effect).

From Equation 1.24, it can be seen that this oscillation is governed by the parameters θ and Δm^2, and can be tuned experimentally by the ratio of L/E. The mixing angle θ dictates the degree of separation between the flavor and mass states, i.e. the amplitude of oscillation. For $\theta = 0$, oscillations do not occur, while $\theta = \frac{\pi}{4}$ corresponds to maximal mixing at some distance between the source and detector. The mass splitting Δm^2 controls the phase difference between the mass state wave functions or the frequency of the oscillation.[16] For a certain value of the mass splitting, the probability of oscillation will vary as the ratio of $\frac{L}{E}$ varies. It is optimal to position a detector at an oscillation minimum or at

$$\frac{\Delta m^2}{4E_\nu} L = \frac{\pi}{2} \Rightarrow \frac{L}{E_\nu} = \frac{2\pi}{\Delta m^2}. \tag{1.26}$$

One must consider that neutrino beams diverge as L^2 and the cross-section decreases with decrease in E_ν. In the case of solar and atmospheric experiments, $\frac{L}{E_\nu}$ are predetermined and thus the range of oscillation parameters that can be scanned is limited to those with observable probabilities.

Measurements of neutrinos from nuclear reactors, accelerators, the sun, and cosmic rays have all been used to develop a consistent model of oscillations and determination of mixing parameters. Table 1.1 summarizes the accepted measured values for the known neutrino mixing parameters.

If non-weakly interacting, beyond-the-Standard Model sterile neutrinos exist, they could mix with the active states requiring the addition of new mixing parameters.[17] However, experimentally it would only be possible to resolve this oscillation if the sterile neutrino mass was much smaller ($\lesssim$ keV) than those expected at the GUT

[16] Equation 1.24 illustrates the major limitations of oscillation experiments: the absolute mass of the neutrinos cannot be determined since it is only sensitive to the difference in mass eigenvalues. Similarly, the ordering of the mass states as $\sin^2(\Delta m^2) = \sin^2(-\Delta m^2)$ cannot be determined via oscillation experiments, labelled the "mass hierarchy" problem.

[17] In the case of one sterile neutrino, a mass splitting, three mixing angles, and two additional CP phases would be required.

Parameter (ordering)	Value	3σ	Source
Δm^2_{21} [$\times 10^{-5}\,\mathrm{eV}^2$]	7.37	6.93-7.96	solar
$\lvert\Delta m^2_{31}\rvert$ [$\times 10^{-3}\,\mathrm{eV}^2$] (NO)	2.56	2.45-2.69	atmospheric
$\lvert\Delta m^2_{32}\rvert$ [$\times 10^{-3}\,\mathrm{eV}^2$] (IO)	2.54	2.42-2.66	atmospheric
$\sin^2\theta_{12}$	0.297	0.250-0.354	solar+reactor+accelerator
$\sin^2\theta_{23}$ (NO)	0.425	0.381-0.615	atmospheric
$\sin^2\theta_{23}$ (IO)	0.589	0.384-0.636	atmospheric
$\sin^2\theta_{13}$ (NO)	0.0215	0.0190-0.0240	reactor
$\sin^2\theta_{13}$ (IO)	0.0216	0.0190-0.0242	reactor

Table 1.1: Current observed neutrino oscillation best-fit parameters and 3σ allowed region according to the 2018 Particle Data Group neutrino review [21]. The normal mass ordering (NO) corresponds to the case where $m_1 < m_2 < m_3$, while the inverted ordering (IO) corresponds to $m_3 < m_1 < m_2$. The CP-violation term δ_{CP} and the Majorana phases $\alpha_{21,31}$ are unknown.

scale, as the mass splitting determines the frequency and L/E. Since a sterile neutrino cannot interact with any detector material, its presence can only be detected by measuring the disappearance or appearance of an active state, preferably at an L/E where active mixing is minimal. In such a case, assuming a 3+1 model with one additional sterile state ν_4, the survival probability of, for example $\overline{\nu}_e$, is analogous to Equation 1.25:

$$P(\overline{\nu}_e \to \overline{\nu}_e) = 1 - \sin^2(2\theta_{14}) \sin^2\left(1.27\Delta m^2_{41} \frac{L[\mathrm{m}]}{E_\nu[\mathrm{MeV}]}\right). \tag{1.27}$$

where θ_{14} is the mixing angle between the first active state and the sterile mass state and Δm^2_{41} is the mass splitting between the two states. This assumes the 2-neutrino approximation, which is the relevent regime for this thesis.

Chapter 2

Reactor antineutrinos and open questions

Nuclear reactors have played a key role in the study of the neutrino and its properties, including the first observation of antineutrinos [12] and the discovery of $\overline{\nu}_e$ oscillations [41], as described in Chapter 1. Emitting a pure, intense isotropic cloud of low energy (1-10 MeV) electron antineutrinos[1], reactors have been used to observe antineutrino oscillations at various baselines and to measure the smallest mixing angle in the PMNS matrix, θ_{13} [46–48], with good precision. The detector technology and strategy has evolved depending on the experimental environment, however, always optimizing the accumulation of $\overline{\nu}_e$ statistics and lowering detector systematic uncertainties. Predicting the antineutrino flux and energy spectrum is challenging due to the complexity of the nuclear physics that determine the dynamics of reactor operation. Recent reactor calculations disagree with experimental measurements revealing a deficit in the $\overline{\nu}_e$ flux and an excess of events in the high-energy region of the spectrum. These observations could indicate the existence of an eV-scale sterile neutrino and insufficient modelling of the antineutrino energy spectrum. At present,

[1]Hereafter, neutrino, antineutrino, electron antineutrino and $\overline{\nu}_e$ will be used synonymously, unless specified otherwise.

these questions are under investigation by state-of-the-art reactor experiments and are the central topic of this thesis.

2.1 Models of antineutrino production in nuclear reactors

Power is generated in nuclear reactors via neutron-induced fission of uranium and plutonium isotopes and the subsequent beta decay of the fission fragments. Fission is characterized by the splitting of a neutron-rich nucleus upon neutron bombardment into two, generally unequal, fragments, along with neutrons and energy. The mass of the two fragments follows a double hump distribution. In the example of ^{235}U, peaks occur at atomic mass numbers, A, 94 and 140. These neutron-rich daughter isotopes are typically unstable, transitioning into stable, longer-lived isotopes via weak beta decay. The stable nuclei with mass A are ^{94}Zr and ^{140}Ce, thus six neutrons must be converted into six protons, with each fission emitting six electrons and six electron antineutrinos. This process is shown in Figure 2.1. In general, $\sim$6 $\overline{\nu}_e$/s/fission are emitted for all actinides used in reactor fuels, corresponding to the emission of $\sim 6\times10^{20}$ $\overline{\nu}_e/\mathrm{GW_{th}}$.[2] There is essentially no contamination from other neutrino flavors to this flux at the relevent energies.

Pressurized water or low-enriched uranium (LEU) reactors are used to produce commercial electricity. They are fueled by unequal mixtures of the actinides ^{235}U (3-5% concentration), ^{238}U, ^{239}Pu, and ^{241}Pu. ^{238}U fissions are induced by fast neutrons (>1 MeV), while the other isotopes fission via thermal neutrons ($\sim$0.025 eV). Research reactors, primarily serving as neutron sources, contain highly-enriched uranium (HEU) fuel with >20% ^{235}U concentration.

[2]The subscript "th" indicates the thermal power of the reactor, i.e. the rate of heat produced by the fissions in the core.

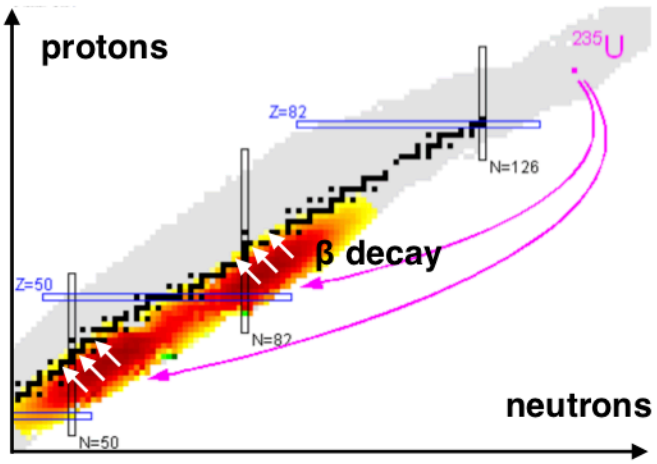

Figure 2.1: Table of nuclides, representing isotopes with different numbers of protons and neutrons. The double hump distribution from the fission of ^{235}U is highlighted. Darker red indicates a higher probability of populating a nuclear state, while yellow represents a lower probability. These fission daughters then undergo beta decay until they reach the line of stability, emitting $\overline{\nu}_e$ in the process.

The total antineutrino spectrum can be calculated by summing over the energy spectra for the contributing actinides,

$$S(E_\nu) = \sum_i \frac{W_{th}}{(f_i/F)e_i} \frac{f_i}{F} \left(\frac{dN_i}{dE_\nu} \right) \tag{2.1}$$

where W_{th} is the thermal power of the reactor, f_i is the number of fissions from actinide i, F the total number of fissions, e_i is the effective energy released per fission, and dN_i/dE_ν is the $\overline{\nu}_e$ spectrum per fission by i's daughter isotopes. [3] The thermal power W_{therm} can be calculated to within a few percent using measurements of the coolant temperature and flow rate [49]. The fission fractions f_i/F are heavily dependent on the reactor operating conditions, particularly the amount of each actinide producing power. In an LEU reactor, the amount of actinide in the fuel can be quite dynamic as the uranium burns up and produces plutonium and fuel replacement occurs in

[3] Neutrinos emitted from spent fuel stored near the reactor site and those produced in the core's structural elements (e.g. aluminum) when bombarded with neutrons can also contribute on the percent-level to the total spectrum.

continuous stages. On average, the f_i/F during operation of an LEU reactor are roughly 58% ^{235}U, 29% ^{239}Pu, 8% ^{238}U, 5% ^{241}Pu [50]. The actinides contribute differently to the antineutrino flux and spectrum, as illustrated in Figure 2.2. The absolute magnitude of dN/dE_ν is greater for ^{238}U and ^{241}Pu as they are more neutron-rich, leading to more beta decays. The individual antineutrino spectra are determined through two methods: *ab initio* summation and β-spectrum conversion calculations.

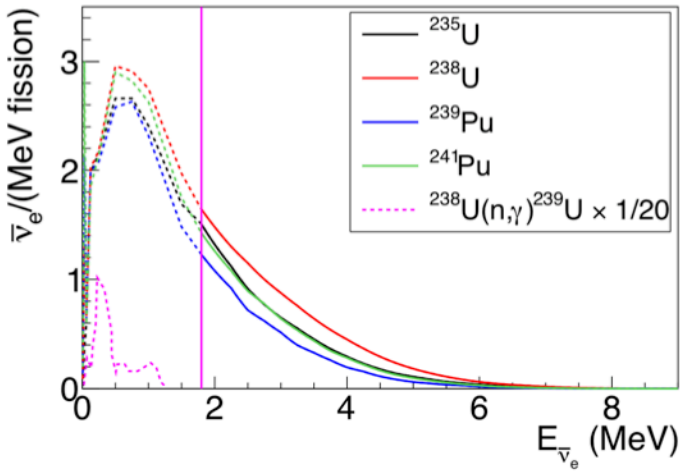

Figure 2.2: Antineutrino spectra for the four major isotopes contributing to reactor antineutrino generation. Also shown is the spectrum contribution from neutron captures on ^{238}U, which are not relevent when considering the IBD detection mechanism. The IBD threshold is indicated by the vertical line at ∼1.8 MeV [50].

The *ab initio* approach sums together the contributions of the thousands of possible beta decay branches from all fission fragments [51]:

$$\frac{dN_i}{dE_\nu} = \sum_n Y_n(Z,A,t) \sum_j b_{n,j}(E_0^i) P_{\bar{\nu}}(E_{\bar{\nu}}, E_0^j, Z). \tag{2.2}$$

The cumulative fission yield, $Y_n(Z,A,t)$, is the number of beta decays of the fragment nucleus (Z,A) after exposure time t, with the label n indicating whether the fragment is in the ground or excited state. $b_{n,j}(E_0^j)$ represents the branching ratio to the β branch j, dependent on the beta decay endpoint energy E_0^i. $P_{\bar{\nu}}(E_{\bar{\nu}}, E_0^i, Z)$ is the spectral shape normalization for each branch j. There are several models that use

this method, for example in Refs. [51, 52]. Figure 2.3 shows the calculated electron spectra and the thousands of β branches that contribute to it.

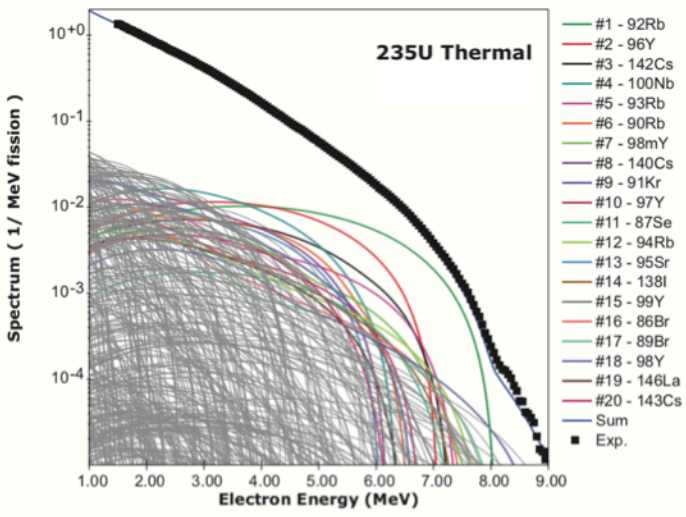

Figure 2.3: Calculated electron spectra resulting from the thermal neutron fission of ^{235}U. Individual β decay branches are shown in gray, while the colored lines represent the most prominent contributions to energies above 5.5 MeV. The black squares show the summation of all the decays. The blue line indicates an experimental measurement of the total spectrum [53].

Ideally, such *ab initio* calculations would encapsulate all of the nuanced nuclear physics required to describe the thousands of decay branches. However, there are several limitations to this approach, contributing to large uncertainties in the predicted neutrino rate and spectrum. These challenges are inherent to the use of experimentally determined nuclear data, namely the fission yields (e.g. ENDF/B-VIII.0 [54]) , beta decay endpoint energies, and branching ratios (e.g. ENSDF [55]). Many of these values either have large associated uncertainties for the dominant fission fractions or are unknown [49]. The nuclear matrix elements between the initial and final states for each β-decay branch can cause the spectrum to deviate from the allowed shape. Significant corrections are required to describe forbidden transitions (non-Gamow-Teller transitions) characterized by non-zero orbital angular momentum transfers and can have a change in parity [56].

In general, It is difficult to fully assess these systematic uncertainties. Currently, active total absorption γ-ray spectroscopy (TAGS) experiments are working to precisely measure the associated γ-ray spectrum of important fission daughters to better understand the beta decay endpoints and branching ratios (for example, Refs. [57, 58]). This requires the use of very efficient detectors sensitive to the weak γ-lines, otherwise the pandemonium effect can bias the spectrum, by under predicting the low energy contribution while over predicting at high energies. At present, *ab initio* models carry an associated 10-20% uncertainty in the prediction of the antineutrino rate and spectrum.

The second approach used to determine the spectra dN_i/dE_ν is the beta conversion method, which involves the conversion of measured, aggregate electron spectra for each fissioning actinide into antineutrino spectra. Obtaining precise and accurate electron spectra is experimentally challenging. The widely-used measurements for the thermal fissions of ^{235}U, ^{239}Pu, and ^{241}Pu come from an experiment in the 1980's by Schreckenbach, *et al* at the Institut Laue-Langevin (IIL) research reactor in Grenoble, France [59–61]. More recently, ^{238}U, a threshold isotope fissioning only by fast neutrons, was measured by Haag, *et al* at a neutron source [62] in Garching, Germany. Essentially, the measurements involve neutrons impinging on foils composed of ^{235}U, ^{239}Pu, ^{241}Pu., and ^{238}U initiating the fission and subsequent beta decay. The resulting electron spectrum is measured with a magnetic spectrometer. The advantage of this technique is its independence from accurate fission yield and branching ratio information, as all possible beta decay branches are automatically accounted for by definition. [4] As the energy from the electron and $\overline{\nu}_e$ represent the total energy of each branch, and as the nuclear recoil energy is negligible, the $\overline{\nu}_e$ spectrum can be deduced by kinematically converting the measured electron spectra.

[4] It should be noted here that the measured aggregate electron spectra lack a contribution for longer-lived, also referred to as non-equilibrium, isotopes that beta decay on day-long timescales, which would contribute to the neutrino spectrum at a reactor. A correction typically needs to be applied to the model to account for these isotopes at specific reactors.

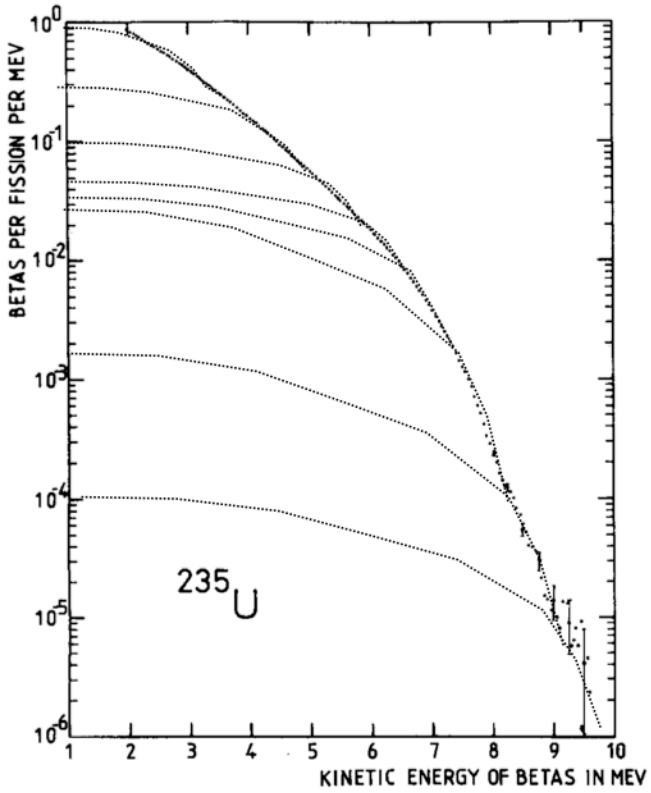

Figure 2.4: ^{235}U β spectrum as measured by Schreckenbach, *et al* [60]. The dotted curves were added to represent 'virtual' β branches used for the conversion of β energy into antineutrino energy.

The conversion procedure starts with the binning of the spectrum defined by "virtual" endpoint energies E_0^i, collapsing the thousands of individual beta decay branches into a set of $\sim$30. Each virtual endpoint is added to a fit of the total aggregate spectrum and the amplitude of each branch is determined. A simple subtraction,

$$E_\nu = E_0 - E_\beta, \tag{2.3}$$

is then performed to convert the measurement into the antineutrino spectrum. By design, this method abstracts the very complicated contributions from nuclear data to ensure a well-produced electron spectrum. Nevertheless, it is not without fault, and assumptions regarding the spectrum shape and its dependence on forbidden tran-

sitions, effective Z, and other nuclear corrections related to the difference between electrons and neutrinos (e.g. Coulomb effects, finite nuclear size, weak magnetism) can lead to nontrivial systematic uncertainties. There are also experimental uncertainties associated with the underlying β spectrum measurements.

Leading predictions of the antineutrino spectrum for ^{235}U, ^{239}Pu, and ^{241}Pu are produced using the conversion method by Huber [63] and a combination of the conversion and *ab initio* calculations by Mueller *et al* [52]. Figure 2.5 shows the comparison between Huber and Mueller, along with an analytic model approximated by Vogel *et al* in 1989 [64]:

$$\frac{dN_i}{dE_\nu} = exp(a_0 + a_1 E_\nu + a_2 E_\nu^2) \tag{2.4}$$

where the fitted parameters a_i are dependent on the fuel type and listed in Ref. [64]. These three models are commonly used as references. Only at high energies do the spectra start to diverge from each other, but this region is stated to be unreliable by the authors due to lack of input measurements. Predictions for modern experiments at LEU reactors, which need to account for all four fissile isotopes, use a hybrid Huber-Mueller model, where Mueller's ^{238}U *ab initio* spectrum is used. The estimated uncertainties on the flux are $\sim$2% [52,63]. The Huber HEU ^{235}U model is the current standard for modelling the antineutrino rate and spectrum for reactors with HEU fuels.

2.2 Detection of reactor antineutrinos

The predominate method to detect reactor $\overline{\nu}_e$ is through the inverse beta decay (IBD) interaction. This charged-current interaction is characterized by the quasielastic scattering of a $\overline{\nu}_e$ on a proton, resulting in a distinct positron and neutron signature (see Equation 1.1). As described in Chapter 1, this process is made possible by the media-

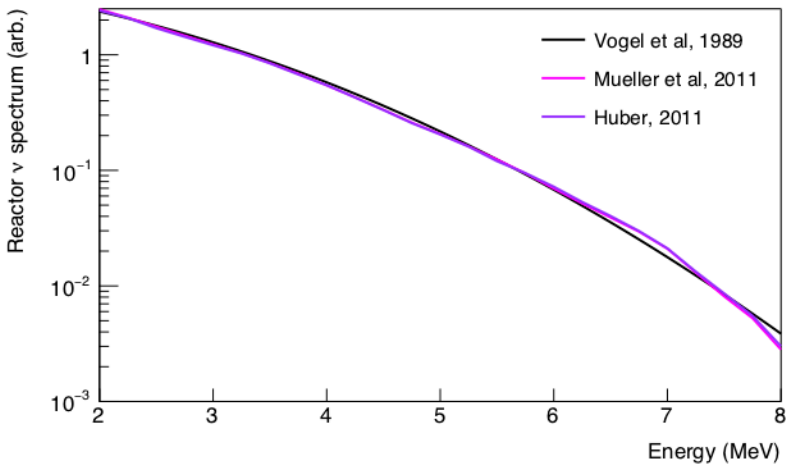

Figure 2.5: Comparison between the three common models of the reactor antineutrino spectrum [52, 63, 64]. All models state that they are valid below 8 MeV, as there are limited measurements in the high energy region.

tion of the W^+, as seen in Figure 2.6. The threshold for the interaction is dependent on the nucleus in which the target proton is bound; the threshold is lower for lighter nuclei. Hydrogen-rich materials, where protons are considered free, are the ideal target for low energy reactor $\overline{\nu}_e$. In the laboratory frame, assuming the initial proton is at rest and neglecting the small mass of the neutrino, the IBD threshold on hydrogen can be expressed as

$$E_\nu^{min} = \frac{(m_e + M_n)^2 - M_p^2}{2M_p} \approx 1.806\,\text{MeV}, \tag{2.5}$$

where m_e, M_n, and M_p are the masses of the electron, neutron, and proton, respectively. The energy of the positron can be approximated at zeroth order in $1/M$,

$$E_e^{(0)} = E_\nu - (M_n - M_p) - \mathcal{O}(\frac{E_v^2}{M_n}), \tag{2.6}$$

to express the IBD cross section in terms of the neutron decay lifetime [49]:

$$\sigma_{tot}^{(0)} = \frac{2\pi^2/m_e^2}{f^r \tau_n} E_e^{(0)} p_e^{(0)} \approx 9.52 \times 10^{-44} \left(\frac{E_e^{(0)} p_e^{(0)}}{\text{MeV}^2} \right) \text{cm}^2, \tag{2.7}$$

where f^r is the neutron decay phase space factor (including Coulomb, weak magnetism, and outer radiative corrections), $\tau_n (= 880.2 \pm 1.0\,\mathrm{s}$ [21]) the mean neutron lifetime, and $p_e^{(0)}$ the momentum of the electron to zeroth order. Even at reactor energies, first order corrections in $1/M$ need to be included in the calculation. A full derivation of the first order IBD cross section, including the angular distribution of the positron, can be found in Ref, [65]. Convolving the Vogel-Beacom IBD cross section with predictions of the emitted reactor spectrum, the detected $\overline{\nu}_e$ spectrum is obtained, as illustrated in Figure 2.7. The detected IBD spectrum peaks around $\sim$3.5 MeV, and only $\sim$30% of the emitted spectrum is above the IBD threshold. Along with the dynamics in the core, the absolute flux or normalization of the $\overline{\nu}_e$ detected spectrum is weighted by the baseline of the detector from the reactor, i.e. $1/L^2$.

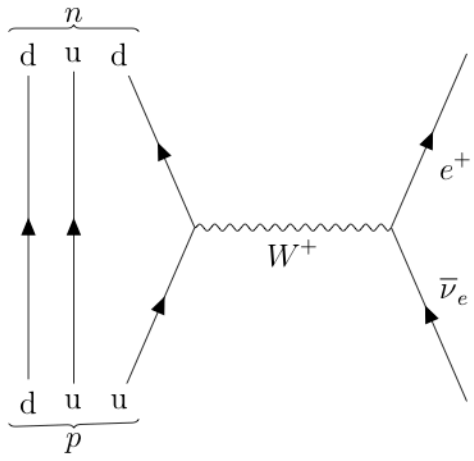

Figure 2.6: Feynman diagram of the inverse beta decay interaction.

Aside from the relatively large cross section (at least compared to that of neutrino-electron scattering), the advantage for reactor experiments to use the IBD interaction lie in the time-correlated positron and neutron products. As the heavy neutron recoil energy is low ($\sim$40 keV), essentially all of the neutrino's kinetic energy is transfered to the positron. A measurement of the positron energy can then be directly related to the $\overline{\nu}_e$ energy (see Equation 2.8). The positron-neutron signature also allows IBD events to be distinguished from radioactive or neutron backgrounds that are produced

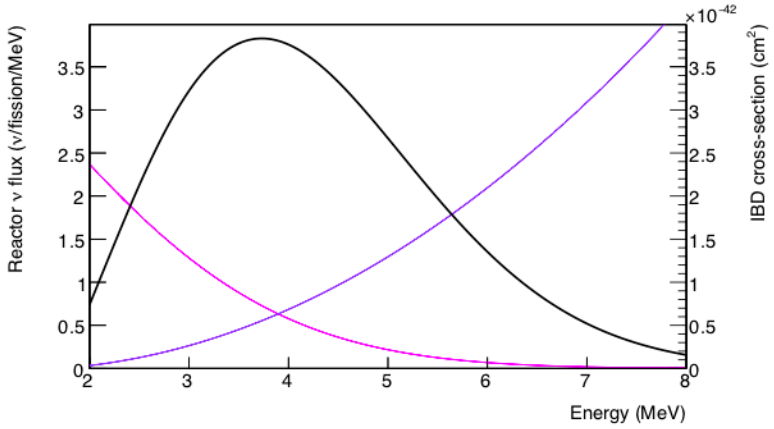

Figure 2.7: Illustration of the $\overline{\nu}_e$ detected energy spectrum (black) resulting from the convolution of the emitted reactor flux (magneta) and the IBD cross section (purple). Here, the Vogel model [64] for ^{235}U is used.

by the reactor, cosmic rays, and radioactive materials in the detector or surrounding environment.

Scintillators are the most common target and detection medium used in reactor neutrino experiments. They are composed of hydrocarbon chains, giving access to a large number of free protons. These materials fluoresce, or scintillate, as charged particles ionize and excite electrons from the host molecules, relaxing back into the ground state. The emitted light can then be detected with photosensors. Liquid (organic) scintillators can be produced in large volumes at effective costs, allowing reactor experiments to construct large detectors to increase the rate of neutrino interactions. In scintillator, an IBD event is identified by two consecutive signals. The first, prompt signal is created by the positron. Carrying the $\overline{\nu}_e$ energy, it will ionize the scintillator and then quickly annihilate on a surrounding electron, producing a pair of two, 511 keV γ-rays. The γ-rays will Compton scatter, freeing more electrons that will produce scintillation. These energy depositions occur on extremely fast time scales ($\mathcal{O}$(ns)) and are recorded as a single signal, giving a measure of detected

positron energy, or prompt energy E_{prompt}. The $\overline{\nu}_e$ energy is then simply written as

$$E_v \approx E_{prompt} + 0.78\,\text{MeV}. \tag{2.8}$$

where the factor of 0.78 MeV accounts for the IBD threshold and detection of the two annihilation γ-rays. It should be noted that this conversion, while accurate, can be quite complex if the detector cannot fully measure the energy of the positron for all energies. This is the case for most experiments, with different levels of complexity, and will be revisited in Chapter 5. The second, delayed signal is produced by tagging the neutron via neutron capture. As these neutrons are thermal, they can capture on various nuclei with high cross sections, for example ^{1}H, which is native to the scintillator, or metals such as ^{6}Li and Gd, which needed to be loaded into the scintillator. Each capture process produces different decay products with various Q-values, as represented in Table 2.1. The concentration of the isotope in the scintillator will determine how fast the neutron is captured. Usually on the order of μs, a reduction in the capture time increases the time-correlation with the positron, heavily suppressing backgrounds. The neutron tag is also spatially-correlated with the positron and topological information can then be used to further reject non-neutrino events, specifically accidental backgrounds where the prompt and delayed signals are from different processes. The specifics of the detector type and experimental environment dictate the use of particular capture nuclei.

2.3 Previous reactor neutrino experiments

As described in Chapter 1, the field of experimental neutrino physics began with the first detection of $\overline{\nu}_e$ at reactors by Cowan and Reines. Both experiments at the Hanford and Savannah River reactors, demonstrated that it is possible to measure neutrinos at very close distances to the core amidst the reactor-related backgrounds.

Capture nucleus	Interaction (Q-value)	Cross section (barns)
^{1}H	$n + p \rightarrow d + \gamma$ (2.2 MeV)	0.33
^{3}He	$n +^{3}$ He $\rightarrow p +^{3}$ H (0.764 MeV)	5300
^{6}Li	$n +^{6}$ Li $\rightarrow \alpha +^{3}$ H (4.78 MeV)	950
Gd	$n +^{155}$ Gd $\rightarrow^{156}$ Gd $+ \gamma$'s (8.5 MeV)	61000
	$n +^{157}$ Gd $\rightarrow^{158}$ Gd $+ \gamma$'s (7.9 MeV)	256,000

Table 2.1: Commonly used thermal neutron capture agents in reactor neutrino experiments. The interactions and approximate cross sections are reproduced from Ref. [54].

Although cosmic rays proved to be a more difficult problem than expected, the scintillator detectors were also able to combat these backgrounds without much overburden or shielding from rock. Reines continued working with reactor neutrinos to understand their fundamental properties using various types of detectors. Measurements of interaction cross sections other than IBD were performed on deuteron (D_2O):

$$\begin{aligned} \overline{\nu}_e + d \rightarrow n + n + e^+ \text{ (charged} - \text{current)} \\ \overline{\nu}_e + d \rightarrow n + p + \overline{\nu}_e \text{ (neutral} - \text{current).} \end{aligned} \tag{2.9}$$

The observed ratio of the charged-current to neutral-current reaction rates was lower than predicted for $\overline{\nu}_e$, hinting at oscillations $\overline{\nu}_e \rightarrow \overline{\nu}_x$ [66]. To explain the size of the deficit, a large mass splitting would be required, on the order of eV^2.

A number of experiments in the 1980's were performed to explore the possible high frequency oscillation parameter space, requiring the detectors to be placed at short baselines ($\sim$meters) from reactor cores. The first detector was built 8.8 m from the ILL 57 MW_{th} HEU reactor core [67]. Using 377 L of liquid scintillator, PMTs, and ^{3}He neutron wire counters, the ILL experiment used the IBD interaction to detect neutrinos. A feature of the scintillator was its ability to distinguish particle types by their scintillation timing profile, a technique referred to as pulse shape discrimination (PSD), allowing efficient identification of the prompt positron and delayed neutron signal. Furthermore, the detector was optically separated into cells

to reduce backgrounds via event topology signatures. Since the ILL reactor does not run continuously, measurements during reactor-on and reactor-off events could be compared, the subtraction indicating $\overline{\nu}_e$ candidates. Using the β spectra measured at the ILL, as outlined in Section 2.1, the absolute rate and energy spectrum of $\overline{\nu}_e$ could be compared to conversion models to search for oscillations. Figure 2.8 shows both the measured prompt positron spectrum and ratio of the observed rate to the prediction as a function of energy. With a total of $N_{observed} = 4890 \pm 180$ counts after 128 days of reactor-on data, the ratio integrated over the full spectrum was reported as,

$$Rate = \frac{N_{observed}}{N_{expected}} = 0.995 \pm 0.035(\text{stat.}) \pm 0.11(\text{syst.}). \tag{2.10}$$

The ILL measurement was consistent with the no-oscillation hypothesis at short baselines, in analyses of both the flux and energy spectrum. It ruled out the large mass splitting suggested by Reines, but was not able to exclude larger regions of the Δm^2 and $\sin^2 2\theta$ parameter space because of the associated systematics with β measurements and their conversion to the normalization and shape of the predicted $\overline{\nu}_e$ spectrum.

Another experiment located in France used a 2800 MW_{th} array of LEU reactors at the Bugey nuclear power plant as a neutrino source [68]. The substantial increase in power provided a higher flux of $\overline{\nu}_e$, however the spectra were more difficult to predict with multiple isotopes and fuel burn-up dynamics adding systematics. To alleviate the uncertainty of the overall spectrum normalization, the detector was designed to make measurements at multiple baselines. As reactors emit $\overline{\nu}_e$ isotropically, the spectral shape should be identical at all baselines while the rate will vary proportionately with $1/L^2$. This multiple detector concept then allows for relative comparisons of the shape and rate at different baselines with appropriate corrections, essentially

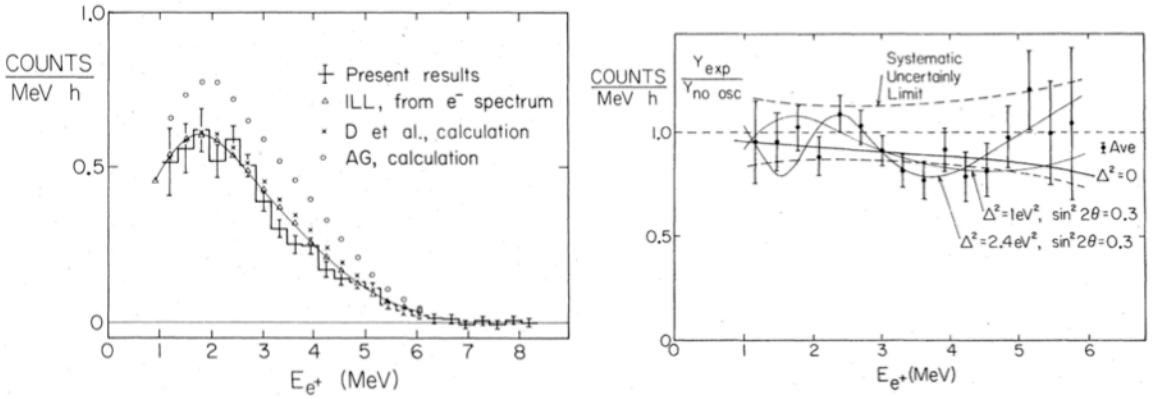

Figure 2.8: **(left)** ILL prompt positron spectrum measurement (crosses) compared to various predictions. The conversion calculation using the β spectra measurements at the ILL are indicated with triangles. **(right)** Ratio of the observed to expected flux as a function of prompt energy. Oscillation models with various mixing parameters are shown in the solid lines [67].

cancelling the large, correlated systematics associated with the predictions.[5] Any measured deviations between baselines are an indication of oscillations. The first experiment used two detectors at baselines of 13.5 m and 18.3 m and resemble the design of the ILL experiment, with each segment containing 32 L of liquid scintillator. A large shield of lead and borated water surrounded the detectors, along with liquid scintillator anti-coincidence veto counters. Initially a 10% flux deficit was reported, in agreement with the Savannah River hypotheses. In conflict, the Goesgen [69–71] experiment also performed searches for short-baseline oscillations at LEU reactors, reporting null results. New measurements by the Rovno [72–74] experiments provided systematic checks at short baselines and confirmed the no-oscillation hypothesis.

Bugey later designed three new, identical detectors to understand if there was a systematics issue causing the disagreement between Goesgen and Rovno [75, 76]. Using a similar optical segmentation scheme, each detector contained 600 L of PSD-capable ^{6}Li-doped liquid scintillator, to provide both the neutrino target and neutron capture agent. This reduced the amount of dead space imposed by the previous

[5]Correlated systematics associated with the detector can also be cancelled with measurements at different baselines.

^{3}He counters and increased the neutron tag efficiency. The segments were defined by steel-backed aluminum foil mirrors enclosed in FEP Teflon to separate the liquid from the metal, as liquid organic scintillators are generally chemically incompatible with metals. PMTs were mounted on both ends of the segment to increase the light collection efficiency, as illustrated in Figure 2.9. The oscillation search was expanded to include measurements at longer baselines, as the deficit in muon-like events seen by Kamiokande suggested a mass splitting around $\sim 10^{-2}\,\mathrm{eV}^2$ (see Chapter 1). One near detector was placed underneath a reactor 15 m from the core, and the two far detectors at 40 m. When the largest reactor was not in operation, the far detectors would measure neutrinos from a reactor at a distance of 95 m.

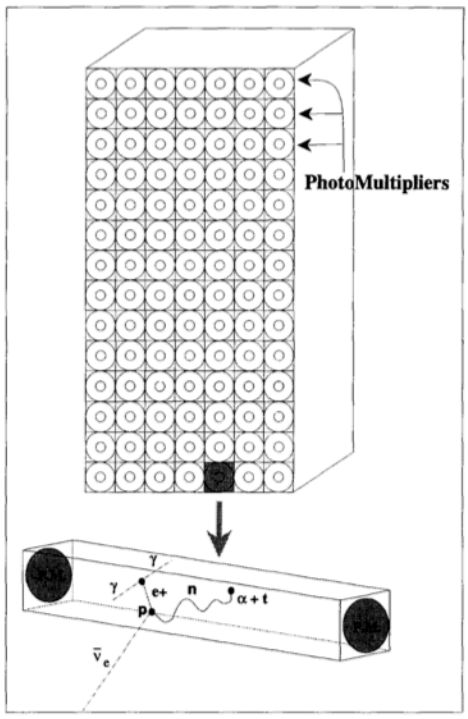

Figure 2.9: Design of Bugey detectors with measurements at 15, 40, and 95 m baselines. An $85\times122.5\times61.8\,\mathrm{cm}^3$ stainless steel tank was divided into a 7×14 array of ^{6}Li-loaded liquid scintillator segments via aluminum foil-covered panels encased in FEP Teflon. 3 in PMTs provided the light readout [75].

Using this experimental concept, Bugey produced the largest data sample of reactor $\overline{\nu}_e$ with the ability to eliminate many of the detector and reactor systematics.

Measurements at multiple baselines with low uncertainties provided sensitivity to a large region of the available (Δm^2, $\sin^2 2\theta$) parameter space. Comparing the relative rates of the prompt positron spectrum between detectors, Bugey saw no evidence of short-baseline oscillations. The exclusion curve is reproduced in Figure 2.10 along with other reactor $\overline{\nu}_e$ measurements and the allowed region favored by Kamiokande.

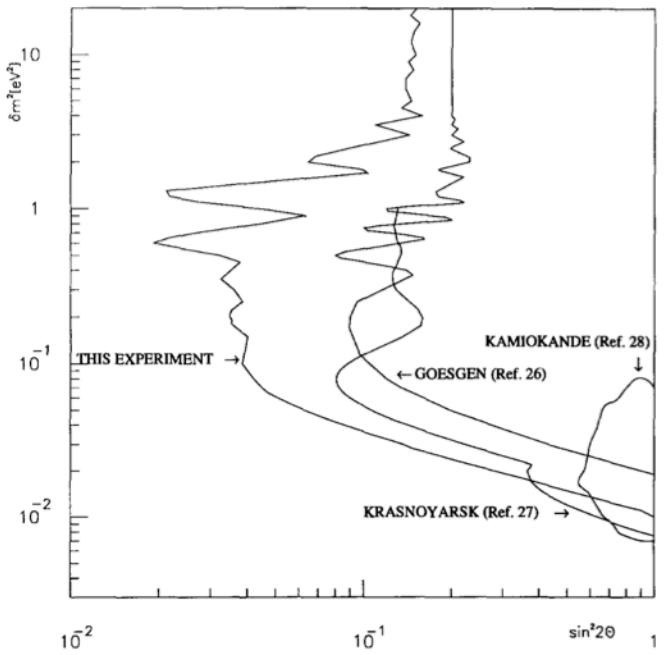

Figure 2.10: Bugey's (labelled "this experiment") 90% C.L. exclusion contour in comparison to other reactor $\overline{\nu}_e$ measurements. Parameters to the right of the curve are eliminated as possible mixing values. The Kamiokande allowed region is shown to be well-excluded by the reactor experiments [75].

Reactor experiments continued to push beyond the large Δm^2_{32} hinted by Kamiokande for atmospheric oscillations ($\nu_\mu \to \nu_x$), by building larger, more precise detectors at longer baselines. The $\overline{\nu}_e \to \overline{\nu}_\mu$ channel would show a large deficit at the expected oscillation minimum, on the order of km-length baselines, if ν_μ and ν_e mixing was large. If ν_τ mixing dominates, then the effect would be very small. Operating at the 8.5 GW_{th} Chooz power station in the Ardenne region of France, the Chooz experiment [77–79] was built in an underground laboratory with 300 mwe[6] of rock overbur-

[6]The unit "mwe" stands for meter water equivalent, to standardize the quantification of cosmic

den at a distance of 1 km from the two LEU reactors. The detector design features several layers of veto and active materials, as seen in Figure 2.11. A cylindrical steel tank enclosed a 90 ton water muon veto, readout by PMTs and optically isolated from the inner detector region. The inner region consisted of 90 tons of liquid scintillator to contain γ-rays and neutrons from IBD interactions that travel outside of the neutrino target, while also protecting the target from the readout PMTs radioactivity. The neutrino target, 5 tons of Gd-doped liquid scintillator, was housed inside an acrylic vessel. With the large active volume and ability to reject backgrounds with active vetos, Chooz was able to achieve a high IBD detection efficiency ($\sim$70%), while maintaining good energy resolution ($12\%/\sqrt{E(\mathrm{MeV})}$). No evidence for $\overline{\nu}_e \to \overline{\nu}_x$ was observed. Despite the systematics associated with the absolute measurements of the $\overline{\nu}_e$ spectrum and flux from a single detector, Chooz excluded a large, new region of the $\nu_\mu \leftrightarrow \nu_e$ parameter space (shown in Figure 2.12).

At a 11.6 $\mathrm{GW_{th}}$ LEU reactor complex in Arizona, the Palo Verde experiment used a larger, 11 ton Gd-loaded liquid scintillator detector to search for $\overline{\nu}_e$ oscillations. At a baseline of 890 m from two reactors and 750 m from one reactor, the detector was protected by 32 mwe. A larger overburden was not required as Palo Verde was constructed using a segmented design, similar to the later Bugey detectors, allowing for topological background suppression. An active muon veto and water buffer surrounded the inner detector. With another absolute measurement, Palo Verde also reported no observation of a flux deficit or spectral distortion, ruling out $\nu_\mu \to \nu_e$ oscillations, as seen in Figure 2.12**(left)**. The results from Chooz and Palo Verde eliminated the possibility of ν_μ–ν_e mixing causing the atmospheric neutrino anomaly reported by Kamiokande. This indicated that the anomaly was a result of ν_μ–ν_τ mixing. The parameter space was required to be expanded into at least five parameters (three mixing angles, two mass splittings). Thus, the reactor neutrino experiments

ray attenuation at underground sites. Buried under 300 mwe of rock would result in the same attenuation if buried under 300 m of water.

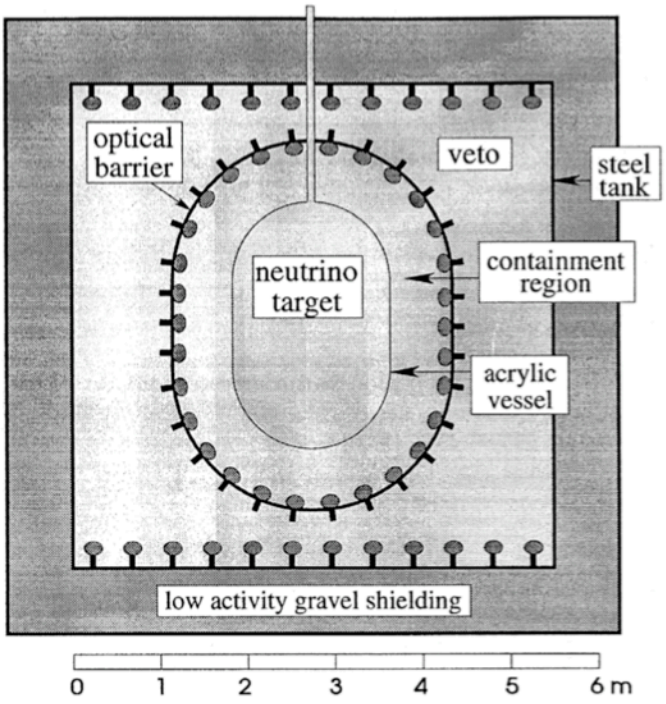

Figure 2.11: Schematic of the Chooz detector. It features three concentric regions: water Cherenkov muon veto, liquid scintillator γ-catcher, and Gd-doped liquid scintillator neutrino target [77]. This design is still widely used in reactor detectors, most notably the precision θ_{13} experiments.

(at baselines $\leq$km) would be purely sensitive to θ_{13} through $\overline{\nu}_e$ disappearance via,

$$P(\overline{\nu}_e \to \overline{\nu}_e) \approx 1 - \sin^2(2\theta_{13}) \sin^2\left(\frac{\Delta m^2_{31} L}{4E_\nu}\right). \tag{2.11}$$

Super-Kamiokande measurements of the atmospheric oscillations $\nu_\mu \to \nu_\tau$ could also provide sensitivity through,

$$P(\nu_\mu \to \nu_\tau) \approx \cos^4\theta_{13} \sin^2(2\theta_{23}) \sin^2\left(\frac{\Delta m^2_{31} L}{4E_\nu}\right), \tag{2.12}$$

as θ_{12} is irrelevent at these baselines. Figure 2.12**(right)** illustrates the exclusions on θ_{13} from Palo Verde and Daya Bay and the allow region from Super Kamiokande. The atmospheric data contrains Δm^2_{32}, while the high statistics from the reactor $\overline{\nu}_e$ experiments lead to a 90% C.L. limit of 0.17 for $\sin^2 2\theta_{13}$ [79].

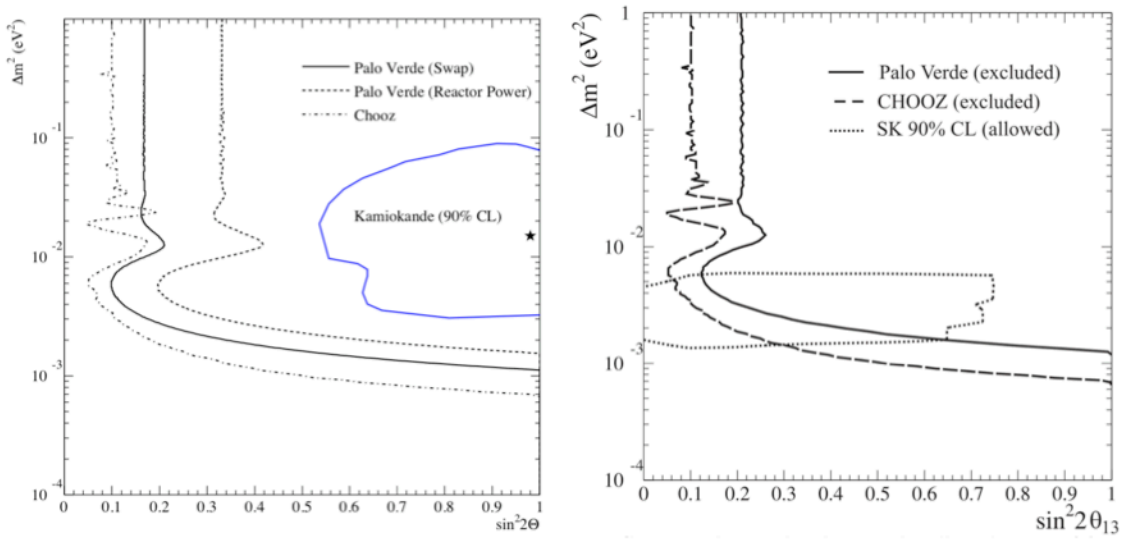

Figure 2.12: **(left)** Two-flavor oscillation exclusions from Chooz and Palo Verde (two different analyses) and the allowed Kamiokande region from atmospheric neutrino mixing [80]. **(right)** The same Chooz and Palo Verde exclusions for $\sin^2 2\theta_{13}$ when interpreted in the three-flavor oscillation scenerio with the Super-Kamiokande allowed region [81].

A new generation of reactor experiments, Double Chooz, RENO, and Daya Bay were constructed to search for a zero or non-zero θ_{13}.[7] Each positioned multiple detectors at different baselines to reduce the systematic uncertainties associated with the reactor and detector, relying on relative measurements of the flux and spectrum. As the detectors and experimental techniques are very similar, only the details of Daya Bay are expanded on here.

Operating at the Daya Bay nuclear reactor power plant in southern China, the Daya Bay Reactor Neutrino Experiment sampled neutrinos from six LEU reactor cores, with a total maximum power output of $17.4\,\mathrm{GW_{th}}$ [46]. Eight antineutrino detectors (ADs) were built identically, each containing 20 tons of Gd-loaded linear alkylbenze (LAB) liquid scintillator serving as the IBD target housed in an acrylic

[7] After the new experiments were designed, small discrepancies between the KamLAND and solar data hinted θ_{13} was small, but non-zero. The T2K accelerator neutrino experiment also disfavored the $\theta_{13} = 0$ scenerio [50].

tank.[8] Concentric layers of undoped LAB scintillator and mineral oil surround the active region, acting as a γ-catcher and radioactivity shield, read out by 8 in PMTs. The ADs are grouped into water Cherenkov tanks in three different underground experimental halls. Two near detector sites (four ADs in total) were used to monitor the $\overline{\nu}_e$ flux, at baselines of 360 m and 500 m with 250 mwe and 265 mwe overburden, respectively. A far site with four ADs was positioned at an average of 1580 m from the reactor array, maximizing the sensitivity to the θ_{13} oscillation maximum [50]. The configuration of the Daya Bay site and AD design schematic are replicated in Figure 2.13.

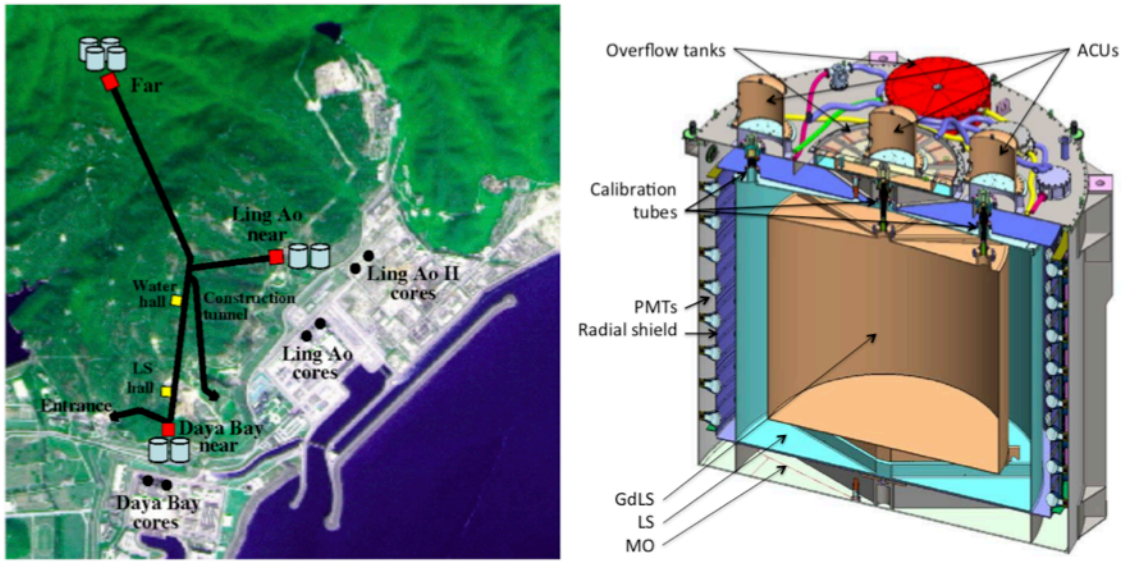

Figure 2.13: **(left)** Layout of the eight Daya Bay near and far detectors in comparison to the six LEU reactor cores. **(right)** Schematic of the Daya Bay antineutrino detectors (ADs), using the concentric materials design: mineral oil radioactivity shield, LAB liquid scintillator γ-catcher, and Gd-doped LAB liquid scintillator neutrino target. All ADs are identical and installed in water pools, which act as a Cherenkov muon veto [82].

As the Daya Bay reactors operate continuously, a subtraction of reactor-on and -off cannot be performed to identify the correlated, IBD events. The experiment showed a clear correlation between the reactor power and IBD detection rate, indi-

[8] Only six Daya Bay ADs were operational for the first measurement of θ_{13} in Ref. [46].

cating that IBD candidates can be identified as reactor $\overline{\nu}_e$ rather than radioactive or cosmogenic backgrounds. Due to the baselines and the overburdens of the Daya Bay detectors, the backgrounds consist mostly of accidental γ-ray coincidences with signals produced by two different sources or processes. Independent of reactor models, Daya Bay discovered the non-zero value of θ_{13} in 2012, by making relative comparisons of the flux from the near and far detectors [46]. Measurements from RENO in South Korea [47] and Double Chooz in France followed shortly after [48]. The current best measurement of $\sin^2 2\theta_{13} = 0.0841 \pm 0.0027(\text{stat.}) \pm 0.0019(\text{syst.})$ is from the Daya Bay 2016 rate and spectral analysis using 1230 days of reactor-on data [83]. Figure 2.14 shows the spectrum measured at the far detector site and the oscillation probability when comparing spectral measurements from the near and far detectors. With more than 2.5 million $\overline{\nu}_e$ events, θ_{13} is the most precisely measured of all the neutrino mixing angles, made possible by the high statistics and small systematics from the multiple, large scintillator detectors at Daya Bay. The non-zero value of θ_{13} enables the search for the CP-violation phase in the neutrino sector and could allow future precision reactor neutrino experiments to resolve the neutrino mass ordering problem [84].

2.4 The reactor antineutrino flux anomaly

Data from all the short-baseline reactor experiments prior to 2010 were in agreement with both the three-neutrino oscillation model, as well as with the predictions of the reactor $\overline{\nu}_e$ energy spectrum and absolute flux. The more modern θ_{13} experiments set out to make precision measurements by comparing the rate and spectrum at different baselines, but could also determine the absolute flux. In preparation for Double Chooz[9], the Saclay reactor neutrino group reevaluated the beta conversion

[9]The first phase of Double Chooz included only a far detector, requiring a reference $\overline{\nu}_e$ spectrum to compare with.

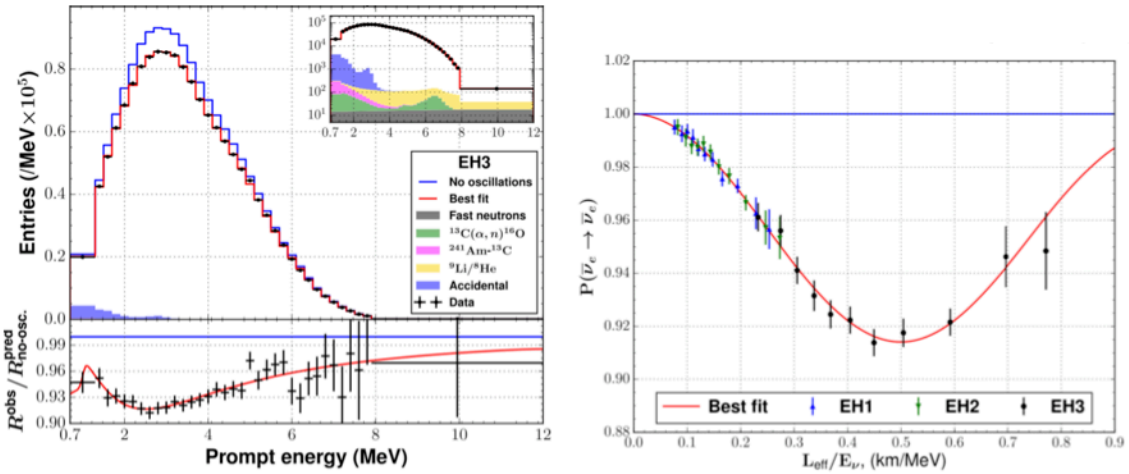

Figure 2.14: **(left)** Reconstruction prompt positron energy spectrum from IBD candidates detected at the Daya Bay far detector site (EH3). The measurements (black) are compared to the no-oscillation model (blue) and the best-fit three-neutrino oscillation model (red). A clear distortion in the shape near the peak is observed. **(right)** Measurement of $\overline{\nu}_e$ disappearance rate by the eight Daya Bay ADs at different values of L/E, due to the oscillation driven by θ_{13} [83].

models for ^{235}U, ^{239}Pu, and ^{241}Pu, including the then current value of the neutron mean lifetime ($\tau_n = 881.5\,\text{s}$) used in Equation 2.7 [52]. The ^{238}U spectrum was calculated by the *ab initio* method. Using a "mixed" approach, the authors state that the systematic uncertainties can be reduced. The new prediction resulted in a 3% energy-independent increase in rate above the calculations from the original ILL conversion. Reevaluating the measurements from the previous experiments with baselines <100 m, the global ratio between observed and predicted $\overline{\nu}_e$ shifted from 0.976±0.024 to 0.943±0.023 [85]. This leads to a total ∼6% or ∼2.5σ deficit of detected reactor $\overline{\nu}_e$, labelled the "Reactor Antineutrino Anomaly" (RAA).

Historically, a deficit in the number of observed neutrinos compared to theoretical models was the result of neutrino oscillations. The RAA authors hypothesized that the disagreement in the reactor sector was due to high frequency, very short-baseline oscillations (meter-length for the energy of reactor $\overline{\nu}_e$), of a fourth, sterile neutrino. As introduced in Chapter 1, a sterile neutrino would not interact in the Standard Model,

but can participate in oscillations with the three active neutrinos. Sterile neutrinos are theoretically well-motivated to explain the small mass generation of active neutrinos through the seesaw mechanism. Generally, these sterile neutrinos have masses on the GUT-scale, but these models often predict multiple sterile neutrinos. To explain the reactor data, the mass splitting between the fourth sterile state and the first mass eigenstate (Δm^2_{41}) would be of order eV^2. Figure 2.15 summarizes the global reactor data in comparison to the 3ν oscillation model and a $3{+}1\nu$ prediction which includes a sterile neutrino with $\Delta m^2_{41} \sim \text{eV}^2$.

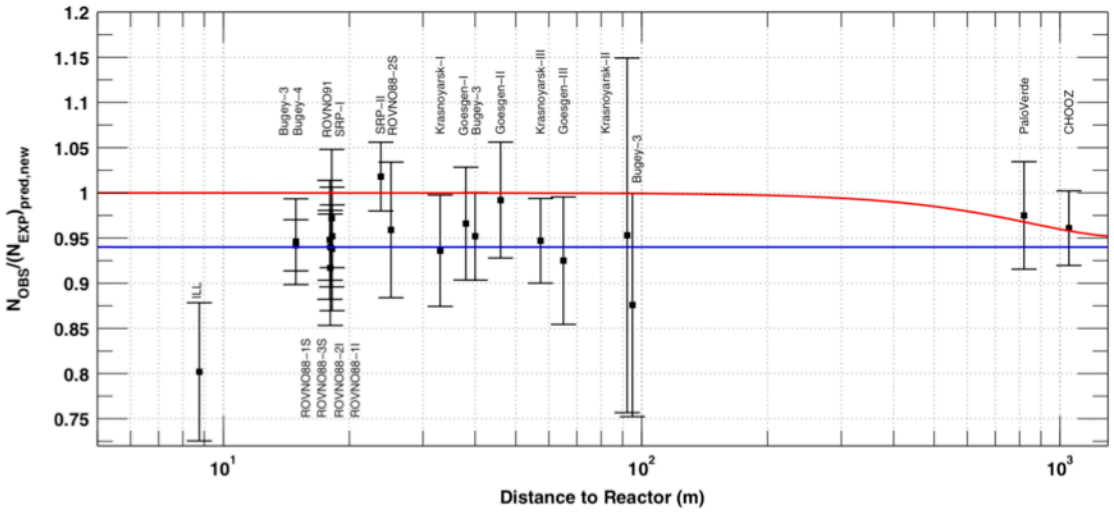

Figure 2.15: Ratio of the $\overline{\nu}_e$ rate measured by previous short-baseline reactor experiments (black) to reactor models compared to the standard 3ν oscillation hypothesis (red). The observed flux deficit is the so-called Reactor Antineutrino Anomaly. For illustration, a sterile neutrino is introduced as a solution, $3{+}1\nu$ model, with mixing parameters $|\Delta m^2_{41}| \gg 1\,\text{eV}^2$, $\sin^2 2\theta_{14}$=0.12 (blue) [85].

As a check, Huber revisited the initial ILL beta conversion calculation [63], producing the model discussed in Section 2.1. The procedure was slightly altered to reduce systematic biases, with the addition of a weight to nuclear charges depending on their contribution to the $\overline{\nu}_e$ spectrum and corrections to the Fermi theory accounting for the difference between electrons and neutrinos. As with the other conversion models, this update also includes the uncertainties from the underlying

ILL β measurement. Comparisons of Huber to the RAA and original ILL ^{235}U spectrum predictions are shown Figure 2.16. A similar $\sim$3% increase in the $\overline{\nu}_e$ rate was obtained.

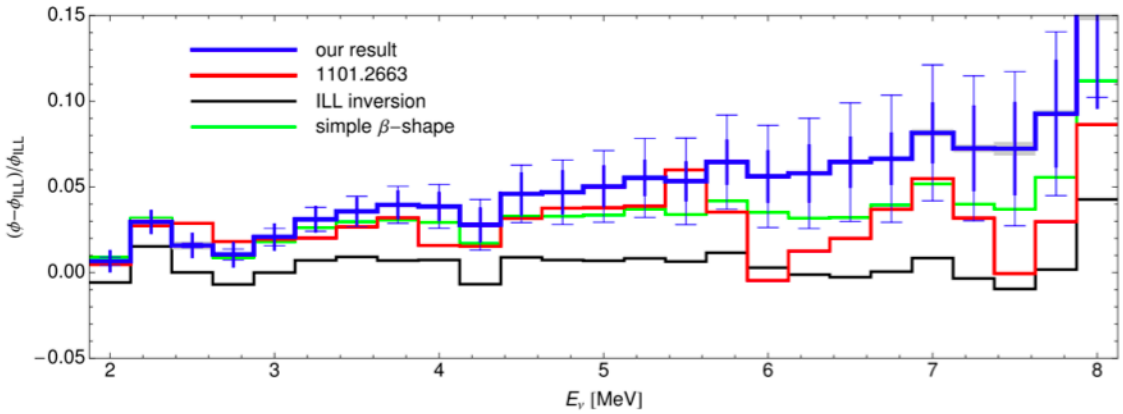

Figure 2.16: Ratio of various ^{235}U spectrum models to ILL conversion. Huber is represented by the blue curve and RAA in red. The black curve is a cross-check of the original ILL conversion procedure performed by Huber [63].

With a re-analysis of the previous reactor $\overline{\nu}_e$ disappearance experiments, the global ratio of observed to predicted $\overline{\nu}_e$ became 0.927$\pm$0.023 [86], corresponding to a 2.9σ deficit. Several other experiments using different neutrino sources have also resulted in anomalous data that can be explained by the existence of similar eV-scale sterile neutrinos. The infamous accelerator experiment LSND observed excesses in the $\overline{\nu}_\mu \to \overline{\nu}_e$ and $\nu_\mu \to \nu_e$ channels [87]. Using a mineral oil Cherenkov detector instead of scintillator, the MiniBooNE accelerator experiment was built to test the LSND result but also observed a low-energy excess [88]. Radiochemical experiments, GALLEX [89] and SAGE [90] (collectively referred to as the gallium experiments), using ^{51}Cr and ^{37}Ar calibration sources observed a deficit in the $\nu_e \to \nu_e$ channel. Combining the GALLEX, SAGE, and reactor experiment data, the RAA authors updated the best-fit parameters for a sterile neutrino to Δm^2_{41}=2.3$\pm$0.1 eV^2, $\sin^2 2\theta_{14}$=0.17$\pm$0.04 [86].[10] A similar analysis was performed by Kopp *et al*, including all ν_e disappearance ex-

[10]Experiments that use identical or similar detectors are assumed to have fully correlated systematic uncertainties.

periments and more rigorously accounted for the correlations between multiple runs of the same reactor experiment [91]. In addition, an uncertainty on the flux normalization was included, slightly shifting the best-fit to Δm^2_{41}=1.74 eV^2, sin^2 2θ_{14}=0.09. The allowed regions for sterile neutrinos from the RAA and Kopp global analyses are reproduced in Figure 2.17. Daya Bay [83, 84], Double Chooz [92], and RENO [93] have also made precise absolute measurements of the flux using their near detectors. With small uncertainties, these new results are in agreement with the global average of the previous reactor neutrino experiments.

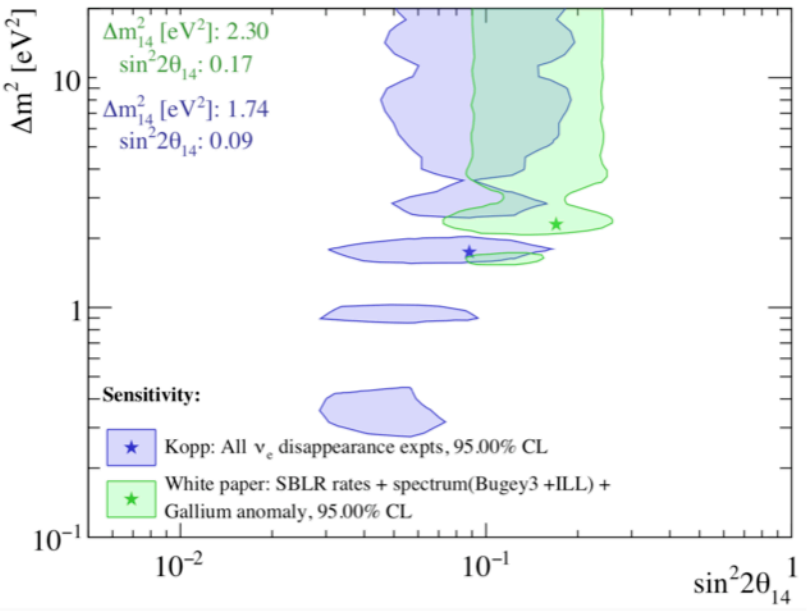

Figure 2.17: Allowed sterile neutrino mixing parameters based on measurements from multiple disappearance experiments. White paper allowed region (green): updated RAA rate+shape analysis including reactor experiments and the GALLEX and SAGE source data. Kopp allowed region (blue): rate+shape analysis of all ν_e disappearance experiments. Sterile neutrino best-fits indicated by stars. Adapted from Refs. [86,91].

Resolving the reactor antineutrino anomaly through very short-baseline experiments is a priority of the reactor neutrino field. In addition, searches for eV-scale sterile neutrinos are also being pursued by various types of experiments in the greater neutrino community, as the existence of such a particle would indiciate a new type of matter beyond the Standard Model framework. The discovery of a sterile neu-

trino would also have major implications on future neutrinoless beta decay ($0\nu\beta\beta$) experiments to determine the Majorana nature of neutrinos and measurements of the CP-violation phase factor [94]. Furthermore, sterile neutrinos would effect the cosmological history of the Universe, having a direct impact on cosmology and astrophysics. An extensive summary of the theory, experimental evidence, and implications of light eV-scale sterile neutrinos are detailed in Ref. [86].

Although sterile neutrinos are well-motivated by some oscillation data and theory, at present, several measurements disfavor their existence in certain mass ranges. The Planck satellite CMB observation has ruled out an eV-scale sterile neutrino in the standard ΛCDM model, through measurements of the effective number of relativistic degrees of freedom, $N_{\text{eff}} = 3.15 \pm 0.23$ [95], which is consistent with the Standard Model prediction of $N_{\text{eff}} = 3.046$. However, it should be noted that some theories can relax the imposed constraints and allow for sterile neutrinos in the early Universe [96]. The IceCube neutrino observatory has ruled out sterile neutrinos in the preferred region of the ν_u and $\overline{\nu}_\mu$ disappearance parameter space [97]. Measurements of the fuel evolution of the Daya Bay reactors hint that there is a discrepancy in the nuclear calculations of the ^{235}U flux, reducing the size of the flux deficit and decreasing the need for a sterile neutrino to explain the data [98].[11]

2.5 Deviations in the reactor antineutrino energy spectrum

In the same absolute flux analyses, the θ_{13} experiments also compared measurements of the prompt positron energy spectrum to the Huber+Mueller LEU prediction, as shown in Figures 2.18, 2.19 and 2.20 [83, 99, 100]. Over the entire energy range of

[11] Although the comparison between Daya Bay and predictions would become more compatible with corrections to the ^{235}U flux calculations, it cannot fully explain the observed 6% deficit [98].

all three experiments, 2σ deviations with a very prominent $\geq 4\sigma$ feature around 4-6 MeV prompt energy (~5-7 MeV neutrino energy). Comparisons to the ILL+Vogel [51] model show similar disagreements. This excess of $\overline{\nu}_e$ events or "bump" at high energies was not reported by previous shape tests performed by Bugey [75], but is clearly independent of the detector baseline and also tracks with the power of the LEU reactors. There is no reasonable particle physics explanation to produce the bump, neither standard L/E neutrino oscillations or mixing from sterile neutrinos. Antineutrinos created by neutron interactions with the reactor structural materials or surrounding spent nuclear fuel cannot contribute to this harder region of the spectrum [101].

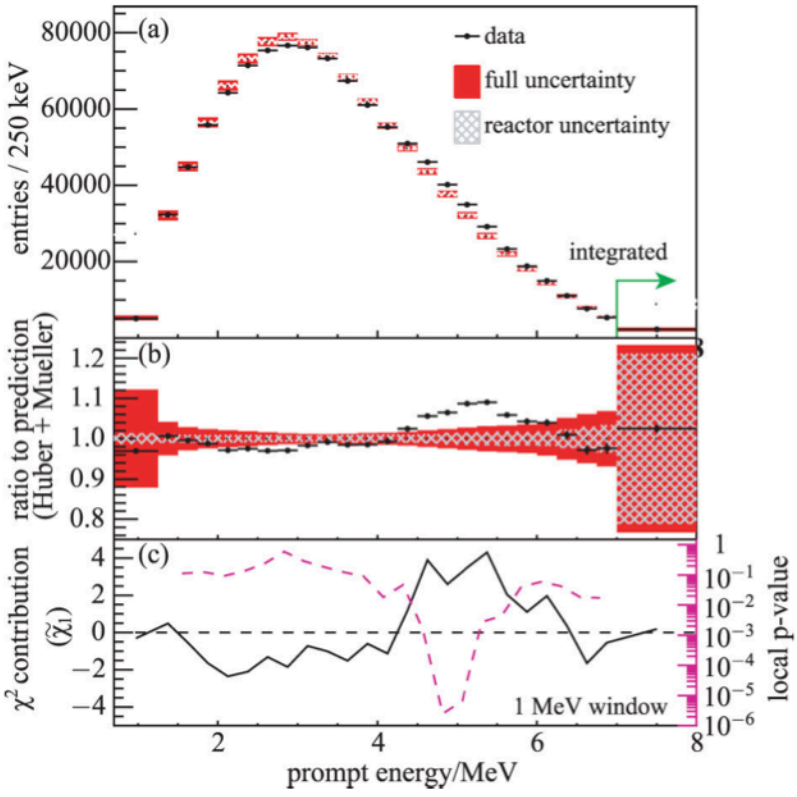

Figure 2.18: Prompt positron energy spectrum measured by Daya Bay near detectors (black) compared to the Huber+Mueller prediction with associated uncertainties (red). The ratio between the observed and predicted spectra is plotted in the middle panel [83].

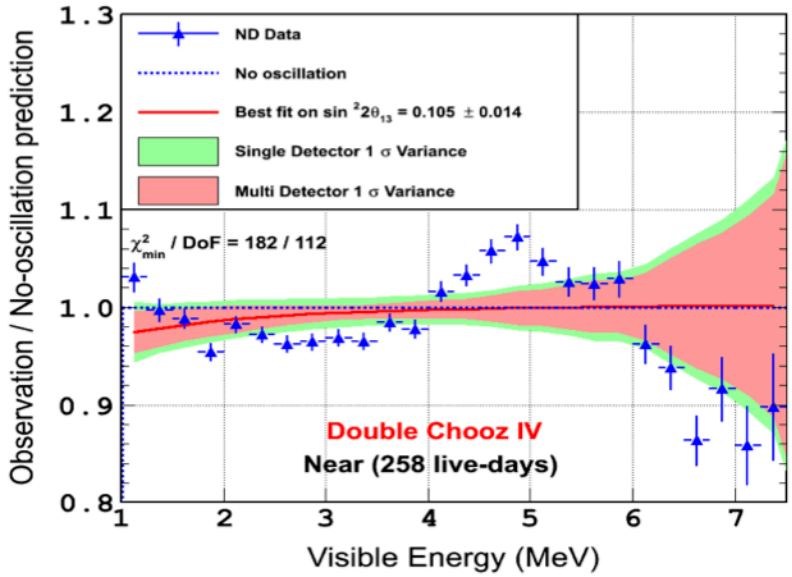

Figure 2.19: Ratio of the prompt positron energy spectrum measured by the Double Chooz near detector (blue) to the Huber+Mueller prediction with associated uncertainties [99].

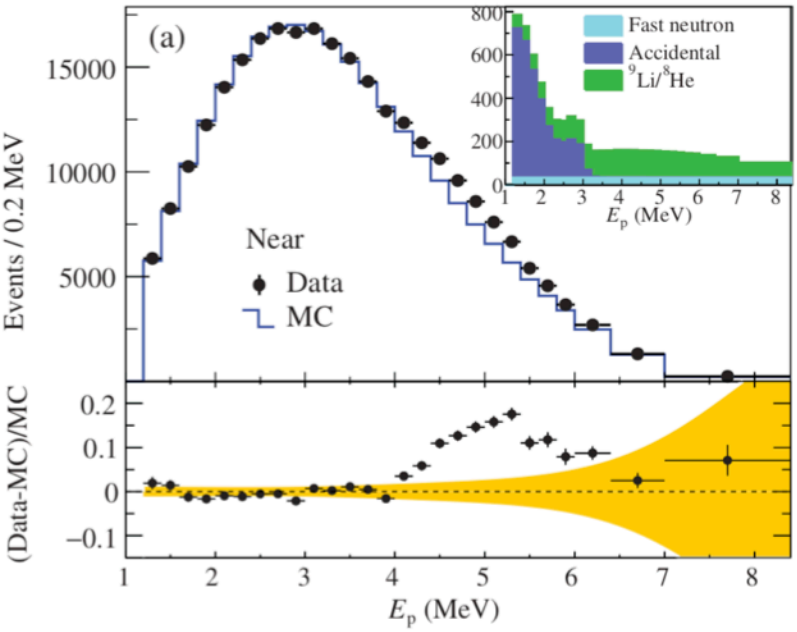

Figure 2.20: Prompt positron energy spectrum measured by the RENO near detector (black) compared to the Huber+Mueller prediction (blue). The ratio between the observed and predicted spectra is plotted below [100].

The origin of the bump must thus be rooted in the nuclear physics describing the emission of reactor $\overline{\nu}_e$. Many hypotheses have been suggested, indicating that either the Huber-Mueller model is missing information or oversimplifying the calculation. As described in Section 2.1, the conversion of ^{235}U, ^{239}Pu, and ^{241}Pu involves shape and other corrections for forbidden transitions. In the bump region, these forbidden β decays dominate (only 10-15 branches in the region) and could be inaccurately converted, not reflected in the uncertainty estimation [49]. Recent *ab initio* calculations were performed using information from two different databases, and showed that one of the libraries predicted the bump indicating that the aggregate β measurements were not complete [102]. However, updates were made with new input from TAGS measurements (see Section 2.1) and reproduced the bump when comparing observations to models built from both databases [101]. Therefore, it is not clear whether the underlying β spectrum from the ILL experiment are wrong, if the nuclear databases have incorrect information, or both. Instead of a global calculation issue there could be problems with the predictions for particular isotopes. The ^{238}U prediction is the most uncertain, stemming from *ab initio* calculations using limited input measurements. One result suggests that, to match the size of the deviation observed by Daya Bay, the shape of ^{238}U spectrum would be unphysical, in total disagreement with experimental measurements [103].

At present, the origin of the bump is still under intense study. The overall consensus in the field is that the $\sim$2% model uncertainties are underestimated, and could be correlated with the flux anomaly if both are modeled incorrectly [50, 56].[12] Precision measurements of reactor $\overline{\nu}_e$ spectra and TAGS analyses are the only avenues to resolve the issue. New measurements at HEU reactors are important to disentangle the isotropic contributions to the bump at LEU reactors, as ^{235}U dominates the $\overline{\nu}_e$ spectrum in both.

[12] The bump does not introduce errors in the precision measurements of θ_{13}, as the feature cancels when comparing the observed spectra between the near and far detectors.

2.6 Current short-baseline reactor experiments

Resolving the reactor $\overline{\nu}_e$ flux and spectrum issues described in Sections 2.4 and 2.5 is of significant interest to the field. Both anomalies can be addressed by a new generation of reactor experiments with detectors at very short-baselines (L$\sim$10), capable of excellent energy resolution. Several international experiments are currently being pursued with various reactor types, detector technologies, and performance parameters. Important features of each effort is summarized in Table 2.2. Sensitivity to eV-scale sterile neutrinos with a range of Δm^2_{41} values is controlled by the baseline(s), while higher statistics allow for an extended search in $\sin^2 2\theta_{14}$. Optimizing the distance between the reactor core (first few oscillation maxima), reactor power, and detector target mass are crucial. It is also beneficial to observe $\overline{\nu}_e$ from a compact reactor ($<1\,\mathrm{m}^2$) where possible sterile neutrino oscillations will not be washed out. Precision measurements of the energy spectrum require high statistics and good energy resolution. The choice of neutron capture agent is dependent on the size of the detector and is key to enhancing the IBD detection efficiency, along with pulse shape discrimination (PSD) capabilities. Generally, the major challenge of short-baseline experiments is to reject the high, correlated cosmogenic and reactor-related backgrounds, due to minimal overburden and proximity to the reactor cores, respectively. When overburden is not available, especially at sites very close to the reactor cores, segmented detectors are advantageous for increasing the signal-to-background with event topology.

Experiment	Reactor specs	Overburden	Baseline(s)	Mass/Volume	Segmentation	Resolution	PSD
DANSS	LEU 3.1 GW_{th}	50 mwe	10.7–12.7 m	1 m^3	2D	17%	No
Refs. [104, 105]	1.5 m r × 3.5 m h		movable	Gd-PS	1×4×100 cm^3		
NEOS	LEU 2.8 GW_{th}	20 mwe	24 m	1 ton	1D	5%	Yes
Refs. [106]	3.1 m d × 3.8 m h			Gd-LS			
Neutrino-4	HEU 100 MW_{th}	3.5 mwe	6–12 m	1.8 m^3	2D	–	No
Refs. [107]	0.35×0.42×0.42 m^3		movable	Gd-LS	0.22×0.225×0.85 m^3		
PROSPECT	HEU 85 MW_{th}	<1 mwe	7–13 m	∼4 tons	2D	4.5%	Yes
Refs. [108, 109]	0.435 m d × 0.508 m h		movable	^{6}Li-LS	117.6×14.5×14.5 cm^3		
SoLiδ	HEU 40–80 MW_{th}	30 mwe	6–9 m	1.6 tons	3D	14.5%	Yes
Refs. [110, 111]	0.5 m d			^{6}Li-PS	5×5×5 cm^3		
STEREO	HEU 58.3 MW_{th}	15 mwe	8.9–11.1 m	1.8 m^3	2D	8%	Yes
Refs. [112]	40 cm d × 80 cm h			Gd-LS	0.369×0.892×0.918 m^3		

Table 2.2: Summary of parameters for several short-baseline reactor experiments in operation. Reactor dimensions are specified according to literature, with radius, diameter, and height labeled by r, d, h, respectively. PS is used as the acronym for plastic scintillator and LS for liquid scintillator. Energy resolutions are reported in $\sigma/\sqrt{E(\mathrm{MeV})}$, as common in the literature. This thesis will detail measurements with the PROSPECT experiment.

Chapter 3

The PROSPECT experiment

3.1 Objectives and design concept

The Precision Reactor Oscillation and SPECTrum experiment (PROSPECT) is designed to comprehensively address both the reactor antineutrino flux and spectrum anomalies through observations of $\overline{\nu}_e$ emitted at very short baselines from the High Flux Isotope Reactor (HFIR) at Oak Ridge National Laboratory in Tennessee, USA [109]. The highly-segmented antineutrino detector (AD) uses $\sim$4 tons of PSD-capable ^{6}Li-loaded liquid scintillator (^{6}LiLS) to detect $\overline{\nu}_e$ through the IBD interaction. With a variable AD position of 7–13 m from the compact reactor core, PROSPECT can search for beyond the Standard Model eV-scale sterile neutrinos and make a precision, high resolution measurement of the $\overline{\nu}_e$ energy spectrum from ^{235}U fissions. Due to the detector segmentation, PROSPECT measures both the relative $\overline{\nu}_e$ flux and energy spectrum at multiple baselines within the detector, providing a method to probe oscillations to sterile states independent of reactor model predictions. This provides a direct test of the sterile neutrino hypothesis, as compared to indirect absolute flux measurements. An isolated measurement of ^{235}U will give insights into the origin of the deviations between the observed LEU $\overline{\nu}_e$ spectrum and predictions, as well

as providing constraints to reactor models. Furthermore, a high-resolution reactor $\overline{\nu}_e$ energy spectrum will be required as a reference for future precision experiments, such as JUNO [84] to uncover the neutrino mass ordering, and reactor monitoring applications.

PROSPECT must collect a high number of $\overline{\nu}_e$ statistics in a very challenging experimental environment. Proximity to the HFIR reactor dictates the distance between the core and the AD, eliminating the option of natural or structural overburden, and introduces a high rate of both reactor-related and cosmogenic backgrounds that can mimic IBD events. Space is also limited in the experimental hall, constraining the volume of neutrino target material, which has effects on the statistics, size of both the active and passive shields, and can introduce position-dependent IBD efficiencies. Furthermore, conventional liquid scintillators are toxic and flammable, and thus are not compatible with working inside the HFIR reactor facility. Through the development of a compact, optically segmented detector optimized to operate with a new, safe ^{6}LiLS, PROSPECT has mitigated many of these obstacles. The detector package also includes a robust design of γ-ray and neutron shielding. When used in conjugation with active background suppression techniques, such as PSD, topology, and fiducialization, the signal-to-background is significantly enhanced. The technology developed by PROSPECT has demonstrated the ability to efficiently measure neutrinos on the Earth's surface, opening the possibilities for future reactor experiments and for use in nonproliferation efforts within applied neutrino physics.

3.2 The High Flux Isotope Reactor (HFIR)

HFIR is a compact, light water moderated research reactor located at ORNL. The cylindrical reactor core is 0.435 m in diameter and 0.508 m in height, composed of inner and outer concentric fuel elements, as seen in Figure 3.1. HFIR burns HEU

(93% ^{235}U enriched) fuel made from a U_3O_8-Al dispersion with burnable ^{10}B neutron poison clad in an aluminum structure [113]. To provide constant coolant channels, the fuel plates are curved. The fuel elements are confined within a beryllium neutron reflector. The whole assembly is contained in a 8-ft-diameter pressure vessel in a pool under ∼17 ft of water, located near grade at 259 m elevation. A constant power of 85 MW_{th} is maintained through each reactor cycle with a lifetime of ∼24 days. The entire fuel assembly is replaced after each cycle, so there is essentially no fuel burn-up. Thus, ∼99% of the $\overline{\nu}_e$ emitted by HFIR are from fissions of ^{235}U throughout each cycle, with minimal fuel evolution [108]. Typically, the reactor operates with a 46% duty cycle (reactor-on time per year), and backgrounds can be measured when the reactor is off. As it provides an intense, steady flux of neutrons, HFIR is primarily used for neutron scattering and radiation damage experiments, trace element detection, and the production of radioactive isotopes for various applications.

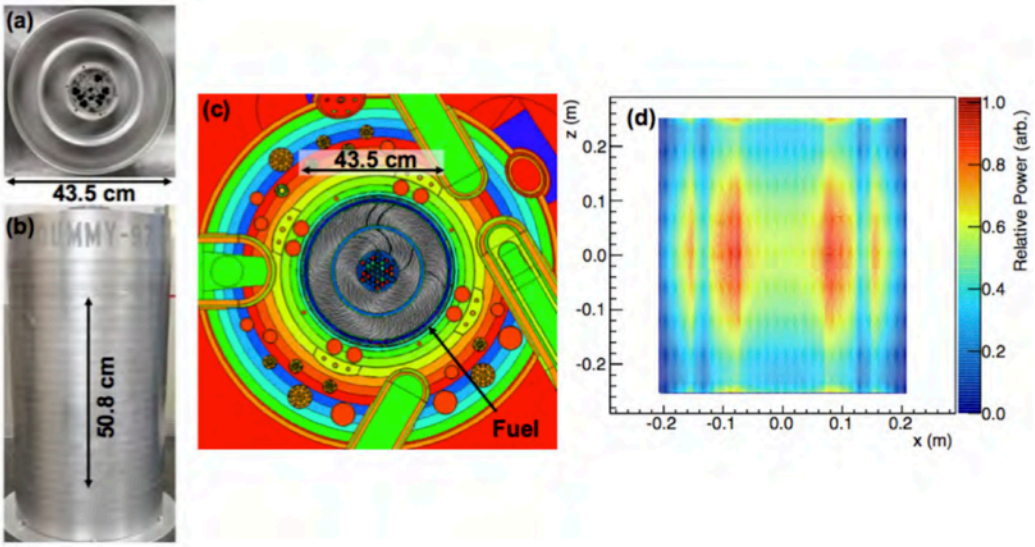

Figure 3.1: **(left)** Photographs of a dummy HFIR fuel element with active fuel diameter of 0.435 m and length of 0.508 m. **(center)** The location of the active fuel in a detailed MCNP model of the full reactor system. **(right)** A centered, cross-sectional projection of the core wide fission power density (i.e. antineutrino production source) [108].

3.3 Experimental strategy

3.3.1 Antineutrino detection

Antineutrinos with energy $\geq$1.8 MeV are detected through the IBD interaction (see Equation 1.1). Organic liquid scintillator is used to provide the free proton target and act as the calorimetry medium. As described in Chapter 2, the prompt positron carries most of the $\overline{\nu}_e$ energy and ionizes the scintillator as it travels through. The positron quickly loses energy and annihilates with a surrounding electron at rest, creating two 511 keV γ-rays. The annihilation γ-rays are detected primarily through Compton scattering. Because of the $\mathcal{O}$(ns) time scale of these energy depositions, the sum of the individual ionization depositions and the 1.022 MeV from annihilation result in a total positron energy signal from 1-8 MeV. Thus, the observable connected to the neutrino energy is the reconstructed visible energy, E_{prompt}, which is measured with high precision and resolution. The delayed neutron will scatter around the scintillator until it thermalizes and captures, acting as a tag for the interaction. PROSPECT dopes the scintillator with ^{6}Li ($\sim$ 0.1% by mass) to reduce the time before capture to $\sim$40 μs. As an exothermic reaction, Q(n,^{6}Li) = 4.78 MeV is released with an α and ^{3}H (see Table 2.1). However, the light output from heavy charged particles with high ionization density is significantly quenched, reducing the visible energy from the process to $\sim$0.55 MeV[1], which is below the IBD threshold. The high ionization density provides the advantage that decay products can be detected within the same segment as the original IBD vertex, traveling only $\sim$10μm, which is ideal for a compact detector.[2] Since hydrogen is abundant in the scintillator, the neutron can also capture on a ^{1}H nucleus (labelled (n,H) hereafter), marked by the emission of a 2.2 MeV γ-ray. Both processes are illustrated in Figure 3.2.

[1] This is often written as $\sim$0.55 MeV$_{ee}$, referring to the energies in their "electron equivalent".

[2] ^{252}Cf calibrations indicate neutrons travel a transverse distance of one segment >85% of the time before capture, while the remaining fraction are captured after two or three segments.

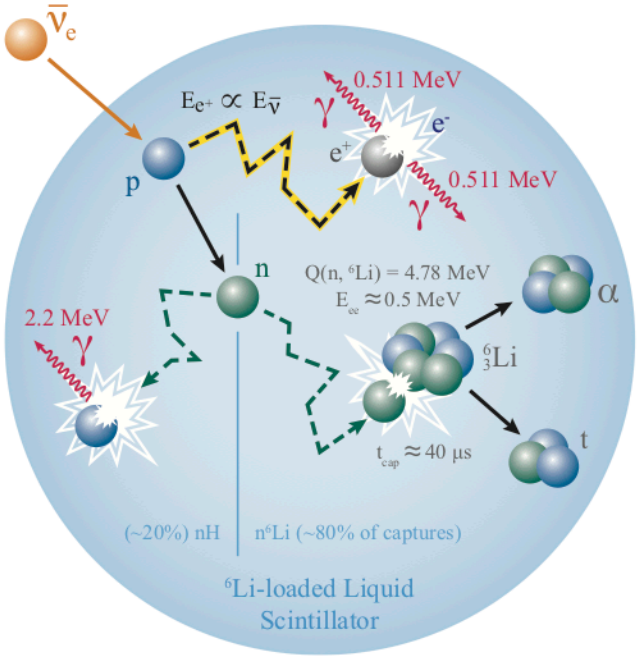

Figure 3.2: Illustration of the IBD process with a ^{6}LiLS target. Both capture processes, (n,^{6}Li) and (n,H) are depicted.

The correlation in time and space between the prompt positron and delayed neutron signals provides a distinct $\overline{\nu}_e$ signature. This is further enhanced when combined with the scintillator's ability to distinguish particle type through PSD, using the simple expression

$$PSD = \frac{Q_{tail}}{Q_{full}}, \tag{3.1}$$

where Q_{tail} is the amount of charge found in the PMT pulse tail and Q_{full} is the total charge, as shown in Figure 3.3. Using this metric, particles can be classified as low dE/dx or electronic recoils and high dE/dX or nuclear recoils. Backgrounds can be greatly suppressed using this strategy, which is of vital importance for measurements at such close proximity to the HFIR core with little overburden. The major sources of backgrounds to IBDs at the HFIR site include high-energy γ-rays and fast neutrons generated by the reactor and those with cosmogenic origins, respectively.

High singles rates[3] can be problematic by overwhelming the data rate and can lead to high accidental or random coincidence rates. Correlated backgrounds identified by a delayed neutron capture on ^{6}Li, are the largest threat to the identification of IBDs, as certain classes can pass a sequence of prompt and delayed timing, PSD, and topology cuts.

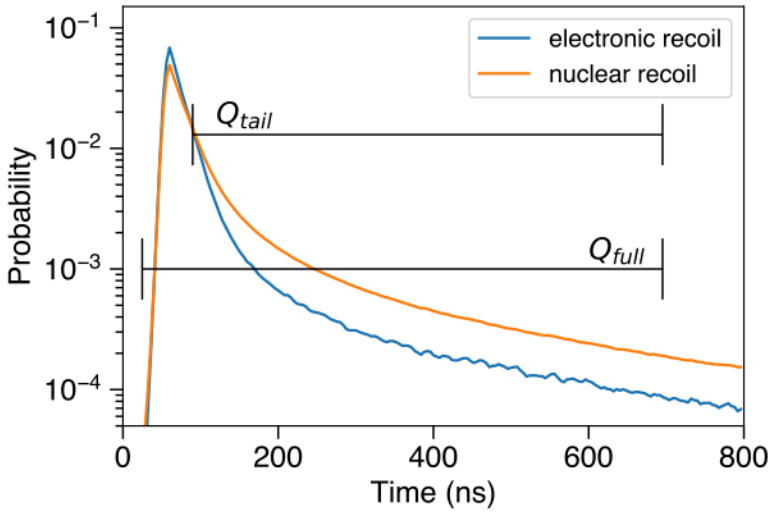

Figure 3.3: Template waveforms from the PROSPECT-50 prototype detector illustrating the difference between electronic and nuclear recoil energy depositions from a ^{252}Cf spontaneous fission source. The fraction of charge in the tail of the pulse with respect to the total integral charge is used as a discrimination metric [114].

3.3.2 Technical goals and requirements

Previous optimization studies of short-baseline antineutrino detectors identified key parameters to enhance sensitivity and precision: energy resolution $\leq 10\%/\sqrt{E(\mathrm{MeV})}$[4], position resolution $\leq$0.20 m, signal-to-background ratio >1:1, scintillator mass of a few tons, and baseline coverage around 3 m [115]. PROSPECT designed a segmented, liquid scintillator detector capitalizing on the properties of ^{6}Li to efficiently identify

[3] "Singles" refer to individual particle detections, contrasted with the correlated event rate generated by coincident pairs of particles within a certain timing window.

[4] It is common in reactor neutrino experiments to quote the RMS or $\sigma/\sqrt{E(\mathrm{MeV})}$ resolution, as opposed to the standard full-width half-max (FWHM) metric.

the neutrons from the IBD interaction in a highly localized region of space with a distinct energy signature to meet these goals. Good PSD allows hadronic signals to be separated from γ-rays, electrons, and other minimum ionization background particles. Optical segmentation improves background suppression by allowing spatial correlation of the prompt and delayed signals while naturally dividing the recorded data into bins of known position and volume. To eliminate the loss of positron energy through non-scintillator materials, the segmentation system (optical grid) must be as low mass as reasonably achievable to provide an acceptable energy response for precision measurement of the $\overline{\nu}_e$ spectrum.

Backgrounds can be further reduced through passive and active techniques. From prototype detector data, a layered approach to shielding is required to suppress reactor-related γ-rays and neutron backgrounds sufficiently to minimize random IBD-like coincidences. Layers of water, polyethylene, borated polyethylene (BPE), and [0.05,0.1] m of lead[5] are most effective, especially when constructed as hermitic layers. However, the presence of high-Z lead can result in cosmogenic spallation near the active detector. Segmentation adds the ability to easily fiducialize the detector in analysis, selecting IBD candidates from specific regions of the detector; using non-fiducial volume as an active veto significantly reduces the correlated neutron background. A simulation of the cosmic neutron event rate within the segmented PROSPECT detector is shown in Figure 3.4. The IBD-like background rate in the outer ring of the detector is 10-100 times that of the inner region. Fiducial cuts can also be made along the length of each segment close to the PMT faces. Topology cuts are optimized in the fiducial volume where IBD-like neutrons and γ-rays are contained, reducing the position-dependency of the detection efficiency and energy response.

Multiple calibration methods are needed to establish the energy response and

[5]Due to weight limitations, 0.025-m-thick lead was used to construct the full detector shield package.

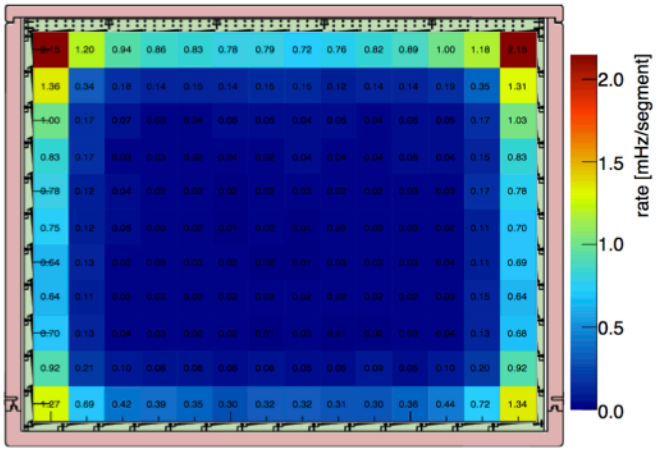

Figure 3.4: Simulated background rate of cosmogenic neutron interactions that mimic the IBD signal after topology cuts and segment-end fiducialization. The background rate in the outermost ring of segments (rows 1 and 11, columns 1 and 14) is considerably higher than in the nominal fiducial volume used in analysis (rows 2–13, columns 2–10). Surrounding the segments is the acrylic support structure and the acrylic containment tank of the inner detector [108].

PMT timing of each segment to IBD interactions. PROSPECT is thus required to accommodate *in situ* radioactive sources or optical pulses for special calibration runs. Fitted deposited energy spectra from MeV-range γ-ray sources, such as ^{137}Cs, ^{60}Co, allow the absolute positron energy scale and scintillator non-linearity to be calibrated. Annihilation γ-rays from ^{22}Na can be used to understand the positron efficiency due to the missing energy difference between the center and edges of the detector. ^{252}Cf and/or AmBe neutron sources allow for the determination of the IBD neutron detection efficiency in each segment. Between source deployments, radioactive and cosmogenic backgrounds such as (n,^{6}Li) capture and through-going muons, can be used to determine the time-dependence of the energy scale, PMT gain and timing, or scintillator performance. Fast laser pulses mimicking the rise time and maximum wavelength emission of the scintillator can also be used to establish the PMT timing for position reconstruction. Spiking the ^{6}LiLS with $\mathcal{O}(10^{-13}\,\mathrm{g})$ of ^{227}Ac can allow

for precision measurements of the position resolution and absolute volume in each segment, using the fast double-α cascade from the "RnPo" decay chain [109]:

$$^{219}Rn \xrightarrow{t_{1/2}=3.96\,s} \alpha + ^{215}Po \xrightarrow{t_{1/2}=1.78\,ms} \alpha + ^{211}Pb. \tag{3.2}$$

The α from ^{219}Rn can take a range of energies between 6.4 and 6.9 MeV, while the ^{215}Po α is monoenergetic at 7.386 MeV.

3.3.3 PROSPECT at the HFIR site

PROSPECT is positioned on the ground level of the HFIR Experiment Room, 5 m above the reactor core plane. Figure 3.5 represents the AD's orientation to scale. In this location, the size, weight, and position of the AD is constrained by geometric limitations of the room and safety requirements. The detector rests on part of the concrete monolith that supports the reactor pool structure and 0.15-m-thick steel reinforced concrete that covers neutron experiments, limiting the detector and shielding weight to 3670 kg/m^2. Other facilities in the Experiment Room require access, further dictating the size and position(s) of the detector, which has a direct impact on the detector mass, shielding thickness, and range of baselines. To optimize the sensitivity to sterile neutrino oscillations, the AD can move between three baseline positions, with average ranges of 7.93 to 12.36 m, as shown in Figure 3.6. For the data described in this thesis, the AD is in Position 1 with a baseline of 7.93 m between the reactor core center and the detector center (coordinates (5.97, 1.19, 5.09) m with respect to the core center).

Extensive background measurements were performed by PROSPECT at the various detector baselines during reactor-on and -off periods. Reactor-related γ-rays can dominate the detector singles rate and also combine to produce accidental backgrounds within the IBD time window. Prompt high-energy γ-rays emitted from short-

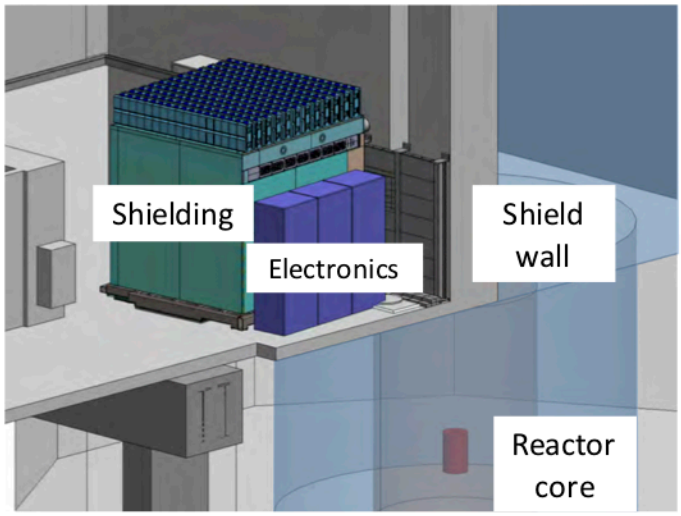

Figure 3.5: Layout of the PROSPECT experiment. The detector is installed in the HFIR Experiment Room next to the water pool (blue) and 5 m above the HFIR reactor core (red). The floor below contains multiple neutron beam lines and scattering experiments [108].

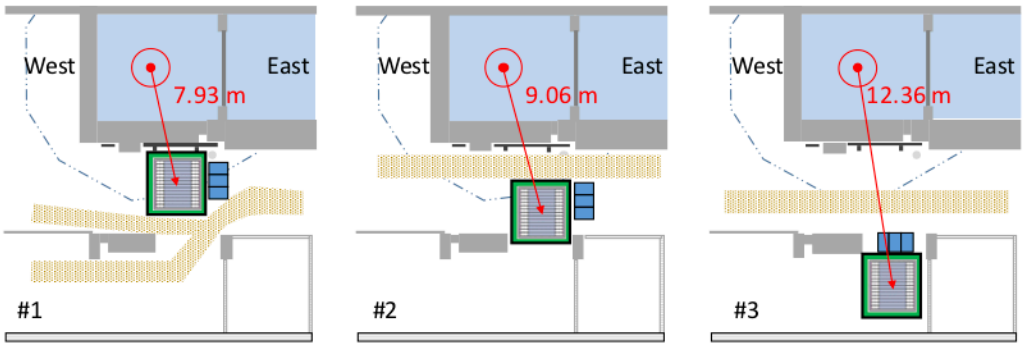

Figure 3.6: Plan view of PROSPECT detector locations in the HFIR Experiment Room. The detector is initially installed in Position 1 at an estimated baseline of 7.93±0.1 m from the center of the reactor core to the center of the active detector. Moves to Position 2 (9.06 m) or Position 3 (12.36 m) are planned. The chassis footprint (green) and inner detector are shown. Electronics racks are shown in blue, the reactor vessel and core in red, and the reactor wall in front of the pool in tan. A dashed line shows the shape of the underlying concrete monolith. Required walkways and clearances that limit possible positions are also shown in beige [108].

lived isotopes can be produced from fast and thermal neutrons interacting with water or iron in structural materials in the vicinity of the reactor. PROSPECT is positioned behind a 1-m-thick concrete wall between the reactor pool and the Experiment Room,

which helps to shield from these particles. However, high-resolution surveys with NaI(Tl) scintillator detectors determined that additional lead shielding was required to manage the γ-ray singles rate near the beam line penetrations [113], as illustrated in Figure 3.7. A permanent local lead wall was built to reduce the flux, with the central part of the wall having a thickness of 0.10 m. Furthermore, the neutron beams transported through piping to scattering experiments can encounter seams or penetrations and interact with materials, creating local "hot-spots" of γ-rays. Some shielding underneath the detector is achieved by partial coverage of the concrete monolith flooring. However, local hot-spots around the monolith are observed from neutron captures on structural iron and can vary with time. Fast neutrons generated by the fissions within the core are efficiently moderated by the reactor pool, eliminating a potentially large, correlated background [113].

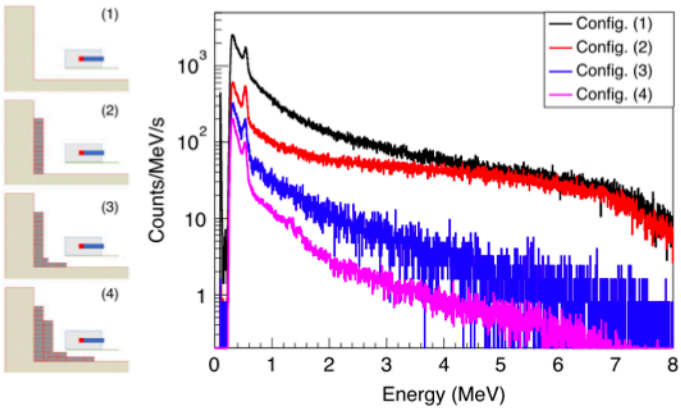

Figure 3.7: Measured energy spectra for a NaI(Tl) detector inside a horizontal lead collimator placed in different configurations from a 102 cm wide lead wall, with the reactor operating at nominal power. This location is in front of a localized γ-ray background source [113].

Cosmogenic neutrons can be produced as cosmic rays interact in the atmospheric column above the detector, in surrounding structures, or within the detector itself through spallation. The HFIR roof is made from 0.2-m-thick steel reinforced concrete, providing very little attenuation of these cosmic particles. The neutrons can

range in energy from thermal to fast (many GeV) and can have distinct correlated signatures. Fast neutrons will interact with the scintillator producing proton recoils and then capture on ^{6}Li. Neutron showers created from muon or neutron spallation can exactly mimic the IBD signature through thermal neutron capture on ^{1}H followed by another capture on ^{6}Li, or by fast neutron inelastic scatter on ^{12}C followed by capture on ^{6}Li. The total flux is dependent on environmental variables such as altitude, barometric pressure, solar activity, and high-Z material that increase spallation. This can translate to time and position variations. Preliminary studies shown in Figure 3.8 suggest that the cosmogenic neutron rate does not substantially vary between different positions from the reactor core.

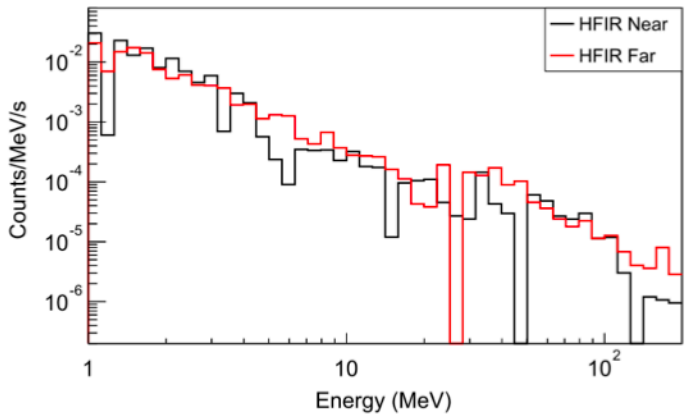

Figure 3.8: The cosmogenic neutron-induced energy spectrum recorded at different baselines from HFIR. Near measurements were taken inside of the Experiment Room, while far measurements were taken outside of the HFIR building. The preliminary spectra illustrate that the cosmic rate is relatively constant, as minimal overburden is provided by the HFIR building. Fluxes do not have atmospheric condition corrections applied [113].

As made clear in Figure 3.6, the detector segments are installed parallel to the reactor wall, slightly off-axis with respect to the reactor core. This orientation was chosen to maximize the size of the active volume according to the constraints described above. As a result, each segment contains a small range of true baselines, with an expected $\overline{\nu}_e$ flux asymmetry from one end to the other, at a maximum of 0.43% [108].

3.4 Achieved parameters

The experimental parameters achieved by PROSPECT in the first few months of operation are listed in Table 3.1. The baseline of the detector was determined by combining survey measurements of the reactor core within the HFIR building to survey measurements of various points on the detector. The following sections and chapters will outline the detector design, calibrations, and analysis where these parameters are extracted and used.

Parameter	Value
Reactor	
Power	85 MW_{th}
Shape	Cylinder
Size	0.43 m d × 0.508 m h
Fuel	HEU
Duty cycle	46%
Antineutrino Detector (AD)	
Total target mass	3680 kg (∼4 tons)
Nominal fiducialized target mass	2581 kg
Dead structural material	3.4%
Center of detector baseline	7.93±0.1 m (9.1, 12.4 m possible)[6]
Detector baseline range	2 m
Energy resolution ($\sigma/\sqrt{E(\mathrm{MeV})}$)	4.5% (oscillation), 5% (spectrum)
Position resolution (x,y)	15 cm
Position resolution (z)	5 cm
Correlated S:B ratio	1.3 (oscillation), 1.7 (spectrum)

Table 3.1: Achieved PROSPECT experimental parameters. Differences between the analyses detailed in this thesis, the first oscillation and spectrum measurements, are highlighted.

[6]Prior to the construction of the detector, it was assumed the baseline would be known sufficiently well to conduct an oscillation search. The estimated uncertainties were included in the sensitivity studies and indicated PROSPECT's ability to scan a sizable region of parameter space. The achieved baseline uncertainties are in-line with those estimates. Future analyses will be conducted to quantitatively understand the required baseline error in the different regions of the allowed parameter space.

3.5 Detector design

The PROSPECT AD is constructed from nested layers of $\overline{\nu}_e$ target material, background shielding, and structural support: an ^{6}LiLS active detector, inner and outer containment tanks, a passive shielding package, and detector movement elements. Models of these components are shown in Figure 3.9. The 3760 L ($2.045\times1.176\times1.607\,\mathrm{m}^3$) of ^{6}LiLS active volume is defined by the walls of the inner acrylic containment tank and is optically segmented into a 14×11 grid, parallel to the reactor pool wall. The optical grid is made from low mass, reflective optical separators held together by 3D printed hollow support rods and was constructed to support *in situ* radioactive and optical calibration sources while minimizing dead material. This system allows light generated in an individual segment to be transported to either end where it is readout by PMT optical modules. The acrylic housings enclosing the PMTs were constructed to be slightly smaller in cross section to allow the liquid scintillator to circulate freely throughout the volume. Acrylic segment supports reinforce the position of the PMT optical modules and provide support to the outer portion of the optical grid. The ^{6}LiLS level reaches beyond the top of the optical grid with a layer of nitrogen cover gas above acting as an expansion volume. All elements in contact with the ^{6}LiLS in the active detector were tested for material compatibility.

Surrounding the active detector are a series of mostly hermetic shielding and structural layers, as illustrated in Figure 3.9. The acrylic containment tank is 0.063-m-thick and is enclosed by a mixed layer of 0.025 m of water or BPE, and [0.025,0.075] m of BPE supported by a 0.025 m aluminum secondary containment tank. A large, layered shielding package rests outside of the aluminum tank, consisting of 0.025 m of lead, 0.10 m of structural polyethylene timbers, and 0.025 m of BPE [108]. The entire package is covered by aluminum paneling for fire safety. Polyethylene WaterBricks [116] containing water cover the top of the detector protected by a fire blanket. The data acquisition (DAQ) and control electronics housed in electronics racks outside

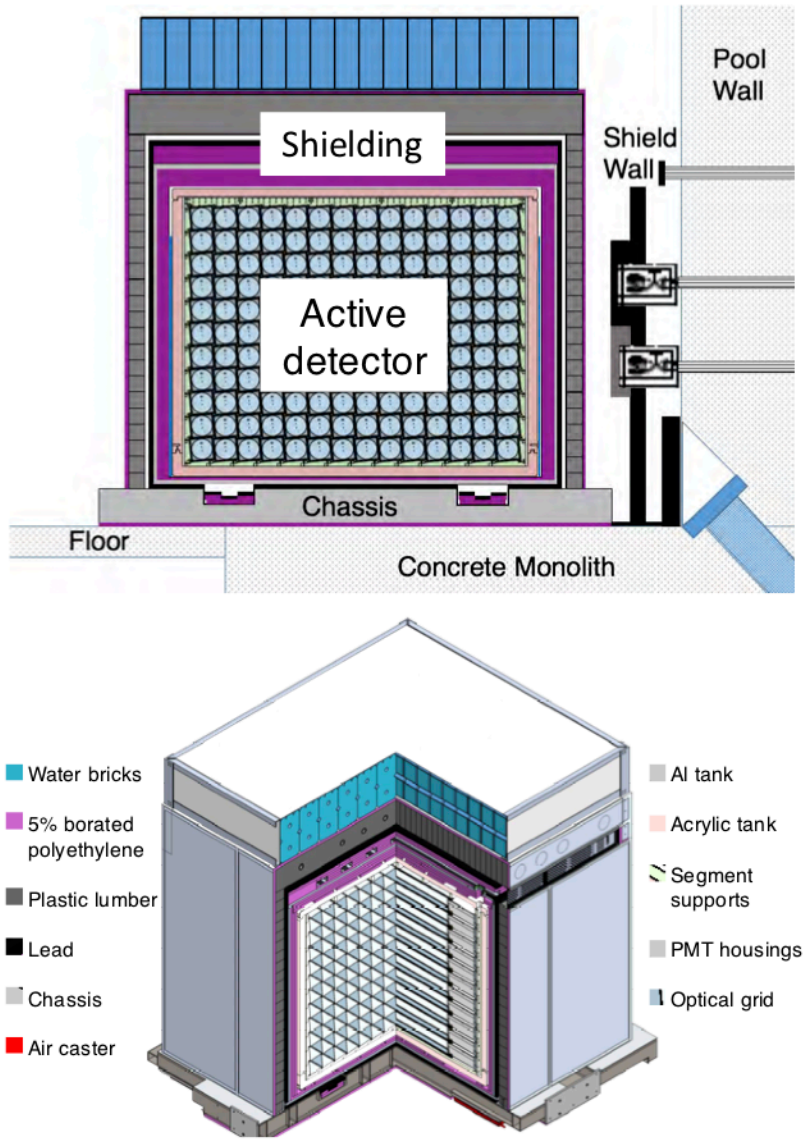

Figure 3.9: **(top)** Schematic of the PROSPECT AD illustrating the active ^{6}LiLS detector volume divided into 14×11 array of optical segments and surrounded by nested containment vessels and shielding layers. Lead shield walls cover penetrations in the reactor pool wall associated with high γ-ray backgrounds. **(bottom)** A cutaway view of the detector and shielding assembly model in three dimensions. The optical grid system, supported by acrylic supports (light green), allows for the PMT optical modules (beige) to be housed on either end of each segment. The acrylic tank is surrounded by borated polyethylene (purple) and a secondary aluminum tank (light gray). [108].

of the shielding package can be viewed in Figures 3.5 and 3.10**(left)**. Light-tight aluminum boxes mounted to the top of the detector on the opposite side of the

electronics racks, shown in Figure 3.10**(right)**, contain the radioactive calibration motor system. The slow-control panel and liquid nitrogen dewar are also pictured. The entire load of the AD assembly is spread across a steel chassis, which enables movement of the detector through forklift channels and air casters.

Figure 3.10: **(left)** Electronics racks and their contents during installation, before being mounted onto the outside of the shielding package. **(right)** View of full PROSPECT detector package from the West face. The calibration motor boxes are mounted to the side of the aluminum paneling, allowing radioactive sources to be transported through Teflon tubing from the top of each segment column. The slow-control panel (blue) is shown along with the liquid nitrogen dewar used for the boil off cover gas.

3.5.1 ^{6}Li-loaded liquid scintillator

The utility of scintillator is its ability to transform energy dissipation in the form of ionization and excitation into the emission of visible or ultraviolet radiation. Organic molecules configured in benzene rings (C_6H_6) are formed from double, π-bonds, where unpaired, valence electrons have delocalized wavefunctions making up the singlet

ground state S_0 (electrons have opposite spins, with a total spin of zero).[7] This electronic structure allows for excitation into higher energy singlet states (e.g. S_1, S_2). Relaxation from the S_1 state is responsible for fast fluorescence with a time constant on $\mathcal{O}$(ns), as transitions from $S_{n\neq 1} \rightarrow S_0$ are non-radiative. Triplet states with a total spin of one can also be excited, but transitions from $T_1 \rightarrow S_0$ are suppressed due to selection rules (i.e. requires a spin flip), resulting in a slower fluorescence with a longer transition time (generally $\mathcal{O}$(ms)). In all cases, the emitted light is always lower in energy compared to the absorbed energy due to the Stokes shift, defined by the eV-scale band gap between S_0 and S_1. These processes are illustrated in Figure 3.11. The wavelength of this light is typically outside of the PMT photocathode sensitivity (blue-visible) and must be shifted by primary and secondary fluors (solute) with overlapping absorption spectrum through the Förster resonance energy transfer process. The response of scintillators is non-linear, dependent on the energy loss behavior of the incident particle, as described by the Bethe-Bloch formula. The ratio of the fast to slow scintillation components is highly correlated to the stopping power dE/dx of the primary ionizing particle, which can be translated via a detection system into waveforms with different charge integrals in the signal tail, forming the basis for the PSD technique [117, 118]. A semi-empirical model for this process is outlined in the classical book on scintillation by Birks' in Ref. [117] and will be discussed in Chapter 5.

Through an extensive R&D program, PROSPECT developed a novel ^{6}Li-loaded scintillator using the commercial EJ-309 solvent (di-isopropylnapthalene) [119]. A high light yield and good PSD capabilities were achieved to meet the requirements for a good energy resolution (of $4.5\%/\sqrt{E(\text{MeV})}$) and excellent separation of electronic and nuclear recoils, respectively. Furthermore, the ^{6}LiLS is non-flammable

[7] Other organic molecules also scintillate, for example liquids with xylene or toluene as the base solvent.

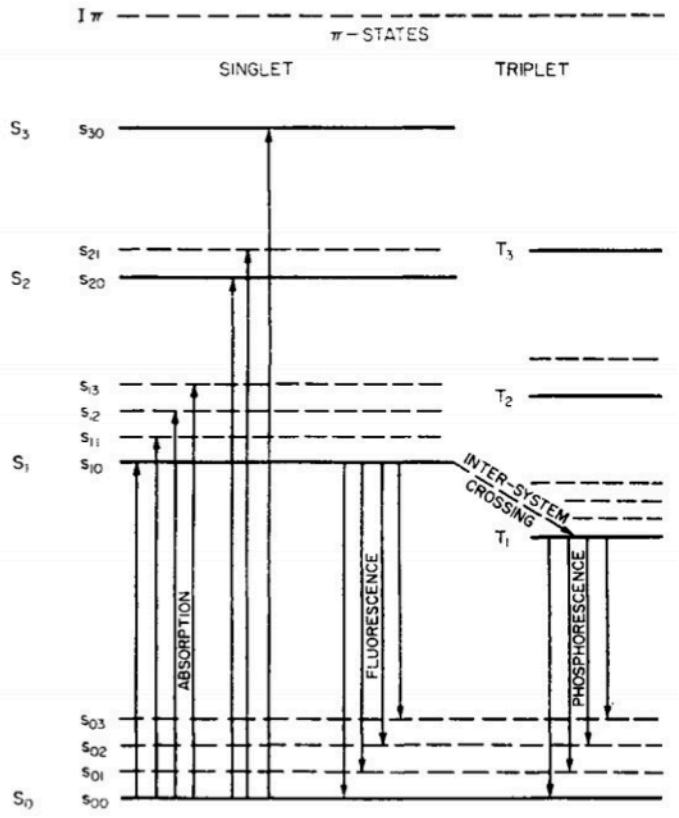

Figure 3.11: Electronic levels of π-bonds in an organic molecule. Singlet states are represented by S_n and triplet states T_n. Absorption, (fast) fluorescence, and phosphorescence (slow fluorescence) transitions are labeled [117].

and has low toxicity, meeting the HFIR safety requirements.[8] The scintillator was produced by adding a non-ionic ether-based glycol surfactant to the base EJ-309, which allowed for the loading of an 95%-enriched ^{6}LiCl aqueous solution in a thermodynamically stable, uniform microemulsion [120]. With a final ^{6}Li concentration of $\sim$0.08% by mass, the loading procedure reduced the light yield of the base EJ-309 by $\sim$30% to 8200$\pm$200 photons/MeV. Two fluors, 2-,5-diphenyloxazole (PPO) and 1,4-bis(2-methylstyryl)benzene (bis-MSB), are used to shift the emission spectrum. Table 3.2 compares the relevent properties for particle detection of EJ-309 to PROSPECT ^{6}LiLS. In addition, $\sim$0.5 Bq of ^{227}Ac ($t_{1/2}$=22 yr) was uniformly dis-

[8] Previous reactor neutrino experiments used pseudocumene or linear alkylbenzene as the base scintillator solvent, which are not suitable for these requirements.

tributed throughout the scintillator to monitor the efficiency, volume, and position resolution of each segment [108]. Collaborators at Brookhaven National Laboratory produced the ^{6}LiLS. The full details of the process can be found in Refs. [108, 121].

Property	EJ-309	PROSPECT ^{6}LiLS
C:H:O ratio	90.6:9.4:0%	84.34±0.11:9.69±0.21:5.97±0.24%
Density (g/mL)	0.959	0.9781±0.0008
Maximum emission (nm)	424	424
Index of refraction (at 424 nm)	1.57	–
Light yield (photons/MeV)	11,500[9]	8200±200

Table 3.2: Properties of EJ-309 scintillator given by Eljen Technology [119] and PROSPECT ^{6}LiLS, as measured by the collaboration. The index of refraction of the ^{6}LiLS was not measured, as the exact value is not crucial for the experimental work.

Liquid scintillators are known to react with other materials and can cause instabilities in the performance of the scintillator while also diminishing the structural integrity of detector materials. Extensive material compatibility and stability tests were completed with the ^{6}LiLS, informing the active detector design [108, 122]. Polylactic acid plastic (PLA), polytetrafluoroethylene (PTFE), fluorinated ethylene propylene (FEP), polyether ether ketone (PEEK), acrylic (clear, white, black), Viton [123], and Acrifix 2R [124] were deemed acceptable materials to be in contact with ^{6}LiLS. Oxygen quenching can also reduce the light yield over time and was observed with PROSPECT prototypes [114]. To minimize the exposure of ^{6}LiLS to oxygen in the air, a cover gas of boil-off nitrogen is constantly maintained in the AD.

3.5.2 Low-mass optical grid

The target volume, $2.045 \times 1.176 \times 1.607\,\mathrm{m}^3$, is optically divided into a 14×11 grid of 154 longitudinal segments with the long axis nearly perpendicular to the reactor core. Each segment is 1.176-m-long with a $14.5 \times 14.5\,\mathrm{cm}^2$ square cross-sectional area and

[9] A newer version of EJ-309 has become available with a light yield of 12,300 photons/MeV, which is currently quoted on the Eljen Technology website [119].

rotated 5.5° from the horizontal. The optical grid is composed of low-mass, highly specularly reflective separators held mechanically rigid by 3D-printed white PLA support rods. Further support and constraint for these components are provided by PMT optical modules on both ends. Acrylic support plates support the entire grid on all external sides. The system was optimized to efficiently propagate scintillation light along the length of a given segment to the PMT modules for readout, with <1% cross-talk between segments. Due to the slight tilt of each segment, the reflective separators cover ∼99% of the total interior surface of each segment, minimizing the exposure of the support rod surface in the optical volume. The tilt combined with the hollow support rods also allows for the deployment of optical and radioactive sources to calibrate each segment *in situ*. To reduce the loss of positron energy in non-scintillating materials, the total mass of the optical grid is 3.4% of the target mass. The spread in the size of each segment was determined to be σ=0.1% from measurements during construction, ensuring the ^{6}LiLS volumes are uniform to within 1% [108]. Isometric drawings of the segmented active volume, a single segment, and support rod are provided in Figure 3.12.

The optical separators are made in a sandwich structure with a carbon fiber backbone, as shown in Figure 3.13**(top left)**. Layers of adhesive-backed 3M DF2000MA [125] specularly reflecting film, optically clear adhesive film, and a thin layer of FEP on the surface are adhered to one another on either side through cold pressure lamination. The outer FEP film is scintillator compatible and heat-sealed to form a liquid-tight enclosure around the sandwich. The glossy twill carbon fiber sheet gives the separator mechanical support, a smooth surface for reflections, and opaqueness to prevent the tranmission of light to neighboring segments. For photons <400 nm, the DF2000MA film is both highly reflective (<99% at normal incidence) and highly specular (<95% at normal incidence) [108]. In the segment, there is an index of refraction mismatch at the interface between the FEP layer (n ∼1.33) and the ^{6}LiLS

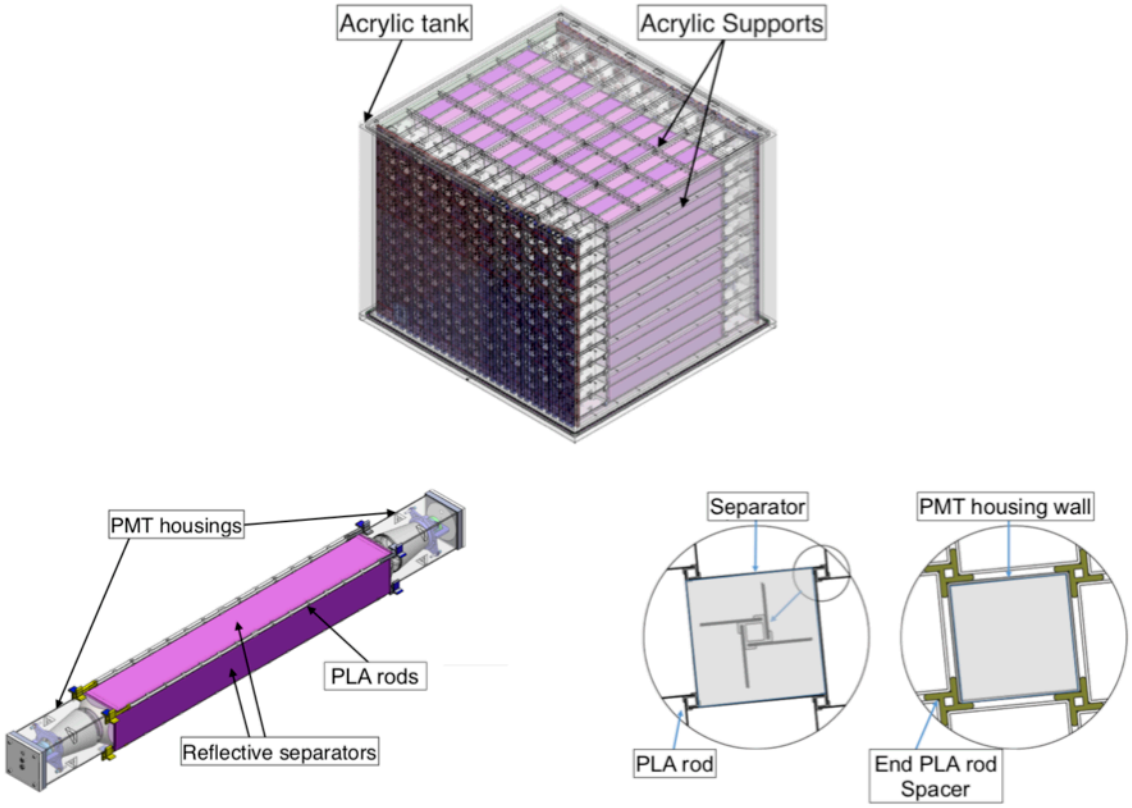

Figure 3.12: Detailed PROSPECT AD schematic. **(top)** The active detector enclosed by liquid-tight sealed acrylic tank and the optical grid is supported by acrylic supports. **(bottom left)** The individual segment with a 12.7-cm-(5-in-)diameter PMT on each end are enclosed by 4 reflective separators. **(bottom right)** The cross-sectional view of the PLA support rods and segment, where the separators are slotted on the hollow support rods to allow calibration sources to be inserted [122].

(n ∼1.5 assuming similar to EJ-309), that allows for total internal reflection at high incident angle.

The support rods were produced by filament-based 3D-printing using white-dyed 100 μm PLA. Nine support rods, 95- to 156-mm-long, are strung together to create string assemblies with total length >1 m to cover the distance between PMT modules. Multiple types of support rods are used on each string depending on the position of the rod assembly in the detector and the type of calibration source it will source, as shown in Figure 3.13**(bottom left)**. PTFE tubes are used to string calibration

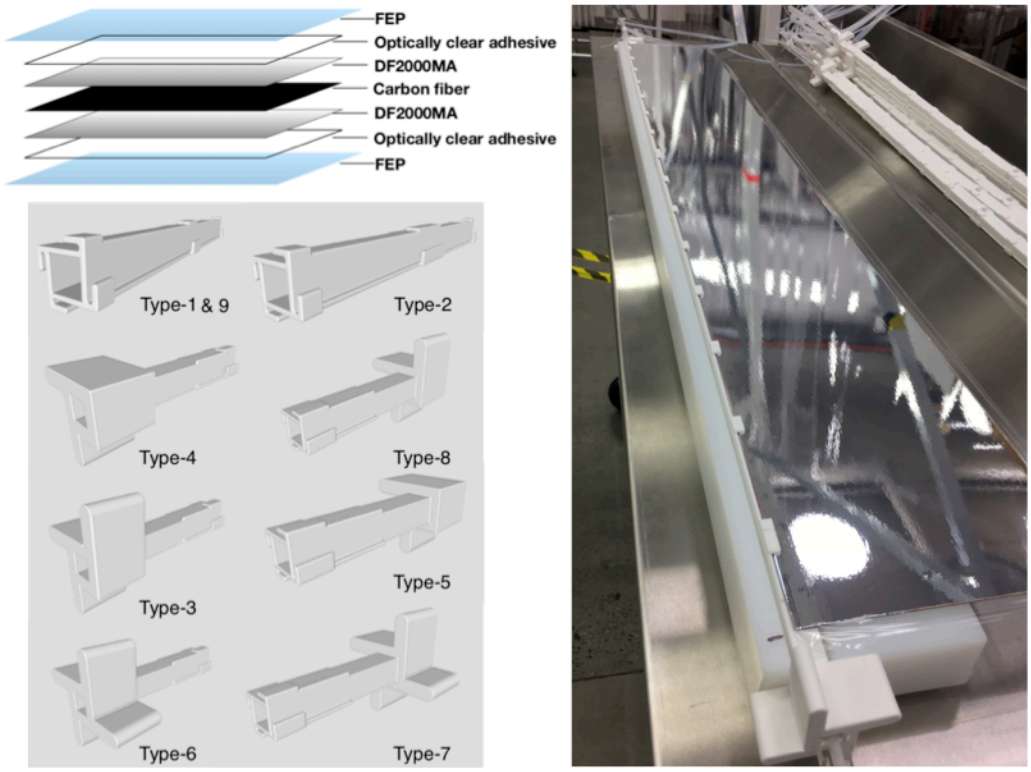

Figure 3.13: **(top left)** Illustration of the sandwich structure of a reflective separator [122].**(bottom left)** Schematic of PLA support rods labeled by type. Types 1,2,9 (center rods) are used to make the length of the support rod string. Types 3–8 (end rods) are used at the ends supported by the PMT modules and have handedness [122]. **(right)** An example of the full separator and support rod string assembly. Support rod tabs can be seen holding the separator in place.

assembly rods, while acrylic square dowels are used for non-instrumented rods. The end rods (types 3–8) serve as the mechanical interface between the optical grid, PMT modules, and exterior acrylic supports. Small tabs protrude from all surfaces of each support rod to grip the four optical separators at the corners of neighboring segments. Figure 3.13**(right)** shows a support rod string assembly attached to a reflective separator during detector construction. Extensive quality control (QC) checks were performed on all separators and support rods during production and detector construction. Components were cleaned before installation into the active volume following a rigorous procedure using solvents safe for each material and deionized

water.

3.5.3 PMT optical modules

PMTs are used to read out scintillation light collected on both ends of the individual segments, as pictured in Figure 3.12. Due to material incompatibility considerations, the PMTs and bases were required to be housed by a scintillator-safe material. Combinations of white, black and clear acrylic were chosen to construct liquid-tight rectangular enclosures. Various mechanical and optical components were used to couple the PMTs inside of the acrylic enclosures, as illustrated in Figure 3.15. The PMT optical modules were designed to accommodate the dimensions and photocathode coverage of two hemispherical, ∼5-in-(12.7-cm-)diameter PMTof the types: Hamamatsu R6594 SEL and ADIT Electron Tubes (ET) 9372KB. To outfit the whole detector, 240 Hamamatsu PMTs were used in the inner segments and 68 ET PMTs were used in the first and last columns and the top row of the optical grid, as shown in Figure 3.14.

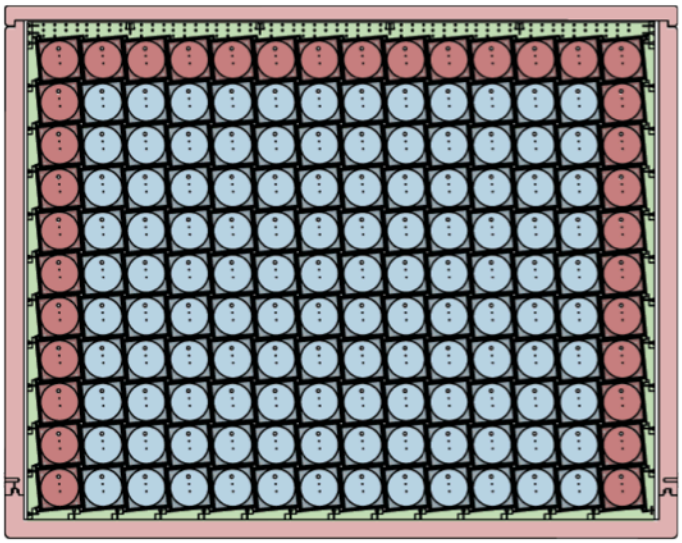

Figure 3.14: Cross section of the active AD showing the installation of 68 ET PMTs (red) in the outer columns and top row. The remaining detector segments are filled with 240 Hamamatsu PMTs (blue). [108].

To make the enclosures, acrylic pieces were bonded together with Acrifix into 350-mm-long boxes and then annealed. A 13-mm-thick ultra-violet transmitting (UVT) acrylic window is positioned on the front face of the module to accept scintillation light and efficiently transport it towards the PMT, minimizing reflections (index of refraction $n \sim 1.5$) and attenuation. The 19-mm-thick back flange is made from black acrylic to eliminate cross-talk and has a 130-mm-diameter circular hole for PMT installation. Both the front window and back flange are $144\,\mathrm{mm}^2$ and were slotted to accept and bond with the 3-mm-thick, $132\,\mathrm{mm}^2$ white acrylic side walls. A 32-mm-thick, $145\,\mathrm{mm}^2$ square section clear back plug with a circular front section and O-ring groove are machined from the same piece to seal the module after all parts were installed [108]. Two threaded PEEK cable seal plugs, spacers, and Viton O-ring[10] assemblies allow for separate PTFE-coded RG188 [127] high voltage (HV) and signal cables to enter the module, while keeping the enclosure liquid tight. A Kynar NPT screw plug is used to seal the filling port. As illustrated in Figure 3.12**(bottom right)**, the modules are supported in the rear by the back plug and in the front by (end) support rods. The front windows extend $\sim 1\,\mathrm{cm}$ into the optical grid, reducing possible cross-talk between segments. The circular section of the back plug provides rotational freedom to square with the front window, ensuring they are parallel to each other. Extensive QC measurements were taken to ensure all modules met the required dimensional tolerance and were liquid-tight.

The PMT is mechanically stabilized by an acrylic support structure and spring-loaded screws, providing uniform and sufficient pressure to the glass PMT stem. The front spherical face of the PMT rests in a DF2000MA, acrylic-backed conical reflector, acting as a light guide towards the photocathode. Different acrylic support and conical reflector shapes were needed to properly secure the Hamamatsu and ET PMTs. Retangular strips of DF2000MA are adhered to the insides of the acrylic

[10]Krytox grease [126] was used to lubricate and ensure good O-ring seals. It was tested for material compatibility with the ^{6}LiLS and deemed acceptable.

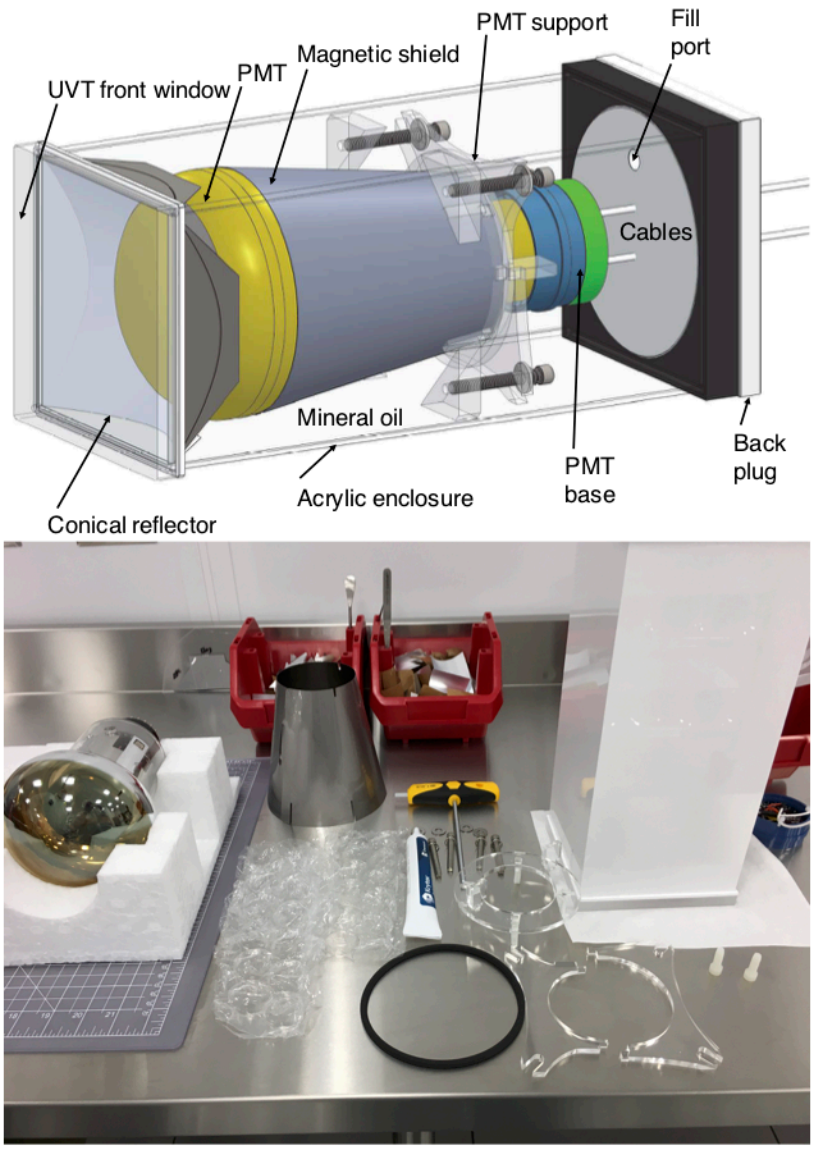

Figure 3.15: **(top)** Model of PMT optical module with major components labeled. Not pictured are the PEEK seal plugs assemblies, Viton O-rings, or bubble wrap expansion volumes [108]. **(bottom)** Photograph of various components used to build the modules.

enclosure walls to cover areas around the conical reflector. Hitachi Finemet [128] was laser cut into a conical section and used to protect the drifting electrons from stray magnetic fields. Printed circuit boards with the voltage dividing scheme for each PMT type were adhered to plastic sockets. Tapered voltage dividers were used to preserve linearity over a wide dynamic range with a negative bias. The base assembly was

connected to the PMT through the provided pins and directly soldered to the 4.88-m-long HV and signal cables. The cables later terminate in a bulkhead panel mounted to the outside of the secondary containment tank. To optimize the light transport between the acrylic front window and the PMT glass, the entire module was filled with optical grade mineral oil. Sheets of ∼300 mL air bubble wrap were placed inside the assembly behind the PMT faces to dampen pressure variations due to thermal expansions. Figure 3.16 shows photographs of the PMT optical modules at different stages of production. All parts were cleaned using rigorous procedures and tested for technical stability. Several rounds of electrical continuity, resistivity, and optical dark box tests were performed on the PMTs during various stages of the module production. Optical, mechanical, and dimensional QC checks of all modules were conducted before installation into the active detector. The photograph in Figure 3.17 from construction shows the coupling between the PMT optical modules and the optical grid to define each PROSPECT segment.

Figure 3.16: Rack of modules, some completed, others missing the PMT and/or mineral oil. The conical reflector can be easily seen in the empty acrylic enclosures.

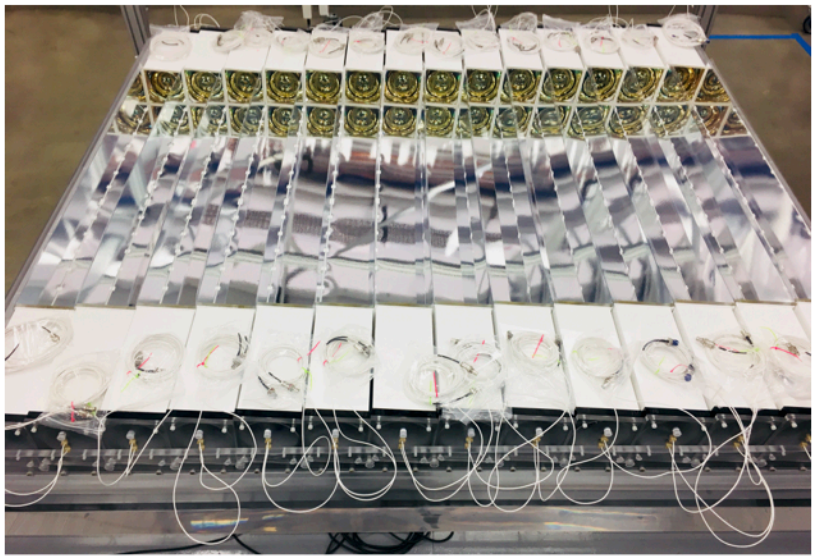

Figure 3.17: Photograph of the first layer of PROSPECT segments defined by the PMT optical modules and optical grid system.

3.5.4 Acrylic support system and tank

A system of acrylic supports is used to define the mechanical structure of the optical grid and PMT optical modules. The grid was built on top of machined, wedge-shaped acrylic segment supports, providing the 5.5° tilt and 0.146 m pitch [108]. Similar vertical supports make up the side walls to define the structure and spacing between layers of PMT modules. Multiple planks are bolted together in ship-lap style using PEEK screws. The top of the optical grid is constrained by machined baffles, tying the whole structure together. Acrylic supports are bolted to each module, in both the horizontal and vertical direction, opposite the side optical grid supports. These slats also provide a vertical path for the cables and calibration tubing to be routed out of active volume. Photographs of various pieces of the acrylic support system are shown in Figure 3.18. As with the other components in the active volume, each component was thoroughly cleaned.

For material compatibility, an acrylic tank was constructed to house the optical grid, PMT optical modules, and acrylic support system inside the ^{6}LiLS volume.

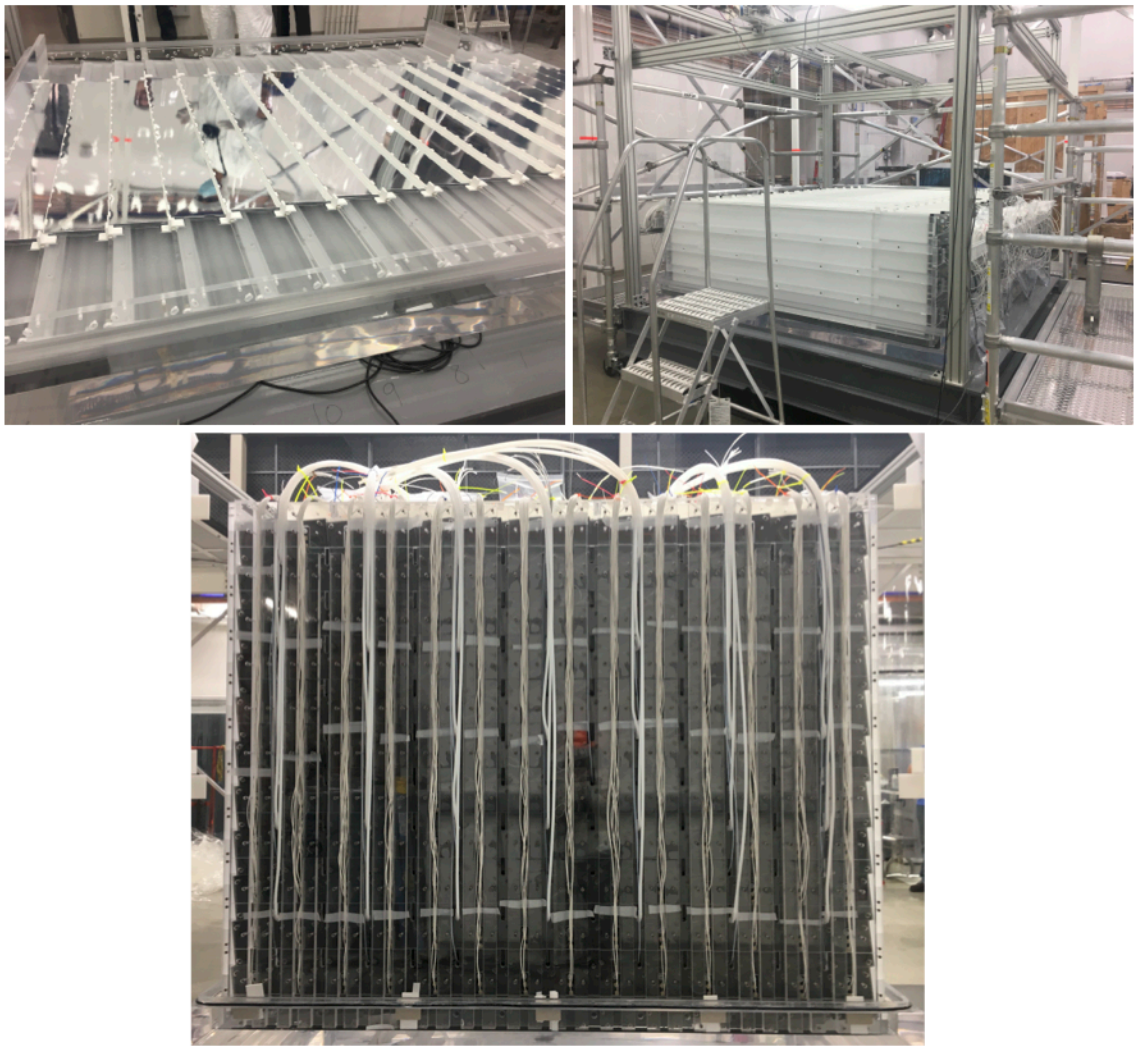

Figure 3.18: Photographs of the acrylic support system. **(top left)** Reflective separator and support rod assemblies installed on top of the bottom wedge planks. Two horizontal planks are also installed upright on either end. Horizontal PMT module support slats can be seen where the bottom planks terminate. **(top right)** Horizontal planks (clear) installed after four segment layers, defining the exterior of the optical grid. **(right)** Vertical and horizontal slats are bolted to the PMT modules to secure their position. They also serve as guides to route the cables and calibration tubes out of the detector.

The inner dimensions of the tank are $2.143 \times 1.995 \times 1.555\,\mathrm{m}^3$. The tank was built in three pieces: 64-mm-thick base with a centered tongue, four 64-mm-thick side walls with a centered grove bonded together, and a 51 mm lid. Fourteen rectangular holes ($0.051 \times 0.076\,\mathrm{m}^2$) were machined into the lid to allow the PMT cables and calibration

tubes to exit. A thin strip of FEP was mounted to the top of the walls to provide a cushion between the wall-lid joint. The base is coupled to the walls between via the tongue-and-grove using an inner, vertically compressed custom 3.2-mm-diameter Viton O-ring. PEEK spacers inserted inside the base constrain the O-ring squeeze. Figure 3.19 shows photographs of the O-ring seal and assembly after the side walls were lowered onto the base. A secondary seal was made on the outside of the tongue-and-groove with a 6.35-mm-diameter neoprene sponge cord and a layer of 0.05-m-wide marine tape [129]. The entire acrylic tank package is compressed by sixteen cable loops, with force evenly distributed over the acrylic lid by aluminum angle brackets and Teflon cushions. After the assembly, two exterior filling ports on the side walls were outfitted with PEEK O-ring seal, push-to-connect plumbing systems for filling and pumping. The entire tank was scrubbed using the acrylics cleaning procedure.

3.5.5 Secondary aluminum containment tank

To provide protection against possible ^{6}LiLS leaks, the acrylic tank in active detector was installed in a secondary containment tank. The tank is made from welded aluminum and has internal dimensions of $2.255 \times 2.205 \times 1.982\,\mathrm{m}^3$. With a wall thickness of 0.025 m, the tank is rigid enough to support the load of the exterior shielding package. In between the acrylic and aluminum tank walls, layers of BPE and deionized water were added to increase the attenuation of thermal neutrons. Instrumentation cables, calibration tubing, and liquid/gas lines are routed out the tank through Icotek cable grommets [130] on the lid. The feedthroughs were made light- and gas-tight after potting with black silicone RTV, that was made by combining clear RTV [131] with graphite powder [132] and silica thickener [133]. The lid was sealed to the walls with a flat neoprene gasket, compressed by bolts. Cables were routed along the top of the lid in aluminum raceways and connected to the bulkhead panel. The detector assembly was shipped in the aluminum tank to HFIR before the shielding package

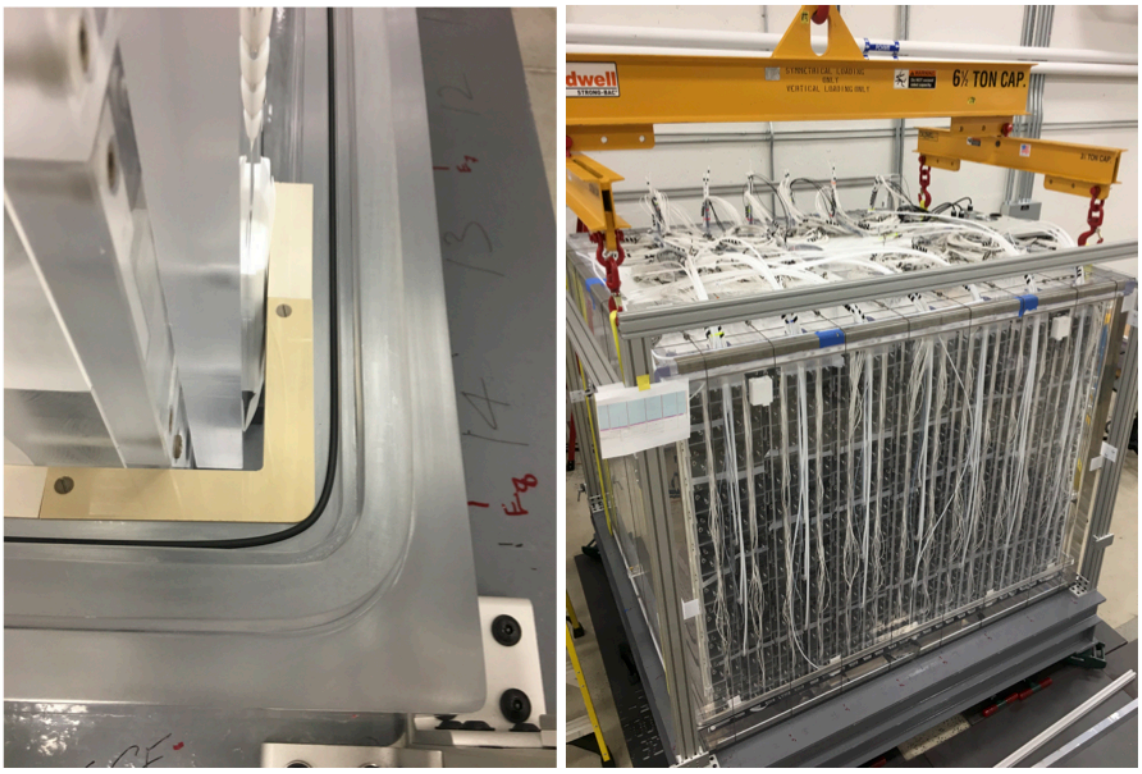

Figure 3.19: **(left)** Photograph of the base with the machine tongue and the interior Viton O-ring. PEEK spacers (tan) define the squeeze of the O-ring. **(right)** The inner AD assembly as the side acrylic walls were lowered onto the base, sealed by the Viton O-ring.

was installed on the outside.

3.5.6 Passive shielding and detector movement system

As described in Section 3.3, background measurements at HFIR led to the design of a layered passive shield package to reduce the γ-rays and high-energy neutron flux into the detector. Hydrogenous material above the detector, followed by 0.025 m lead and 5%-BPE, was determined to be the optimal layering scheme given the safety and geometric constraints at HFIR [108]. The aluminum tank bottom and walls are surrounded by 0.025 m layer of lead bricks. On top of the tank, a layer of lead bricks spreads the load across a 0.127-m-thick support layer of BPE. Penetrations and cracks in the BPE are reduced as much as possible, but are required to accomodate cables

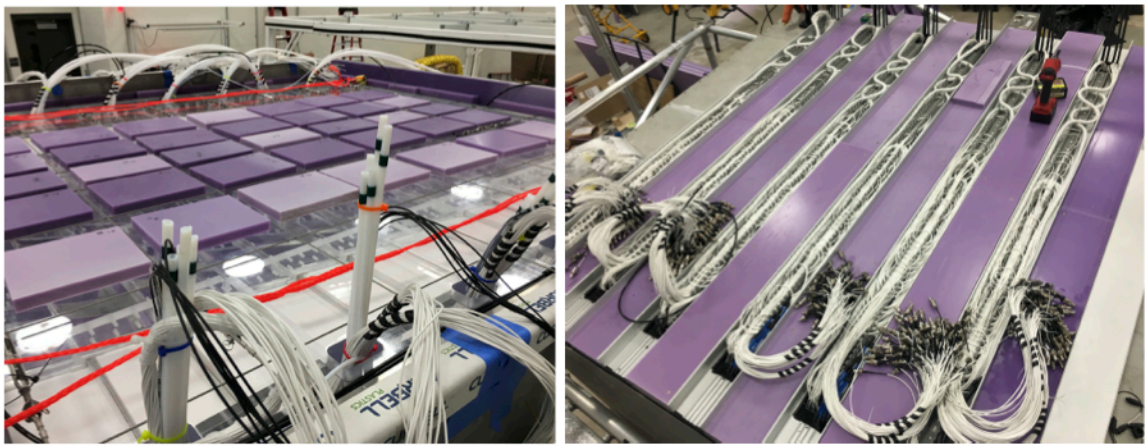

Figure 3.20: Photographs of the components installed inside and outside the aluminum tank. **(left)** Top of acrylic tank after installation into the aluminum tank, with BPE shielding tiles. The tensioning cables are visible. **(right)** Top of the aluminum tank after the lid was sealed. Cables were snaked to ensure they were all the same length when exiting the raceways. Aluminum lids and BPE were added later to provide protection and a supportive surface to add flat layers of shielding. The potting of the Icotek cable grommets is also pictured.

and limited by the geometry of manufactured sheets. A structure made from $0.102\,\mathrm{m}^2$ HDPE beams are bolted around the lead layer. On top, a roof of $0.064{\times}0.241\,\mathrm{m}^2$ beams are transversed by steel pipes for structural support. Outside the HDPE structure is another layer of 0.025-m-thick BPE to attenuate the 2.2 MeV γ-rays produced by thermal neutron captures in the HDPE [108]. The whole shielding package is covered with thin aluminum sheets to meet the fire safety requirements of HFIR. A layer of $0.23{\times}0.15{\times}0.46\,\mathrm{m}^2$ WaterBricks filled with tap water interlock on the top of the shield, covered with a fiberglass fire blanket.

The detector and shielding packages distribute their weight ($\sim$40 tons) on a rectangular, 210-mm-thick welded steel chassis with dimensions of $3.242{\times}2.946{\times}0.21\,\mathrm{m}^3$. Figure 3.21 shows a model of the chassis with supporting forklift channels, six Aero-go air casters [134], and layers of shielding. This system allowed for the detector to be installed into position at HFIR with a forklift and tilted during the ^{6}LiLS filling. The air castors will be used to move the detector from its current baseline (Position 1).

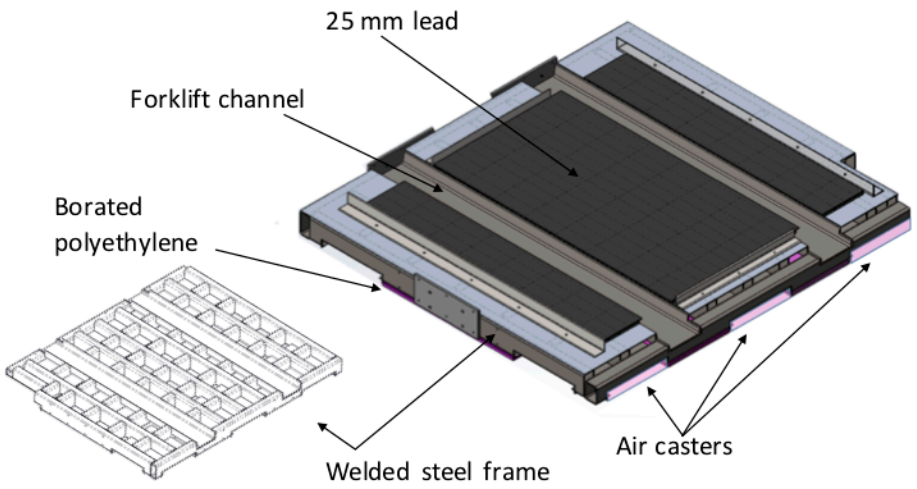

Figure 3.21: Model of detector support chassis. The welded 210-mm-thick steel frame supports the detector during movement by the air caster system and distributes the weight of the detector over the maximum allowed floor area. Six air caster lifting pads slide into slots at the bottom of the detector. Two deep channels run across the frame at the top to allow a forklift to lower the detector onto the frame. A 25 mm BPE layer below and a 25 mm lead layer on top complete the passive shielding package.

3.5.7 Radioactive and optical source calibration systems

The physics goals of PROSPECT require an accurate knowledge of the ^{6}LiLS response to different interaction types. Due to the segmentation, *in situ* calibration techniques are required to monitor the behavior of each individual segment. Radioactive γ-ray sources are used to determine the energy reconstruction parameters (scale, resolution, non-linearity, missing energy), position reconstruction, and segment-to-segment variations. Neutron sources are used to understand the IBD neutron capture efficiency and ^{6}Li capture time. A fiber optic-laser system is used to measure the timing difference between PMTs, single photoelectron (SPE) response, electronics linearity, and scintillator stability. Both systems deploy sources through the hollows of the support rods in the optical grid throughout the detector. The positions of the radioactive and optical sources are shown in Figure 3.22.

The radioactive source calibration uses 35 independent stepper motor drive units

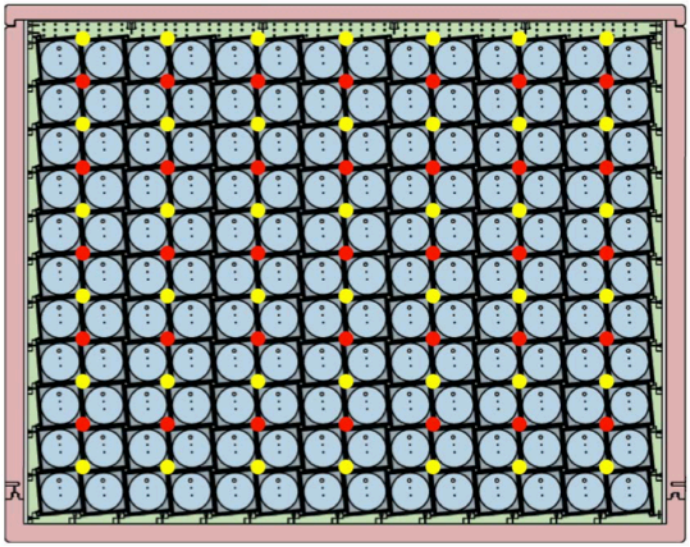

Figure 3.22: Cross section of the AD illustrating the locations of the source tube (red) and optical insert (yellow) positions, in between the segments of the inner detector [108].

Source	Decay mode	γ-ray energy (MeV)	Primary purpose
^{137}Cs	β^-	0.662	segment variations
^{22}Na	β^+	2×0.511 (annihilation), 1.275	positron, edge effects
^{60}Co	β^-	1.173, 1.332	energy scale
^{252}Cf	n (fission)	prompt γ's, 2.223 (n,H) capture	neutron response

Table 3.3: Radioactive calibration sources and their primary purpose. All reported γ-ray energies are from de-excitations from excited nuclear states, unless otherwise noted. All sources are used to determine the energy scale, resolution, and non-linearity. ^{252}Cf data was only available for the spectrum measurement analysis.

to move γ-ray, neutron, and e^+ emitters throughout the active volume to calibrate the energy and positon response of each segment, as well as topological effects. The position of the source is repeatable within ∼1 mm with an absolute position accuracy of 1 cm along each segment. Table 3.3 lists the sources currently deployed by PROSPECT. The sources are individually encapsulated and serialized in tiny aluminum cylinders sealed with a set-screw and epoxy, as seen in Figure 3.23**(left)**. The assembly couples to a 3 mm wide, AT3 pitch polyurethane toothed drive (timing) belt, reducing friction and buckling inside the calibration tubes. A 3D-printed pulley

is attached to a NEMA 23 stepper motor [135] to push the belt through the calibration tubes inserted in between segments. The belt is held tightly to the pulley by a spring-loaded jockey. Two micro-switches are used as safety stops preventing the source capsule or belt from detaching, and also to control the home position. All of the components are housed in a 3D-printed belt guide, shown in Figure 3.23**(right)**. The motors are controlled with Arduino micro-controllers [136] and the full system can be remotely operated through a slow-control web interface [137]. While the detector is in data-operation, the calibration sources are retracted and stored in tubes above the detector and detector shielding. No additional shielding is used to attenuate the flux from the sources in the home position.[11]

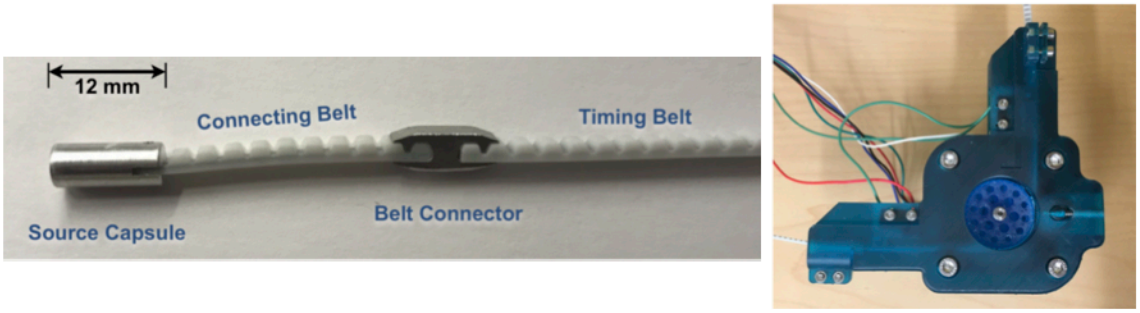

Figure 3.23: Photographs of the **(left)** drive belt-source capsule assembly and **(right)** 3D-printed belt motor drive and pulley assembly.

Complying with scintillator compatibility requirements, the calibration tubing was produced from 0.375-in-outer-diameter and 0.125-in-inner-diameter PTFE tubes. The tubing was received in a coil from the manufacturer and straightened in a custom annealing oven. The support rods were strung onto the tubes and installed during the inner detector construction. An acrylic piece was required to bend the PTFE 90° with a 1.5 in radius (to accommodate the size of the source capsule) and transition the tubes from the segments to their vertical position to be routed out of the top of the detector. Both ends of the tubes terminate outside of the active volume,

[11] The data set included in this thesis was taken before the ^{252}Cf source was installed. With the source added, calibration studies are consistent with no neutron leakage into the detector [138].

blackened and sealed to ensure light- and gas-tightness. Tubes are grouped together by detector column through a plumbing manifold to a single tube that routes to the motor drive boxes. Figure 3.24 illustrates a typical path for a source capsule through the calibration system.

The optical calibration system (OCS) uses a light source embedded in 42 of the support rods to calibrate the PMT timing difference, SPE, and PMT electronics linearity. A 15 mW single mode fiber laser diode [139] with an average wavelength of 450 nm is split in 45 channels by a custom Thorlabs splitter to provide the light. The system is driven by a laser diode driver [140], supplying pulses up to 800 mA with <10 ns width and 0.5 ns risetime. The relative intensity of two auxiliary channels are monitored by photodiodes [141] also in the splitter chain. A TTL signal is output with each pulse, which is later converted to a NIM pulse and saved with the digitized datastream for reference.[12] To transport the light from the driver to the segments, 3.0-m-long optical fibers [142] run from the splitter output to the bulkhead panel connecting to 5.5-m-long fibers that service the detector. The cables are encased in a PTFE sheath, acting as a barrier between the casing of the optical fiber and the scintillator inside the segment support rod assemblies. At the center of each rod assembly, the fiber terminates at a conical reflector cone, distributing the light radially. A machined Teflon diffuser disk, embedded in a hole cut through the center support rod, uniformly distributes the light into the center of each of the four adjacent segments. A schematic and photographs of the OCS optical fiber assembly are shown in Figure 3.25. The current and pulse width of the laser driver is varied from low intensity (SPE) to study the PMT gains and to higher intensities to measure the timing differences in each segment, linearity, and scintillator stability. During data-taking, the OCS is pulsed between 10–20 Hz to continuously monitor the timing offsets and ^{6}LiLS attenuation length.

[12]The output TTL can also be used as a trigger with modifications to the software threshold.

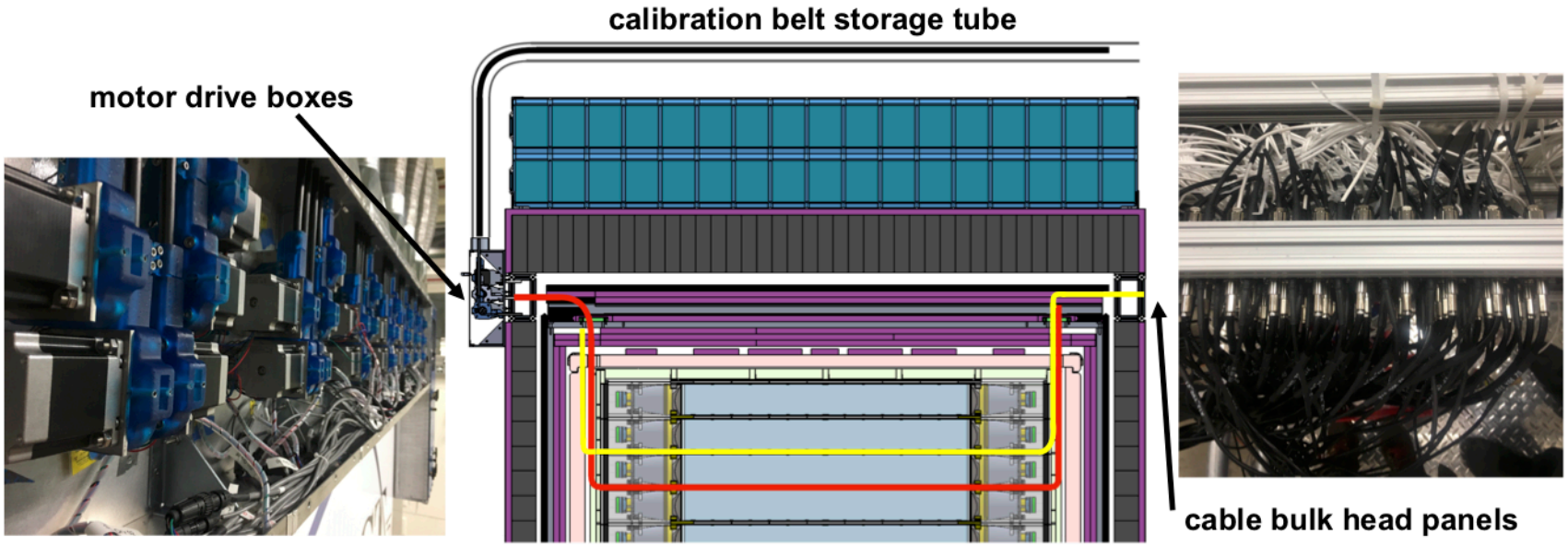

Figure 3.24: View of the AD along the segments illustrating the routing of the typical radioactive source calibration tubes (red) and optical inserts (yellow). Also shown are the radioactive calibration motor drive boxes and bulkhead panels where all cables, including the laser optical fibers, transition to their respective electronics outside of the detector.

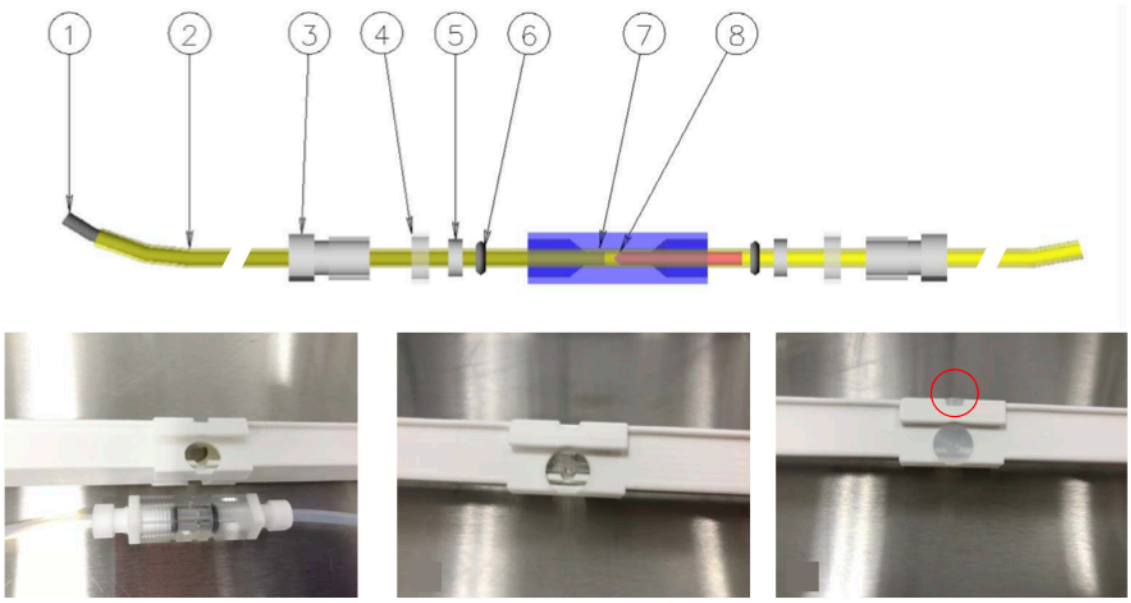

Figure 3.25: **(top)** Components of the optical fiber assembly: (1) optical fiber cable, (2) PTFE tube, (3) compression nut, (4,5) spacer washers, (6) Viton O-ring, (7) square clear acrylic body, (8) conical reflector cone. The optical fiber assembly, shown assembled in **(bottom left)** is inserted into the square bore of the center support rod. **(bottom center)** shows the assembly inserted in the pinwheel before being covered **(bottom right)** by a Teflon diffuser disk. Most of the disk is covered by a reflective optical separator (not shown), leaving only the small area shown circled in red in inside the optical volume. Pulsed light from the optical fiber is reflected into a radial direction by the conical reflector cone. The light passes through the acrylic body and enters four Teflon diffusers embedded in the support rod before entering the center of the segment. Each fiber optic assembly delivers light to four adjacent segments [108].

3.6 Detector control and monitoring

3.6.1 High voltage

The 308 PMTs are biased independently through a high voltage supply, providing a gain of $5{\times}10^5$ to achieve linear response through energies up to ~10 MeV during normal data taking. HV is provided by 20, 16-channel ISEG modules [143], powered by two Weiner MPOD crates [144] with ethernet interfaces. Custom software was built to communicate with the HV cards over a local DAQ network. The operational voltages and currents are stored in a database for monitoring purposes.

3.6.2 Nitrogen cover gas system

Nitrogen gas boiled off from liquid nitrogen is used to reduce the amount of dissolved oxygen in the ^{6}LiLS. The gas forms a blanket between the liquid level in the active detector volume and the acrylic tank lid. A mass flow controller is used to adjust the input nitrogen rate and the output is monitored by a flow meter and oil-filled bubbler. The pressure is monitored by absolute and differential pressure transducers at each inlet/outet along the plumbing in the gas panel and in the aluminum tank above the water. The composition of the gas outlet is monitored by oxygen and water[13] sensors.

3.6.3 Environmental monitoring

Resistance temperature detectors (RTDs) monitor the ^{6}LiLS temperature at various locations in the active detector. The 11 RTD sensors and cables are encased in PTFE sheaths inside the segment support rod assemblies. An additional RTD is also mounted inside the water volume in the aluminum tank. The RTDs are readout by ADAM ethernet I/O modules [145]. Ultrasonic sensors [146] are used to measure the ^{6}LiLS and water levels.

3.7 Data acquisition system

The PROPSECT DAQ system was built to satisfy three main requirements. Digitization of PMT waveforms are needed to perform PSD analyses, where the integration of different pulse shapes can distinguish particle types. For precision measurements of the $\overline{\nu}_e$ spectrum, the full prompt spectrum must be measured, up to $\sim$10 MeV. Additionally, the ability to track the electron spectrum (endpoint $\sim$14 MeV) from cosmogenically produced ^{12}B is extremely useful for constraining the energy scale and scintillator non-linearity at high energies where γ-sources are limited. Thus,

[13] This sensor is a hybride of pressure, temperature, humidity sensors.

the DAQ must have a wide dynamic range to measure energies from 0 to 14 MeV with good linearity and high resolution. The high rate of data during reactor-on time (∼40 kHz) would result in very large data streams due to the size of individual waveforms. Efficient triggering with zero length encoding (ZLE) is needed to record waveforms only from channels active in each event.

CAEN V1725 Waveform Digitizer Modules (WFDs) [147] were selected as they meet the above criteria and do not require analog preprocessing of the PMT anode signal [108]. The WFDs have a 14-bit, 250 MS/s (simultaneous on each channel) digitization conversion and 50 Ω analog input impedance with 2 Vpp dynamic range on MCX coaxial connectors. On-board local triggering between channels is a useful feature. Digitized waveforms are directly saved for off-line analysis with no on-board calculations. A total of 21, 16-channel WFD boards are powered by two Weiner VME crates [148] controlled over ethernet. Board firmware communication and data transfer is achieved over optical fibers terminated in two, four-channel PCI express optical fiber link cards (5–10 MB/s) [149] installed in two DAQ computers. A run control computer coordinates acquisition processes on the DAQ computers, as illustrated in Figure 3.26.

Clock distribution between the WFD boards is established through a daisy chain through "CLOCK IN" inputs and "CLOCK OUT" outputs in a phase lock loop (PLL). The first board is configured as the master reference, propagating a 62.5 MHz square wave to successive boards in the chain. The phase of the signal must match that of the internal voltage crystal oscillation (50 MHz) internal to each board, otherwise the PLL signal will unlock and the DAQ computer kills the process. Each waveform receives a timestamp from this process. The run start/stop for all boards can be synced through a hardware gate or software trigger. Cables between neighboring boards are ∼0.05 m, with one cable distributing the clock between VME crates. Propagation delays are measured and corrected in the physics data stream.

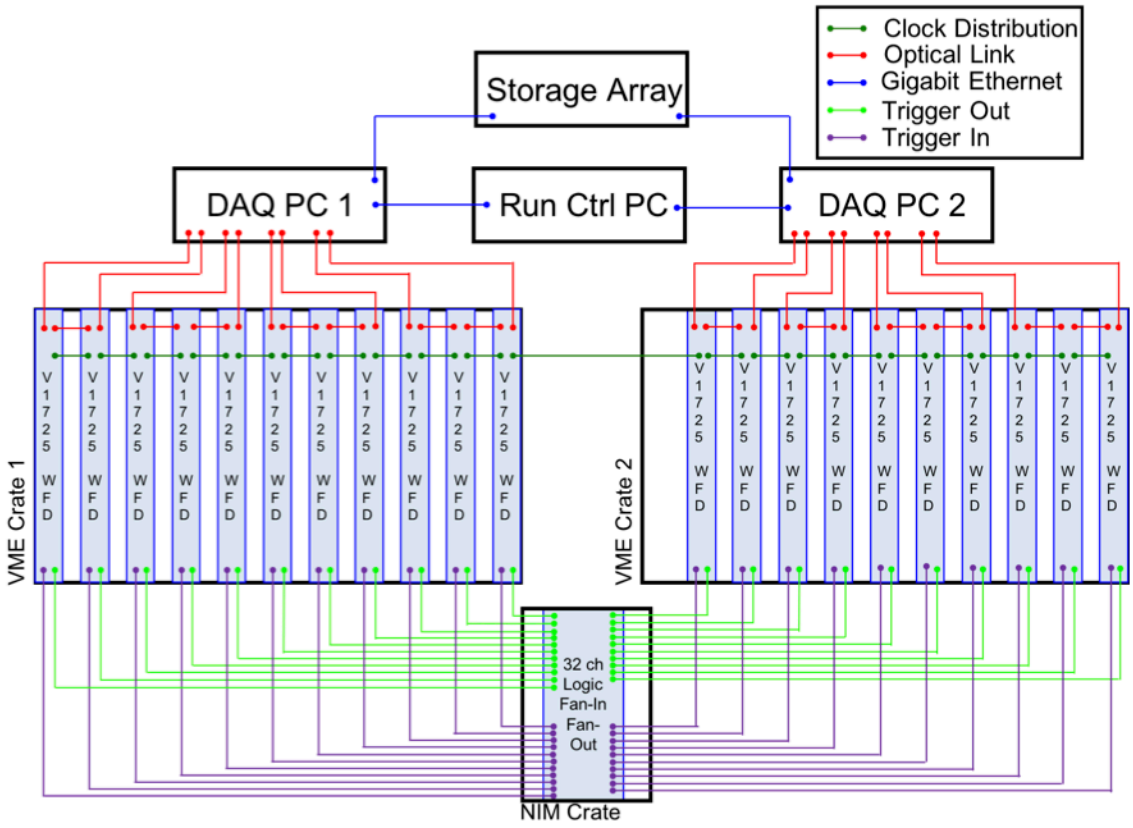

Figure 3.26: Schematic diagram of the DAQ system [108].

Triggering is performed via the on-board V1275 firmware. An on-board logical OR (local, segment-wise) NIM trigger is generated if both PMTs in any segment exceed a 5 photoelectron signal (50 ADC channels/PMT, ∼100 keV) within 64 ns of each other during a 148-sample (592 ns) acquisition window. This logic signal is sent to the input of a custom logic fan-in/fan-out NIM module [150], copied, and globally distributed to all boards through a trigger input port. Waveforms in all PMTs are then acquired, but only recorded to disk if they exceed a ZLE threshold of ∼2 photoelectrons (20 ADC channels/PMT, ∼40 keV), along with pre-and post-threshold regions of 24 and 32 samples, respectively [108]. This efficiently suppresses recording waveforms with zero or very small energy depositions on an event-by-event basis (average segment multiplicity per trigger is ∼4). In this scheme, a low ZLE threshold can be set to collect energy from the IBD positron with depositions primarily in one segment while

also collecting the small scatter signals from the successive 511 keV annihilation γ-rays. A small hardware deadtime of <2% reactor-on (1% reactor-off), introduced by new event triggers that arrive towards the end of the acquisition window, is accounted for with analysis cuts.

Each WFD board has two memory buffers, mimicking the data collection and transfer flow on the optical link. The DAQ control software continuously checks the buffers and establishes a data transfer process when filled. Waveform data and run metadata (e.g. start time, thresholds) are stored on spinning hard disks installed in the two DAQ computers. Upon arrival, the data is transferred to a multi-disk, network-mounted storage array via ethernet. The raw data production rates vary depending on the running mode of the PROSPECT AD and the status of the reactor. Typical data rates for various conditions are given in Table 3.4. The raw data is transferred to Lawrence Livermore National Laboratory for long-term storage and data processing.

Quantity/Run condition	Reactor-on	Reactor-off	Calibration
Acquisition event rate (kHz)	28	4	35
Segment event rate (kHz)	115	35	190
Average segment multiplicity	4.0	7.0	5.5
Max optical link rate (MB/s)	3.0	1.0	7.2
Min optical link rate (MB/s)	1.1	0.6	2.2
Data volume per day (GB)	671	312	476

Table 3.4: Approximate data acquisition and transfer parameters for three typical operating conditions. The calibration case has five ^{137}Cs sources deployed within the AD while the reactor is off. The average multiplicity is higher for the reactor-off condition because muons and other cosmic events have high multiplicity, which make up a greater fraction of events in this state [108].

Chapter 4

Detector prototypes, construction, and installation

The PROSPECT detector was designed to simultaneously search for sterile neutrino oscillations and perform precision measurements of the $\overline{\nu}_e$ spectrum. Through an intensive R&D program, several prototypes were built at Yale University to characterize and optimize the liquid scintillator performance, optical transport, and background rejection capabilities of the detector. Figure 4.1 illustrates the evolution of prototype detectors and their deliverables to the overall design of the AD. Some of the prototypes were also deployed at HFIR to take measurements in the reactor environment, serving as benchmarks for simulations. Construction of the PMT optical modules and PROSPECT detector package took place from November 2016–January 2018. The detector was shipped from New Haven, CT, USA to Oak Ridge, TN, USA in February 2018 and installed at HFIR. Full detector operations began in March 2018.

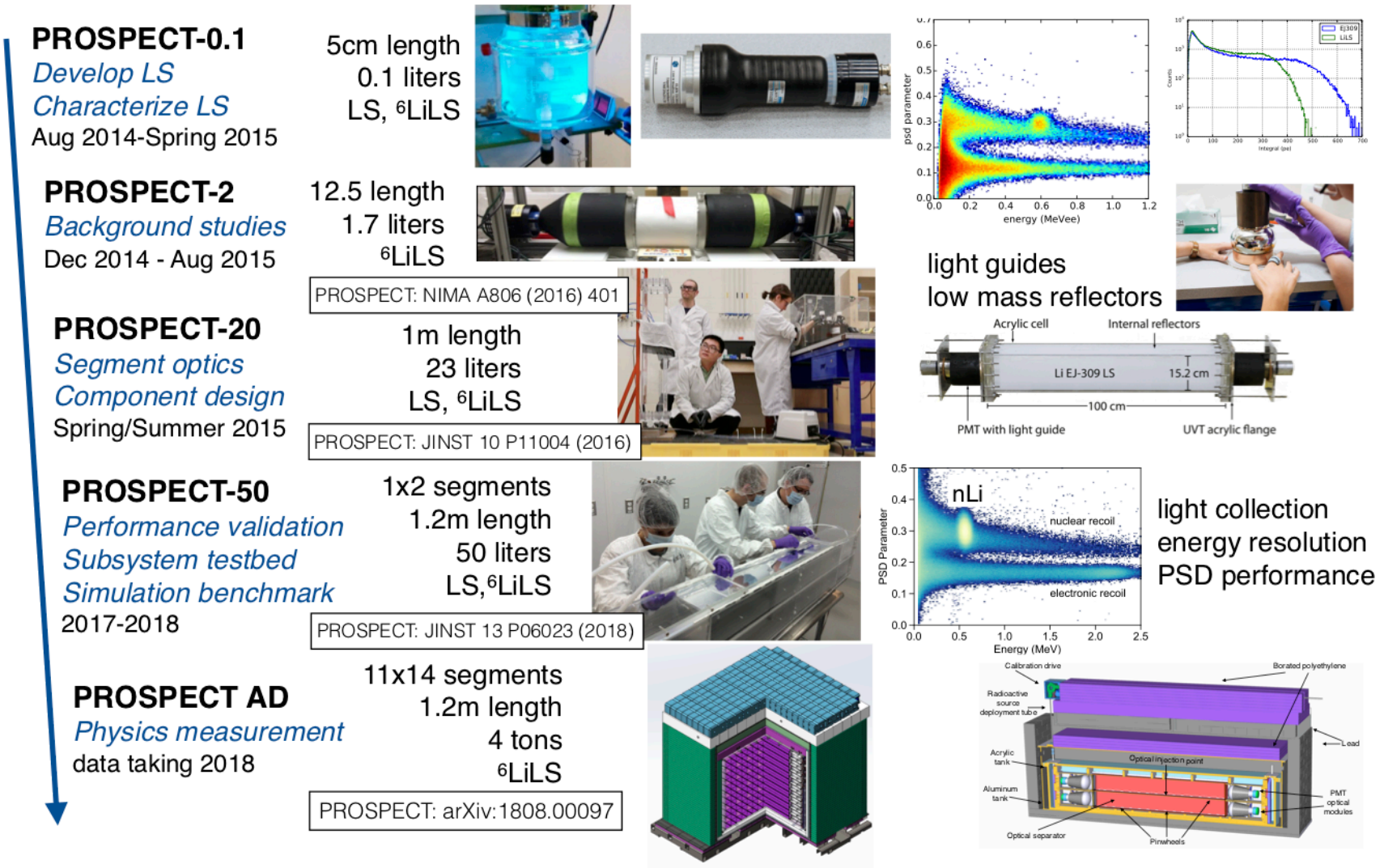

Figure 4.1: Summary of PROSPECT detector R&D path with various prototypes. Each prototype was built to study specific aspects of the detector design. All detectors were constructed and run at Yale University. PROSPECT–2 and PROSPECT–20 were also deployed at the HFIR site.

4.1 PROSPECT prototype detectors

4.1.1 Vial studies and PROSPECT–0.1: ^{6}LiLS characterization

As described in Chapter 3, PROSPECT was required to develop an ^{6}LiLS from a low-toxicity, high-flashpoint solvent. Three scintillator bases were studied for feasibility: LAB, UltimaGold [151], and EJ-309. ^{6}Li-doped samples of each were compared using a ∼20 mL vial held in a reflective acrylic holder coupled to a 2 in PMT. Using γ-ray and neutron sources, the relative light yield (in photoelectrons, PE) and PSD were measured, as shown in Figure 4.2. ^{6}Li-loaded EJ-309 was selected for PROSPECT as it was found to optimize both the light yield and PSD performance. It should be noted that the light output of the base EJ-309 is quenched by ∼30% when loaded with ∼0.1% ^{6}Li by mass, directly leading to a slight degradation of the PSD. With a measured light yield (LY) of 8200 photons/MeV, the light collection in a PROSPECT segment was projected to be >500 PE/MeV through:

$$PE = LY \times \epsilon_c \times QE, \tag{4.1}$$

where ϵ_c is the geometric collection efficiency (25% from simulation) and QE the quantum efficiency of the PMTS (Hamamatsu R6954 ∼25%). When considering only photostatistics, a resulting $4.5\%/\sqrt{(E(\mathrm{MeV})}$ could be achieved.

A setup made from a 0.1 L scintillator cell with a reflective interior optically coupled to a 3 in Hamamatsu R6091 PMT was assembled to characterize the PSD of the PROSPECT ^{6}LiLS. Figure 4.3 shows the prototype, known as PROSPECT-0.1, along with PSD measurements using a ^{252}Cf source. The electronic (low PSD parameter) and nuclear (high PSD parameter) recoil bands are well-separated. The prominent (n,^{6}Li) thermal capture signal around 0.55 MeV is clearly observed with a

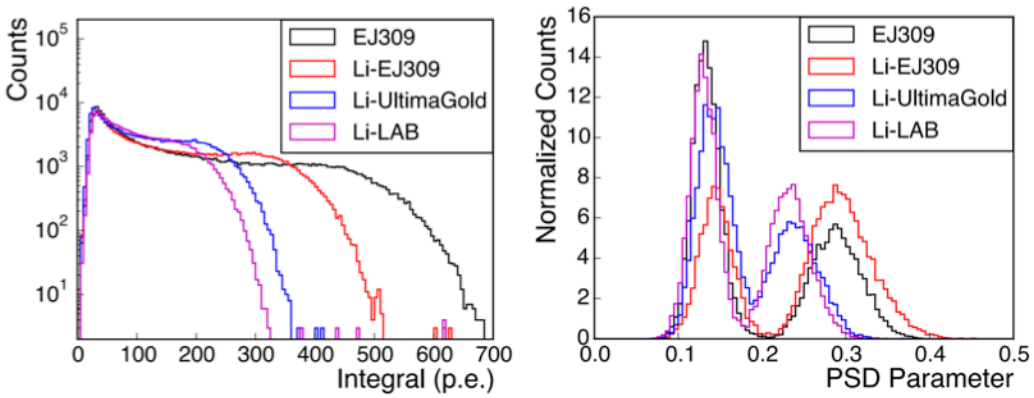

Figure 4.2: Comparison between unloaded EJ-309 and three different ^{6}LiLS formulations. **(left)** Response to ^{60}Co, demonstrating the relative light yield. **(right)** Comparison of PSD distributions when exposed to ^{252}Cf spontaneous fission source. Li-EJ309 has the best performance amongst Li-loaded materials [109].

PSD figure-of-merit of 1.79, which is defined as

$$FOM = \frac{|\mu_1 - \mu_2|}{FWHM_1 + FWHM_2}, \tag{4.2}$$

where μ_1, μ_2 represent the mean of the electronic and nuclear recoil distributions, and FWHM$_1$, FWHM$_2$ the full-width-half-max of each distribution. Fitting the peak results in an energy resolution of 5.2% at $\sim$0.55 MeV. The detector was also operated at HFIR in a lead cave to take preliminary background γ-ray measurements.

4.1.2 PROSPECT–2: Background studies

To understand the background rejection capabilities of the ^{6}LiLS and passive shielding, a 1.7 L prototype detector (known as PROSPECT-2, as it contains about 2 L of scintillator) was deployed at the HFIR site. The detector is made from a cylindrical acrylic vessel coated on the exterior with EJ-510 TiO_2 diffuse reflective paint [153]. It is capped on both ends by 5 in ET 9823KB PMTs coupled directly via EJ550 optical grease [154]. A CAEN 1720 (12-bit, 250 MS/s) [155] was used to readout both PMT channels. Initially a small shielding package with an active muon veto was attempted

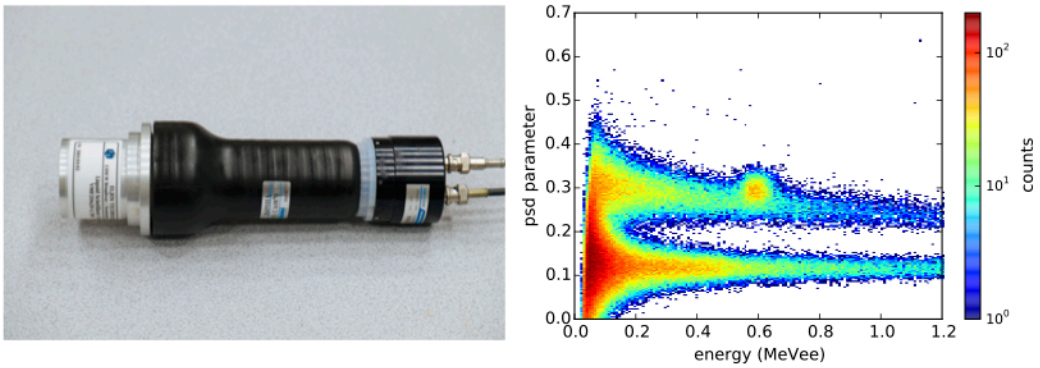

Figure 4.3: **(left)** Photograph of the PROSPECT-0.1 detector filled with ^{6}LiLS. **(right)** PSD versus energy distribution when exposed to ^{252}Cf. Clear separation between the electronic and nuclear recoil bands are visible, along with a prominent signal at the (n,^{6}Li) capture peak [152].

and later upgraded to include more low-Z material, illustrated by the photographs in Figure 4.4. A large aluminum tank (dubbed "the coffin") was used to enclose the detector in layers of HDPE, BPE, and lead. This design, which inspired the shielding package for PROSPECT, allows low energy neutrons to thermalize and capture, reducing high energy capture γ-rays, while also stopping external and neutron-capture produced γ-rays. Neutrons produced from cosmic rays in the high-Z γ-ray shield are thermalized in subsequent layers of BPE [113].

The effectiveness of the shielding design can be assessed using PSD measurements in both the IBD-like prompt positron energy region [1,5] MeV and IBD-like delayed neutron energy region [0.5,0.8] MeV during reactor-on and -off periods. Data sets with 109 hours of reactor-on and 348 hours of reactor-off data were collected with PROSPECT-2. Figure 4.5 demonstrates that while an increase of events is observed when the reactor is on, the excess rate is mainly due to γ-ray Compton scatters in the detector. This indicates that only accidental, IBD-like coincident backgrounds can be attributed to the reactor, such as γ-rays that penetrate the shield. As the rate of neutron events remains constant with the change in reactor status, it is clear that the shielding (and water pool) efficiently attenuates thermal and fast neutron flux from

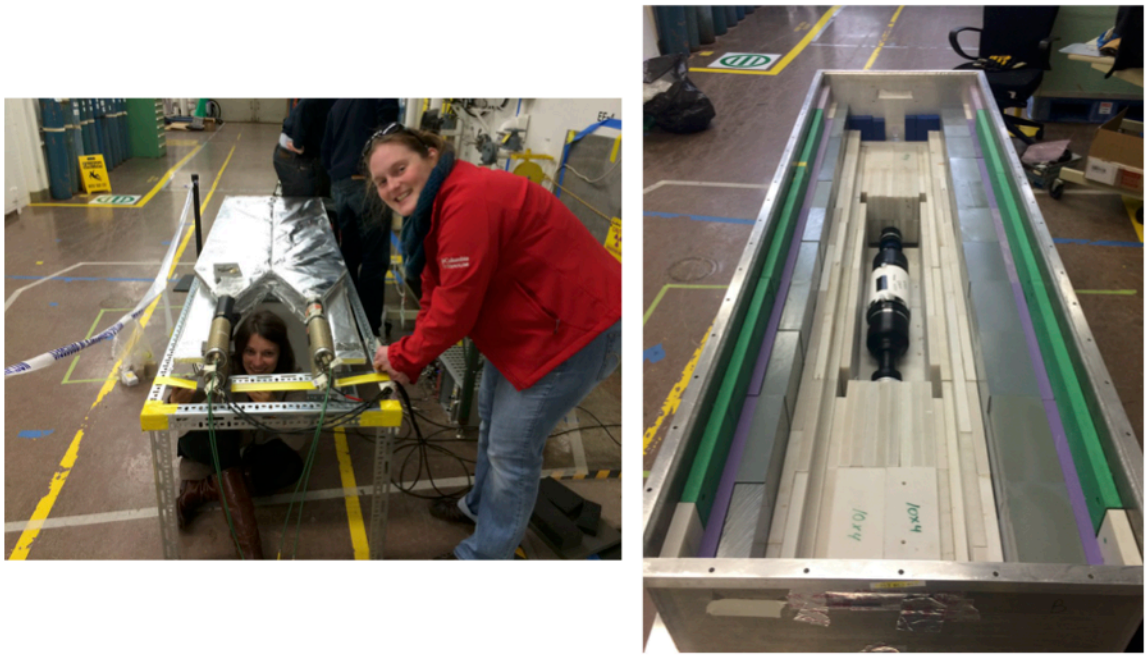

Figure 4.4: Photographs of different deployments of the PROSPECT-2 detector. **(left)** Construction of exterior shielding with an active muon veto. **(right)** A more robust, layered shielding package inside of an aluminum tank. The PROSPECT AD shield is modelled from this design.

the reactor. More details about PROSPECT-2 are published in Ref. [113].

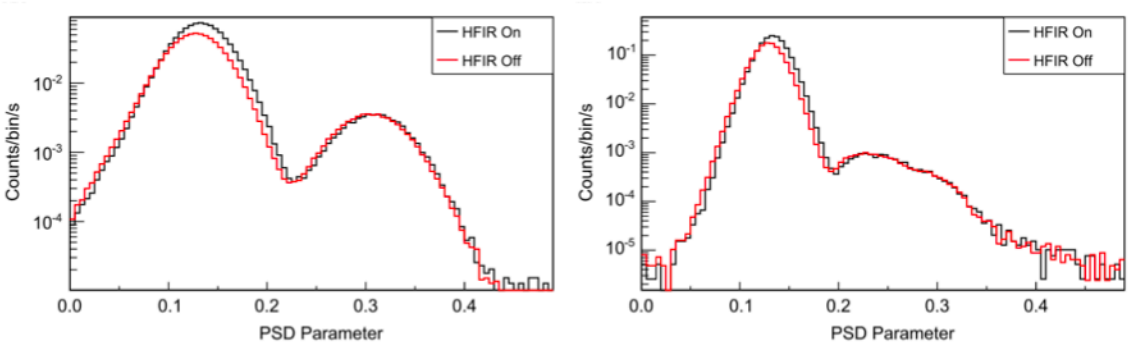

Figure 4.5: PSD parameter distributions are compared for reactor-on and reactor-off data for two energy ranges in the PROSPECT-2 detector:**(left)** [0.5,0.8] MeV, corresponding to neutron capture on ^{6}Li, and **(right)** [1,5] MeV. The similarity of the distributions at high PSD parameter values indicates no presence of reactor-correlated thermal or fast neutrons [113].

4.1.3 PROSPECT–20: Optimization of optical transport

PROSPECT-20 is a 23 L acrylic cell prototype designed to study of the optical behavior of a full-sized PROSPECT segment with different detector components. The goal of this detector was to optimize the light collection and PSD performance by varying the optical separator and PMT configurations. The interior dimensions of the cell are $100\times15.2\times15.2\,\mathrm{cm}^3$, constructed from a 1-cm-thick UV-absorbing (UVA) acrylic barrel terminated by 2.5-cm-thick square flanges bolted to window plates (originally UVA, then upgraded to UVT), and sealed with Viton O-rings. Acetel valves with Viton O-rings are used for liquid filling and gas plumbing. The design supports the insertion of optical separators, reducing the interior cross section to $14.5\times14.5\,\mathrm{cm}^2$. Initial tests used exterior optical separators, changing the cross section to $17.2\times17.2\,\mathrm{cm}^2$ when including the acrylic walls. The separators were coupled using glycerin to the acrylic or uncoupled to allow for total-internal-reflection. Specularly reflecting separators made from 3M Enhanced Specular Reflector (ESR) [156] and diffuse reflecting separators made from WhiteOptics White98 film [157] were tested. Two, 12.7-cm-diameter Hamamatsu R6594 PMTs with mu metal shields were used for read out. The hemispherical PMTs were optically coupled to the window plates through UVT acrylic light guides with a 5 mm minimum thickness and RTV silicone, as seen in Figure 4.6.[1] Uniform axial pressure was applied to the PMT-light guide assemblies through laser-cut plates and threaded rod mounted to each flange. A CAEN V1730 WFD (14-bit, 500 MS/s) [158] was used for digitization. Initial studies at Yale focused on measurements with the base EJ-309 scintillator. Great care was taken during the filling process to reduce exposure to oxygen, pumping scintillator via a peristaltic pump and Teflon tubing from a nitrogen-filled glove box. The acrylic cell was pre-purged with nitrogen prior to filling. Figure 4.6**(top right)** illustrates

[1] In the photographs, the light guides are shown with a reflective film that was added after the initial studies.

the filling procedure, where the cell is held vertical to reduce gas bubbles. Many lessons about scintillator handling and material compatibility were learned during this procedure.

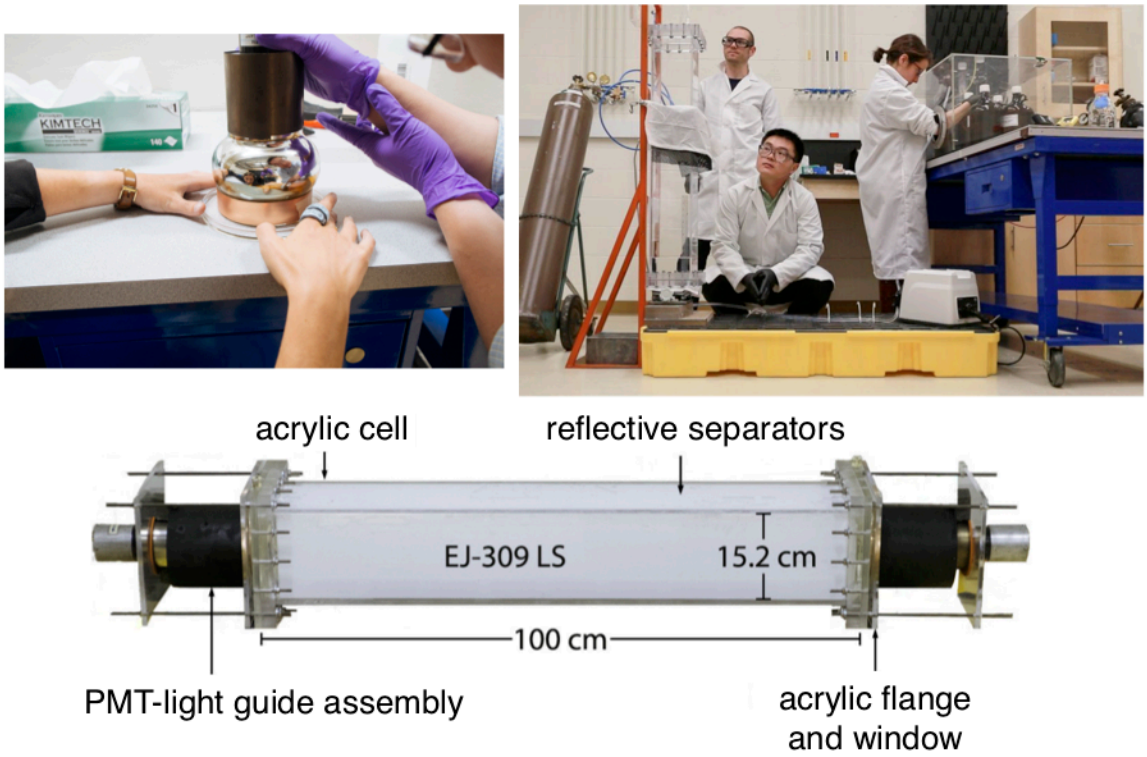

Figure 4.6: Photographs of the PROSPECT-20 assembly process. **(top left)** Potting of PMTs with RTV silicone in light guides enclosed in reflective film. **(top right)** Filling the detector with scintillator. The acrylic cell is held vertical to reduce gas bubbles. Scintillator is handled in a nitrogen glove box. **(bottom)** Labelled PROSPECT-20 detector [159].

Sources were deployed along the exterior of the detector to study the response. ^{207}Bi was used to characterize the photoelectron collection in different configurations and ^{252}Cf was used for neutron studies. When stepping the source in increments along the segment, it was shown that the light collection is position-dependent, indicating that two PMTs are essential as shown in Figure 4.7**(right)**. When the signals from the two PMTs are combined (sum or geometric mean), the response becomes more uniform, resulting in an average light collection of 841$\pm$17 PE/MeV. Double-ended read out also allows for position reconstruction along the segment axis (z-position) using

the timing and charge collection difference in the PMTs. PROSPECT-20 demonstrated that excellent PSD could be achieved in a long, rectangular PROSPECT segment. Using PSD around the (n,^{6}Li) capture region ([0.5,0.7] MeV), the detector can reject 99.99% γ-rays, while maintaining 99.9% of the neutron events [160]. Double-ended read out also enhances the PSD. Furthermore, the studies indicate that the light collection, PSD, and transport uniformity are optimized with specularly reflecting separators and by exploiting total-internal-reflection (uncoupled).[2] Diffuse separators introduced large light collection non-uniformities. Figure 4.7**(right)** summarizes the different configurations studied and shows that while there is some correlation between light collection and PSD performance, both parameters need to be optimized for a given geometry. The full details of the EJ-309 optical transport studies with PROSPECT-20 are published in Ref. [160]. The results were helpful for benchmarking the response of PROSPECT segments and provided useful information regarding the construction of long liquid scintillator detectors. Later measurements with ^{6}LiLS and internal optical separators demonstrated an average light collection of 522$\pm$16 PE/MeV, indicating PROSPECT would meet the target resolution of $4.5\%/\sqrt{E(\text{MeV})}$. The PSD separation between electronic and nuclear recoils remained intact, with the addition of a prominent neutron capture peak.

A second PROSPECT-20 detector was built and deployed at HFIR to characterize the optical performance during different statuses of the reactor. It was filled with ^{6}LiLS and positioned in the same aluminum coffin with the layered shielding as PROSPECT-2, as seen in Figure 4.8**(left)**. WaterBricks [116] were added to the exterior to demonstrate the effectiveness of neutron attenuation with hydrogenous material. Nine months of data were collected through multiple reactor cycles. Analysis showed that coincident accidental backgrounds are constant in time, while the

[2]The final design of the PROSPECT optical separators (outlined in Chapter 3) does not include an air gap for total-internal-reflection between the reflector material and FEP exterior layer. It is difficult to implement a sufficiently uniform air gap in practice.

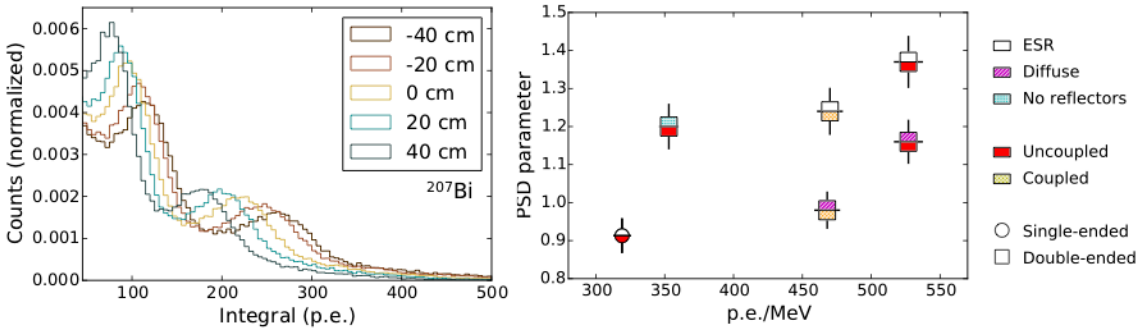

Figure 4.7: **(left)** Photoelectron spectra from one PMT in response to ^{207}Bi source deployments through a range of positons along the PROSPECT-20 EJ-309 cell (0 cm represents the center of the detector). Excellent uniformity in light collection along the cell is maintained when spectra from both ends are combined. **(right)** Distribution of the PSD performance versus light collection for events between 1.0 and 3.0 MeV in response to a center-deployed ^{252}Cf source in various configurations. The legend describes the different configuration options for each point. The spread in both quantities highlights the importance of carefully optimizing segment design for both light collection and PSD [160].

correlated backgrounds exhibit a similar timing structure to IBD events. PSD selections requiring the prompt signal to be within the electronic recoil band indicate that the correlated backgrounds are dominated by fast neutron recoils followed by (n,^{6}Li) capture. After multiple analysis cuts, reactor-on and reactor-off IBD-like spectra were compared, as seen in Figure 4.8**(right)**. There is a small difference between the two periods, demonstrating that IBD-like backgrounds are due to cosmogenic events, while reactor-generated correlated backgrounds are negligible [109]. Measurements from PROSPECT-20 at HFIR were used to benchmark and validate the PROSPECT simulation.

4.1.4 PROSPECT–50: Demonstration of detector performance

PROSPECT-50 is a two-segment, 50 L demonstrator detector that was built and operated at Yale Wright Laboratory. Each segment is $117.6\times14.5\times14.5\,\mathrm{cm}^3$ and contains an ^{6}LiLS volume of 25 L. Several iterations of the detector were made to finalize

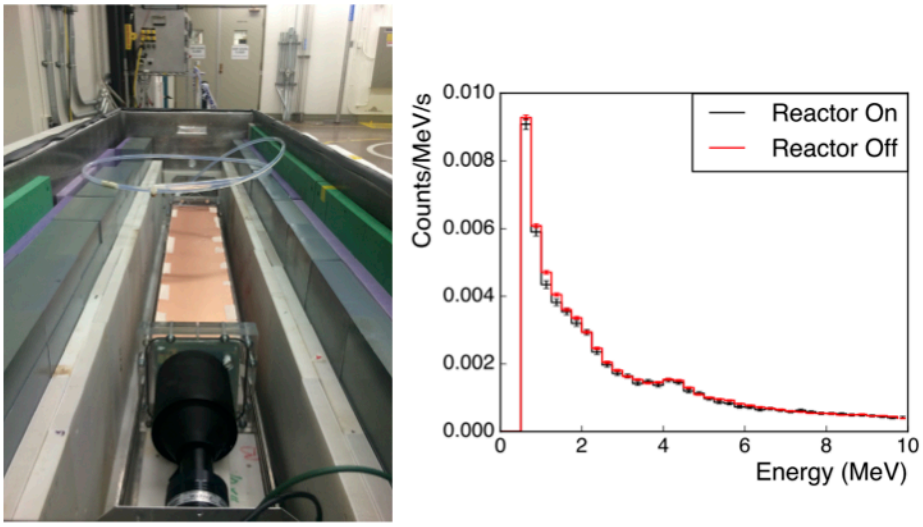

Figure 4.8: **(left)** Photograph of the PROSPECT-20 ^{6}LiLS detector in the shielding package at the HFIR site. **(right)** Comparison of PROSPECT-20 IBD-like event prompt energy spectra with HFIR on (black) and off (red) [109].

the component designs and material choices. The final version, PROSPECT-50X, was built with production parts to construct the low-mass optical grid capped with PMT optical modules and *in situ* calibration access. Studies of the light collection, energy resolution, and PSD capabilities were performed, along with measurements of the ^{6}LiLS effective attenuation length, position reconstruction, and neutron capture time. Lessons regarding the construction of the optical grid and long-term stability of the ^{6}LiLS were learned. Ultimately, PROSPECT-50 demonstrated the performance of a large-scale ^{6}LiLS segmented detector and prepared the collaboration for the construction of the PROSPECT AD.

The PROSPECT-50 optical grid is supported by acrylic wedges in an acrylic tank inside a secondary aluminum containment tank, as illustrated in Figure 4.9. The aluminum tank rests in a 10-cm-thick lead castle, with layers of BPE placed above the detector. The optical separators are constrained by the support rods and PMT optical modules. One segment is made from Hamamatsu PMT modules and the other from ET PMT modules, as both are used in the AD. One radioactive source calibration

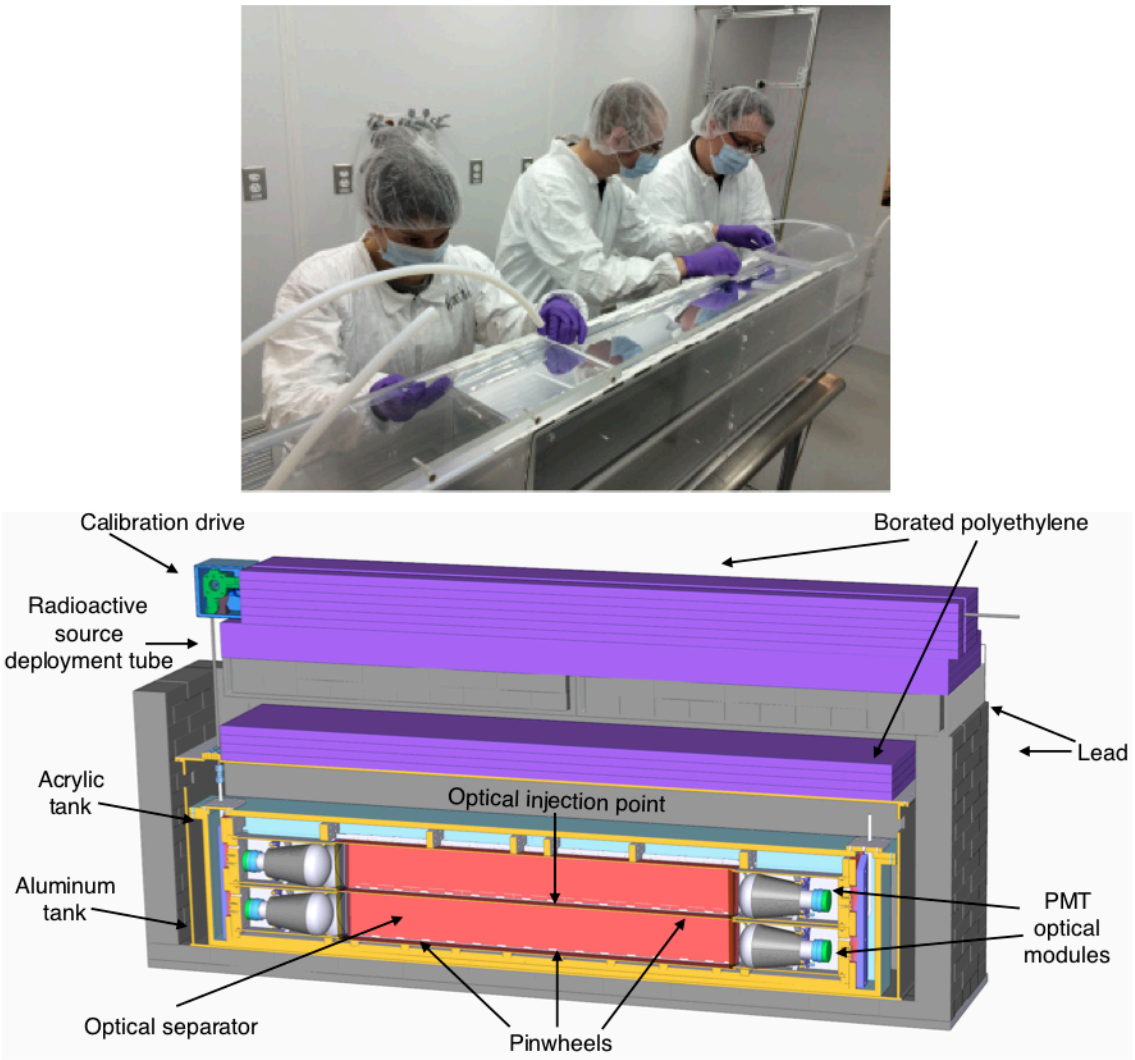

Figure 4.9: **(top)** Photograph of the PROSPECT-50 assembly at Yale University. **(bottom)** The PROSPECT-50 detector design. The detector has two $117.6\times14.5\times14.5\,\mathrm{cm}^3$ optical segments (red), each viewed by two 12.7-cm-diameter photomultiplier tubes (white/gray) contained in an acrylic enclosure filled with mineral oil for separation from the scintillator. BPE (green/purple) and lead (dark gray) surround the detector. The support rods (labelled "pinwheels") are visible [114].

tube (0.375-in-outer-diameter, 0.25-in-inner-diameter PTFE) is installed between the two segments. The source capsule is driven by a similar stepper motor drive, as described in Chapter 3. γ-ray sources are deployed through the system, while neutron calibrations are performed with the source outside of the detector volume. The OCS uses a CAEN SP5601 LED [161] pulse driver that injects a 5 ns wide, 405 nm

wavelength light pulse in the center of the two segments. During PROSPECT-50 operation, the driver is triggered at 20 Hz to monitor the SPE response of the PMTs and allow for gain drift corrections. Calibration runs triggered on the OCS signal to determine the gain and timing offsets of the PMTs. A simplified version of the PROSPECT DAQ system with CAEN V1725 WFDs is used to record PMT waveforms. An external trigger produced by the OCS initiates the digitization of all four PMT signal, regardless of energy deposition levels. A slow control system continuously monitors the environmental temperature, pressure, and humidity sensors. An excess of ∼20 L of ^{6}LiLS is maintained as an expansion volume between the optical grid and acrylic tank lid, covered with a nitrogen gas blanket. The scintillator was spiked with ^{227}Ac, similar to the production PROSPECT ^{6}LiLS.

The detector response was mapped using internal ^{137}Cs and external ^{252}Cf sources. The effective attenuation of the ^{6}LiLS, which includes the bulk attenuation inherent to the scintillator, imperfect reflective surfaces, and other geometric variables, was studied by stepping the ^{137}Cs source in 10 cm increments along the segment axis. Figure 4.10**(left)** shows the maximum of the measured Compton spectrum for each PMT, where the number of detected photoelectrons is enhanced closer to the PMT face. Adding the charge measured by the two PMTs results in a higher light collection. There is slight non-uniformity towards the center of the detector, which can be corrected for with position reconstruction. Fitting the curves with simple exponentials ($Ae^{-x/\lambda} + C$) results in an effective attenuation length of λ=85±3 cm. Depositions from the α + H^3 pairs from (n,^{6}Li) capture (∼0.55%), γ-ray from (n,H) capture (2.2 MeV), and γ-ray from the beta decay of ^{137}Cs are used to measure the energy response of a segment. An average light collection of 850±20 PE/MeV is observed.

The energy resolution is extracted by fitting the (n,^{6}Li) peak with a Gaussian and comparing the (n,H) and ^{137}Cs Compton edges to smeared simulations. Although photostatistics dominate the resolution, the width receives contributions from energy-

independent geometric effects from the mismatch in area between the square segment and round photocathode. These contributions are represented in fit parameters b and a, respectively. Fits of the three features, as shown in Figure 4.10**(right)**, reveal an achieved resolution of $\sigma = \sqrt{a^2 + b^2/E} = 4.0{\pm}0.2\%$ at 1 MeV.[3]

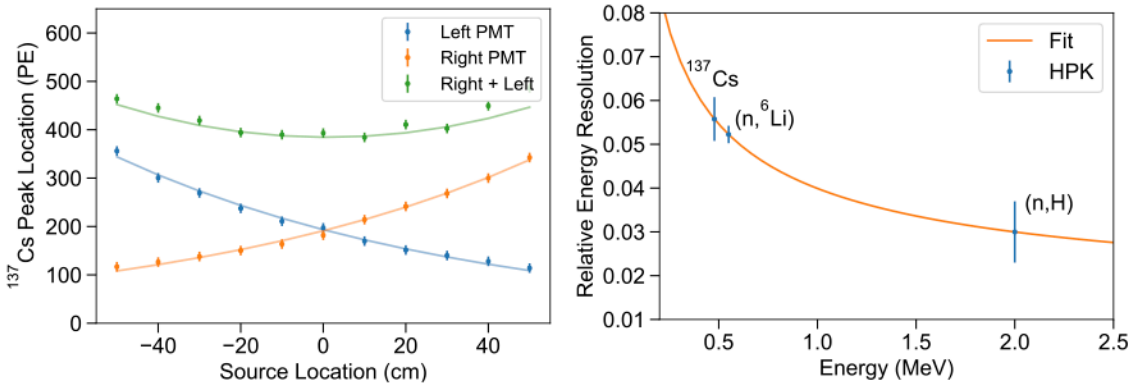

Figure 4.10: **(left)** Measurements of ^{137}Cs spectra in photoelectrons with PROSPECT-50. The source was positioned in 10 cm increments along the segment axis. The average number of detected photoelectrons at the various positions with a fit attenuation length of 85±3 cm. **(right)** Relative energy resolution as a function of nominal energy for (n,^{6}Li) capture, (n,H) capture, and ^{137}Cs. The fit contains a term for photon statistics and position-dependent collection effects. A resolution of $\sigma = 4.0{\pm}0.2\%$ at 1 MeV is measured. Note these data are from the segment with Hamamatsu PMTs [114].

The neutron source was also used to study the PSD performance and capture time in the detector. Figure 4.11**(left)** shows the PSD as a function of energy when combining the charge from both PMTs in the segment. Distinct electronic and nuclear recoil bands are observed between PSD parameters of [0.14,0.20] and [0.24,0.36], respectively, and a prominent feature at ∼0.55MeV indicates the (n,^{6}Li) captures. The quality of separation for both the prompt-like region between 1-3 MeV, as a substitute for the IBD prompt positron events, and the delayed-like neutron capture region from 0.4-0.7 MeV results in a FOM = 1.5, as defined in Equation 4.2. Events identified as proton recoils that occur within a 300μs window before a delayed neutron capture

[3]The quoted resolution is for the segment with Hamamatsu PMTs. The resolution for the segment with ET PMTs is slightly worse due to their poor SPE resolution.

(n,^{6}Li) capture are fit with a simple exponential ($Ae^{t/\tau} + C$) and give a measure of the characteristic capture time, τ=42.8$\pm$ μs.

The full details of the PROSPECT-50 detector response are published in Ref. [114]. Ambient backgrounds were also used to track the behavior of IBD-like and neutron backgrounds and their correlation with atmospheric conditions over time. Figure 4.12 illustrates the selection of events with prompt electronic recoils with delayed (n,^{6}Li) (IBD-like) and prompt nuclear recoils with delayed (n,^{6}Li) (FN recoil + nLi). As the neutrons originate in cosmic rays, there is a high anti-correlation between the rate and environmental barometric pressure due to the amount of shielding the air density provides. Tracking these events is essential for PROSPECT to normalize the time-varying, IBD-like reactor-off rate for subtraction with reactor-on data.

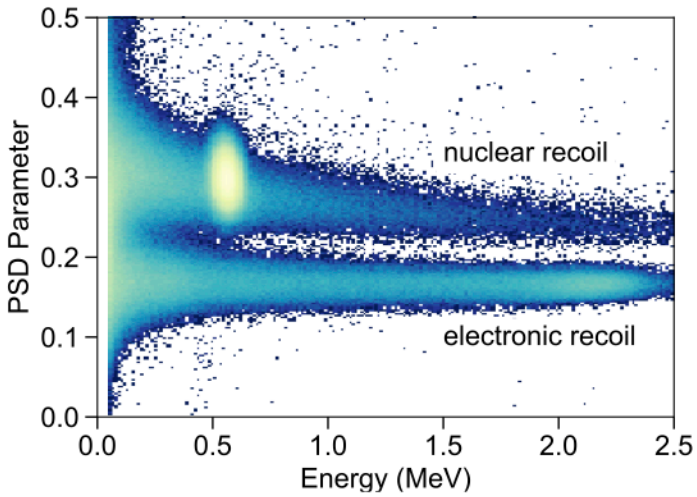

Figure 4.11: PROSPECT-50 PSD parameter distribution as a function of energy when exposed to a ^{252}Cf neutron source [114].

4.2 PROSPECT construction

The construction of all components and the detector itself took place from November 2016–January 2018. The PMT optical modules, inner detector, and detector package were assembled at the Yale Wright Laboratory. The optical separators were produced

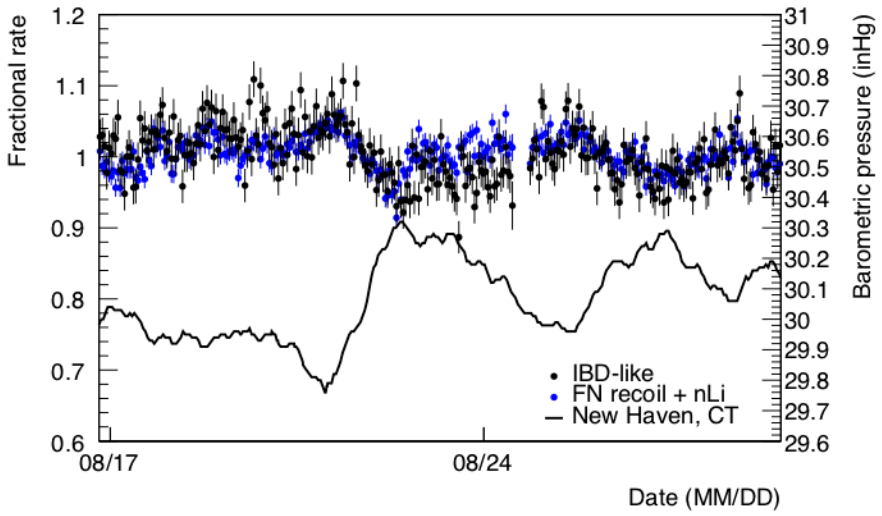

Figure 4.12: Comparison of IBD-like (black) and fast neutron (blue) correlated event types with barometric pressure. Neutron captures are anti-correlated with pressure, as a denser air column leads to more effective shielding. Measurements of atmospheric-corrected cosmic neutron events can thus be used to correct the time-varying background component of reactor-on spectra in PROSPECT [162].

at the Illinois Institute of Technology. The inner detector was then shipped without scintillator (dry) inside the secondary aluminum tank to ORNL in February 2018. Once moved in position at HFIR, the AD was filled with ^{6}LiLS and the passive shield package was assembled. After commissioning, the detector was operational in March 2018.

4.2.1 PMT optical module assembly

The 308 (plus spare) PMT optical modules were assembled and tested in a class 1000 clean room by trained shifters from the collaboration, following the sequence illustrated in Figure 4.13. Acrylic enclosures built by PolyFab [163] in Massachusetts (specifics outlined in Chapter 3) were checked for defects upon arrival and cleaned. Each individual module was etched with a serial number and entered into the optical

module QC database where dimensional measurements, performance metrics, and other notes were logged during the assembly process. Internal parts made from laser cut acrylic and machined PEEK, along with cables were received and cleaned. All components were cleaned following a rigorous cleaning procedure, including multiple rinses in 10 MΩ-cm (0.1 μsiemens/cm) deionized water and solutions of 10% ethanol or 1% Alconox detergent [164], depending on material compatibility. An ultrasonic cleaner was used when appropriate. At the end of the sequence, the parts were rinsed multiple times until the collected rinse measured 10 MΩ-cm with a calibrated conductivity meter. Once dry, the conical reflectors and PMT support structures were assembled. The acrylic backing of the conical reflectors were carefully coated with adhesive-backed DF2000MA and cut to size using an exacto knife. To make the cone shape, the ends of the single piece of reflective acrylic were cemented together using a thin piece of acrylic and Weld-On 16 [165], as shown in Figure 4.14**(left)**. The support plates were constructed from multiple pieces of acrylic with a profile matching the shape of the PMTs cemented to an acrylic ring.

Before the acrylic enclosures entered the assembly line, QC measurements were performed on a granite table with a height gauge and gauge blocks to ensure that the dimensions of the back plug, front window, and body were within the specified tolerance. The enclosures were then outfitted with reflective film on the side walls near the front window and the reflector cone. The back plug for each module was pre-assembled by threading the signal and HV cables through the PEEK seal plug assembly and installing the Viton O-ring, then directly soldered to a PMT base. The BNC (signal) connectors were tested for an impedance of $\sim$50 Ω and the SHV (HV) connectors attached to the voltage dividers were required to be $\sim$7.93 MΩ for Hamamatsu or $\sim$8.3 MΩ for ET, respectively. Each PMT was then covered with the Finemet magnetic shield, connected to the base, and installed into enclosure. Figure 4.14**(right)** illustrates this process. The bubble wrap expansion volume was

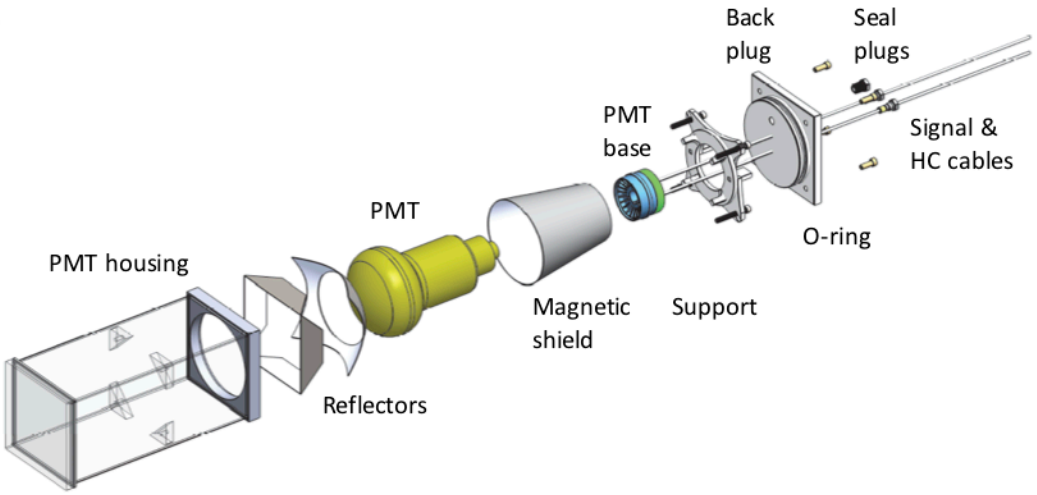

Figure 4.13: Schematic of PMT optical module assembly sequence. Starting with a cleaned acrylic enclosure that has passed QC inspection, reflectors are glued to the front side walls, the conical reflector is squeezed through the back opening and pushed against the front window. The PMT and magnetic shield are pushed against the conical reflector and secured in place with an acrylic support. A back plug assembly is made by threading the cables through the seal plugs and soldering to the PMT base. The base is pushed onto the PMT pins, seal screw plugs are tightened around the cables and temporary screws secure the plug to the back of the housing [108].

carefully added around the PMT bulb and the whole assembly was secured by bolting the PMT support with spring-loaded screws to internal acrylic arms. To finish the process, the O-ring was greased with Krytox and the back plug was pressed into the back flange and retained by temporary nylon screws.[4] The impedance was checked again, with Hamamatsu registering ∼5 MΩ or ET ∼6 MΩ with the extra photocurrent from the connected PMT.

Each module was pressured with 55 mbar of nitrogen gas and submerged under water to check for leaks. Modules that passed were stacked in a custom-made dark box for 48 hours to monitor the current stability (burn-in) at the operating voltage of -1500 V, as shown in Figure 4.15**(left)**. The modules were then filled with mineral oil pumped from a drum outside of the clean room using a peristaltic pump. They were

[4]These were later removed during detector installation as the PMT modules were bolted the acrylic support structure using PEEK screws.

Figure 4.14: Photographs of various steps in the PMT optical module assembly sequence. **(left)** Cementing of conical reflectors after the reflector material has been adhered to acrylic backing and cut. **(right)** Installation of PMT with base and magnetic shield from the back of the acrylic enclosure.

left to rest for a few days and refilled to remove remaining air bubbles. This was a messy process, requiring an extensive clean of each module. The same basic cleaning procedure for acrylics was used, however individual modules were scrubbed, soaked in tubs for hours, and then hand rinsed to ensure the conductivity of the rinse water registered as pure deionized water. Modules were stacked again in the dark box for final optical tests and impedance checks before installation into the detector.

4.2.2 Optical separators and support rod production

The optical separators were produced in a class 10000 clean room to reduce debris causing non-uniform surfaces. Carbon fiber sheets were CNC-cut to the nominal dimensions for the separator backbone. A cold roll silicone laminator was used to laminate the adhesive-backed reflective film to the carbon fiber, followed layers of adhesive and FEP on each side. This process is pictured in Figure 4.16**(left)**. Col-

Figure 4.15: Photographs of various steps in the PMT optical module assembly sequence. **(left)** Optical modules stacked in custom-made dark box for optical and electrical QC tests. **(right)** Collaborators being trained to clean the modules after the full sequence. This required a good deal of scrubbing, soaking, and rinsing to remove excess, slippery mineral oil.

laborators worked with thermoforming experts at Ingeniven [166] in New Hampshire to heat seal the FEP around the perimeter of the separators. Any excess FEP was trimmed using a scalpel and straight-edge. QC checks were performed at multiple stages of the procedure to ensure that the dimensions were within tolerance and to inspect for defects. 10% of the separators were randomly chosen for optical UV-Vis reflectance measurements. The separators were bagged and shipped to Yale University for the detector assembly. Upon arrival, each separator was cleaned with scratch-free wipes using the cleaning procedure described above. Inspections for defects were also performed.

The support rods were 3D-printed from white PLA by Autotiv Manufactoring [167]. The printing filament was 100 μm-in-diameter. Due to material compatibility considerations, 10-20% of the rods were rejected due to burns in the plastic. The tabs on each rod were filed to remove rough edges that could cause abrasions on the optical separators during assembly or detector movement. Several QC checks were performed, including test stringing on both the acrylic square dowels and PTFE calibration tubing. The rods were bagged and shipped to Yale University for the detector assembly. Upon arrival, the rods were cleaned in batches in an ultrasonic cleaner using the cleaning procedure described above. Once dried, the rods were strung on the acrylic square dowels, as shown in Figure 4.16**(right)**. These rods were later installed in the detector and remained in position, except for segments that would support the radioactive calibration and were replaced with the PTFE tubing. Rod assemblies that support the optical source (see Chapter 3) were strung in a special sequence using two machined rods with a U-channel to allow the routing of the optical fiber. More details on the production, QC, and testing of the optical separators and support rods can be found in Ref. [122].

4.2.3 Inner detector assembly

The inner detector was assembled in a custom-made, soft-walled class 10000 clean-room by a small team of highly-trained collaborators. A photograph of the set-up is shown in Figure 4.17. The detector load was distributed across a painted steel base lifted on four Hilman rollers [168], allowing for movement upon completion. The surface was flat to <0.13 mm and supported an adjustable rectangular 80/20 [169] frame attached to vertical posts to provide a reference for QC survey measurements. An array of acrylic blocks were uniformly positioned between the steel base and the base of the acrylic tank to allow for tensioning cables and lifting straps to be threaded under the assembly. Scaffolding was required to surround the base area during later

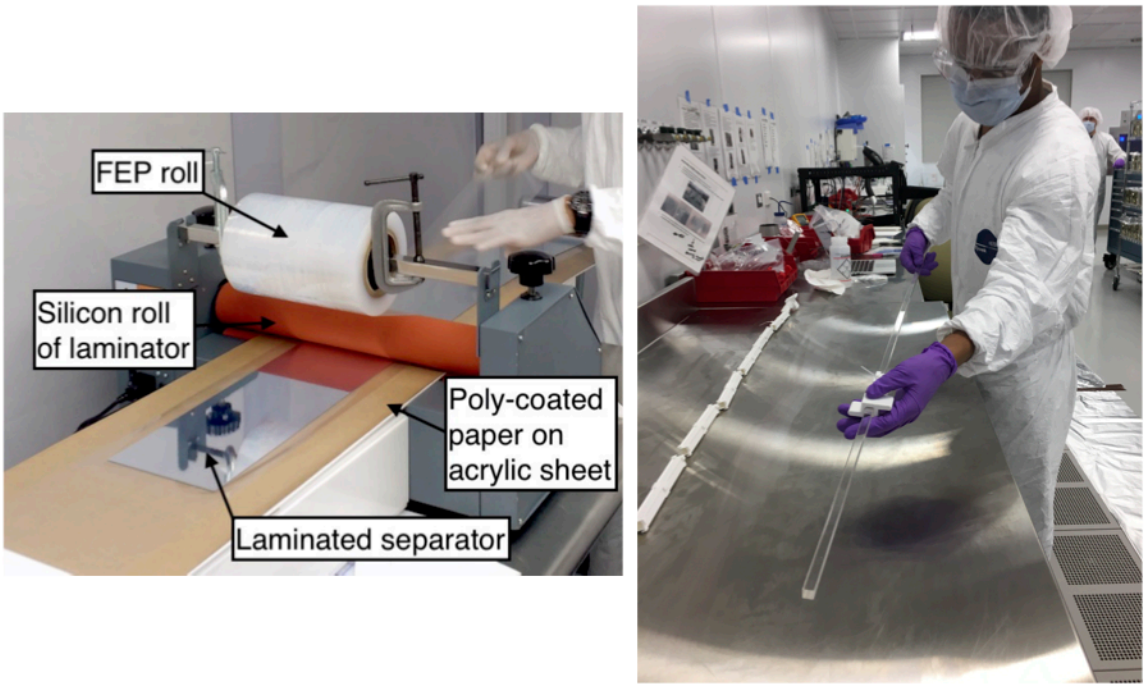

Figure 4.16: **(left)** Photograph of lamination setup, showing the FEP film being laminated to one side of the optical separator [122]. **(right)** Stringing support rods onto an acrylic dowel in preparation for the detector assembly. Note this support rod assembly does not support calibration access in the detector.

stages of the assembly.

The optical grid and acrylic supports were installed on top of the acrylic base. A layer of wedge-shaped acrylic planks were bolted together in shiplap style, centered, and surveyed, giving the initial dimensions and coordinates of the inner detector. Optical separators were pre-assembled to support rod assemblies using a machined low density polyethylene jig; the extra FEP film on the edge facing the support rod assembly was folded underneath the separator. The bottom layer of each optical grid row was assembled by installing a sequence of horizontal separator-rod assemblies. Vertical assemblies were installed starting from one end against an acrylic support wedge, placing PMT modules in between each segment, held in place by an acrylic horizontal support bolted with PEEK screws to the row of modules beneath it. Thin, 0.13 mm FEP sheets were used to insert the PMT modules securely between the

Figure 4.17: Panorama photograph of the inner detector assembly clean room. The detector building area is surrounded by scaffolding to assist with the construction as the layers were built up. An 80/20 aluminum frame around the area supports metrology instruments. Optical separators are secured to the support rod assemblies before insertion.

end support rods while protecting the separator surfaces from sharp edges. The temporary nylon screws in the module back plugs were removed, bolting the back plug to acrylic supports with PEEK screws. A visual inspection of the row was completed before the next layer of horizontal separator-rod assemblies. An acrylic support wedge was then installed to the bare end of the grid to constrain the layer. QC survey measurements were performed using a laser gauge and laser-cut aluminum gauges to ensure the module and support rod positions were within tolerance. Figure 4.18**(top)** illustrates this process, where the laser gauge moves across a linear slide rail to survey the profile of the layer. Teflon shims of various thickness were inserted on the top of a given support rod and/or module back plug to minimize the accumulation of height variations. This procedure was repeated to build all 14 rows, with each layer supported by the layer beneath it. Two assemblers were positioned on either side of the assembly to lay the components, while two others prepared the instrumentation and provided spotting, as seen in Figure 4.18**(bottom)**.

Acrylic baffles were installed on top of the grid, providing a vertical constraint to the optical grid and serving as a tie-in for the vertical support wedges. Vertical acrylic supports were bolted to the horizontal PMT module supports providing further mechanical constraints and a path for cable routing. The square dowels in the separator-rod assemblies that support radioactive source calibration were removed and replaced with pre-straightened PTFE tubing. The length of each tube was measured and recorded as a reference for the source motor drive system. Optical fibers were installed in the separator-rod assemblies that support optical source calibrations. RTD temperature sensors on long cables were strung through 10 support rod assemblies. Teflon shims were positioned between the base of the acrylic supports and the acrylic tank base to prevent movement during transportation. An interior Viton O-ring was installed along the tongue of the base, constrained by PEEK spacers; a larger neoprene sponge cord was installed on the outside of the tongue. Both O-rings

Figure 4.18: **(top)** Performing QC measurements on the last built layer. A motorized laser gauge is mounted on a linear slide rail spanning the width of the detector to measure the vertical profile of the reflective surfaces. Two different laser-cut aluminum gauges (one pictured) in combination with plastic feeler gauges are used to measure the profile of the PMT module back plugs and the end support rods that rest on the front window. **(bottom)** Detector assembly midway through the top row. A vertical optical separator is inserted into the support rods (white tabs) and PMT modules of previously installed layer. The white PMT module bodies and clear front windows are visible on the near side while the far side shows the PMT faces and conical reflectors. Photograph taken by Mara Lavitt.

were greased with Krytox.

The walls of the clean room were removed and the acrylic walls were lifted and sealed onto the base. A temporary blocking system was installed to allow for cables and tubing to be routed through the holes in the acrylic tank lid before lifting it onto

the acrylic walls. A strip of 0.05-m-wide marine tape was adhered around the joint for extra seal protection. The lid was then mounted into place, cushioned by 0.381 mm Teflon strip to prevent acrylic-on-acrylic contact, as shown in Figure 4.19**(top)**. The O-rings were further compressed by 16, evenly-spaced stainless steel cables surrounding the exterior of the acrylic tank, resting on 2.5-mm-thick aluminum angles cushioned by plastic on the edges. The cables were tensioned via turnbuckles placed on the top of the tank. A test port between the two O-rings was tested with 7 kPa of nitrogen gas to verify the quality of the seal [108].

4.2.4 Detector package assembly

Upon completion of the inner detector construction, the secondary aluminum tank was prepared on Hilman rollers in the high bay area of the Wright Lab. The inside walls of the tank were lined with sheets of BPE while the bottom was tiled, creating channels for the tension cables and lifting straps. Aluminum U-channels were bolted to the bottom to allow forklift access. This tank assembly weighed ∼3 tons. The ∼5 ton (dry) inner detector was transported to the high bay and prepared for lifting. Two lifting straps were threaded underneath the detector and attached to a custom H-beam lifting fixture with shackles. The two exterior filling ports on the side walls of the acrylic tank were were outfitted with PEEK fixture with an O-ring seal and push-to-connect plumbing system for filling and pumping. The assembly was lifted ∼2.5 m above the aluminum tank. Fine adjustments of the aluminum tank position were achieved by adjusting the Hilman rollers, as horizontal movements of the crane were quantized. The detector was lowered in, as seen in Figure 4.19**(bottom)**, concentric with the aluminum tank to within 1 cm [108]. Remaining gaps between the BPE and acrylic tank were shimmed with BPE planks. Another pressure test of the seal was performed using the PEEK plumbing system.

Figure 4.20**(left)** shows the layers of BPE shielding that were installed on top

Figure 4.19: **(top)** Adding the acrylic tank lid after the inner detector was assembled and the acrylic side walls were installed. **(bottom)** The inner detector being lifted into secondary containment tank. Layers of BPE and plumbing lines were installed prior to the lift.

of the acrylic tank. Holes were cut to allow cables, calibration tubes, filling and gas lines, and instrument cables to exit the tank. The tank lid was lifted onto a blocking system and cabling was routed through cutouts. A neoprene gasket with bolthole cutouts filled with washers was fixed to the top perimeter of the tank to

Figure 4.20: **(left)** Layers of BPE installed on top of the inner detector before the secondary tank lid is laid. Notches are cut into the edge pieces to allow for cabling and tubing to exit. **(right)** Collaborators helping to route cables through Icotek grommets. Equipment for the level sensor installation is also shown.

provide a light- and gas-tight seal. The lid was lowered and bolted with Icotek cable feedthrough systems mounted around each lid cutout. Cables and tubes were then routed through grommets held by the Icotek system, as shown in Figure 4.20**(right)**. The scintillator and water level sensors were also installed. Aluminum raceways with cutouts were bolted on top of the BPE sheets. Cables were bundled tightly using cable wrap and were braided through cable trays mounted to the raceways to ensure the cables were uniform in length when exiting. A blowout-line manifold was installed on one end of the calibration tubing using push-to-connect fixtures, which would later route to the motor drive boxes; the other ends, along with gas and fill lines, were made light-tight using black heat shrink. The long optical fibers were tightly coiled into an electrical enclosure, with the connections remaining free. A potting mixture made from silicone RTV and graphite was poured into the Icotek fixtures, the liquid constrained by temporary dams, and left to cure ensuring the detector was light- and gas-tight. Lids were installed on the raceways and BPE strips were placed in-between, to create a flat surface on the top of the tank, shown in Figure 4.21**(left)**.

The bulkhead feedthrough box was constructed and connected to the HV and

Figure 4.21: **(left)** Top of the detector package after cable routing. Lids to cable raceways and BPE strips are installed to create a flat surface for shielding to rest on. **(right)** Photograph of the exterior shielding package (black) construction, next to detector assembly.

signal cables for a test commissioning of the detector. The DAQ system was built to test all components and create a plan for setup at HFIR. All electrical connections were intact and cosmic muons were observed to interact with the mineral oil in the PMT optical modules. Figure 4.21**(right)** shows the pre-assembly of the shielding package, which ensured that all of the lumber fit properly and to avoid machining and drilling work at HFIR. The radioactive source calibration drive system and slow control boxes were also pre-assembled at Yale, including all of the necessary electrical work. Figure 4.22**(left)** highlights the 3D-printed drive pulley assemblies after the switches were soldered to the appropriate connectors. The detector was purged with argon and nitrogen and sealed for shipment. A large forklift was used to lift the detector into a foam-lined shipping crate and subsequently lifted into an air-ride trailer in route to ORNL, as shown in Figure 4.22**(right)**. 7 g shock sensors were adhered to the outside of the aluminum box and shipping crate with a accelerometer, GPS, humidity, and temperature sensor on board.

Figure 4.22: **(left)** 3D-printed pulley assemblies for the radioactive calibration drive motors after installation of electronics. **(right)** Detector packaging lifted onto a truck at the Yale Wright Laboratory for delivery to Oak Ridge.

4.3 Installation at HFIR

Upon arrival to ORNL, the detector was unloaded in a HFIR maintenance facility and connected to a nitrogen cover gas system. The ^{6}LiLS was shipped in multiple drums from Brookhaven National Laboratory inside temperature-controlled trucks. Using a peristaltic pump with Teflon and Viton plumbing, the ^{6}LiLS was transferred from the drums to a large Teflon-lined ISO tank, previously purged with nitrogen. The ^{227}Ac-spiked drum was mixed in to achieve the required, uniform activity throughout the scintillator. Samples from each drum were measured by UV-Vis spectrometer for QC. The ISO tank was transported outside of the HFIR building and covered with a plastic tent to protect it from weather, as illustrated in Figure 4.23**(left)**. The detector package was removed from storage and placed on the chassis with a large forklift. Figure 4.23**(right)** shows the air caster system being used to fine-tune the position with respect to the reactor in Position 1 and to slightly tilt the detector to prevent trapped bubbles in the optical grid. Teflon plumbing was installed between the ISO tank and detector for ^{6}LiLS filling. The height of the liquid was monitored by the level sensors. PMTs were powered on during the filling and a large change

in the number of counts was observed as the liquid level rose. A total of 4340 kg of ^{6}LiLS was pumped into PROSPECT. The detector position was restored from the tilt and water was pumped into the space between the acrylic and aluminum tanks.

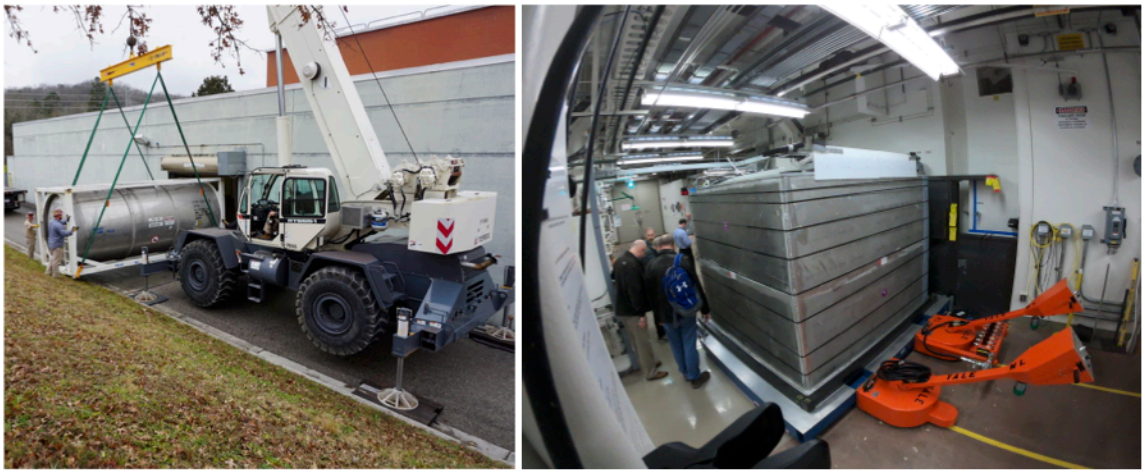

Figure 4.23: **(left)** ISO tank holding ^{6}LiLS transported outside the HFIR building. The tank is significantly larger than required, but was recycled from a previous experiment. **(right)** Fisheye view of the detector package and chassis after being moved into Position 1 by the air casters and air drive motors (orange) [108].

A layer of 0.025 m interlocking lead bricks was stacked around the perimeter of the aluminum tank. The HDPE beam structure was assembled around the lead, secured by lag screws, as seen in Figure 4.23**(left)**. The bulkhead panel was installed on the top of the wall on one side of the detector along with a the calibration system transition box on the opposite side. HDPE roof beams reinforced with steel pipes were added to the top. Figure 4.24 shows the PMT and environmental monitoring instrumentation cables being routed from the bulkhead panel to three electronic racks next to the detector. All plastic surfaces were covered by thin aluminum sheeting. An array of filled WaterBricks were added to the roof, surrounded by a fire blanket.

Commissioning tests were performed to ensure that all electrical connections were intact and to determine that the ^{6}LiLS volume was stable. Initial calibrations allowed for the adjustment of the nominal operation voltages for each PMT to achieve the desired 5×10^5 gain. With the reactor on, first data was taken in March 2018. Fig-

Figure 4.24: **(left)** Layers of lead (gray) and BPE (black) shielding installed on the exterior of the detector package by HFIR workers. **(right)** Electronics racks after components were installed and cables connecting to the feedthrough bulkhead panels.

ure 4.25 illustrates a few of the event types observed by PROSPECT at the surface next to HFIR, including straight-going muons, cosmogenic showers, and $\overline{\nu}_e$-induced IBD events.

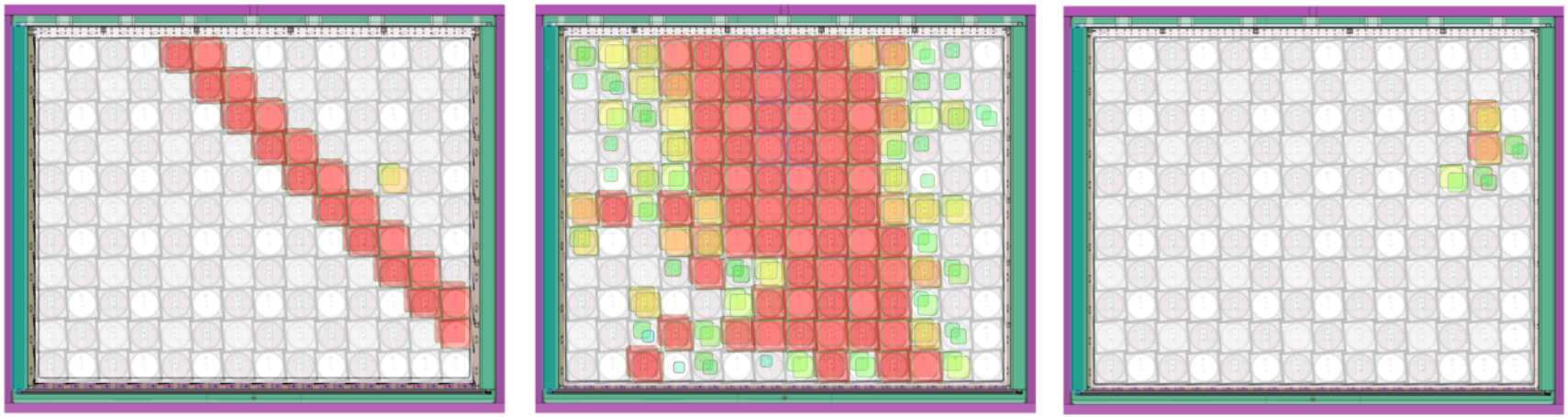

Figure 4.25: Event displays from commissioning superimposed on a cross-sectional view of the detector. Each hit represents a cluster (promptly-time-correlated signal within a segment, `DetPulse` objects) as seen by individual PMTs, where the color and size represent the amount of energy deposited. These displays give visualization of different event classes: **(left)** muon track, **(center)** cosmogenic shower, and an **(right)** IBD candidate.

Chapter 5

Calibration, reconstruction, and detector performance

The ultimate goal of the PROSPECT detector is to record PMT waveforms for every particle that passes through the scintillator. It is the job of calibration and reconstruction to use these waveforms to uncover the physics event information through models. Due to the limitations of the detector hardware, an exact event unfolding is impossible and the extracted parameters will only represent an averaged representation of the true physics. Distinct energy depositions occurring close in space, within a segment, and time $\mathcal{O}$(tens ns), are grouped into effective pulses and reconstructed as point-like events. These interactions are characterized by the time, total (quenched) deposited energy, position along the segment axis, and average PSD parameter.

There are several analysis steps required to transform the PMT waveforms into reconstructed physics quantities, carried out by progressive stages in the `PROSPECT2x_Analysis` [170] framework. Figure 5.1 illustrates the process. Raw binary data recorded by the DAQ is converted into `ROOT` waveforms that can be easily inspected by analyzers. Properties of each waveform from the individual PMTs are characterized and reformatted into detector pulses saved as `DetPulse` objects. These pulses

are then grouped as segment pulses and calibrated to form `PhysPulse` variables. This stage involves reconstructing the time, position, energy, and PSD of an event observed by both PMTs in a segment. Reconstructed pulses are then clustered into prompt and delayed events based on the timing sequence and event selection, generically labelled as `PhysClusters`. Databases are used to facilitate these calculations over all PMT and segment channels, across every data run. The detector energy scale, including shifts, resolution, and nonlinearity, is validated by comparing radioactive source calibration data to GEANT4-based [171] `PROSPECT-G4` [172] Monte Carlo. If a shift in the energy scale is observed in the reconstruction, the calibration of `DetPulse` is adjusted accordingly and reprocessed. The data-driven scale parameters are then used to constrain the `PROSPECT-G4` to model the IBD response during particular data taking periods. Calibration and standard operation data are used to ensure the stability of the calibration over time across the entire detector.

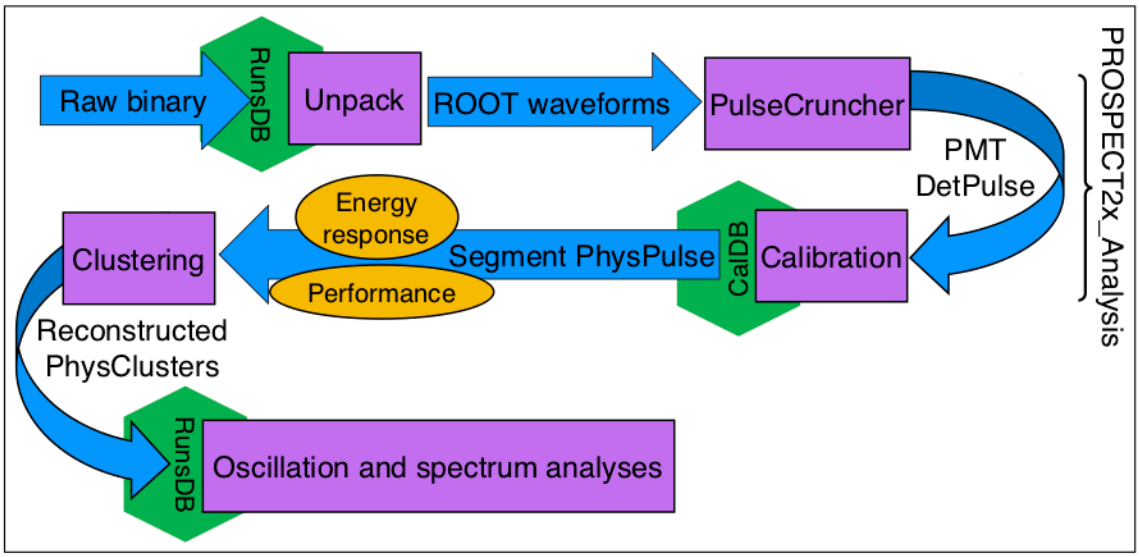

Figure 5.1: High-level schematic of the PROSPECT data analysis system. Different shapes represent various parts of the process: data structures (arrows), processing software (boxes), databases (hexagons), and calibration checks (ovals). The `PROSPECT2x_Analysis` system is used to convert the raw data collected by the DAQ to reconstructed (IBD) events for higher-level physics analyses.

5.1 Waveforms to detector pulses

5.1.1 Unpack: Raw binary to ROOT waveforms

The 308 PMTs generate an analog voltage pulse that contains contributions from multiple scintillation interactions that occur within the same segment during the acquisition window. The DAQ digitizes the pulse, dependent on the specifications outlined in Chapter 4. One digitized sample is recorded every 4 ns, where the voltage less than 2 Vpp is converted into a binary value up to 2^{14} ADC channels, i.e. each bit represents 1.2×10^{-4} V increments. Figure 5.2 illustrates the digitization of the PMT waveform. The data is compressed into binary format with run headers provided by digitizer metadata, where files from each WFD board are written separately to disk. Metadata from the runs database (`RunsDB`), which stores summary information for each approximately one hour long run, is used to keep track of the file names, timestamps, and reactor status. The PROSPECT `UnPack` program combines the data files from all WFD boards into a single file and converts the binary format into `ROOT` [173] waveforms in `TTree` format. A map linking DAQ hardware channels to logical PMT channels[1] is made and stored as a `TMap`. The important parameters contained in the unpacked `TTree` include the event number (grouping close-time-spaced triggers), PMT channel number, number of samples, and array of waveform sample values.

5.1.2 PulseCruncher: ROOT waveforms to detector pulses

The `PulseCruncher` program repackages the waveform information into a summary of the pulse attributes. Peak finding is applied to every waveform to identify the signal, passing a minimal software threshold. To locate the peak in the sometimes

[1] PMTs are labelled from 0 to 307. The east side of the detector is labelled as even numbers, the west with odd numbers. PMT 0 is located at the bottom of the east side of the detector, facing the reactor (north).

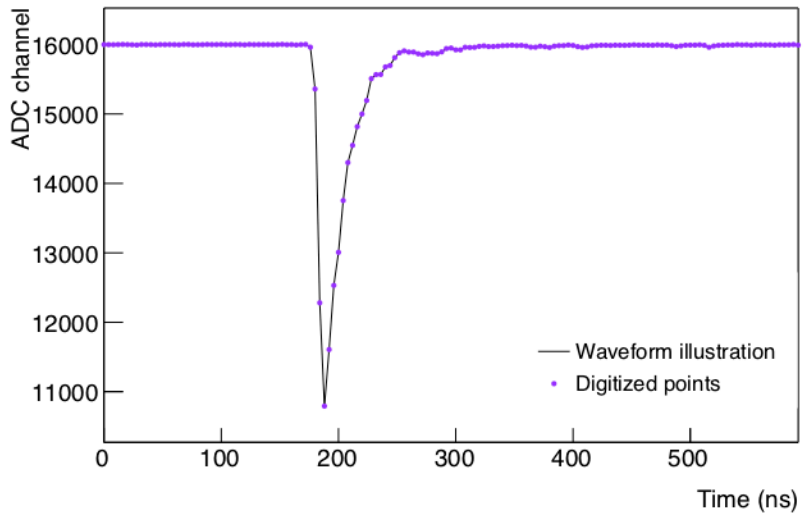

Figure 5.2: Example of digitized PMT waveform. The digitizer samples (purple) the pulse (black) every 4 ns and assigns an ADC channel value (up to 2^{14}) to the observed voltage.

noisy data, multiple local maxima are found by scanning the waveform for samples with lower values on either side of the point; a pre-defined range is set to exclude local maxima around other maxima. The found maxima are then "dilated", where each sample around a maximum is given the maximum value, creating plateaus [174]. The dilated waveforms are then scanned to find the centers of the local maxima plateaus and provide the location of the global maximum or peak of the pulse.

Multiple time windows are defined and referenced from the pulse peak to calculate the average baseline, leading-edge rise-time, baseline-subtracted pulse integral, and PSD parameter. Table 5.1 details the software parameters used in this thesis.

No calibrations are performed at this stage in the analysis chain. The output is a `DetPulse` object that represents a characterization of each detector event observed by the individual PMTs and includes: event number from `UnPack`, PMT number, arrival time from the file start (interpolated from the leading edge), pulse area, height, baseline (in ADC channels), leading edge rise time (∼20-80% of height level-crossing), and PSD (as defined in Equation 3.1).

Parameter	Value
Local maxima range	10
Low-level peak threshold	30
Baseline low edge	-30
Baseline high edge	-5
Integration low edge	-3
Integration high edge	25
PSD low edge	-3
PSD divider	11
PSD high edge	50

Table 5.1: Values of parameters used by the `PulseCruncher` program to convert digitized waveform samples into detector pulse information. The values are in number of samples referenced from the peak of the pulse.

5.2 Calibration: Detector pulses to segment pulses

`DetPulse` objects then undergo a significant calibration process where PMT pulses are converted into segment pulses, requiring pulse matching. Pulses from the individual PMTs are paired together if they are coincident within a few nanoseconds; any pulses detected by a single PMT are assumed to be noise and are discarded. The calibration is then performed on pulse pairs in each segment. Differences in the clock of each digitizer board and any timing offsets between the PMTs are corrected. Maps between PMT timing differentials and position along each segment are produced. Variations in PSD, light attenuation, and effective gain along the segments are measured and stored in look-up maps in the calibration database (`CalDB`).[2] The calibration begins using look-up curves from previous runs to roughly estimate the initial fit parameters, which are then fine-tuned for the specific run. Although not required for every variable on a short timescale (e.g. scintillator properties), calibrations are performed about every hour during each data run. Data from special calibration source runs are

[2]The gain of each PMT is not determined in this analysis chain as it is not required for the calibration. Rather, the effective gain of the scintillator, PMTs, and electronics in each segment is considered, as described later in this section. The OCS system has been used to measure the gains by operating the PMTs at a higher gain of $\sim 3\times10^6$ to observe the single photoelectron peak and extrapolate to the nominal 5×10^5 setting.

used to validate the process. Corrections are applied to ensure a uniform response across the segment lengths. Segment pulses are then reconstructed as `PhysPulse` objects, including total deposited energy, position, and PSD parameters. Global energy reconstruction issues, such as missing energy and scintillator nonlinearity, are not corrected for, but rather are accounted for in the detector response, which will be discussed in Section 5.4.

5.2.1 PMT timing offset corrections

Light produced in the center of a segment should register as a zero timing differential between the two PMTs, everywhere in the detector. However, because of slight variations in the PMT electronics and WFD board clock offsets (in 8 ns shifts), a timing offset correction is required for each PMT pair. Downward, through-going relativistic muons provide an ideal sample for measuring this effect, as many segments across the detector will trigger with each event. The track is selected to include only straight-line trajectory events that pass through or "clip" the segment corners, depositing a moderate amount of energy in each segment such to avoid saturating the dynamic range of the WFDs.

With the corner-clipping hit coincidences between segments, two timing matrices are produced. The first matrix describes the average arrival time registered by each PMT of segment i,

$$t_i = \frac{t_i^0 + t_i^1}{2}, \tag{5.1}$$

where t_i^0 is the arrival time observed by PMT 0 in segment i and t_i^1 by PMT 1. The estimated muon transit time through each segment time is subtracted out. The

second matrix collects the differential timing between PMTs in the same segment,

$$dt_i = t_i^1 - t_i^0. \tag{5.2}$$

The matrices can be used to solve a system of linear equations to obtain the average timing characteristics $\bar{t}_i$, $\overline{dt}_i$ of all segments. From $\bar{t}_i$, the segment offset from the DAQ clock (fixed such that $\sum \bar{t}_i$=0) can be extracted. The average peak offset of the PMT differentials $\overline{dt}_i$ define the center position, $\overline{dt}$=0, of the whole detector. Figure 5.3 shows an example of the resulting look-up maps that are stored in the `CalDB`. The OCS system is used to validate these calibrations, however some additional absolute offsets between segments grouped around one optical fiber are observed, indicating these fibers were not installed at the exact center of the respective segment (up to ∼1.5 ns offsets). When these corrections are applied to the pulses, a uniform response to the event is obtained between PMTs and segments.

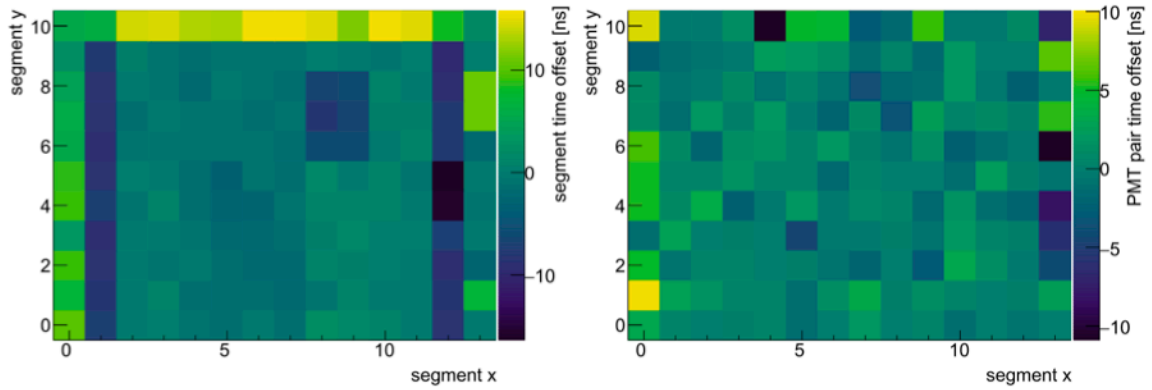

Figure 5.3: Examples of segment timing look-up maps. Segment x is the row number 0 to 13 and y the column number 0 to 10. **(left)** The segment timing offsets to global event clock. Systematic differences in signal propagation times are observed between the WFD boards, creating the block-like structure. **(right)** PMT timing differential offset in each segment. A wider scatter in ET (outer sides, top) PMTs compared to the Hamamatsu (inner) and PMTs is observed. From collaboration Ref. [175].

5.2.2 PMT timing to segment position map

The PMT timing differential is used in the position reconstruction chain, mapping the timing of an event to the absolute position within a given segment, or z-position. The detector has an inherent feature to aid this transformation: the support rod tabs along each segment edge. Using samples of corner-clipping muons, the tabs near these events cause local distortions to the timing and collection of the light, creating a tiger-striped pattern that can act as an internal ruler. Figure 5.4 illustrates this effect for a particular segment.

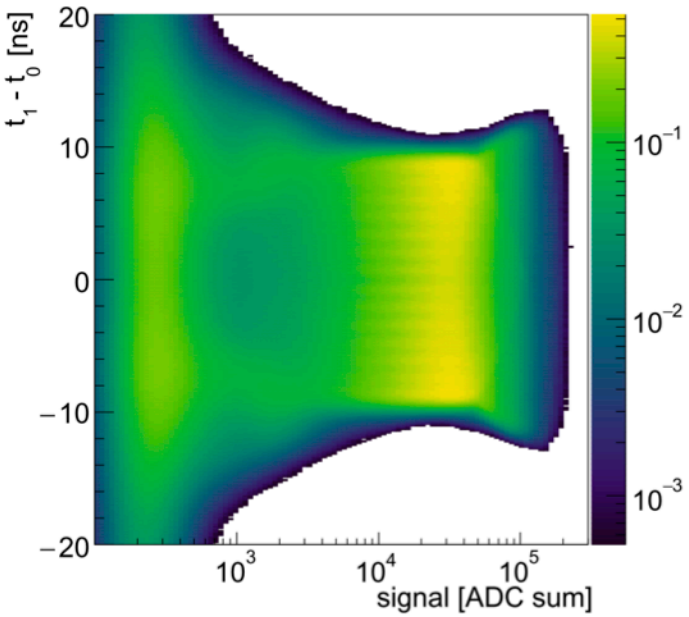

Figure 5.4: dt as a function of signal amplitude for muon track hits. The tiger-striping effect is observed at intermediate signal levels. From collaboration Ref. [175].

A slice of the dt distribution for intermediate signals is fit for every segment, as seen in Figure 5.5**(left)**. The envelope of the distribution determines the end positions of the segments, between the PMT front window and the end of the active optical grid, and is fit with an "M-shaped" curve, $M(dt)$. The fine structure, the ripples caused by the local light transport distortions, is modelled as a sinusoidal curve, such

that the overall fit $n(dt)$ takes the form,

$$n(dt) = M(dt)\left[1 + kcos\left(\frac{2\pi}{\delta}(adt + bdt^3)\right)\right], \tag{5.3}$$

where $\delta = 78.5\,\text{mm}$ is the average spacing between the support rod tabs, and k, a, b are the fit parameters. The phase term, $z(dt) = adt + bdt^3$, gives the mapping between the PMT timing and segment position, as shown by the distributions in Figure 5.5**(right)**. The effective index of refraction, with contributions from all the scintillator properties, can be derived as $n_{\text{eff}} = c/2a$ with values between [2.3,2.6] at the center of the segment, where c is the speed of light. The cubic term altered by the magnitude of b is related to the change in light transport near the ends of the segments. The small mismatches between the data and sinusoidal fit vary slightly from segment-to-segment due to small variations in the support rod positions. Scans of radioactive γ-ray calibration sources along the segment length are used to validate the performance of this model, and have confirmed the $z(dt)$ maps to $\pm 1\,\text{cm}$ across all segments.

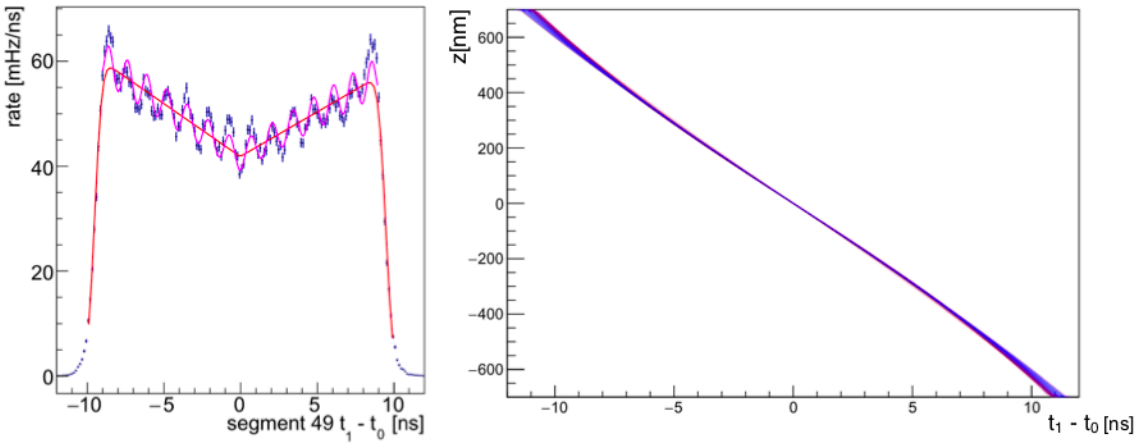

Figure 5.5: Examples of segment timing-to-position maps.**(left)** Ripples in light collection rate as a function of PMT differential timing (blue), due to support rod tabs altering the light transport characteristics of corner-clipping muons. The sinusoidal model (magenta) is overlaid by the total fit (red). **(right)** $z(dt)$ maps for all segments with Hamamatsu (blue) and ET (red) PMTs. From collaboration Ref. [175].

5.2.3 Position-dependent PSD

Due to the bulk attenuation properties of the scintillator and geometric effects in the detector segments, the light transport characteristics are position-dependent. As light travels farther (events move away from the PMT faces towards the segment center), trailing, fast scintillation photons shift to later times and broaden the PMT pulse. This has a direct consequence on the PSD calculation and causes a non-uniformity along the segment length. Figure 5.6**(left)** shows this attenuation effect, which to first approximation can be modelled as a simple exponential form, $Ae^{kdt} + C$. At the ends of the segments (>50 cm from the center on either side), pulses are further broadened by light scattering around the corners before traversing to the opposite PMT, resulting in large PSD values. Events from these regions are excluded from the analysis and thus are not included in the attenuation fit. With position-dependent corrections, the PSD response is unified along the axis of each segment, as seen in Figure 5.6**(right)**.

5.2.4 Position-dependent effective attenuation

To fully understand the position-dependence of the effective attenuation, it is necessary to extract light collection curves from data, relaxing the assumption of a simple exponential model. The approach is to measure complementary quantities that can be combined to give the relative light collection efficiency $\eta^i(dt)$ for the two PMTs i =0, 1 as a function of the dt. Using the dt-position mapping from above, this quantity can then be converted into a function of z and stored as a look-up curve in the `CalDB`. The relative efficiency could be directly measured through tracking of the (n,^{6}Li) capture peak, however the statistics are limited and the individual signal distributions, S_0 and S_1, vary significantly across a given segment length.

The ratio R between signals (in units of ADC channels) registered by the two

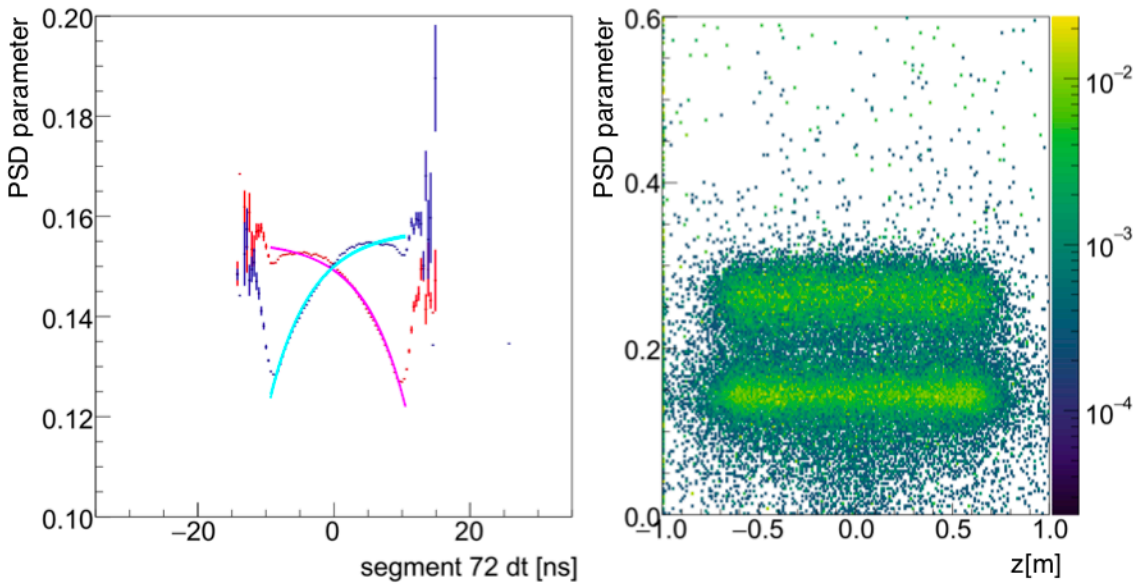

Figure 5.6: Examples of PSD position-dependence. **(left)** PSD as a function of dt for PMTs (blue, red) in a particular segment. Exponential fits modelling the attenuation are overlaid (cyan, magenta). **(right)** PSD after position-dependent corrections have been made along with the mapping dt to absolute position. From collaboration Ref. [175, 176].

PMTS,

$$R(dt) \equiv \frac{S_1}{S_0}, \tag{5.4}$$

is independent of the total charge collected in the event. Thus, the abundant, non-clipped muon samples that pass through the bulk of each segment can be used to measure the effect at various z positions. Figure 5.7**(left)** shows an example of the $ln(R)$ versus dt distribution for a particular segment. A cubic polynominal fit is used to better model the deviations observed at the ends of the segments.

The geometric mean signal S (in units of ADC channels) registered by the combined PMTs,

$$S(dt) \equiv \sqrt{S_1 S_0}, \tag{5.5}$$

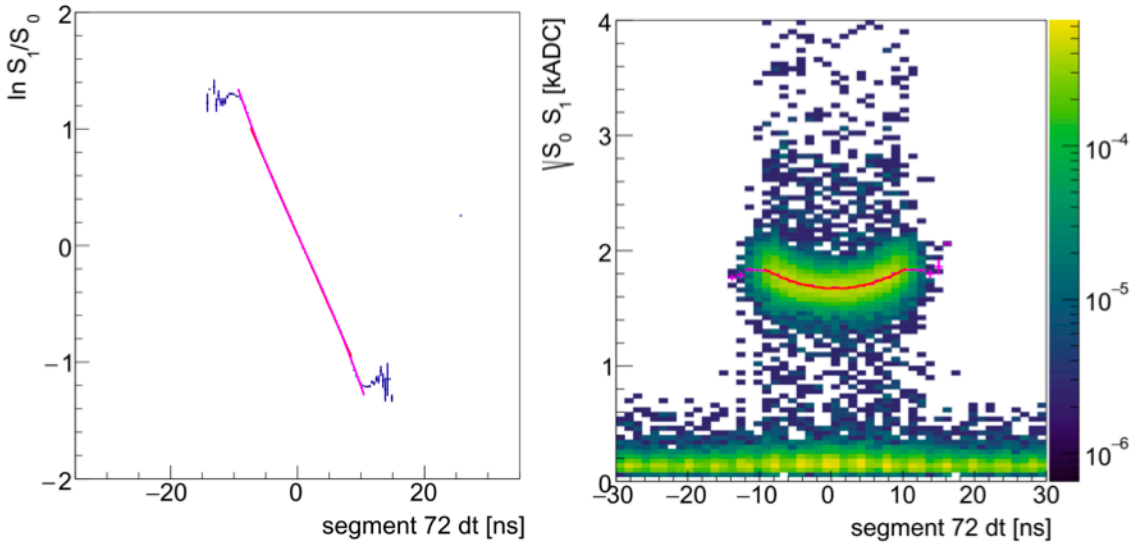

Figure 5.7: Examples of light collection position-dependence. **(left)** $ln(R)$ as a function of dt (blue). A straight-line fit (red) is shown to illustrate how the data deviates near the ends of the segments. The cubic polynomial fit (magneta) better models those data points. **(right)** Neutron capture signals as a function of dt. A quadratic fit (red) is used to determine the average collection in each dt slice. From collaboration Ref. [175].

is dependent on the total charge collected in the event. Thus, a spectral feature with a distinct energy is required to track the change of S at various z positions. The (n, ^{6}Li) capture peak, selected by PSD cuts, is used since the statistics of S are fairly constant throughout each segment. Figure 5.7**(right)** shows an example of the S versus dt distribution for a particular segment. A quadratic polynominal nicely models these events and the peak at each dt slice is extracted to represent the average collection.

The ultimate light curves can be generated using these parameters via:

$$\eta^0(dt) \equiv \frac{S(dt)\sqrt{R(dt)}}{S(0)\sqrt{R(0)}}; \eta^1(dt) \equiv \frac{S(dt)\sqrt{R(0)}}{S(0)\sqrt{R(dt)}}, \tag{5.6}$$

with normalization such that $\eta^i(0)$=1 at the segment center (z=0). Using the timing-

to-position mapping and the simple light transport model,

$$z = \frac{c}{n_{\text{eff}}} \frac{dt}{2}, \tag{5.7}$$

$\eta(dt)$ is converted into $\eta(z)$. Figure 5.8 shows the light curves η^i for all the PMTs from a specific data set. These are stored in the `CalDB` and are used to reconstruct event energy.

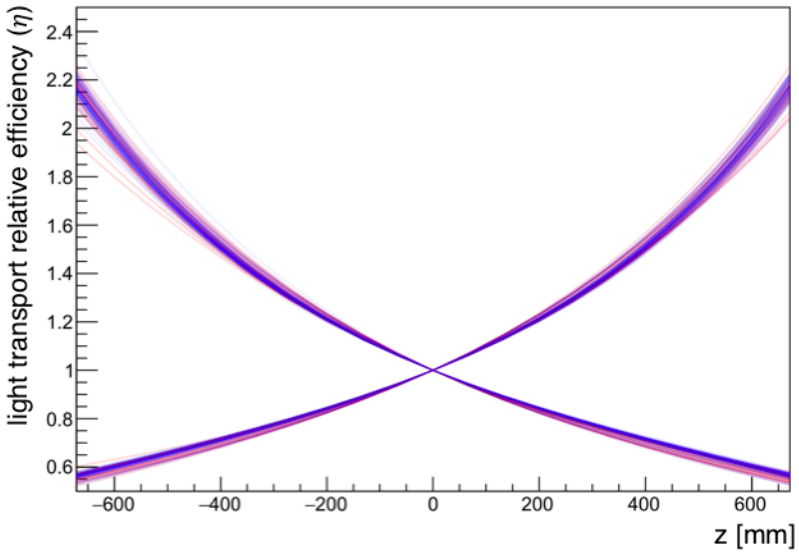

Figure 5.8: Example light curves used to calibrate the relative collection efficiency as a function of z-position along the segment length, with Hamamatsu (blue) and ET PMTs (red). The distributions are normalized such that the center of the segment (z=0) has an η^i=1. From collaboration Ref. [175].

5.2.5 Effective gain stability

The final component of the calibration is to standardize the energy response across the detector over time. This effective gain combines effects from both scintillator output, PMT, and electronics gain. Essentially, the effective gain acts as a scale factor (in units of ADC channel/MeV) that converts the signal (in ADC channels) to energy (MeV) at $z = 0$. Neutron capture events are monitored to provide a reference during

reactor-on and -off data taking periods. The gain factor for each PMT is calculated via:

$$g_0 \equiv \frac{S}{\sqrt{R}E_n}; g_1 \equiv \frac{S\sqrt{R}}{E_n}, \tag{5.8}$$

where E_n is the visible, quenched energy of the neutron capture peak ($\sim$0.55 MeV). The absolute scale is later adjusted by calibration data and will be described in Section 5.4. A smoothed average over multiple data runs is used to determine the gain factor, which is added to the `CalDB`. Once the data is calibrated, the gain stabilization procedure is validated by observing reconstructed neutron capture events, as illustrated in Figure 5.9.

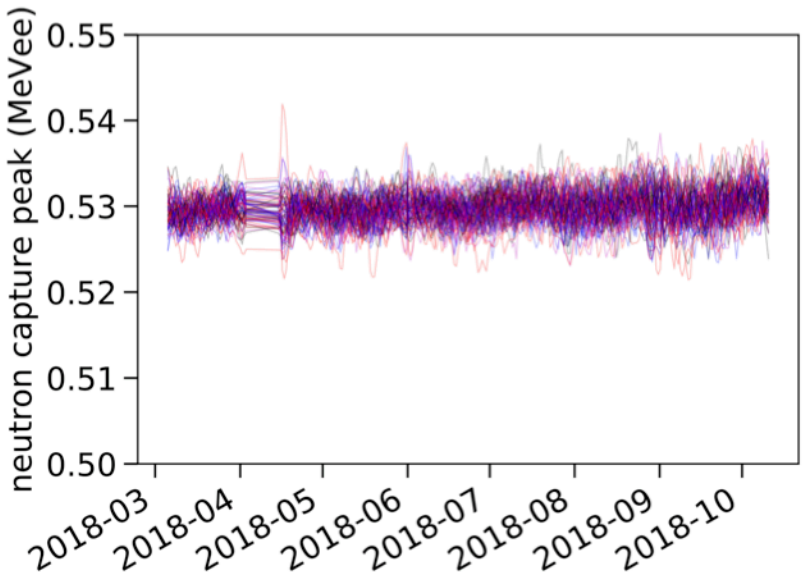

Figure 5.9: Smoothed average of reconstructed neutron capture peak energy after gain stabilization from all segments (with Hamamatsu PMTs) over time. The capture peak energy is stable, indicating the gain calibration is functioning properly. From collaboration Ref. [177].

5.2.6 Reconstructed variables

Calibrations are applied to the `DetPulse` objects to create reconstructed segment events, or `PhysPulse` objects. Simple variables stored in these files include: event number after combining PMT signals, segment number, and event time relative to start of run. Reconstructed variables, using information from the `CalDB`, include: dt, z, PSD, and E_{rec}. The quantity dt is calculated by adding the calibrated PMT offset to the timing differential. The position z is determined through a weighted sum from the ratio R and timing dt based position estimates as summarized in the look-up curves defined above, i.e.

$$z = \frac{z_R(R)/\sigma_R^2(R) + z_t(dt)/\sigma_t^2(dt)}{1/\sigma_R^2(R) + 1/\sigma_t^2(dt)}, \tag{5.9}$$

where $z_R(R)$ is the position mapping found from the specific point in Figure 5.7**(left)** and $z_t(dt)$ in Figure 5.5**(right)**. The errors $\sigma_R(R)$ and $\sigma_t(dt)$ represent the inherent signal and timing resolution combining as an overall uncertainty in position.[3]

The calculations for PSD and E_{rec} are statistically optimized, i.e. the uncertainties are minimized, through a photoelectron-weighted sum of the signals. Since the measured signal is directly converted into units of energy (MeV) by tracking the (n,^{6}Li) capture peak, the nominal resolution (in units of PE/MeV), $R_{E,i}$ at the segment center, and effective gain are required to convert the individual PMT i=0,1 signals to the average detected photoelectrons, N_i:

$$N_i = R_{E,i}\frac{S_i}{g_i}. \tag{5.10}$$

Essentially, N_i is calculated using the R and S look-up curves following the definition of gain in Equation 5.8. $R_{E,i}$ is fixed to 250 PE/MeV for each PMT based on data, but the value is not crucial as it effectively cancels in the reconstruction

[3]It is assumed that the fluctuations in $z_R(R)$ and $z_t(dt)$ are statistically-independent.

calculations. Then, the photoelectron-weighted, position-corrected PSD is expressed as,

$$PSD = \frac{[PSD_0 + \overline{PSD}_e(1 - PSD_0(dt))]N_0 + [PSD_1 + \overline{PSD}_e(1 - PSD_1(dt))]N_1}{N_0 + N_1}, \tag{5.11}$$

where $\overline{PSD}_e$ is the average of the electronic recoil band. Weighting by $\overline{PSD}_e$ allows both the electronic and nuclear recoil bands to be proportionally corrected for position dependence. The single segment, reconstructed energy is calculated via:

$$E_{rec} = \frac{N_0 + N_1}{R_{E,0}\eta_0(z) + R_{E,1}\eta_1(z)}. \tag{5.12}$$

Here, $R_{E,i}$ and $\eta_i(z)$ combine as the PE/MeV conversion factor, visualized in Figure 5.10.

5.3 Clustering: Segment pulses to physics

After the calibration is completed, a window analysis can be performed to identify prompt and delayed coincident events. All pulses are scanned and `PhysPulse` depositions within $dt = 20\,\text{ns}$ of each other are grouped into time-coincident detector-wide clusters. These objects are then time-stamped by the median timestamp of the individual ionizations. Using the reconstructed energy-PSD relation (as an example, see Figure 4.11), the events can be classified as electrons, γ-rays, positrons (electronic recoils), fast neutron recoils (nuclear recoils), or neutron captures on lithium ((n,^{6}Li)). The application of another time window, usually on scales of hundreds of μs, allow for the identification of prompt and delayed coincidences grouped into reconstructed `PhysClusters`. The exact value of the window and the cuts on `PhysPulse` are dependent on the specific physics analysis. Clustering can be performed to identify specific

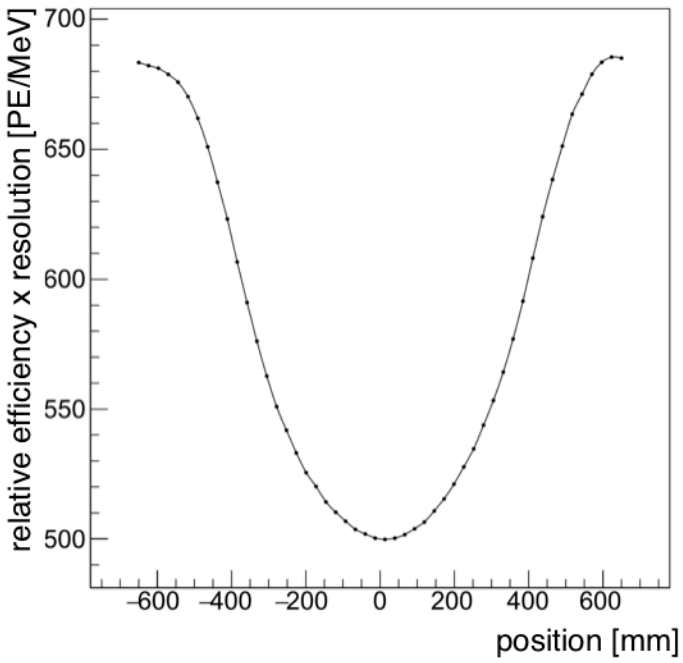

Figure 5.10: Example of PE/MeV conversion from one detector segment, combining the light transport efficiency and resolution. This mapping allows detected photoelectrons to be interpreted as a given reconstructed energy depending on the events position along the z-position of the segment.

types of background or calibration events, as well as IBD candidates. In the case of IBDs, a delayed neutron capture is identified preceding a prompt positron signal with $dt = 119\,\mu$s. These events, when coupled with the reactor status information from the `RunsDB`, are used in the high-level oscillation and spectrum analyses. A more detailed discussion on the clustering and event selection of IBD candidates is presented in analysis Chapters 6 and 7.

5.4 Detector energy response

Before physics analyses proceed with event clustering, the reconstructed energy scale is validated through comparisons of calibration data to `PROSPECT-G4` Monte Carlo. The relative energy scale is determined through measurements of the (n,^{6}Li) capture peak, as described previously. However, the quenched energy of the decay products is

highly dependent on the properties of the scintillator and can only be approximately modelled. Using multiple γ-ray sources and a continuous, high-energy electron spectrum, the absolute scale can be corrected. Furthermore, as the reconstructed energy spectrum is the summation of all energy depositions within a prompt event cluster, both the scale and segment multiplicity[4] are affected by energy losses, resolution, and scintillator nonlinearity. These response mechanisms can change with variations in the scintillator performance and detector geometry (veto size, dead PMT channels). It is necessary to include all of these factors through a data-constrained Monte Carlo and construct a robust IBD response model for specific analysis data sets. Such a model allows for the generation of the detector response matrix, which maps the true $\overline{\nu}_e$ energy to the reconstructed prompt energy and enables the conversion of reactor antineutrino models into PROSPECT detected spectra.

This thesis details two results, the first search for eV-scale sterile neutrino oscillations and the first $\overline{\nu}_e$ spectrum measurement with PROSPECT. The data sets, including calibration source data, used for these analyses are slightly different as they were completed sequentially. The oscillation and spectrum measurements use different parameters to understand the energy scale, but the overall concept and the outcome is quite similar. Below, the improved method used for the spectrum analysis is detailed, with notable differences highlighted. Table 5.2 summarizes the energy response parameters for both analyses. The detector response matrices specific to the oscillation and spectrum analyses are shown in Chapters 6 and 7.

5.4.1 Radioactive calibration samples

Radioactive calibration data from the γ-ray sources listed in Table 3.3, along with the 2.2 MeV γ-ray from ^{252}Cf-induced (n,H) captures, provide spectral lines that can be

[4]The multiplicity in this context refers to the number of segments a given particle interacts with along its track through the detector.

compared to Monte Carlo.[5] For these studies, sources are deployed at the center of the detector to understand the total detector energy response.[6] The data, taken during reactor-off periods, is reconstructed following the scheme outlined previously, where an additional software threshold is imposed to unify the low-energy event selection, which can vary based on event position and scintillator performance. An event-level Gaussian smearing is applied to E_{rec} according to the lowest segment resolution observed from the (n,^{6}Li) capture peak width in order to unify the response across the detector over time. Full detector spectra and Compton scatter spectra in single segments are produced. Background data with no source deployed is subtracted from the measured spectra, while also providing a data set to measure the cosmogenically-induced ^{12}B electron spectrum:

$$n + {}^{12}C \rightarrow p + {}^{12}B \xrightarrow{t_{1/2}=20.20\,ms} e^- + {}^{12}C, \tag{5.13}$$

with endpoint energy of Q=13.37 MeV [178].

(n,H) capture events are selected by tagging 3-15 MeV prompt γ-rays and identifying electronic recoil clusters with a delay of 200μs. This correlated signal is subtracted from accidental coincidences, where the energy cluster registers 200μs before the prompt signal. Approximately 17500 ^{12}B events were selected by requiring prompt, PSD-identified proton recoil depositing 0.7-10 MeV in a single segment to be followed [3,30] ms later by a delayed electron signal with <20 MeV distributed throughout three segments. The prompt and delayed events are required to have a small, 3D separation (xyz) from each other and occur inside the fiducial volume, specified by each analysis. Figure 5.11 shows the time and distance separation distributions measured for the spectrum analysis, fit to a half-life of $t_{1/2}$ = 19.9$\pm$0.4 ms and a σ spread of

[5] ^{252}Cf data was only available for the spectrum measurement analysis, and is therefore absent in the oscillation energy scale study.

[6] Edge effects, i.e. escaping γ-ray energy from the perimeter of the detector, are studied with edge-deployed sources when estimating the systematics.

2.91 cm, respectively. The reconstructed ^{12}B endpoint is Q = 13.36±0.18 MeV.

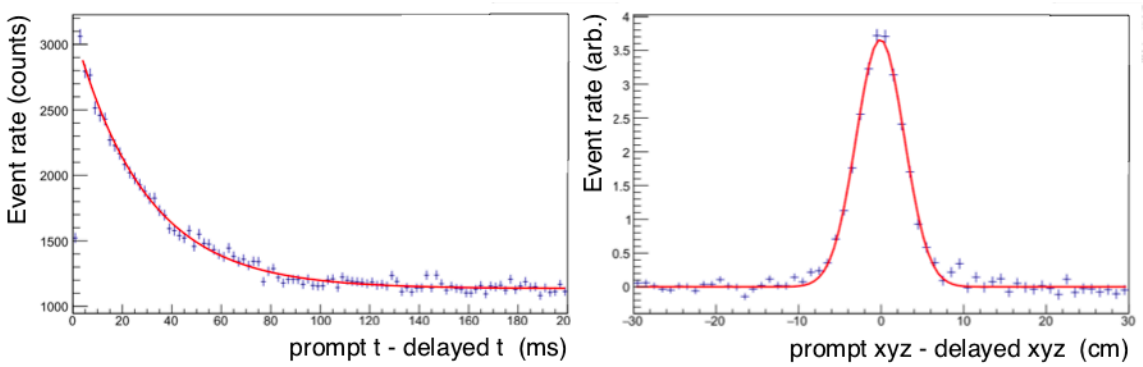

Figure 5.11: Measured ^{12}B event distributions for the spectrum analysis. **(left)** Time separation between prompt proton recoils and the delayed electron, modelled with an exponential. **(right)** Distance separation between prompt proton recoils and the delayed electron, modelled with a Gaussian. From collaboration Ref. [179].

5.4.2 Simulated detector model

The `PROSPECT-G4` package follows a similar analysis pipeline as the PROSPECT data, beginning with simulated waveforms generated from PMT pulse templates and applying a Gaussian smearing to reconstructed energy, PSD, and z-position after the calibration step. A detailed detector geometry, using the optical grid component dimensions obtained during detector construction QC, is implemented to optimize the modelling of energy loss through inactive material. The thickness of the optical separators (1.18±0.05 mm), imposes the greatest impact and uncertainty on loss. Missing energy from particles escaping the detector is handled directly by the underlying GEANT-4 processes.

Scintillator properties, including density and composition, are also included. However, the model does not attempt to detail the microphysics of optical photon transport. Rather, corrections are directly applied to the simulated photoelectrons. The Monte Carlo must be specifically tuned to handle the contributions to the energy response from scintillator nonlinearity, which primarily affects low-energy electronic

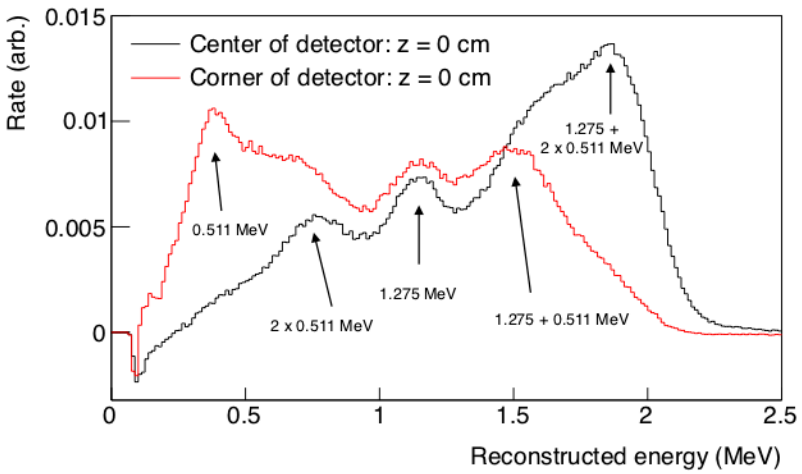

Figure 5.12: ^{22}Na spectrum measured at different locations in the detector (edge vs. the center). The reconstructed energy scale is shifted from the true energy due to the nonlinearity of the scintillator output from multiple Compton scatters of multiple γ-rays [180].

recoils. An example from calibration data of the multiplicative effect of nonlinearity on multi-γ-ray events is shown in Figure 5.12, where the reconstructed energy of the expected peaks are shifted from the true energy. There are two components to this effect, ionization quenching due to the non-radiative recombination of scintillator molecules and Cherenkov radiation absorption by the scintillator with unknown re-emission dynamics. Quenching, or the light output per track length (dL/dx), is modelled in the MC by the generalized Birks' law for organic scintillators [181]:

$$\frac{dL}{dx} = \frac{\frac{dE}{dx}}{1 + k_{B1}\frac{dE}{dx} + k_{B2}\left(\frac{dE}{dx}\right)^2}, \tag{5.14}$$

where dE/dx is the ionization stopping power of the particle, and k_{B1}, k_{B2} are the Birks' constants[7] responsible for shifting the reconstructed energy and segment multiplicity. Cherenkov processes can add light to a given event as the spectrum generally peaks in the UV-blue range, which can be absorbed and re-emitted by the scintillator.

[7]The Birks' constants are not comparable between different experiments, as they are dependent on the energy difference between simulated photoelectron steps.

The number of Cherenkov photons (N) is simulated by assuming uniform generation in the 200-700 nm wavelength band (λ)[8],

$$\frac{d^2N}{dxd\lambda} = \frac{2\pi\alpha z^2}{\lambda}\left(1 - \frac{1}{\beta^2 n^2(\lambda)}\right), \tag{5.15}$$

where α is the fine structure constant, z is the particle charge, β is the particle speed, and $n(\lambda)$ is the wavelength-dependent index of refraction of the scintillator. However, the dynamics of the scintillation absorption and emission is not well understood. Therefore the Cherenkov contribution is accounted for through a correction to the reconstructed energy,[9]

$$E_C = k_C \sum_{\lambda} N_\lambda E_\lambda, \tag{5.16}$$

where k_C is a detection efficiency proxy for the scintillator absorption-emission process, and $N_\lambda E_\lambda$ the summed energy of the Cherenkov photons for a given λ.

5.4.3 χ^2 minimization of simultaneous response fit

To constrain the energy response model, the energy spectra and multiplicity (for γ-ray sources only) from the calibration data and `PROSPECT-G4` Monte Carlo are simultaneously compared with a summed χ^2. One thousand Monte Carlo samples are generated based on ranges of floating parameters k_{B1}, k_{B2}, and k_C, and an additional

[8]This is an unrealistic assumption, as the emission of a photon with wavelength λ is inherently related to the index of refraction $n(\lambda)$, and thus the threshold for will vary (especially between 200-300 nm) [182]. However, at this stage only a simple model could be implemented, and is reflected in the large systematic error.

[9]Several approximations are made, and it is understood this model is not perfect. The rate of photons, transmission, and detection efficiency are assumed to be constant for all wavelengths.

energy shift factor, β_{rec}[10] to minimize the χ^2,

$$\chi^2 = \chi^2_{k_{B1}} + \chi^2_{k_{B2}} + \chi^2_{k_C} + \chi^2_{\beta_{rec}}. \tag{5.17}$$

Fits are performed around the 3σ region of each γ-ray feature and the 3-13.5 MeV region of the electron spectrum. Figure 5.13 shows the good agreement between the data and Monte Carlo used for the spectrum analysis. Additional figures are shown in the respective results chapters. The best-fit parameters for the oscillation and spectrum analyses are listed in Table 5.2. Errors are dominated by the model systematic uncertainties, and are later input into the covariance matrices representing the total measurement uncertainty for each analysis. Using the obtained best-fit parameters, the Monte Carlo is regenerated and compared to single-segment data, by summing energy deposits in individual segments.[11] This procedure validates that the Monte Carlo is capable of reproducing the data on both the segment- and detector-level scales. If large deviations are observed, a new detector fit will be performed. In most cases, the software threshold must be increased to satisfy variations in the low-energy spectra or segment multiplicity.

In the case where the best-fit β_{rec} shows an absolute energy shift, the calibration of `DetPulse` to `PhysPulse` is reprocessed accordingly. Tracking the (n,^{6}Li) capture peak allows for good determination of the relative energy scale across all segments over time, but assumes that this quenched featured occurs at 0.55 MeV. The calibration-Monte Carlo comparison helps to correct any systematic bias in the absolute energy scale introduced during the data calibration.

[10] In the oscillation analysis, only one Birks' constant, k_{B1}, was considered and the photostatistics component of the energy resolution was added to the fit. In the spectrum analysis, the resolution is determined after the best-fit parameters are established.

[11] The oscillation analysis uses the best-fit parameters from single segment fits to determine the total detector energy scale.

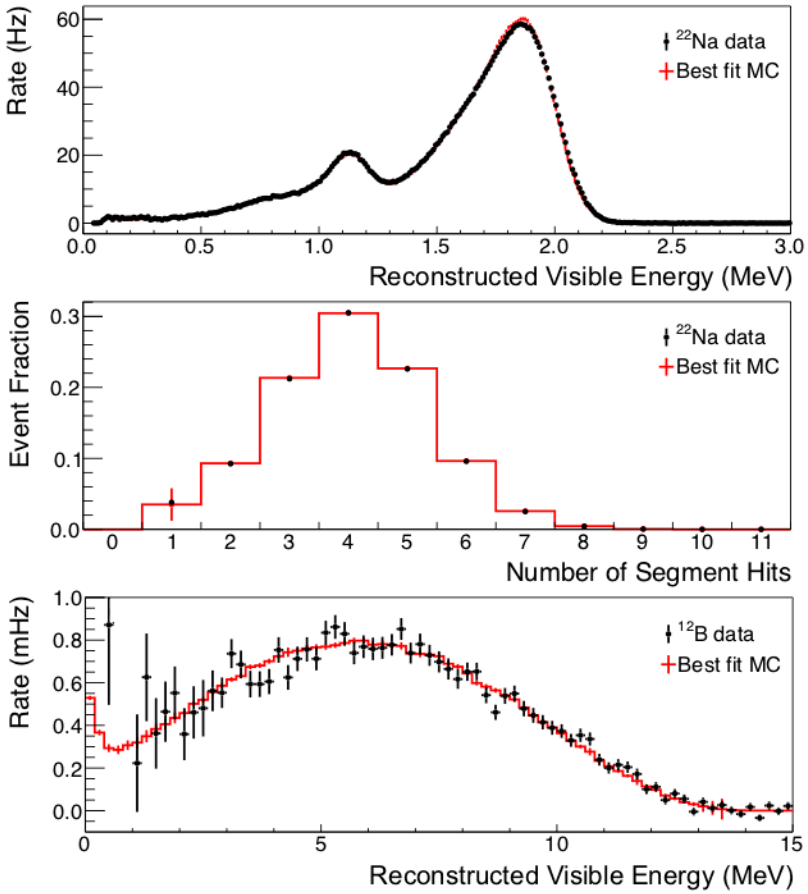

Figure 5.13: Comparisons of full detector reconstructions between data (black) to the best-fit Monte Carlo (red). **(top)** ^{22}Na energy spectrum. **(middle)** ^{22}Na segment multiplicity. **(bottom)** ^{12}B energy spectrum. From collaboration Ref. [183].

5.4.4 Energy resolution fit

The regenerated Monte Carlo is used to measure the resolution of the reconstructed energy, at the time of the γ-ray calibrations, by relaxing the uniform segment resolution smearing imposed on the reconstructed data. Each simulation is smeared according to a Gaussian distribution and compared to data until the χ^2 is minimized. The resulting data points, for the spectrum analysis, can be seen in Figure 5.14. A fit is performed according to,

$$\frac{\sigma}{E_{rec}} = \sqrt{a^2 + \frac{b^2}{E_{rec}} + \frac{c^2}{E_{rec}^2}}, \tag{5.18}$$

Parameter	Oscillation analysis	Spectrum analysis
Input		
Software threshold	–	85±5 keV
Resolution smearing	–	400±8 PE/MeV (5% at 1 MeV)
Best-fit parameters		
k_{B1}	0.100±0.0008 mm/MeV	0.122±0.0002 mm/MeV
k_{B2}	–	0.032±0.0002 mm/MeV
k_C	51±2%	41±4%
β_{rec}	99.93±0.4%	100.36±0.6%
b	4.45±0.04%	–
Energy resolution		
$\sigma/\sqrt{E_{rec}(\text{MeV})}$	4.5%	4.8%

Table 5.2: Input and best-fit parameters from energy response studies used in the oscillation and spectrum analyses. The oscillation analysis uses single segment simultaneous fits to determine the parameters, while the spectrum analysis fits total detector spectra. The parameter k_C is expressed as the Cherenkov light collection efficiency, and the error was conservatively inflated from the fit uncertainty, as the model is oversimplified. See Equation 5.18 for a description of the best-fit energy resolution model. From collaboration Ref. [179, 184].

where the parameters a, b, c alter the light collection through geometric effects, photostatistics, and PMT quantum efficiency, respectively. Dominated by the photostatistics term, the best-fit resolution for the spectrum analysis is 4.8% at 1 MeV, as indicated in Table 5.2.

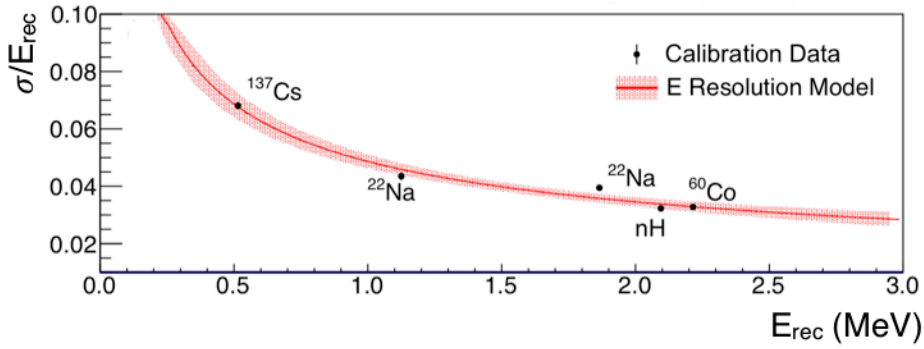

Figure 5.14: Energy resolution of the full detector based on different calibration sources (circles) fit to function (red) in Equation 5.18. The red band represents the uncertainty of the energy resolution model. From collaboration Ref. [179].

5.4.5 Effect of dead channels

During the data collection periods considered in this thesis, a number of the PMT channels displayed instabilities and are no longer in operation. The data suggests that ^{6}LiLS has penetrated into the optical modules, interacting with the voltage divider electronics, causing erratic behavior in the PMTs. Figure 5.15 illustrates such "ingress" events that originate in the ^{6}LiLS within an optical module, escape out of the front window, and later detected by the opposite PMT. Due to the longer transit time with multiple photons, the tail of the waveform is extended and the event is registered with PSD above the nuclear recoil band. Studies have shown that there is correlation between the rate of ingress events and PMT behavior, although the details of the failure is not fully understood.

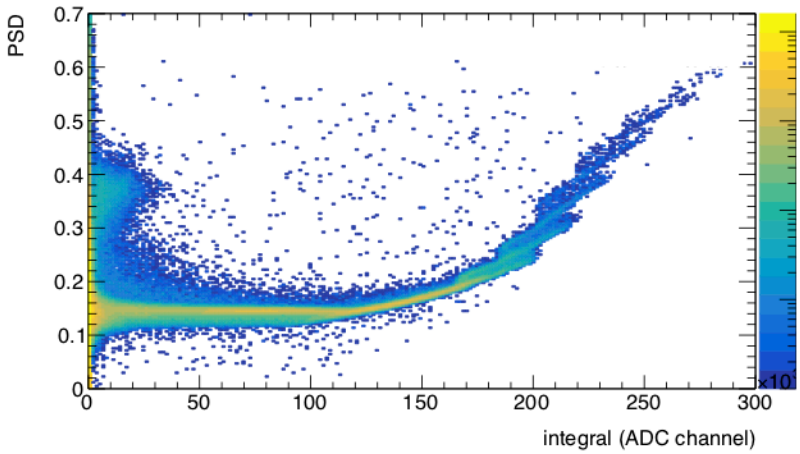

Figure 5.15: PSD as a function of DetPulse integral from one PMT in a particular segment in the AD during reactor-off operation. Ingress events, from ^{6}LiLS leaking in the PMT optical module, are observed above the nuclear recoil band, with $PSD > 3$. From collaboration Ref. [185].

In both the oscillation and spectrum analyses, only segments with both PMTs working were used. This lowers the relative IBD detection efficiency of segments neighboring the dead channels, as this reduces the acceptance of neutron captures that may register outside of the primary interaction segment. Furthermore, this in-

creases the amount of inactive material in the fiducial volume, increasing missing energy from γ-rays and consequently affecting the response. The simulation scheme described above accounts for this by turning off the appropriate channels in the detector geometry for a given calibration period. With no strong position-dependence to the failure, ehe fraction of dead volume is described for each analysis in Chapters 6 and 7.

5.5 Detector performance

Once the energy scale is confirmed, the performance and stability of other reconstructed variables are measured to ensure the uniformity of the `PhysPulse` calibration. It is crucial to demonstrate the PSD capability of the full PROSPECT AD, as it is expected to be one of the most powerful tools for background rejection. Figure 5.16 illustrates the excellent PSD performance in both single segments and when combining events throughout the entire detector. As described above, the data is calibrated such that reconstructed electronic and nuclear recoil PSD bands are stable across data sets and throughout the detector.

Intrinsic and deployed radioactive sources are used to demonstrate the stability of the reconstructed energy, position resolution, and detection rates. The (n,H) capture and ^{137}Cs γ-ray events are selected by the scheme described above. RnPo double-α events from the ^{227}Ac decay chain (see Equation 3.2) are selected by identifying the PSD-selected delayed ^{215}Po α, with separations of $<$200 mm and $<$13 ms away from the prompt ^{219}Rn α, in the appropriate quenched energy windows according to Equation 3.2. Accidental backgrounds are subtracted with measurements from an off-time window that is 10 lifetimes away from the candidate ^{215}Po event [186]. Similarly,

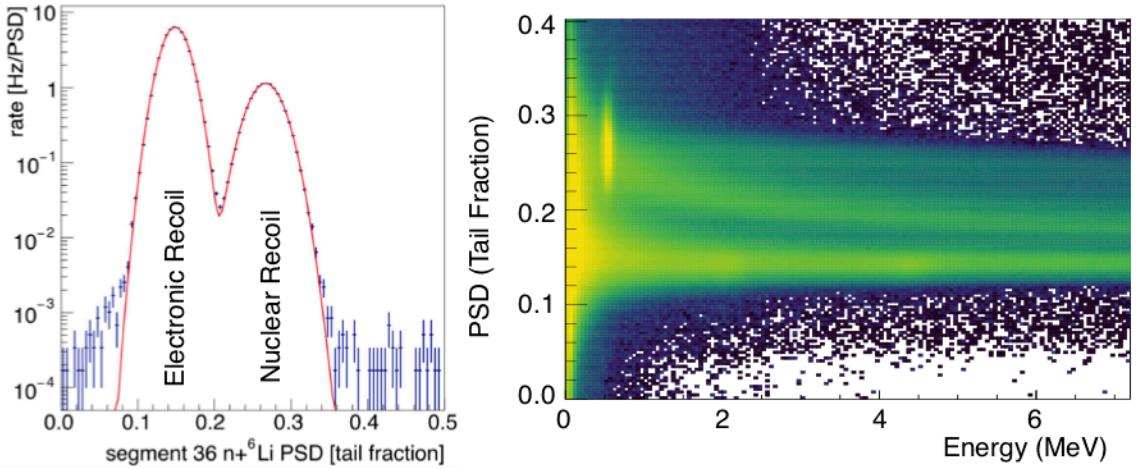

Figure 5.16: Demonstration of PSD performance, from a selection of prompt energy depositions correlated with a subsequent (n,^{6}Li) capture. **(left)** PSD distribution in a single segment on a semi-log plot. A clear separation between electronic and nuclear recoils is observed. **(right)** Full detector PSD as a function of reconstructed energy. The (n,^{6}Li) peak is easily distinguished from the other nuclear recoil events. The split in the high PSD band around 0.25 is most likely due to the ability to separate proton recoils from heavier charged particle recoils (e.g. carbon) [108].

accidental-subtracted, time-correlated "BiPo" events from the ^{238}U chain,[12]

$$^{214}Bi \xrightarrow{t_{1/2}=19.9\,m} \beta^- + ^{214}Po \xrightarrow{t_{1/2}=0.164\,ms} \alpha + ^{210}Po \tag{5.19}$$

are measured. Similar to the event structure of IBDs, the β has a Q-value of 3.275 MeV with associated γ-rays up to 2.7 MeV, while the α has an energy of 7.687 MeV, which is quenched to ∼0.84 MeV in PROSPECT [187]. These events are selected by identifying a delayed α with nuclear recoil PSD 1.14 ms away from a prompt electron-γ cluster, and do not contaminate the IBD sample.

Figures 5.17 and 5.18 illustrate these event selections and the associated reconstructed variable. The reconstructed energies and resolutions are stable to within ∼1% across all segments and data sets. A position resolution of 5 cm is measured, which is three times smaller than the size of the segment cross-sections, and stable

[12]PROPSECT is not completely gas-tight, therefore leakage of ^{222}Rn gas from the ^{238}U chain enables the uniform decay rate in the detector.

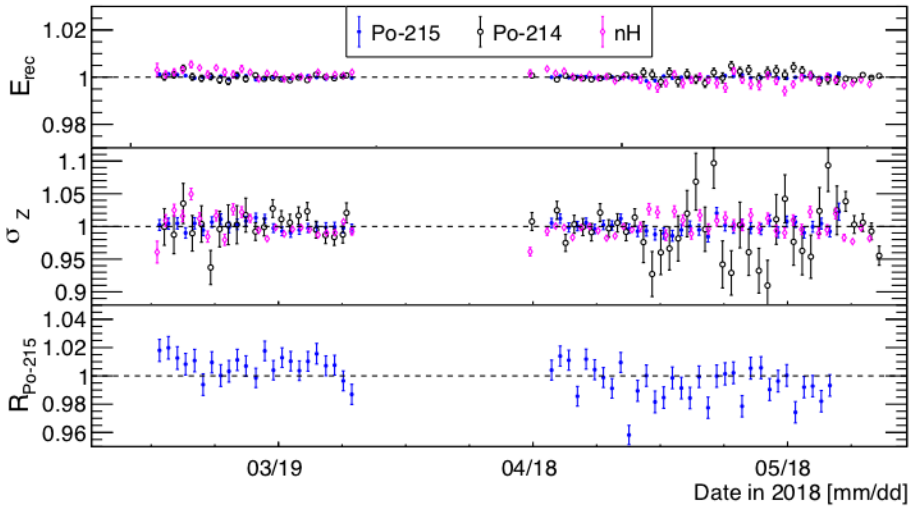

Figure 5.17: Detector time stability of the reconstructed energy (E_{rec}), z-position resolution (σ_z), and detection rate (R) measured for the oscillation analysis dataset. Quantities are calculated from ^{214}Po (black) and ^{215}Po (blue) α decays and (n,H) captures (magneta) uniformly distributed throughout the detector. All quantities are shown relative to the average of all points in the dataset. All error bars represent statistical uncertainties [188].

within 10%. The RnPo detection rate is uniform within ∼2%, which is consistent with the expected ∼0.7% variation from the ^{227}Ac half-life over this time period.[13] Overall, the reconstruction is extremely stable for both the calibrated oscillation and spectrum data sets.

[13]Later analysis showed the ^{227}Ac decay rate is ∼1.6% faster than expected and is observed systematically in all segments [189]. The cause of this is currently being investigated.

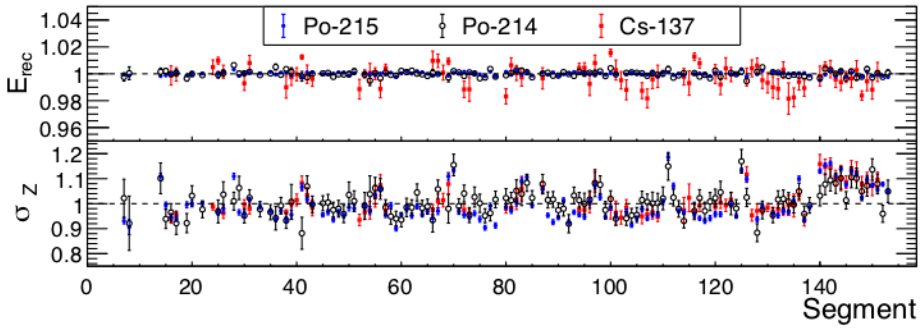

Figure 5.18: Segment-to-segment uniformity of the reconstructed energy (E_{rec}) and z-position resolution (σ_z) measured for the oscillation analysis dataset. Quantities are calculated from ^{214}Po (black) and ^{215}Po (blue) α decays uniformly distributed throughout the detector and deployed ^{137}Cs sources (red). All quantities are shown relative to the average of all points in the dataset and error bars represent statistical uncertainties [188]. The larger values of σ_z are due to segments instrumented with ET PMTs.

Chapter 6

First search for eV-scale sterile neutrinos with PROSPECT

PROSPECT's first experimental goal is to perform a model-independent search for eV-scale sterile neutrino oscillations through $\overline{\nu}_e$ disappearance from the HFIR ^{235}U reactor. The $\overline{\nu}_e$ spectrum is measured at baselines from 6.7 to 9.2 m throughout the segmented detector in Position 1, resulting in a relatively high total detection rate, if no oscillations, of 771 IBD events per day. The IBD event selection was optimized to increase the statistical power of the signal, by optimizing the effective relative uncertainty of the reactor-on measurements and subtracted reactor-off backgrounds. A correlated signal-to-background ratio of 1.3 is achieved, with a 5σ detection rate of neutrinos in <2 hours. With 33 operational days of reactor-on and 28 operational days of reactor-off data, a search for sterile neutrino oscillations is conducted using the Feldman-Cousins [190] prescription for determining confidence intervals. No sterile neutrino oscillations are observed within the PROSPECT sensitive parameter space and the Reactor Antineutrino Anomaly best-fit hypothesis (see Chapter 2) is excluded at a level of 2.2σ.

6.1 Oscillation search strategy

To conclusively claim a discovery a sterile neutrino, it is necessary to directly measure the oscillation pattern over a range of baselines rather than inferring its existence through an indirect, flux deficit measurement. Furthermore, due to the complexities involved in predicting the reactor $\overline{\nu}_e$ spectra, it is crucial to conduct statistical hypothesis tests that are independent of input models. PROSPECT achieves this by comparing measured prompt energy spectra at different baselines, referred to as L vs. E spectra, to predicted L vs. E spectra. The various baselines are defined by the distance between the center-position of each segment in the detector relative to the center of the reactor core, as shown in Figure 6.1.

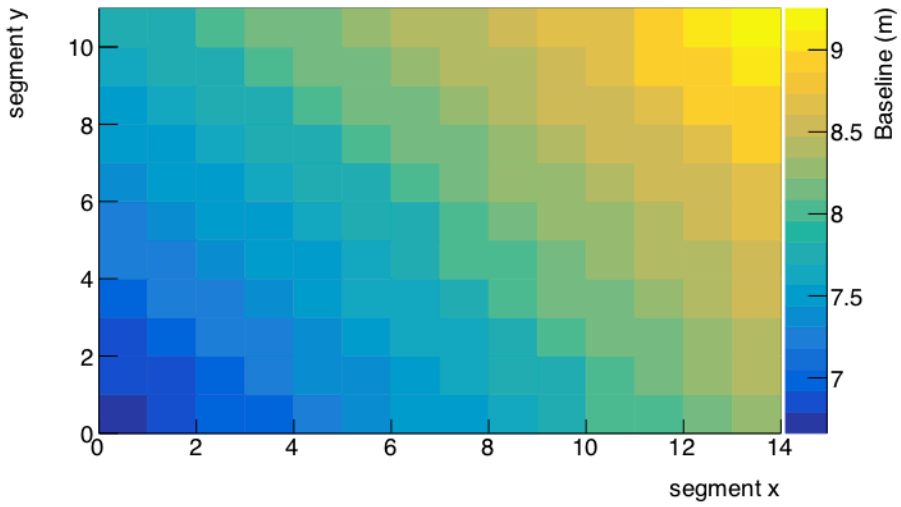

Figure 6.1: Distribution of segments representing degenerate baselines in meters from segment center to the reactor core center.

Comparisons of the relative spectra are pursued with a covariance matrix-based χ^2 test statistic:

$$\chi^2 = \Delta^T V_{tot}^{-1} \Delta, \tag{6.1}$$

where V_{tot}^{-1} is the inverse of the covariance matrix constructed from the statistical and systematic uncertainties. Δ is a 96-element vector summarizing the relative agreement between the observed ($O_{l,e}$) and predicted ($E_{l,e}$) L vs. E spectra in the lth baseline bin and eth energy bin, respectively:

$$\Delta_{l,e} = O_{l,e} - O_e \frac{E_{l,e}}{E_e}, \tag{6.2}$$

with observed and predicted total detector spectra normalizations,

$$O_e = \sum_{l=1}^{L} O_{l,e}, E_e = \sum_{l=1}^{L} E_{l,e}, \tag{6.3}$$

where $L = 6$. Illustrated in Figure 6.2, the predicted L vs. E spectra, $E_{l,e}$, is modelled with oscillations according to Equation 1.27,

$$E_{l,e}(\Delta m^2_{41}, \theta_{14}) = E_{l,e}(0,0) \left(1 - \sin^2 2\theta_{14} \sin^2(1.27\Delta^2_{41}\frac{L}{E})\right), \tag{6.4}$$

where θ_{14} and Δm^2_{41} describe the mixing between the first active neutrino flavor state and one additional sterile state in the 2-neutrino approximation. The search proceeds by minimizing the χ^2, as defined in Equation 6.1, by varying the sterile neutrino oscillation parameters. The choice of $\Delta_{l,e}$ definition used to calculate the χ^2 has been shown to alleviate the dependence of the fit results on input reactor $\overline{\nu}_e$ models.

6.2 Data set and processing

Data for this analysis was collected after detector commissioning in March 2018 to July 2018, with calibrations using the `Analyzed_NuFact_v1` processing configurations. A total of 33.01 operational days of reactor-on data was recorded over two reactor cycles. Reactor-off backgrounds were measured after each cycle totaling

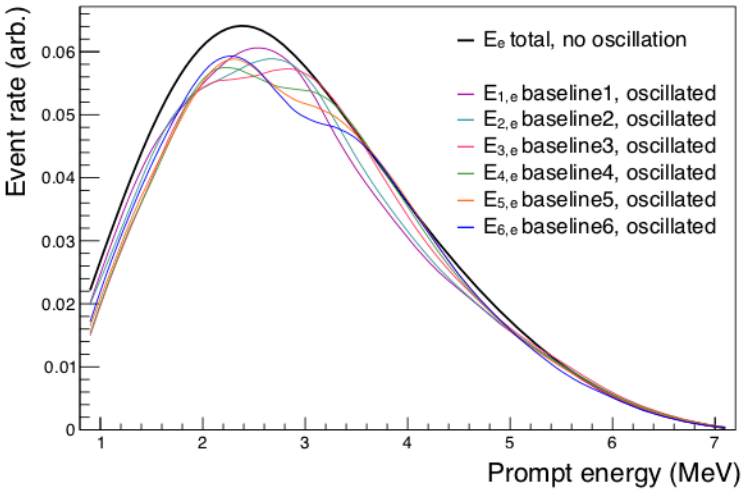

Figure 6.2: Illustration of the predicted spectra used in Equation 6.2. The black spectrum represents the predicted total detected prompt energy summed over all baselines assuming no oscillations, E_e. This spectrum is then used to normalize the predicted L vs. E spectra (colored) at different baselines including the sterile neutrino oscillations. This allows the search to be independent of input reactor $\overline{\nu}_e$ models.

27.95 operational days of data. Accounting for trigger pile-up (average 2% reactor-on, 1% -off) and shower veto (average 6% reactor-on, 5% -off) deadtimes, the collection times are reduced to 30.26 and 26.19 exposure days for reactor-on and -off statuses, respectively. The variation in shower veto deadtimes between reactor-on and -off periods is due to the higher rate of high-PSD PMT ingress events from accidentals, which are vetoed as fast neutron showers. Although these events would be reconstructed outside of the segments, there is no z-position fiducial cut on the shower vetos, since the goal is to eliminate background processes throughout the entire detector. Each run containing approximately one hour of data was manually sorted into reactor-on and reactor-off files by on-shift collaborators responsible for monitoring the DAQ operations. After the full data set was collected and processed, runs occurring during reactor status transitions, i.e. when the power is ramping up or down for a given cycle, are examined in the slow control database to ensure they have been categorized appropriately using the correlated trigger rate as an indicator of reactor status.

The data is processed according to the chain outlined in Chapter 5. A uniform calibration is performed across the entire data set, accounting for variations between segments and over time. `PhysPulse` objects are then input into the `P2kIBDPlugin` program and are reconstructed into `IBDClusters` through a cut-based analysis. Details of the event selection are described in Section 6.3. For each prompt positron, neutron capture pair, an `IBDCluster` object is created containing reconstructed variables for the prompt event which will be used in subsequent analysis, including: event number, sum of reconstructed visible energy (E_{prompt}), reconstructed energy of the maximum deposition (E_{max}), segment number with the reconstructed IBD vertex (identified by E_{max}), and the xyz-position of maximum deposition. Characteristics of the tagged (n,^{6}Li) capture event are also stored for auxiliary analysis.

Segments where one or both PMTs failed are excluded from this analysis, some of which are in the fiducial region: segment number (0, 1, 2, 3, 4, 5, 6, 9, 10, 11, 12, 13, 18, 21, 23, 24, 27, 32, 34, 40, 44, 52, 68, 79, 86, 102, 115, 122, 127, 130, 139). Figure 6.3 shows the loss of ^{6}LiLS volume due to dead segments, an 18% reduction of the nominal fiducial region. IBD event candidates that originate in the inactive segments with prompt γ-rays and a delayed neutron that are identified in the active volume can be reconstructed around 0.5 MeV if only one annihilation γ-ray is detected. Such events have a noticeable impact on the detector response, but are excluded from the analysis as they are outside of the pre-determined region of interest from 0.8-7.2 MeV. Interactions that occur within dead material where both 511 keV γ-rays are detected can leak into the IBD sample.

6.3 IBD event selection

PROSPECT selects IBD-like candidates with analysis cuts optimized to identify prompt positron signals correlated in time and position with a tagged, delayed (n,^{6}Li)

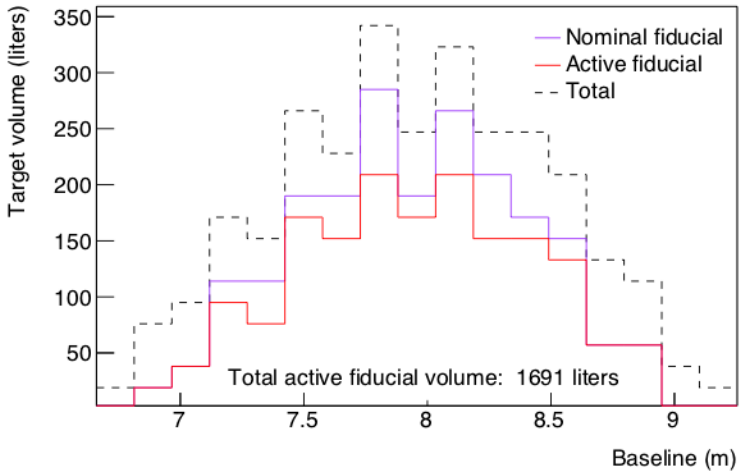

Figure 6.3: Distribution of ^{6}LiLS volume versus baseline. The total volume (dashed black), nominal fiducial volume (purple), and active fiducial volume for the oscillation analysis (red) are shown. The exclusion of dead segments results in a 18% reduction from the nominal fiducial volume. This assumes an active volume of 19 L per segment, including the z-position fiducial cut.

capture from reactor-on and reactor-off data. Accidental candidates are selected following the same criteria, except the sample is acquired from a long, off-time window to accumulate statistics and is scaled appropriately. Table 6.1 summarizes the cuts used in the sterile neutrino oscillation analysis. A description of each cut is detailed below, where each level includes the restrictions from those preceding it. The selection criteria was defined and frozen using 3 days of unblinded reactor-on data and the full reactor-off set to confirm the stability of the cuts; remaining data was blinded by removing events with energies within the region of interest. Constraints on the spatial extend of the prompt event, energy scattered outside of the maximum-energy segment (i.e. from the 2, 511 keV γ-rays), or time between the first and last pulse in the prompt cluster were shown to have little impact on the overall selection efficiency. Events with E_{prompt} between [0.8,7.2] MeV proceed to the oscillation search.

6.3.1 Cut 1: Delayed neutron capture tag

The neutron capture tag cut is designed to identify an isolated (n,^{6}Li) event. The cluster is required to have summed E_{rec} between 0.48 and 0.60 MeV. Clusters containing a pulse $>3.6\sigma$ above the mean of the electronic recoil band ($\overline{PSD}_e$) are rejected.

6.3.2 Cut 2: Prompt PSD

Prompt clusters with any pulse $>3.0\sigma$ above the mean of the electronic recoil band ($\overline{PSD}_e$) are rejected. This cut rejects fast neutron-induced proton recoils proceeding the thermalization and capture of the neutron.

6.3.3 Cut 3: Trigger pile-up

New events arriving at the end of the data acquisition do not re-trigger the DAQ and their waveforms will be truncated. This cut imposes a software veto on pile-up clusters, rejecting clusters with $dt < 800$ ns from the proceeding cluster. Applied to both the prompt and delayed events, a 2% (1%) reactor-on (-off) deadtime is introduced.

6.3.4 Cut 4: Prompt-delay time coincidence

Correlated prompt and delay events are accepted and paired if they coincide within dt = [1,120] μs of each other. This cut is designed to balance the number IBD-like pairs accepted with neutron captures in the tail of the time distribution (mean capture time τ ~40 ns), without acquiring additional accidentals which have a constant rate in this time window.

To measure accidental prompt and delayed events, this cut is adjusted to accept clusters with a dt = [-12,-2] ms. This provides a high-statistics sample of the coincident accidental backgrounds using an off-time window, which is scaled and used

in subsequent correlated-accidental IBD-like subtractions. Due to the statistics, this only introduces a small uncertainty into the subtraction.

6.3.5 Cut 5: Neutron shower veto

The neutron shower veto cuts reject cosmic ray shower events, relative to delayed neutron captures. Muons, identified by a summed $E_{rec} \geq$15 MeV, can initiate neutron spallation on the surrounding lead producing multiple neutrons. Events within a muon-neutron capture separation of dt = [0,100] μs are rejected. Due to the several hundred Hz total muon rate, the time scale of this cut must remain reasonably short, as it introduces a significant deadtime: average 6% (5%) reactor-on (-off). Showers from fast neutron primaries are rejected if a (n, ^{6}Li) capture or recoil ($3\sigma > \overline{PSD}_e$, $E_{rec} > 0.25$ MeV) occurs in a window of dt = [-200,200] μs of the (n,^{6}Li) candidate. The total deadtime is less sensitive to the size of neutron veto window, since these events are less prevalent.

6.3.6 Cut 6: Prompt-delayed distance

The total IBD interaction and decay products is highly localized in space when using ^{6}Li as a capture agent. Prompt and delay events are accepted if the total Δxyz-separation ($\Delta xyz = \sqrt{dx^2 + dy^2 + dz^2}$) of 180 mm if identified in the same segment and 140 mm if registered in directly adjacent segments. Accidental backgrounds are strongly suppressed through this topological cut, as shown in Figure 6.4

6.3.7 Cut 7: Fiducialization

A 3D fiducialization cut is used to reduce the IBD-like background rate around the outer edge of the detector from cosmogenic particles penetrating the passive shield. The sides and top of the detector are affected by these events, however products

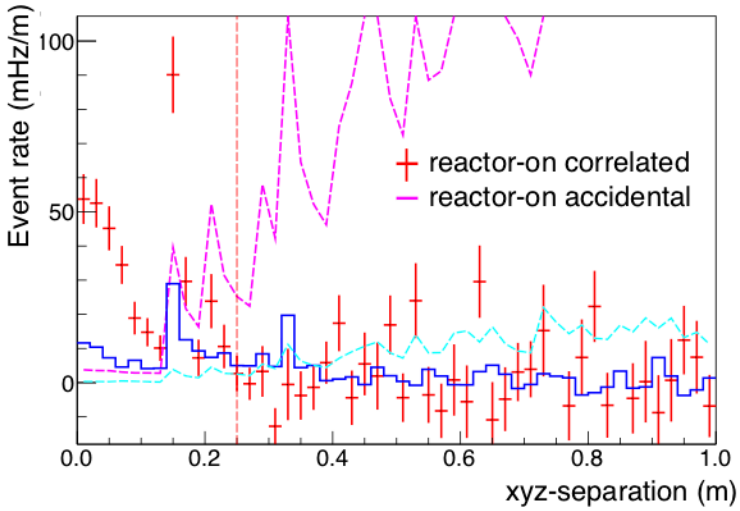

Figure 6.4: Example of the effect on the IBD-like rate from the prompt-delayed distance cut on PROSPECT-G4 simulation. The red data points represent the reactor-on correlated (accidental subtracted) event rate. The magenta line shows reactor-on accidental events, where the jagged nature is due to the x-y component of Δxyz being quantized by segment.The cut preserves the IBD candidate signal while strongly suppressing accidentals, as it is unlikely for random events to occur in the same segment. The blue lines refer to simulated reactor-off correlated (blue) and accidental (cyan) spectra. From collaboration Ref. [191].

from the beam lines underneath the floor are problematic for the bottom of the detector. Thus, IBD candidates with either prompt (identified by the maximum energy segment) or delayed events in the outermost layer of segments (xy-position), or with a reconstructed z-position outside [-448, 448] mm (one segment width) of either segment end are rejected. Deposited energy from the prompt annihilation γ-rays in the cut region is considered, as long as the event vertex is within the fiducial volume.

Additionally, at the start of data taking, a high accidental correlated (and singles) rate was observed on the south side of the detector opposite the reactor. This section of the detector is not shielded by the monolith concrete under the floor resulting in a larger flux of γ-rays from the beam line products underneath the concrete floor. Segment numbers (23,24,25,26) are excluded from the analysis to manage the accidentals

rate.

6.4 Measured backgrounds and subtraction

6.4.1 IBD-like event distributions

As described previously, time-correlated cosmogenic neutron events and accidental coincidences of reactor-related γ-rays with (n,^{6}Li) captures are the primary backgrounds to the PROSPECT IBD signal. Reactor-on measurements contain the $\overline{\nu}_e$ signal, along with cosmogenic and reactor-related correlated and accidental events; reactor-off measurements include only the cosmogenic correlated and accidental background. The IBD event selection is applied to reactor-on and -off measurements, providing the IBD-like sample in both data sets. Figure 6.5 shows the measured IBD-like correlated and accidental rates for the oscillation data set. The accidental rate is scaled to match the statistics of the correlated sample, as noted in Section 6.3.4, and is subtracted from the raw correlated+accidental measurement. The clear decrease in IBD candidate events with time demonstrates PROSPECT's ability to observe changes in the reactor status through measurements of the $\overline{\nu}_e$ flux. Furthermore, the uniformity of the rate illustrates the stability of the IBD event selection.

The reactor-on and -off events are expected to vary with their detected position throughout detector. Figure 6.6 illustrates these correlated and accidental distributions as a function of segment number. Correlated events are more prominent near the edge of the detector, where cosmogenic products have the greatest effect in both the reactor-on and off scenerios. A hot spot in the reactor-on accidental rate is observed towards the lower corner of the detector, opposite the reactor location. This portion of the detector has the least shield coverage, as it does not rest on the concrete floor monolith and there is a break in the passive shield due to the fork lift channels. To support neutron scattering experiments, a beam line runs underneath the floor and

Cut level: type	Acceptance value(s)
1: delayed (n,^{6}Li) capture	$3.6\sigma > \overline{PSD}_e$, E_{rec} = [0.48,0.60] MeV
2: prompt PSD	$3\sigma < \overline{PSD}_e$
3: trigger pile-up	dt = [-800,800] ns
4: prompt-delayed time coincidence	dt = [1,120] μs
5: neutron shower veto muon-induced fast neutron-induced	delay (n,^{6}Li) tag prompt muon ($E_{prompt} > 15$), dt = [0,100] μs prompt recoil ($3\sigma > \overline{PSD}_e$, E_{rec} >0.25 MeV) or (n,^{6}Li), dt = [-200,200] μs
6: prompt-delayed distance coincidence	Δxyz = [180, 140] mm
7: fiducialization	z: include [-448, 448] mm x, y: exclude outer shell x, y: exclude segments (23,24,25,26)

Table 6.1: Summary of IBD event selection cuts used in the oscillation search analysis. The neutron shower veto is used to reject candidate IBDs within a given time window of muon or fast-neutron induced events, tagged by a delayed (n,^{6}Li) capture. The Δxyz cut corresponds to the 3D distance separation in the same (same, adjacent) segments. Accidental IBD-like candidates are selected using the same criteria, with the exception that the prompt-delay time coincidence is taken from the off-time window dt = [-12,-2] μs.

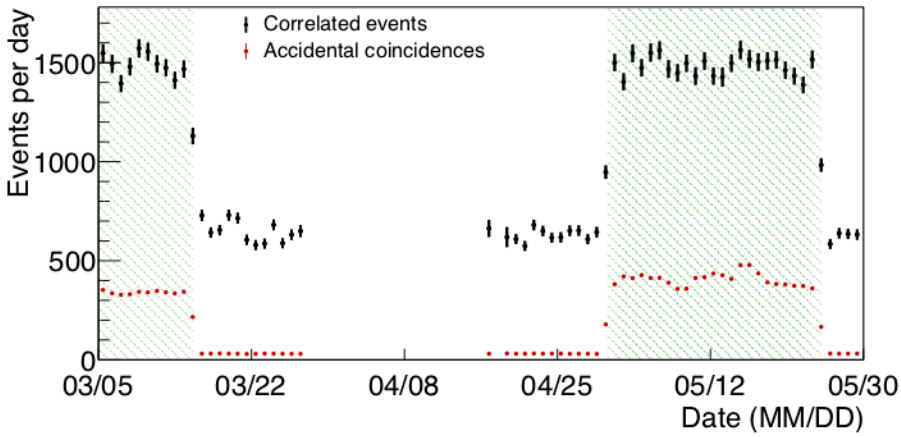

Figure 6.5: Accidentals-subtracted daily IBD-like candidates (black) and calculated accidental coincidences (red) as a function of time. The IBD candidate event rates are corrected for time-dependent variations in detector veto and exposure time. Shaded regions (green) correspond to reactor-on periods. The gap in reactor-off data points corresponded to a planned period of detector maintenance and calibration [188].

neutrons that capture on surrounding material, creating the large measured γ-ray flux. The number of reactor-off accidentals is substantially lower than the reactor-on measurement, which is expected as the number of ambient γ-rays significantly decreases.

Energy spectra are created by binning IBD candidates into 200 keV-wide energy bins, as seen in Figure 6.7. Prominent features near ~2.2 MeV and ~4.9 MeV are mirrored in the reactor-on and -off correlated spectra, due to cosmogenic events that are difficult to mitigate. The 2.2 MeV peak is the result of muon- and fast neutron-induced spallation on detector material. Multiple thermal neutrons are emitted in these showers and can undergo a prompt (n,H) capture, producing the 2.22 MeV γ-ray, and delayed (n,^{6}Li). The shower veto helps to eliminate these event types, but is not 100% efficient.

Cosmogenic fast neutrons can also inelastically scatter via $^{12}\mathrm{C}(n, n'\gamma)^{12}\mathrm{C}$, referred to as (n,C*) in the remaining text, in the detector volume and produce a prompt 4.43 MeV γ-ray and delayed (n,^{6}Li). Pulses from the inelastic scatters of proton

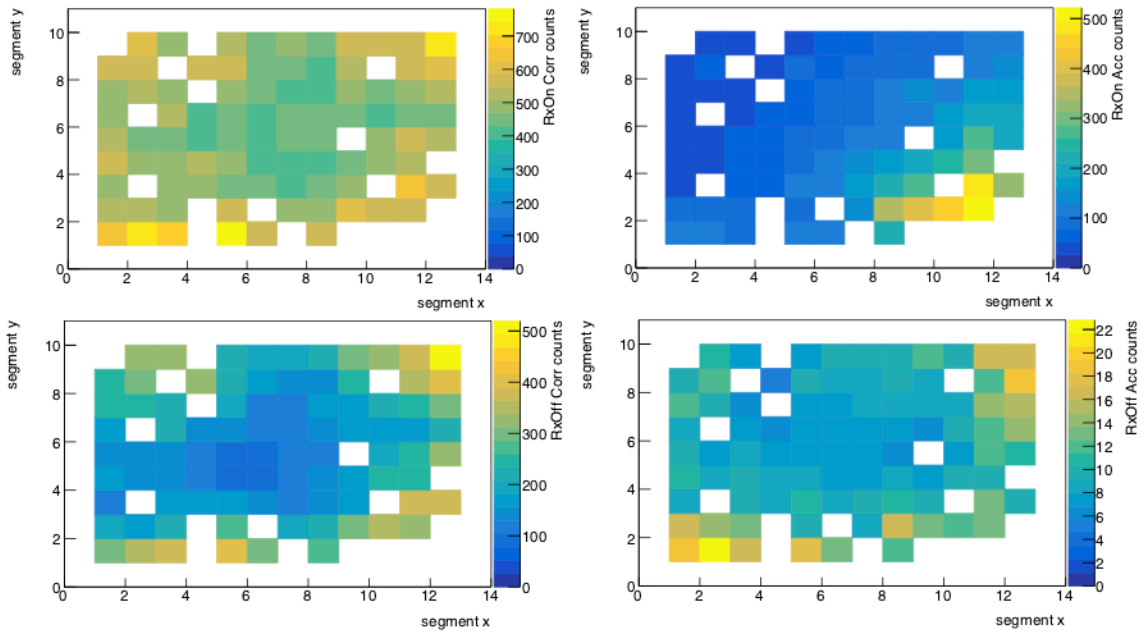

Figure 6.6: 2D distributions of IBD-like segment event rates for reactor-on and reactor-off data sets, including fiducialization and dead segments. For reference, the reactor is closest to segment 0, at coordinates (0,0). **(top left)** Reactor-on accidental-subtracted correlated IBD-like rate. **(top right)** Reactor-on accidental IBD-like rate. A hot spot is observed at the bottom of the detector, opposite the reactor, where a large flux of γ-rays created from the beam line products underneath the floor. **(bottom left)** Reactor-off accidental-subtracted correlated IBD-like rate. The event rate decreases towards the center of the detector where cosmogenics are more efficiently shielded. **(bottom right)** Reactor-off accidental IBD-like rate. From collaboration Ref. [192].

recoils created by the thermalization of the scattered neutron can be mixed with the prompt event, increasing the PSD slightly, but not enough to push it outside of the electronic recoil band. These interactions are difficult to reject and the measured peak is reconstructed at ~4.9 MeV and the continuum broadened. Peaks at higher energies in the reactor-on accidental spectrum are due to the beam line neutron capture events, specifically from ^{56}Fe in rebar in the concrete floor, which has two strong γ-ray lines at 7.631 MeV and 7.645 MeV and two weaker lines at 6.3 MeV and 5.5 MeV [193]. A small number of accidental events from surrounding ^{208}Tl is visible near 2.6 MeV and ^{40}K at 1.4 MeV, although very prominent in the γ-rays singles spectrum (not

pictured).

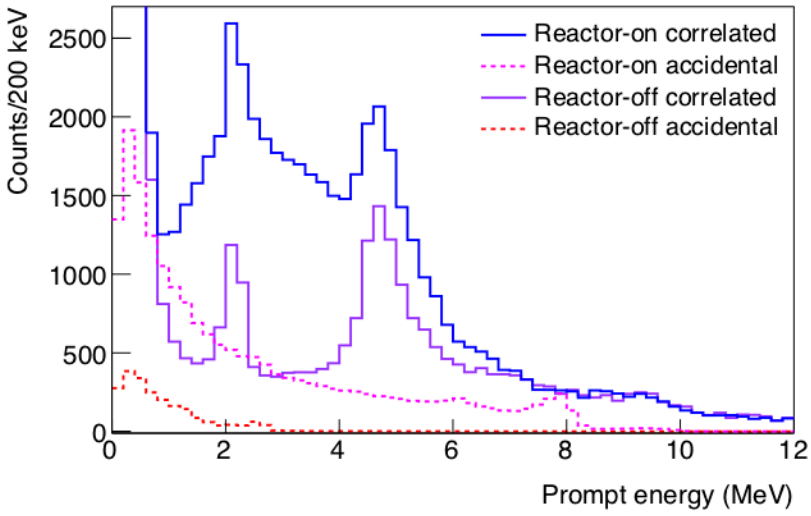

Figure 6.7: Measured prompt energy spectra in raw counts of reactor-on correlated (blue), accidental (magneta) and reactor-off correlated (purple), accidental (red) IBD-like candidates. Visible peaks in the correlated spectra are due to muon (∼2.2 MeV) and fast neutron (∼4.9 MeV) induced events. Peaks at higher energy in the reactor-on accidentals are due to γ-ray lines from the neutron capture of beam products on ^{56}Fe in rebar in the concrete floor. The 2.6 MeV peak from natural ^{208}Tl is sightly visible in both reactor-on and -off accidentals. From collaboration Ref. [192].

6.4.2 Atmospheric correction

The intensity of the cosmic ray flux observed on the Earth's surface is dependent on the mass of particles in the atmosphere, or more practically the atmospheric pressure. Neutrons are especially sensitive to the pressure, as low-Z atoms provide more effective overburden. Both reactor-on and -off distributions contain cosmic neutron samples, and thus can vary with time-specific environmental conditions. Neutron monitors correct the change in count rate via [194]:

$$dN = -\beta N dp, \tag{6.5}$$

where dN is the change in the count rate N, β is the attenuation coefficient, and dp is the atmospheric pressure change. The corrected pressure is then found by,

$$N_{corrected} = N_0 e^{\beta(p_0 - p)}, \tag{6.6}$$

where N_0 is the initial measured count rate and p_0 is the reference pressure. The attenuation coefficient is typically determined empirically. However it can be absorbed into the Taylor coefficients by expanding to first order around p through the approximation:

$$N_{corrected} \approx ap + b. \tag{6.7}$$

Thus, to account for the relative differences in atmospheric pressure between the reactor-on and -off datasets, the reactor-off correlated IBD-like rate is scaled based on the time-averaged atmospheric pressure ($\overline{p}_{on}$, $\overline{p}_{off}$, respectively) measured during each data period via:

$$\alpha = \frac{a \cdot \overline{p}_{on} + b}{a \cdot \overline{p}_{off} + b}. \tag{6.8}$$

Multiple cosmogenic event types are measured. Fast neutron events with prompt proton recoils and a delayed (n,^{6}Li) captures provide a high-statistics sample to trace the behavior across the data sets. The event selection is identical to those outlined in Table 6.1, with the exception that the prompt event must be 3σ from the mean of the electronic recoil band. The IBD sample is not used to avoid biasing the measurement from unexpected, but possible fluctuations in the $\overline{\nu}_e$ signal. Figure 6.8 shows the rate of these events and their anti-correlation with atmospheric pressure, measured hourly by meteorologic stations located at ORNL [195] and Oak Ridge [196]. The linear relationship between the averaged tracer events and pressure results in a cosmogenic scaling factor of α >99.8%. As the oscillation search is not sensitive to the background

subtraction at this small level, no scale factor was applied to the reactor-off data, thus $\alpha = 1$ for this analysis.

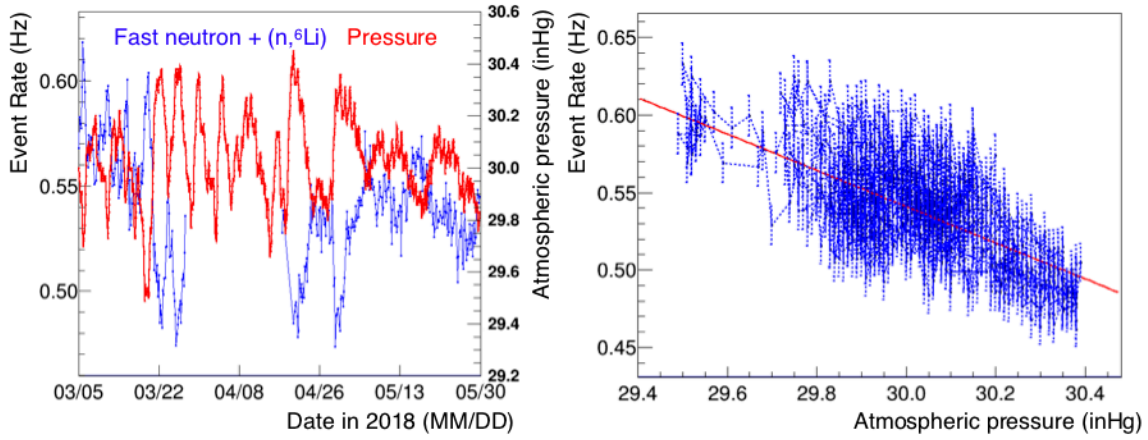

Figure 6.8: **(left)** Rate of fast neutron recoil + (n,^{6}Li) capture coincidences (blue) and atmospheric pressure (red) as a function of time, including both reactor-on and -off data sets. One data point is averaged over eight hours. (right) Linear fit to time-averaged reactor-on and -off event rate as a function of atmospheric pressure. From collaboration Ref. [197].

6.4.3 Background subtraction

To determine the total detector IBD signal, measured reactor-on and reactor-off, correlated and accidental prompt energy spectra are subtracted. The bin-by-bin subtraction requires scaling factors to match reactor-on and -off statistics by exposure time and the subtraction of scaled off-window accidental IBD-like candidates. To optimize the statistical power of the subtraction, the measured reactor-off sample is roughly equal to the reactor-on sample, as the uncertainty is proportional to twice the number of background counts. The number of IBD candidates, N_{IBD}, is then calculated as

$$N_{IBD} = \sum_{i=1} N_i = \sum_{i=1} N_{i,on,corr+acc} - \sum_{i=1} (t_{IBD}/t_{acc}) N_{i,on,acc} - \sum_{i=1} (t_{on}/t_{off}) \alpha [B_{i,off,corr+acc} - (t_{IBD}/t_{acc}) B_{i,off,acc}], \quad (6.9)$$

with a fractional uncertainty per bin ($\sigma_i / N_{IBD,i}$):

$$\frac{\sqrt{\begin{array}{l}(N_{i,on,corr+acc} + (t_{IBD}/t_{acc})^2 N_{i,on,acc}) \\ \quad + (t_{on}/t_{off})^2 \alpha^2 (B_{i,off,corr+acc} + (t_{IBD}/t_{acc})^2 B_{i,off,acc})\end{array}}}{N_i}, \quad (6.10)$$

where $N_{i,on,corr+acc}$ is the number of detected reactor-on IBD candidates per bin, $N_{i,on,acc}$ is the number of off-window measured accidental reactor-on samples, $B_{i,off,corr+acc}$ is the measured reactor-off IBD-like candidates, and $N_{i,off,acc}$ is the number of off-window measured accidental reactor-off samples. The ratio t_{IBD}/t_{acc} compares the IBD time window to the accidental off-time window, which is $119{\times}10^3$ ns/10^6 ns for this analysis. t_{on}/t_{off} the ratio of reactor-on to reactor-off exposure times, including deadtime corrections. The cosmogenic scaling factor α is described above, which has a negligible error and is not included in the uncertainty calculation.

Figure 6.9 shows the total detected IBD spectrum in prompt energy, after the scaled subtractions. The overall envelope of the measured spectrum is roughly in agreement with expectations, with a threshold turn-on and smooth fall-off at higher energies. Both the (n,H) and (n,C*) background peaks are eliminated, but conservative systematic uncertainties are included in the oscillation search to account for any variation in subtraction, as described in Section 6.7. Following a similar subtraction procedure, the L vs. E spectrum are produced by identifying candidates by their maximum energy deposit in individual segments. These segments are grouped into 6 baseline bins with 16, 400 keV-wide energy bins ranging [0.8,7.2] MeV, as illustrated in Figure 6.10. These spectra are input into the χ^2 as $O_{l,e}$ in Equation 6.2.

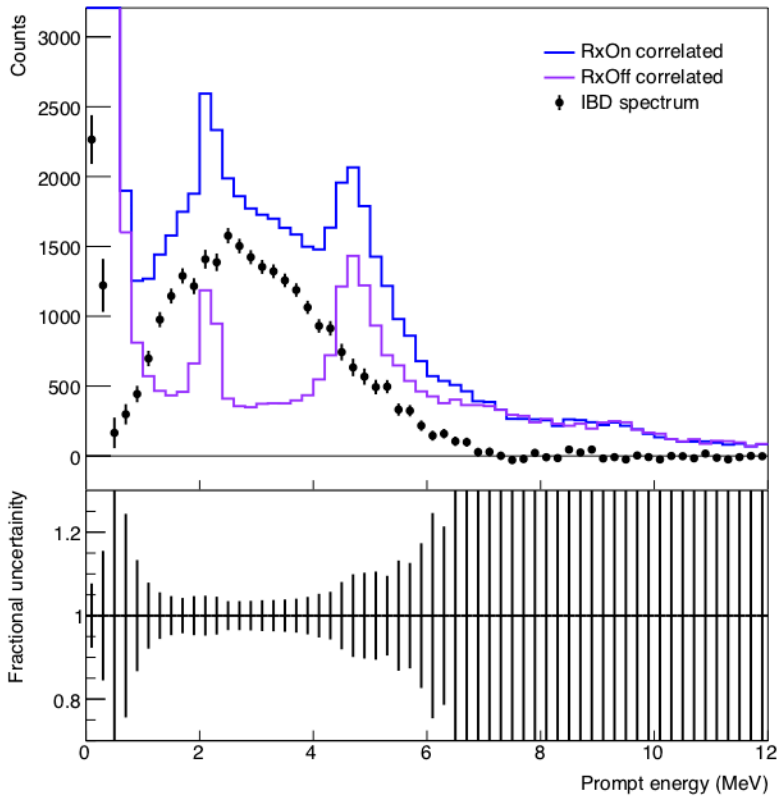

Figure 6.9: Detected IBD candidates (black) in total counts (per 200keV) with corresponding fractional uncertainty per bin. Reactor-on correlated (blue) and reactor-off correlated (purple) spectra are also shown to illustrate the subtraction and signal-to-background ratio. From collaboration Ref. [198]. The source of the excess in the low-energy bins has not yet been determined. These points are excluded from the analysis.

6.4.4 Data set statistics

The relevent statistics of the oscillation search measurement are summarized in Table 6.2. A total of 25461 IBD candidates were detected, at a rate of 771 per day. Averaging the correlated background rate over the reactor-off sample, the $\overline{\nu}_e$ signal is observed at 5σ statistical significance within 2 hours of the reactor-on measurement. This is possible due to the correlated signal-to-background ratio of 1.32, which was

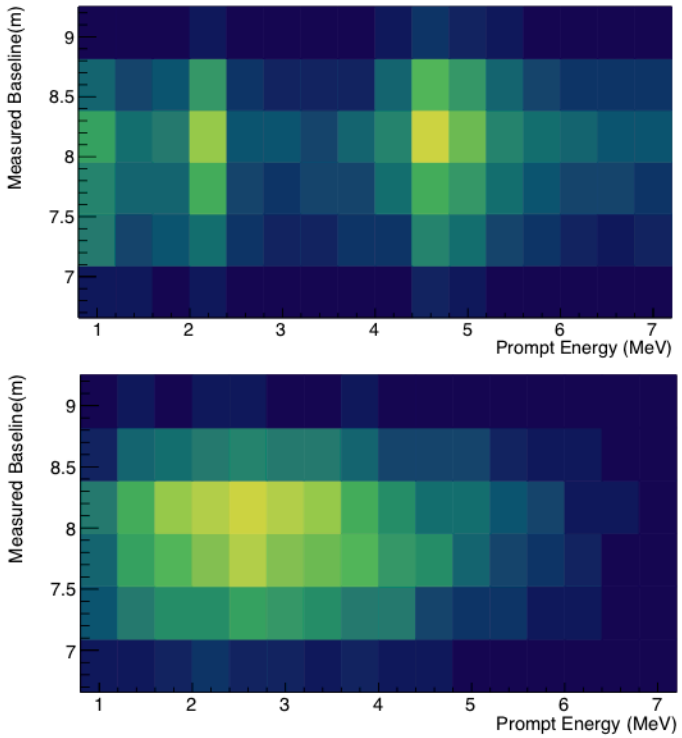

Figure 6.10: **(top)** Reactor-off correlated+accidental L vs. E spectrum. The (n,H) and (n,C*) background features are prominent. **(bottom)** IBD signal L vs. E spectrum. Updated from collaboration Ref. [199].

the best achieved by a near-surface neutrino detector at the time of writing.[1]

6.5 Cross-checks

As the oscillation analysis is sensitive to the reconstructed position distribution of IBD candidates, cross-checks were performed with data binned by measured baseline. Due to slight differences in the light collection in each segment and the presence of dead PMT channels, the number of IBD events is corrected by the relative detection efficiency. Figure 6.11**(top)** shows the IBD efficiency model from `PROSPECT-G4`. The simulation, which includes the detector geometry and energy response models detailed in Chapter 5, generates baseline-weighted IBD events with a flat (constant)

[1]The spectrum result surpassed this achievement, with a signal-to-background fo 1.7, which will be described in Chapter 7.

Type	Value
Reactor-on (30.26 exposure days)	
Correlated+accidental	56378±237
Accidental (scaled)	11580±12
Correlated	44797±238
Reactor-off (26.19 exposure days)	
Correlated+accidental (scaled)	20262±153
Accidental (scaled)	925±4
Correlated (scaled)	19337±153
Detection	
IBD candidates	25461±283 (771/day)
Correlated S:B	1.32:1
Accidental S:B	2.20:1

Table 6.2: Summary of IBD-like event statistics for the oscillation search data set in the region of interest between [0.8,7.2] MeV. Uncertainties include statistics only. Reactor-off and accidental effective samples are scaled according to Equation 6.9. Signal-to-background is denoted by S:B.

energy spectrum. The relative, energy-dependent efficiency is obtained by summing projections of the efficiency as a function of energy $\epsilon_{segment,i}$ over all bins ranging from 0-12 MeV, folded with the IBD yield (Y_i) per bin obtained by the Huber model for ^{235}U fission:

$$\epsilon_{segment} = \sum_i \frac{\epsilon_{segment,i} Y_i}{Y_i}. \tag{6.11}$$

Each segment efficiency is normalized by the total input IBD yield ($\sum_i Y_i$) within the fiducial volume.[2] The total detector efficiency for this analysis is ∼37%, with the largest contribution to the non-uniformity from neutron captures in dead segments. When applied to the 2D IBD distribution map, Figure 6.11**(bottom)**, it is qualitatively clear that the $\overline{\nu}_e$ flux is greatest near the reactor and falls as the radial distance increases. Uncertainties in the efficiency estimation are not included.

[2]Events outside of the z fiducial region are not removed.

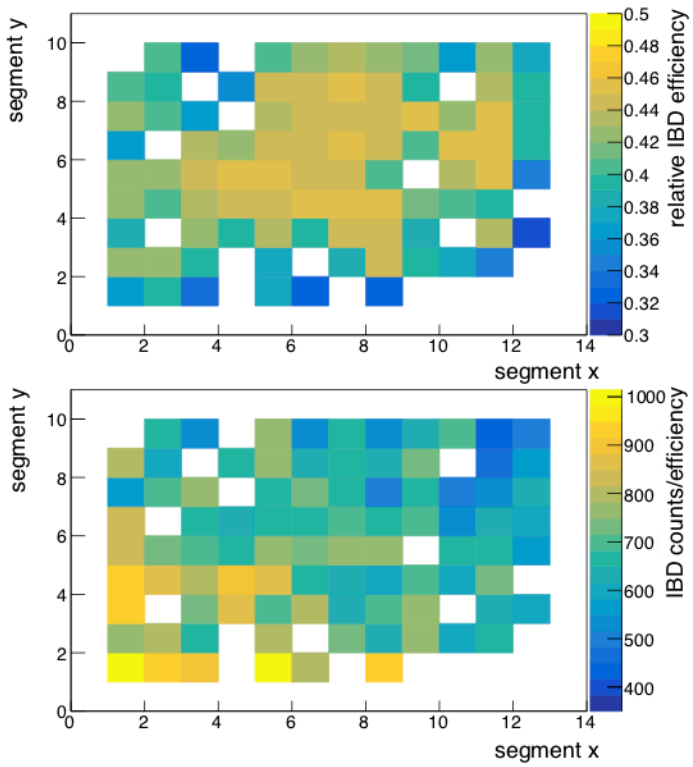

Figure 6.11: **(top)** Relative IBD detection efficiency per segment, generated from PROSPECT-G4, for the oscillation data set. **(bottom)** 2D distribution of efficiency-corrected IBD events per segment. The reactor, below-grade, is closest to coordinates (0,0). From collaboration Refs. [192, 200].

Grouping the segments according to the 15-unique baselines given in Figure 6.1, the expected $1/r^2$ variation is confirmed. Figure 6.12**(top)** shows the IBD event rate where each baseline bin is weighted by the active mass (19 L $\approx$ 19 kg) and the relative efficiency. Only 14 data points are observed, as the 15th baseline bin is excluded due to the fiducialization cut. Very good agreement between the data and the $1/r^2$ fit is observed, with one free parameter and a $\chi^2/ndf<1$. An observed $\sim$40% decrease in flux from the front to the back of the detector is observed due to the granularity of the PROSPECT segments. The baseline distribution is also in agreement with the generated PROSPECT Monte Carlo, including no $\overline{\nu}_e$ oscillations, as illustrated in Figure 6.12**(bottom)**.[3] A normalized 3+1ν model including oscillations with the

[3]Neutrons from the IBD interaction are boosted away from the reactor position. This direc-

RAA best fit sterile neutrino mixing parameters is also shown. Visually, this model is also in agreement with the data. Due to the small expected oscillation in the total $\overline{\nu}_e$ flux at these short baselines, PROSPECT gains sensitivity by including energy information into the oscillation search, rather than relying on pure $1/r^2$ measurements.

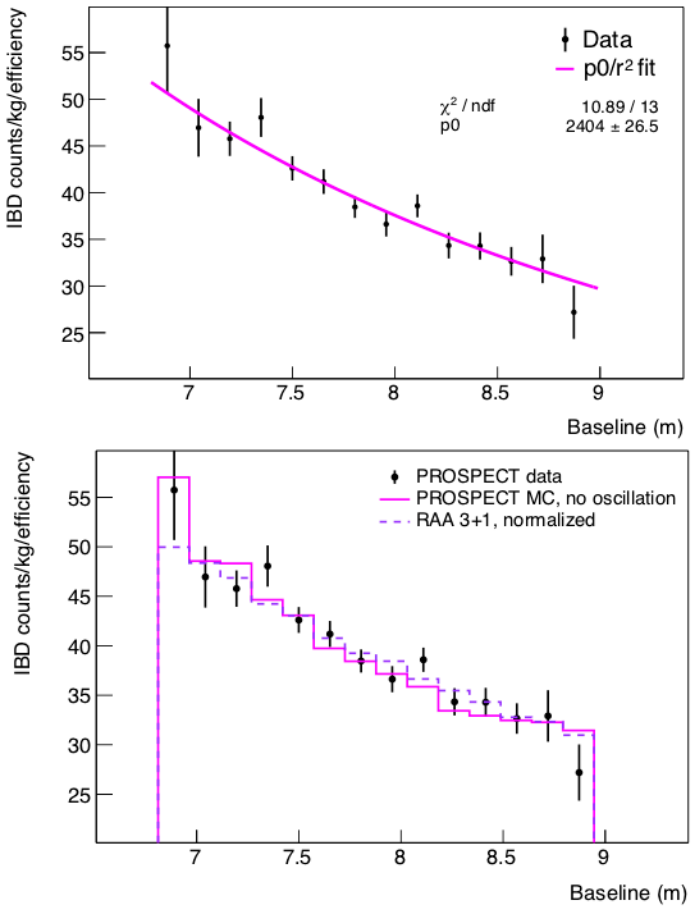

Figure 6.12: **(top)** Background-subtracted IBD event rate versus baseline with $1/r^2$ fit in good agreement. The rate is weighted by active mass and efficiency corrected. Error bars include statistics only. **(bottom)** Comparison of IBD rate versus baseline of PROSPECT data, Monte Carlo assuming no oscillations, and a 3+1 oscillated model using the RAA best fit parameters. The RAA model is normalized by the ratio of the data-to-Monte Carlo integrals. From collaboration Refs [188, 192] and modified Ref. [201].

tionality was not originally implemented into the `PROSPECT-G4` model and neutrons are generated isotropically.

6.6 Model generation and inputs

6.6.1 Reactor and detector model

Input reactor predictions are compared to measurements to search for possible sterile oscillations, according to Equation 6.1. A Monte Carlo analysis within the PROSPECT `OscSens_CovMatrix` [202] package[4] is used to generate $\overline{\nu}_e$ events that interact with a model detector and produce L vs. E spectra predictions. The reactor is modelled as an object with 10^7 fission points where neutrinos emanate and travel isotropically, the flux weighted by the power distribution of the core provided by HFIR. Figure 6.13 shows the axial and radial distributions of the relative power. A simplified model of the detector, a box the size of the PROSPECT fiducial volume, is positioned according to the survey measurements. Segments are defined by imaginary boundaries. The proton density of EJ-309 is used, $5.461\times10^{28}/\mathrm{m}^3$ [119], which essentially cancels when the relative spectra are calculated. Neutrinos are detected as a function of true baseline from the reactor and are collapsed into segment bins, as defined by Figure 6.1.

The predicted $\overline{\nu}_e$ spectrum is generated using the Huber ^{235}U flux model and the Vogel-Beacom IBD cross section. Additional corrections are made to account for non-^{235}U generated contributions to the $\overline{\nu}_e$ flux. The HFIR core contains 250 kg of aluminum (compared to the 10 kg of uranium fuel). Through neutron activation, ^{28}Al can produce antineutrinos via:

$$^{27}Al + n \rightarrow {}^{28}Al \xrightarrow{t_{1/2}=2.24\,min} {}^{28}Si + \beta^- + \overline{\nu}_e, \tag{6.12}$$

where the β endpoint is Q=2.86 MeV. Therefore, only low-energy $\overline{\nu}_e$ are created but the contribution changes as the reactor cycle proceeds.[5] This process is modelled for

[4] `PROSPECT-G4` could be used to generate the Monte Carlo, but is more complicated than required.

[5] ^{235}U is depleted throughout the cycle, although the power (number of fissions) is kept constant

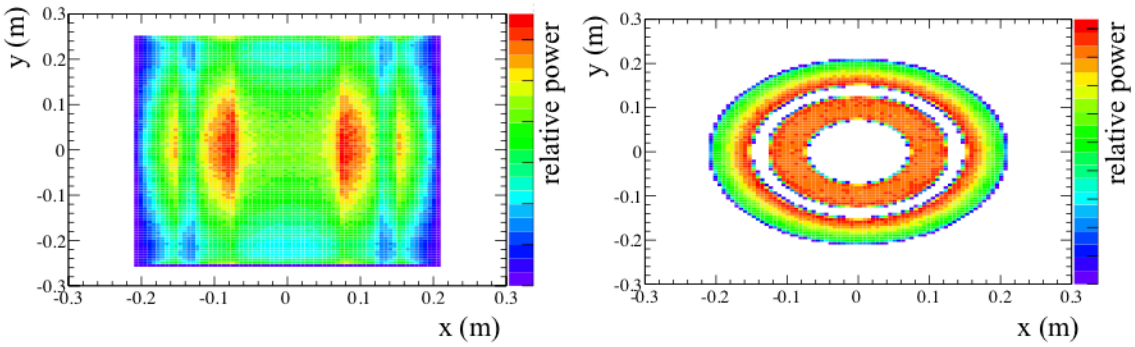

Figure 6.13: Power output distribution on the HFIR core. The shaded regions represent the fission interaction points, where power (and neutrinos) is created. The ring structure marks the absence of ^{235}U where neutron reflector structures are positioned. **(left)** Axial distribution. Similar to Figure 3.1, except binned according to the 10^7 fission points. **(right)** Radial distribution. From collaboration Ref. [199].

the reactor cycles used in this analysis and the total $\overline{\nu}_e$ spectrum due to ^{28}Al is shown in Figure 6.14**(top left)**. Further corrections are required to account for $\overline{\nu}_e$ produced by longer-lived fission products, referred to as non-equilibrium isotopes. The ILL β spectrum measurements [59, 60] that the Huber conversion model relies on, were acquired after irradiations of $\mathcal{O}(day)$ timescales, as compared to the 24 day-long irradiations of a HFIR cycle. A number of fission products have longer β decay half-lives, unable to reach equilibrium within a day. This time- and energy-dependent accumulation of $\overline{\nu}_e$ is modelled by interpolating corrections based on 450-day predictions by Ref. [52]. Figure 6.14**(top right)** shows the non-equilibrium addition to the total detected $\overline{\nu}_e$ spectrum. An increase of 1.3% in the $\overline{\nu}_e$ rate is applied to the spectrum from these contributions, illustrated in Figure 6.14**(bottom)**.

Currently, corrections to the $\overline{\nu}_e$ flux from longer-lived isotopes in spent nuclear fuel stored ∼15-20 m from the detector are not considered. The rate is expected to be ∼0.425 per day on the first day of the reactor cycle (compared to the detected 771 IBD/day) [203], much less than the contribution to an LEU reactor spectrum due to relative differences in cycle length and fission yields. Isotope production within

by increasing the neutron flux. The increase in flux leads to an increased rate of ^{27}Al activation.

the HFIR core has been shown to have a negligible affect on the flux [204] and no correction is applied.

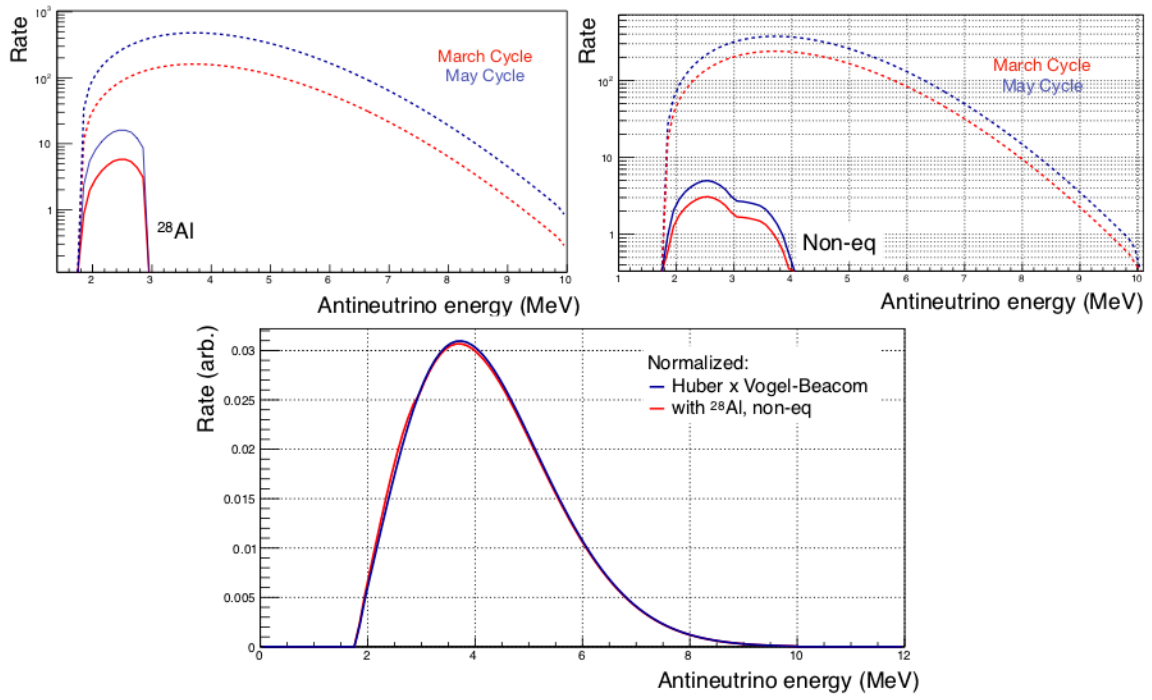

Figure 6.14: **(top left)** ^{28}Al contribution to total $\overline{\nu}_e$ spectrum, for the March and May reactor cycles used in this analysis data set. **(top right)** Non-equilibrium contribution to total $\overline{\nu}_e$ spectrum. **(bottom)** Comparison of total $\overline{\nu}_e$ spectrum from Huber flux and Vogel-Beacom cross-section model normalized to the predicted spectrum with ^{28}Al and non-equilibrium corrections. From collaboration Refs. [205–207].

6.6.2 Detector response model

As described in Chapter 5, a detector response model is required to convert predicted true antineutrino energy into detected prompt energy spectra. The energy scale is dependent on the scintillator performance and volume of inactive material, which can vary with time. Calibration data are used to constrain the response characteristics in `PROSPECT-G4` for individual data sets. Table 5.2 lists the best-fit parameters used to model the energy nonlinearity, scale, and resolution for the oscillation analysis. Figure 6.15 shows the strong agreement between measured and best-fit Monte Carlo

reconstructed energy for two of the γ-ray sources deployed in the center of the detector.[6] The total detector energy scale expressed as the ratio of reconstructed energy to the simulated energy is consistent to within $\pm 1\%$.

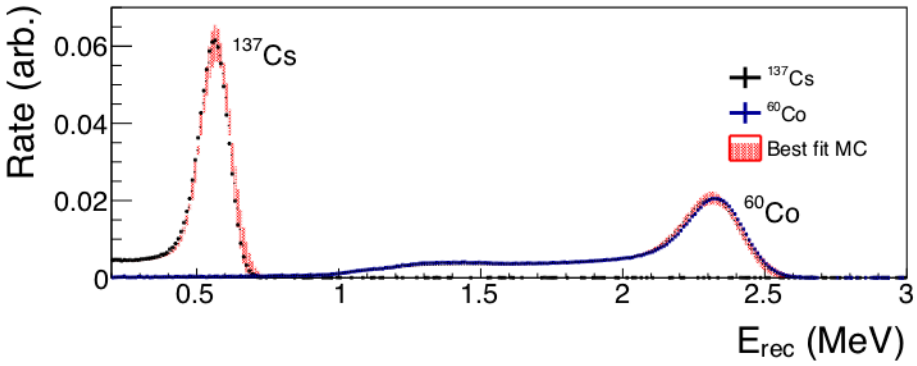

Figure 6.15: Measured and best-fit simulated total detector E_{rec} for ^{137}Cs and ^{60}Co γ-ray calibration sources deployed near the detector center [188].

Using this model, a detector response matrix is generated by simulating a baseline-weighted, flat energy spectrum in each segment. The Monte Carlo data is run through the same analysis pipeline as the PROSPECT data, including the same calibration and reconstruction procedure for the particular data set. Energy depositions in dead segments are discarded. Figure 6.16 provides an example response matrices for an individual segment and the full detector, where the color scale represents the probability that a $\overline{\nu}_e$ with some true energy will register as some E_{prompt} in the detector. It is clear that the response is more complicated than a simple shift in energy. The predicted $\overline{\nu}_e$ spectrum per segment is folded with the respective response matrix, converting predicted energy spectra into the PROSPECT prompt energy space.

[6] Improvements to the complicated reconstruction model were made for the spectrum analysis to allow for better agreement between data and Monte Carlo.

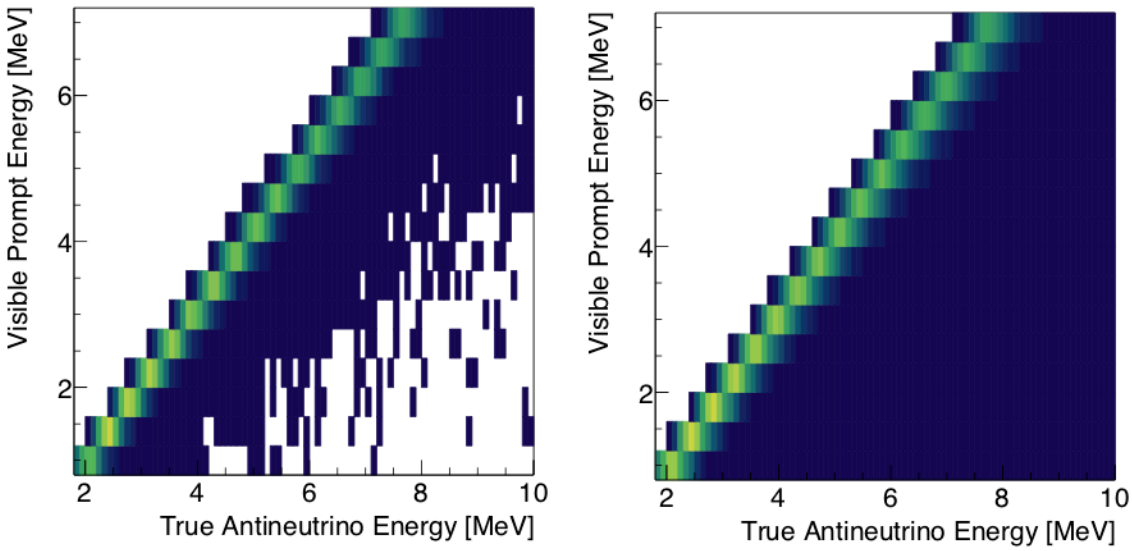

Figure 6.16: Detector response matrices used in the oscillation analysis. **(left)** Response of an individual segment. **(right)** Full detector response. Updated from collaboration Ref. [199].

6.6.3 L vs. E spectra

The predicted total prompt spectrum, in the case of no oscillations (null hypothesis), can be summarized as,

$$E_{null}(L, E_{prompt}) = P_{th} \cdot S(E)/4\pi L^2 \cdot t \cdot \epsilon_D(L, E_\nu, E_{prompt}) \cdot \sigma(E) \cdot \rho_P V_D, \quad (6.13)$$

where L is the baseline of the $\overline{\nu}_e$ event, P_{th} the average power of HFIR, $S(E)$ $(= dN/E_\nu)$ the Huber flux prediction, t exposure time, $\sigma(E)$ the Vogel-Beacom IBD cross section, ρ_P the proton density, and V_D the active volume. The $\epsilon_D(L, E_\nu, E_{prompt})$ represents all detector effects, including the response that maps true $\overline{\nu}_e$ energy into E_{prompt}. Predicted prompt energy spectra for each segment are collapsed into 6-baseline bins, from 6.7 to 9.2 m, defined at the outset of the sterile neutrino search analysis to create L vs. E spectra. For each set of oscillation parameters defined by a log-log $\sin^2 2\theta_{14}$-Δm^2_{41} grid, oscillations are modelled using Equation 6.4 to simulate

oscillated $E_{l,e}$. The ratio of each $E_{l,e}$ to the predicted total null spectra E_e is then scaled by the measured total prompt spectrum O_e, eliminating the dependence on the specific reactor model. This quantity is compared to the measured L vs. E spectra $O_{l,e}$ in the oscillation fitter.

6.7 Uncertainty characterization

Both statistical and systematic uncertainties are captured in covariance matrices and required for the χ^2 comparison in Equation 6.1. This method is advantageous for representing both uncorrelated and correlated errors in the position-energy bins considered in the oscillation fit. A covariance matrix V_i is created for the statistics and each systematic uncertainty using a combination of methods, including `PROSPECT-G4` simulations, toy models, and data measurements. Assuming that all errors are Gaussian, the matrices are added together to form V_{tot} and normalized (reduced) to provide a statistics-independent measure of the correlations.

The statistical uncertainties are directly calculated from the reactor-on signal and reactor-off background measurements using Poisson statistics, following Equation 6.10 for position-energy bins. This results in an uncorrelated, diagonal matrix. Additional, off-diagonal terms are required to account for the correlation between the measurement $O_{l,e}$ and the baseline-integrated prediction scale factor O_e (see Equations 6.2 and 6.3). Thus, the full statistical covariance matrix is expressed as,

$$V_{stat,l,e} = \sigma^2_{stat,l,e}\left(1 - 2\frac{O_{l,e}}{O_e}\right) + \sigma^2_{stat,e}\left(\frac{O_{l,e}}{O_e}\right)^2 \tag{6.14}$$

Furthermore, off-diagonal terms from position bins with the same energy are included to account for the correlations introduced by the use of the O_e. Monte Carlo toys were produced to estimate these correlations.

Uncertainties in the response model, treated as correlated between segments and

energy bins, are taken from the simultaneous data-Monte Carlo fit for each energy parameter with slight inflations to be conservative. Due to the complicated correlations between the parameters, several `PROSPECT-G4` data sets were produced by varying the parameters by $\pm 1\sigma$ to create prompt energy spectra, assuming underlying Gaussian distributions. These spectra are used as toys to generate the response covariance matrix. Beyond the response model, an energy loss systematic is required to assess the ability of `PROSPECT-G4` to produce the correct amount of missing energy escaping two prompt, 511 keV annihilation γ-rays. ^{22}Na calibration source data with deployments near the center and the edge of the detector at different z-positions was compared with Monte Carlo. The reconstructed energy was summed by adding depositions from one ring of segments surrounding the source (e.g. 4 segments), two rings of segments (e.g. 16 segments), and three rings (e.g. 36 segments). Dead segments are excluded. The largest shift observed between the spectra was taken as the uncertainty, for this analysis $\sigma = 30$ keV The covariance matrix is calculated by generating 10000 PROSPECT-like toy spectra using the Huber ^{235}U input model, each modified by a random pull from a Gaussian with 1σ. Each energy bin is shifted via $(E_{e,mod} = E_e(1 + pull))$, as show in Figure 6.17**(left)**. The covariance between energy bins is calculated and normalized via:

$$(V)_{ij} = \frac{1}{N} \sum_{toys} \frac{(E_i^{toy} - E_i^{null})(E_j^{toy} - E_j^{null})}{E_i^{null} \cdot E_j^{null}}, \tag{6.15}$$

where N is the number of toys, i, j are the energy bins, and E^{toy}, E^{null} are the toy spectra and unmodified null spectra, respectively. Figure 6.17**(right)** illustrates the unnormalized energy loss matrix for one baseline. Two energy loss systematics are added to account for correlated shifts in energy between segments, taken as 100% correlated, and total uncorrelated losses near the edge of the detector.

Uncertainties in the IBD detection efficiency and total detector energy resolution

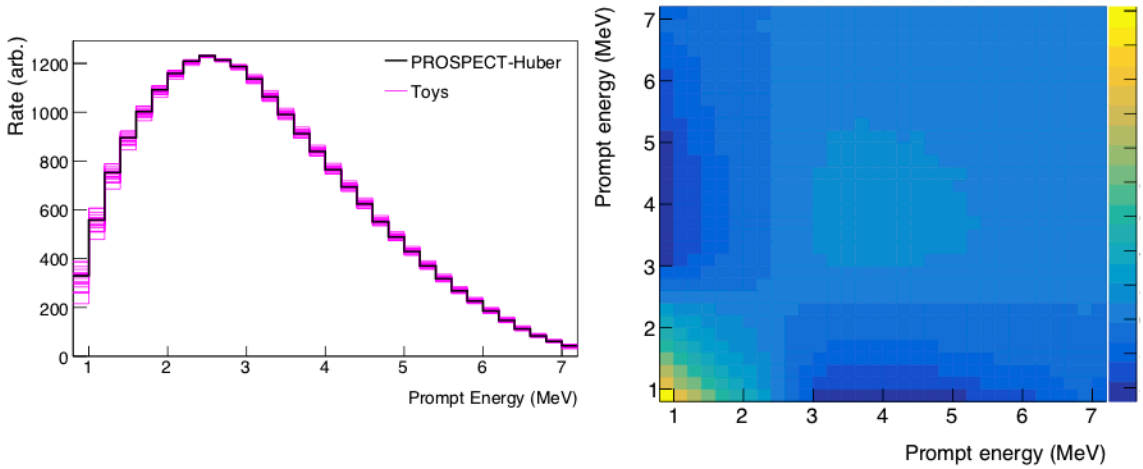

Figure 6.17: **(left)** Toy models (pink) generated from Gaussian random pulls with a σ the size of the energy loss shift between data and Monte Carlo. The unmodified PROSPECT-like Huber spectrum is shown for comparison (black). **(right)** Unnormalized energy loss covariance matrix for one baseline bin. The color scale is linear. Modified from collaboration Ref. [208, 209].

are estimated using toys and treated as uncorrelated. Fully correlated systematics for background normalization that accounts for the variation in cosmogenics and energy scale between reactor-on and reactor-off data sets are conservatively determined using the fast neutron and BiPo measurements, respectively. An estimated uncorrelated 5% uncertainty is placed on the variation of the (n,H) and (n,C*) peaks from Monte Carlo toys. Fits of the measured RnPo rates in each segment are used to determine the uncorrelated volume systematic, conservatively estimated to be 5% at maximum. Survey measurements indicate a baseline uncertainty of 10 cm. The ^{28}Al and non-equilibrium contributions to the spectrum are conservatively assumed to be 100% uncertain, as their impact on the overall spectrum are of order 1%. Table 6.3 summarizes the systematic values estimated for the oscillation analysis. The full (non-reduced) baseline-energy signal and background covariance matrices, including statistics and systematics, are shown in Figure 6.18.

Systematic parameter	Value	Uncertainty (σ)
Background		
Normalization	–	5%
Uncorrelated (n,H) to (n,C*) peak	–	5%
Energy scale	–	0.2%
Detector effects		
Birks' nonlinearity k_{B1}	0.100 mm/MeV	0.012 mm/MeV
Cherenkov nonlinearity k_C	51%	4%
Energy scale β_{rec}	1	0.7%
Energy resolution	4.45%	0.2%
Energy loss	–	30 keV
Uncorrelated IBD efficiency	–	5%
Uncorrelated volume	–	per segment
Uncorrelated energy resolution	4.45%	0.2%
Uncorrelated energy loss	–	30 keV
Baseline uncertainty	793.2 cm	10 cm
Reactor model		
^{28}Al spectrum correction	–	100%
Non-eq spectrum correction	–	100%

Table 6.3: Summary of the estimated systematics in the oscillation analysis. All uncertainties are correlated unless otherwise noted. Energy response uncertainties are slightly inflated compared to the parameter fit uncertainties listed in Table 5.2 to remain conservative.

6.8 Confidence region assignment

Confidence intervals for the sterile neutrino oscillation search are assigned using frequentists tests.[7] In the standard method, the confidence region is defined by comparing the best fit oscillation model and data to a fixed $\Delta\chi^2$ given the pre-defined confidence level (C.L.). In this search, the confidence interval at 95% C.L. with two degrees of freedom would include mixing parameters with a minimum of $\Delta\chi^2$ of 5.99. However, as $\sin^2 2\theta_{14}$ oscillates and at higher Δm^2_{14} the oscillations approaches the bin size, this method is not satisfactory. It could result in an empty confidence in-

[7]Frequentist confidence intervals, in this case at 95% confidence, can be interpreted as: if the PROSPECT experiment was performed 100 times, 95% of the experiments would result in oscillation parameters within the given confidence region.

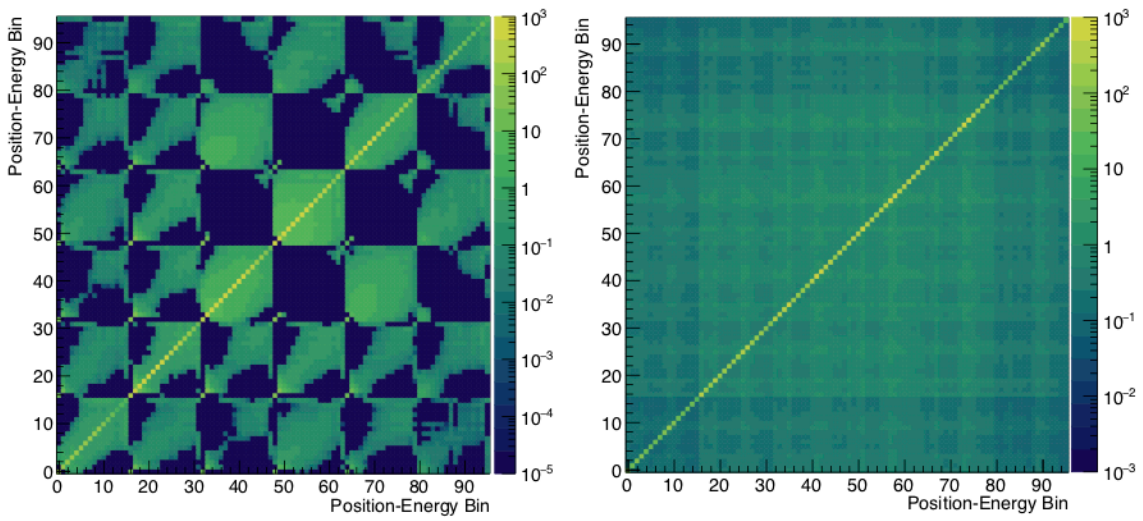

Figure 6.18: **(left)** Signal covariance matrix. **(right)** Background covariance matrix. From collaboration Ref. [210].

terval within an unphysical regime, which could be mistaken as ruling out all of the possible parameters. However, this interpretation is incorrect, and rather indicates that the observation is in the small percentage of experiments that do not contain the true value. The Feldman-Cousins prescription [190] addresses these issues and is used to give the correct confidence interval assignment in this analysis. Essentially, the method involves producing an ensemble of Monte Carlo toy experiments for each point on the $\sin^2 2\theta_{14}$ -Δm^2_{41} grid to define variable critical $\Delta\chi^2_C$ values that determine if the given point is accepted at 95% C.L.

Practically, the confidence interval assignment is implemented as follows. The predicted L vs. E spectra produced for each point on the $\sin^2 2\theta_{14}$ -Δm^2_{41} grid are fluctuated by the statistical and systematic uncertainties to create 1000 toy data sets. This is achieved by applying a Cholesky decomposition to the total covariance matrix to add sets of correlated fluctuations to the predictions. A minimum $\chi^2_{toys,min}$ is calculated for each toy data set by comparing the toy with the predicted L vs. E spectrum for each point, following Equation 6.1, possibly resulting in best-fit parameters different from the true parameters used to produce the predicted spectrum. The

$\Delta\chi^2_{toys}$ is then defined as

$$\Delta\chi^2_{toys} = \chi^2_{toys,min,true} - \chi^2_{toys,min,best-fit}, \tag{6.16}$$

where $\chi^2_{toys,min,true}$ is for the true oscillation parameters and $\chi^2_{toys,min,best-fit}$ is for the obtained best-fit oscillation parameters for the particular toy model.

The critical $\Delta\chi^2_C$ corresponding to confidence interval α for each point on the $\sin^2 2\theta_{14}$ -Δm^2_{41} grid is defined such that

$$\frac{\sum_0^{\chi^2_C} P(\Delta\chi^2_{toys})}{\sum_0^{\infty} P(\Delta\chi^2_{toys})} = \alpha, \tag{6.17}$$

where $P(\Delta\chi^2_{toys})$ is the probability density distribution of the $\Delta\chi^2_{toys}$. Points in the grid with

$$\Delta\chi^2_{data} > \Delta\chi^2_C \tag{6.18}$$

are excluded at α C.L., where $\Delta\chi^2_{data}$ is the difference between the data and best-fit minimized χ^2. Figure 6.19 shows the distribution of $\Delta\chi^2_C$ values, which vary, as compared to the standard method in which all of the points would have a value of 5.99 as prescribed by the χ^2 table for two degrees of freedom at 95% C.L. Furthermore, a comparison of probability density distributions generated for use in this analysis (Feldman-Cousins) and the standard method are illustrated. Use of the standard method would imply the null hypothesis is less compatible with the PROSPECT data then suggested by the Feldman-Cousins confidence interval assignment.

6.9 Oscillation search results

Figure 6.20 illustrates the binning scheme that is implemented in the oscillation fit. For each baseline, the ratios between individual measured IBD E_{prompt} spectra ($O_{l,e}$)

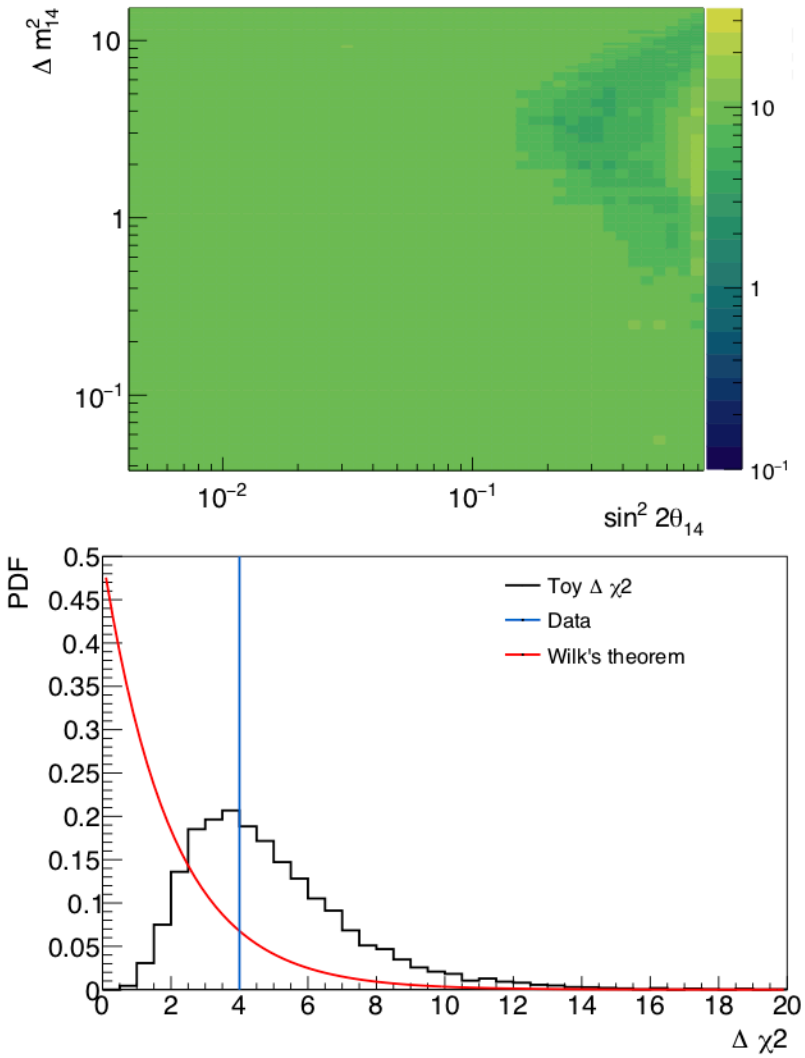

Figure 6.19: **(top)** Distribution of critical $\Delta\chi^2_C$ values indicating 95% C.L. Using the standard method, all points on the grid would have a value of 5.99, taken from the χ^2 table for a fit with two degrees of freedom at 95% confidence. for each mixing parameter set on the log-log grid. **(bottom)** Comparison of $\Delta\chi^2$ from Feldman Cousins prescription (toys, black) to standard method (Wilk's theorem, red) for the null oscillation hypothesis. All values below the one experimental instance (data, blue) are excluded. The ratio of the exclusion region to the integral of the PDF determines the confidence interval. The p-value for the standard method (0.14) suggests that the null hypothesis is less compatible with the data then it is, where the toy method results in a p-value of 0.58.

and the total spectrum normalized by the null prediction ($O_e \frac{E_{l,e}}{E_e}$) are shown. Models for the null hypothesis and oscillations with the Reactor Antineutrino Anomaly (RAA) [52] are added for comparison. Statistical and systematic uncertainties are

applied to the data points to qualitatively assess the agreement between the measurement and expectations. There is no observation of significant deviations from the null hypothesis observed throughout the various energy spectra at different baselines.

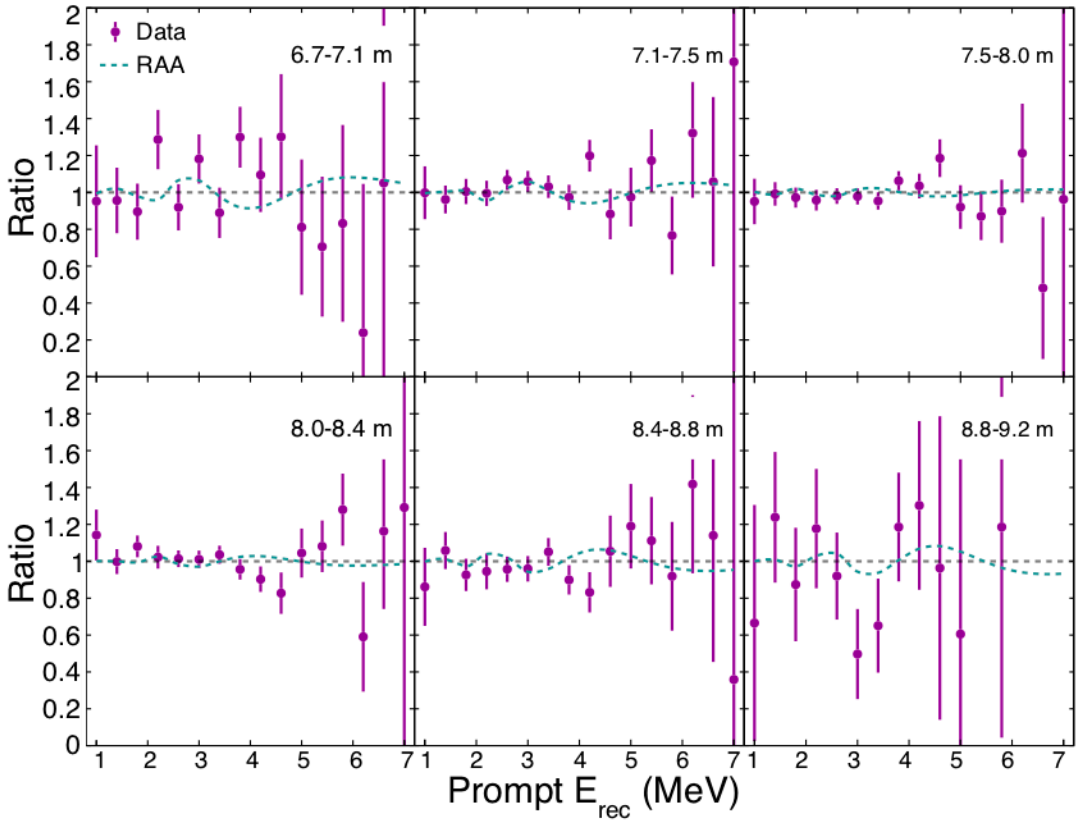

Figure 6.20: Ratio of measured IBD prompt E_{rec} spectra in 6 baseline bins from 6.7 to 9.2 m to the baseline-integrated spectrum. Also shown are the no-oscillation (gray, dashed) expectation and an oscillation prediction corresponding to the best fit Reactor Antineutrino Anomaly (teal, dashed) oscillation parameters [52]. Error bars indicate statistical and systematic uncertainties, with statistical correlations between numerator and denominator properly taken into account [188].

The level of agreement is quantified using the χ^2 defined in Equation 6.1 and the fit scheme outlined above. Good agreement between the measurement and the null oscillation hypothesis ($\theta_{14} = 0$) is found with a $\chi^2/ndf = 61.9/80$. [8] Allowing free oscillation parameters, a global minimum of $\chi^2_{min}/ndf = 57.9/78$ is found at (Δm^2_{41},

[8]The number of degrees of freedom is reduced from the 96 baseline-energy bins to 80 as the ratio includes the 16 energy bins from the total measured spectrum.

$\sin^2 2\theta_{14}) = (0.5\,\mathrm{eV}^2, 0.35)$. The comparison of critical and data $\Delta\chi^2$ (Equation 6.18) values assuming the null oscillation hypothesis results in a p-value of 0.58. Thus, the data is compatible with the standard 3ν framework. Based on the 33 operational days of reactor-on measurements, no sterile neutrino is observed. Figure 6.21 shows the PROSPECT 95% exclusion curve and the expected sensitivity. The data set excludes a large portion of the RAA allowed region and disfavors the best fit point at 2.2σ C.L. with a p-value of 0.013. Statistics are the limiting factor in the sensitivity coverage, with the energy response as the largest systematic. In regions of high Δm^2_{14} oscillations would be faster than the bin size, resulting in an averaged flux deficit in the measurement. No absolute flux normalization is assumed in the fit, making it impossible to distinguish between the no oscillation and sterile neutrino oscillation scenerio, thus reducing the sensitivity. The coverage of low values of Δm^2_{14} is constrained by the maximum baseline, i.e. L/E is small. The jagged behavior of the exclusion curve is due to the oscillatory nature of $\sin^2\theta_{14}$. If a particular value of $\sin^2\theta_{14}$ cannot be excluded, multiple sets of $(\Delta m^2_{41}, \sin^2 2\theta_{14})$ are allowed, where the size of the region depends on the position within the log-log grid.

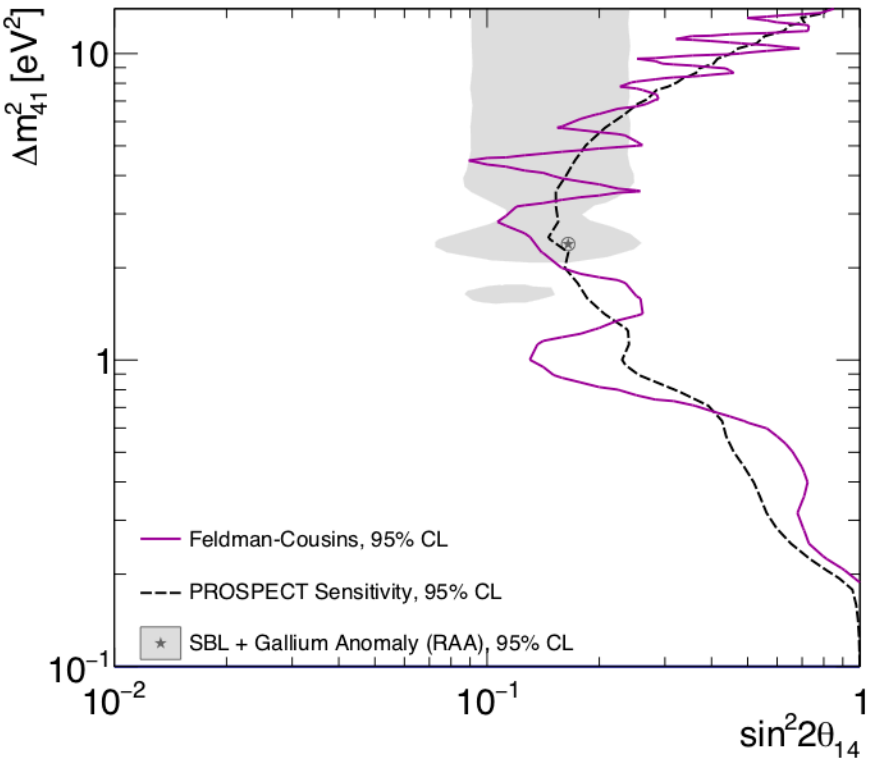

Figure 6.21: Sensitivity and 95% confidence level sterile neutrino oscillation exclusion contour from the 33 operational day PROSPECT reactor-on data set. The best fit of the Reactor Antineutrino Anomaly (RAA, star) [85] is disfavored at 2.2σ confidence level [188].

Chapter 7

First precision measurement of the ^{235}U antineutrino spectrum with PROSPECT

PROSPECT's second experimental goal is to make the world-leading measurement of the ^{235}U antineutrino energy spectrum. A precision measurement from the HFIR HEU reactor can address the isotopic origin of the 5-7 MeV $\overline{\nu}_e$ excess observed by LEU experiments as compared to the Huber-Mueller model [52,63]. The total detector $\overline{\nu}_e$ spectrum is measured at a distance of 7.9 m from the core center to detector center, resulting in a total detection rate of 668 IBD events per day. The IBD event selection was optimized to increase the signal-to-background of the measurement, providing a clean IBD sample as the spectrum is very sensitive to the background subtraction. An improved correlated signal-to-background ratio of 1.7 is achieved, which leads the record of antineutrino detection on Earth's surface. With a reactor-on exposure of 40.2 days (3426 MW-days) and 37.8 days of reactor-off, 31678±304 (stat.) $\overline{\nu}_e$-induced IBD events were detected from ^{235}U fissions. Comparing the PROSPECT prompt energy spectrum to the Huber model, a global $\chi^2/ndf = 51.4/31$ is observed and

further tests suggest that ^{235}U is not the sole isotope responsible for the event excess observed at LEU reactors.

7.1 Data set and processing

Data for this analysis was collected from April 2018 to July 2018, with calibrations using the `Analyzed_2018A` processing configurations. A total of 46.74 operational days of reactor-on data was recorded over two reactor cycles. Reactor-off backgrounds were measured before and after each cycle totaling 42.69 operational days of data. Accounting for trigger pile-up (average 2% reactor-on, 1% -off) and shower veto (average 12% reactor-on, 11% -off) deadtimes, the collection times are reduced to 40.26 and 37.80 exposure days for reactor-on and -off statuses, respectively. Data runs of approximately one hour in length were classified as reactor-on and -off and processed following the same procedure described in Section 6.2.

An 85 keV software threshold is applied to reject low-energy pulses with non-uniform event reconstruction, caused by variations in the hardware thresholds over time. A Gaussian smearing is applied to the E_{rec} of each event to unify the resolution across the detector to the lowest segment of 400 PE/MeV. Segments with at least one dead PMT are excluded, including those in the fiducial region: segment number (0, 1, 2, 3, 5, 6, 9, 10, 11, 12, 13, 18, 21, 23, 27, 31, 32, 34, 41, 44, 48, 52, 56, 63, 69, 79, 86, 87, 115, 122, 127, 139). This results in a 24% volume reduction of the nominal fiducial region, as shown in Figure 7.1. As in the oscillation analysis, events originating in the inactive volume with one annihilation γ-ray reconstructed around 0.5 MeV are eliminated from the region of interest between 0.8-7.2 MeV.

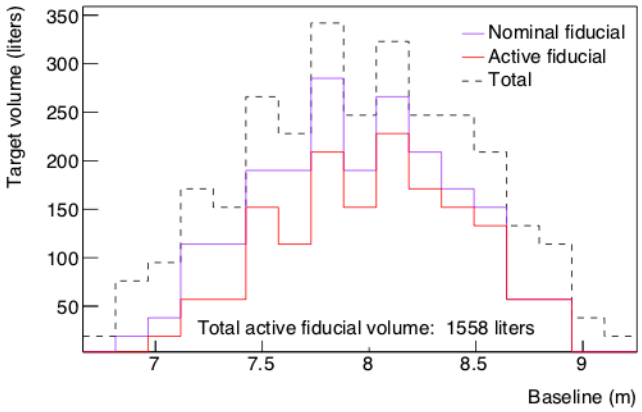

Figure 7.1: Distribution of ^{6}LiLS volume versus baseline. The total volume (dashed black), nominal fiducial volume (purple), and active fiducial volume for the spectrum analysis (red) are shown. The exclusion of dead segments results in a 24% reduction from the nominal fiducial volume. This assumes an active volume of 19 L per segment, including the z-position fiducial cut.

7.2 IBD event selection

The IBD selection scheme used to identify IBD-like candidates in the oscillation analysis (see Section 6.3) was optimized for effective statistics, as the ratios of L vs. E spectra are less sensitive to the absolute spectrum shape. The selection resulted in large spectral features from (n,H) and (n,C*) interactions that can affect the reactor-on and reactor-off subtraction in the case of time-dependencies. Thus, a re-optimization of cuts was performed to increase signal-to-background and reduce the cosmogenic background peaks for the spectrum analysis. This choice results in a decrease in statistics, but a more pure IBD sample.

Cuts that could contribute to the background features, including constraints not implemented in the oscillation analysis, were studied using the reactor-off data set. Each cut was studied in detail to ensure that no energy biases are introduced to the data. The selection was then implemented on the reactor-on set, the subtraction was performed, and an effective statistic (relative bin-to-bin statistics + 5% correlated

systematic) was calculated to determine the cut performance. To avoid visual bias, the IBD spectrum was not revealed. Table 7.1 summarizes the IBD selection optimized for the spectrum analysis. Events with [0.8,7.2] MeV are used to build the spectrum.

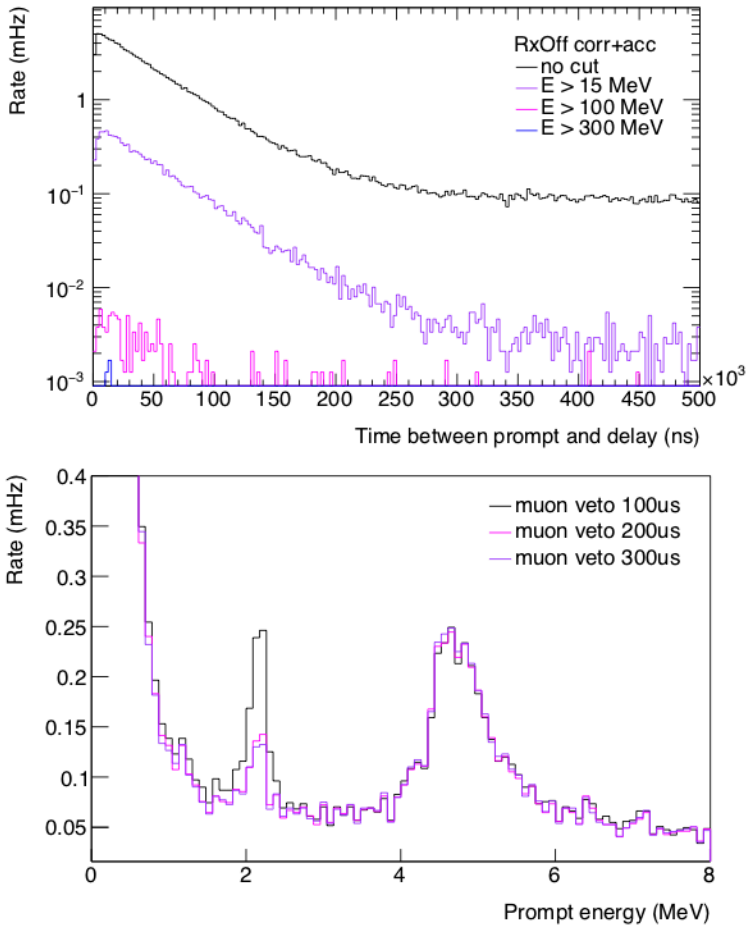

Figure 7.2: **(top)** Time difference between the prompt and delayed events defining the neutron shower. Various energy selections are shown to represent a muon ($E >$ 15 MeV, purple) and hadronic ($E >$ 300 MeV, blue) prompt. **(bottom)** Deadtime-corrected reactor-off spectra for various muon veto time windows. This cut has a large impact on the magnitude of the (n,H) feature. For reference, the oscillation analysis used a muon veto window of 100μs. From collaboration Refs. [211–213].

The shower veto times were found to have the largest impact on the shape of the background spectrum, specifically the magnitude of the (n,H) peak. The cut is designed to reject IBD-like candidates within neutron showers initiated by cosmic muons and fast neutrons. As no events can be accepted in the given time window, the

Cut level: type	Acceptance value(s)
1: delayed (n,^{6}Li) capture	$3.6\sigma > \overline{PSD}_e$, -$3\sigma < \overline{E_{rec}} < 3\sigma$
2: prompt PSD	$2.5\sigma < \overline{PSD}_e$
3: trigger pile-up	dt = [-800,800] ns
4: prompt-delayed time coincidence	dt = [1,120] μs
5: neutron shower veto	delay (n,^{6}Li) tag
muon-induced	prompt muon ($E_{prompt} > 15$), dt = [0,200] μs
fast neutron-induced	prompt recoil ($3\sigma > \overline{PSD}_e$, E_{rec} >0.25 MeV) or (n,^{6}Li), dt = [-250,250] μs
6: prompt-delayed distance coincidence	Δxyz = [180, 140] mm
7: fiducialization	z: include [-444, 444] mm
	x, y: exclude outer shell, second bottom layer
	x, y: exclude segments (23,24,25,26)

Table 7.1: Summary of IBD event selection cuts used in the spectrum analysis. The neutron shower veto is used to reject candidate IBDs within a given time window of muon or fast-neutron induced events, tagged by a delayed (n,^{6}Li) capture. The Δxyz cut corresponds to the 3D distance separation in the same (same, adjacent) segments. Accidental IBD-like candidates are selected using the same criteria, with the exception that the prompt-delay time coincidence is taken from the off-time window dt = [-12,-2] μs.

veto can introduce a significant deadtime, and the window is required to optimize the rejection and loss of exposure time. Figure 7.2**(top)** shows the time distributions between prompt and delay shower tags for various energy ranges. At moderate energies ($E > 15$) where minimum-ionizing muon events are expected, it is clear that extending the veto by several lifetimes ($dt \sim 300\mu$s) allows for a cleaner selection of IBD events. However, such a selection increases the deadtime to $\sim$18%. There is little activity at higher energies ($E > 100\,\text{MeV}$) where a hadronic component could be present in the shower, therefore no additional veto was implemented. Figure 7.2**(bottom)** shows the effect on the background spectrum with various muon veto window sizes. As expected, the larger window rejects more thermal neutrons resulting in a reduction of the (n,H) peak. As the spectrum measurement is statistics-limited, a muon veto window of $dt = 200\mu$s was chosen to balance the signal purity with deadtime. The fast neutron-induced veto has a small affect on this feature, and the window was increased to $dt = 250\mu$s for this analysis.

The change in shower veto cuts had a negligible impact on the magnitude of the (n,C*) peak. This feature is difficult to reduce as the prompt pulse has components from the 4.4 MeV excitation γ-ray and proton recoils from the scattered fast neutron. The PSD of the overall signal is slightly increased, however not far enough away from the electronic recoil band mean for it to be rejected. To help sharpen the peak, the prompt PSD cut was slightly tightened compared to the oscillation analysis, at the cost of a statistics loss.

The delayed neutron capture acceptance criteria was altered, to be defined by the mean energy ensuring better selection efficiency over time as the detector performance varies and the capture width increases. The z-position fiducial cut was slightly changed to an account for a dimension mistake made in the oscillation analysis. Due to the loss of more PMTs during the spectrum analysis data set, the xy fiducialization excludes the outer shell and the second layer from the bottom of the detector. This

allows for a more uniform response throughout the detector and provides a proper γ-ray catcher for the segments near the floor. Although the topological behavior of prompt events is observed to be different for reactor-on and -off events, cuts focused on isolating the positron and the annihilation γ-rays, including constraints on multiplicity and energy outside of the maximum energy segment, were found to have no impact on the background reduction.

7.3 Cross-checks

Prior to building the total IBD spectrum from the reactor-on and -off data sets, multiple validations of the background subtraction were performed, inside and outside the analysis region of interest. These cross-checks are essential for ensuring that the energy reconstruction and selection criteria are robust against any time or position-dependence of the cosmogenic or reactor-related backgrounds and changing detector geometry with inactive segments. Consistency tests were first applied to the reactor-off and reactor-on samples independently before proceeding with on-off subtractions.

Of primary concern is the stability of IBD-like backgrounds over time. As previously described, the cosmogenic fast neutron and muon rate at near-surface positions varies with atmospheric pressure. If the cut values are sensitive to these changes, the magnitude of the prominent (n,H) and (n,C*) spectral features can have a large impact on the background subtraction. To verify the time independence of the selection efficiency, the reactor-off data set was split into two time periods. The two samples had roughly equally statistics and were divided such that no data cycle was split. An atmospheric correction of $\alpha = 1.005$ was applied to account for small variations in atmospheric conditions, as detailed in Section 6.4.2. Figure 7.3**(top)** shows the comparison of the two samples, illustrating the consistency in both the rate and shape and validating the stability of the atmospheric scaling, energy reconstruction,

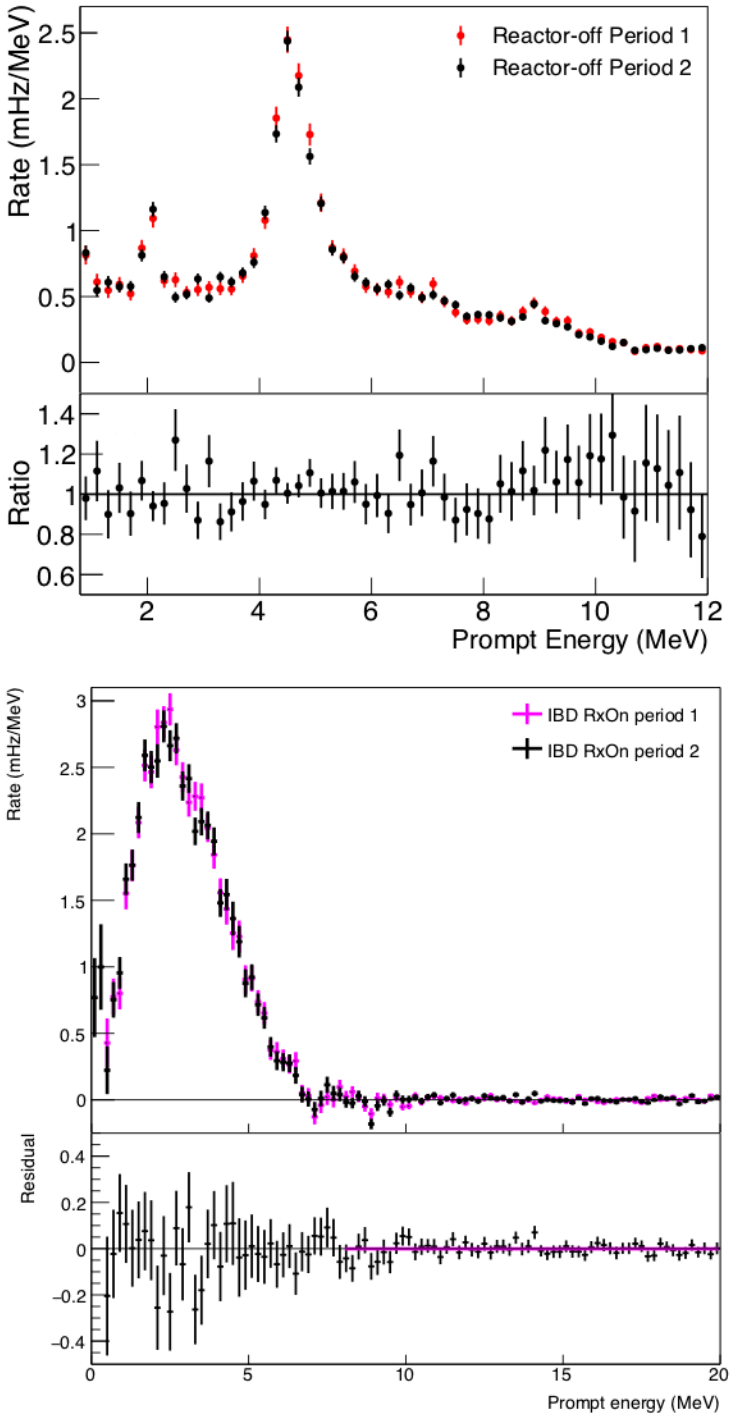

Figure 7.3: **(top)** Reactor-off IBD-like spectra from 0.8-12 MeV, where the data set is split into two time periods. Statistical errors are shown. The consistency of the ratio with unity ($\chi^2/ndf = 35.58/56$) between periods demonstrates the stability of cosmogenic IBD-like candidates after accounting for atmospheric conditions [183]. **(bottom)** IBD spectra from 0-20 MeV, where both the reactor-on and -off data sets are split into two time periods. Statistical errors are shown. No significant deviations are observed. Beyond the region of interest, from 8-20 MeV, the residual is consistent with zero, with a best-fit constant of -0.0007 and $\chi^2/ndf = 40.22/59$. From collaboration Ref. [214].

and IBD selection. The ratio of the two spectra are in good agreement with unity, with a $\chi^2/ndf = 35.58/56$, when including statistical errors only. Similar tests were performed on subtracted spectra, by dividing both the reactor-on and -off data sets prior to subtraction, as shown in Figure 7.3**(bottom)**. Atmospheric scale factors of $\alpha = 0.9895$ and $\alpha = 0.9929$ were applied to data periods one and two, respectively. No significant differences are observed. The ratio of the two periods is consistent with unity, with a $\chi^2/ndf = 18.6/32$ in the region of interest. Above 8 MeV, the IBD spectrum falls to zero as expected, with a best-fit constant of -0.0007 and $\chi^2/ndf = 40.22/59$.

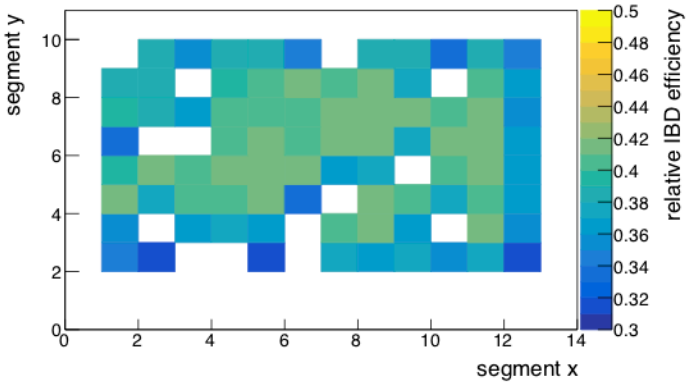

Figure 7.4: Relative IBD detection efficiency per segment, generated from `PROSPECT-G4`, for the spectrum data set. From collaboration Ref. [215].

To verify the position-dependence of events, independent spectra were generated based on the reconstructed IBD vertex and dividing the samples into divisons across the detector. All spectra were normalized by baseline to remove the expected $1/r^2$ dependence from the reactor and corrected for mass and relative detection efficiency. Figure 7.4 shows the relative IBD efficiency map for the spectrum data set, where the average efficiency has decreased by ~5% compared to the oscillation data set, due to the increase of inactive segments. By splitting the detector into quadrants and near-far halves from the reactor, consistent spectra were observed, indicating that the cut selection sufficiently handles the spatial variation of the correlated and accidental

backgrounds. The detector was also divided into exclusive inner and outer regions to ensure the PROSPECT-G4 model could reproduce the expected energy shift from γ-ray leakage. The most extreme variant, with an inner region of 10×6 segments surrounded by an outer region of a single layer of segments, is shown in Figure 7.5. A clear difference between the peaks is observed, where the outer spectrum is shifted downwards due to escaping energy. The Monte Carlo generally reproduces this behavior and the magnitude of the shift.[1] This suggests that the model can successfully account for γ-ray leakage and that there are no unexpected background features in the outer layer of the detector.

7.4 Spectrum measurement

Using the same procedure outlined in Section 6.4, correlated and accidental IBD candidates were measured from reactor-on and reactor-off samples. The prompt energy spectra, in 200 keV-wide bins, are shown in Figure 7.6. With more reactor-off data than the oscillation analysis, the general structure of the background is similar, with the exception of the reduced ratio of the (n,H) to (n,C*) peak, due to the increased muon shower veto time window. The (n,C*) peak and continuum has shifted slightly downwards towards $\sim$4.5 MeV as a result of the new prompt PSD selection criteria. The accidental rate is larger compared to that measured in the oscillation analysis and is suspected to be a result of varying operations at the Materials Irradiation Facility (MIF) at HFIR. Similar weak lines from accidental coincidences of natural ^{208}Tl and ^{40}K are observed.

According to Equation 6.9, a series of bin-wise subtractions were performed to produce the final IBD candidate energy spectrum. An atmospheric correction factor of $\alpha = 0.991\pm0.004$ was applied to account for variations in pressure during data taking

[1] It should be noted that this model does not include corrections for $\overline{\nu}_e$ from ^{28}Al, ^{6}He, or non-equilibrium isotopes.

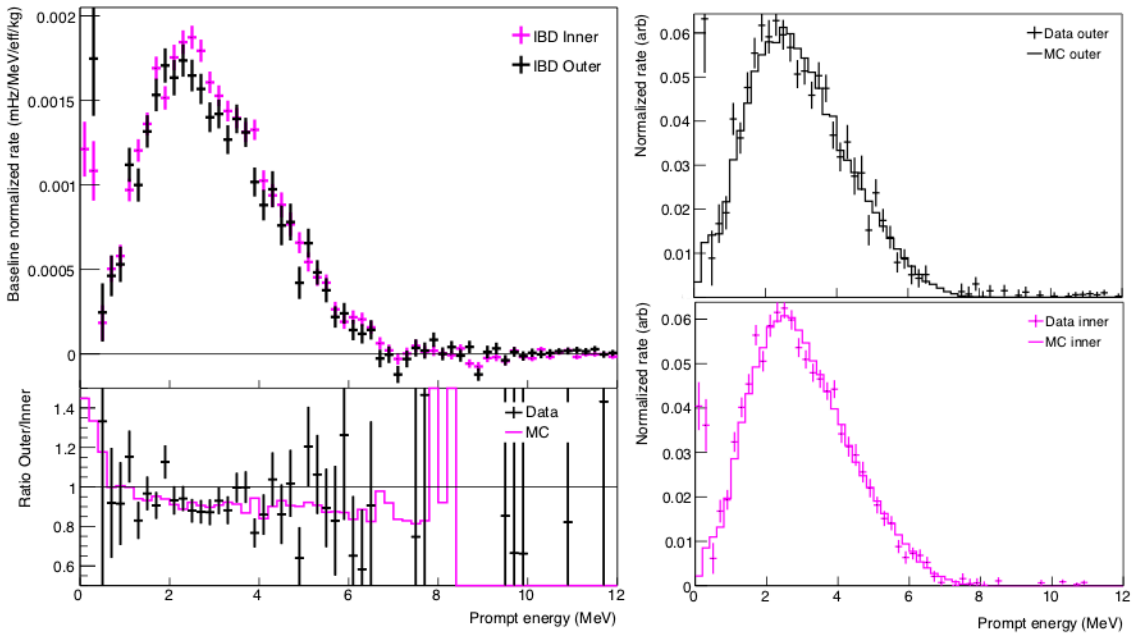

Figure 7.5: **(left)** Comparison of IBD spectra from outer (black) and inner (magenta, 10×6 segments) detector regions. A shift from energy leakage is observed. The bottom panel shows the ratio of outer/inner for the data and Monte Carlo, where the slope is in general agreement. As the spectra fall to zero, statistical fluctuations cause negative counts, pushing those points outside of the ratio range. **(top right)** Outer spectra for data (points) and model (line). **(bottom right)** Inner spectra for data (points) and model (line). The PROSPECT-G4 model is normalized to the data integral in the region of interest (0.8-7.2 MeV). Contributions from ^{28}Al or non-equilibrium isotopes are not included in the model, which has a slight effect at low energies. From collaboration Ref. [214].

periods, which can change the underlying fast neutron background spectrum. Figure 7.6 shows the first precision $\overline{\nu}_e$ prompt energy spectrum measured by PROSPECT from 0.8-12 MeV. As expected, the spectrum increases from the IBD threshold and then falls to zero at higher energies. The shape does not appear smooth, in particular around the peak. These features could be interpreted as fine structure corresponding to the individual $\overline{\nu}_e$ contributions from strong fission (high yield) fragments. However with the current statistics, it is not possible to distinguish between this scenerio from fluctuations. The small deviation around 9 MeV is suspected to be a statistical artifact, as the comparison of two reactor-off samples (Figure 7.3) shows a ∼2 sigma

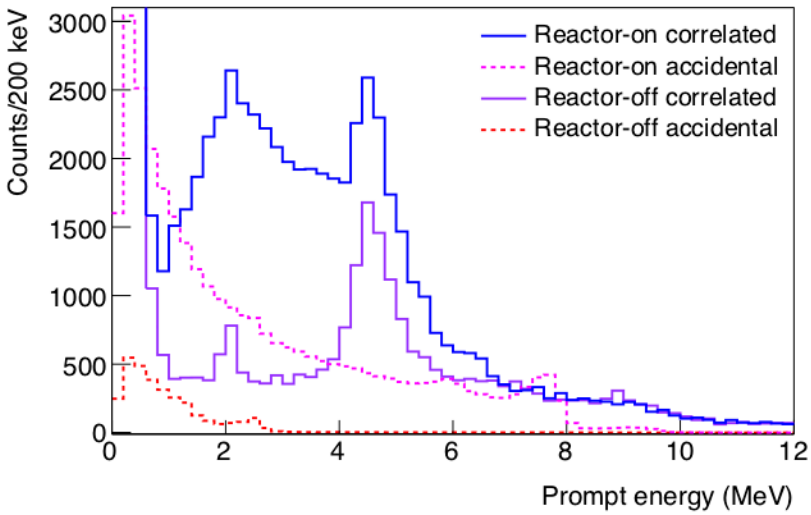

Figure 7.6: Measured (smeared) prompt energy spectra in raw counts of reactor-on correlated (blue), accidental (magneta) and reactor-off correlated (purple), accidental (red) IBD-like candidates from the spectrum analysis data set. Visible peaks in the correlated spectra are due to muon-(∼2.2 MeV) and fast neutron-(∼4.5 MeV) induced events. Peaks at higher energy in the reactor-on accidentals is due to γ-ray lines from the neutron capture of beam products on ^{56}Fe in rebar in the concrete floor. The 2.6 MeV peak from natural ^{208}Tl is sightly visible in both reactor-on and -off accidentals.

difference in this bin.

The relevent statistics of the spectrum measurement in the region of interest from 0.8 to 7.2 MeV are summarized in Table 7.2. A total of 31678 IBD candidates were detected, at a rate of 678 events per day. The correlated signal-to-background ratio has been greatly improved over the oscillation analysis at 1.7, which is the best achieved by a near-surface neutrino detector to-date. In less than half of the exposure time, PROSPECT has measured roughly six times the statistics of the ILL experiment [67] described in Chapter 2, and is now the world-leading measurement of the ^{235}U $\overline{\nu}_e$ spectrum.

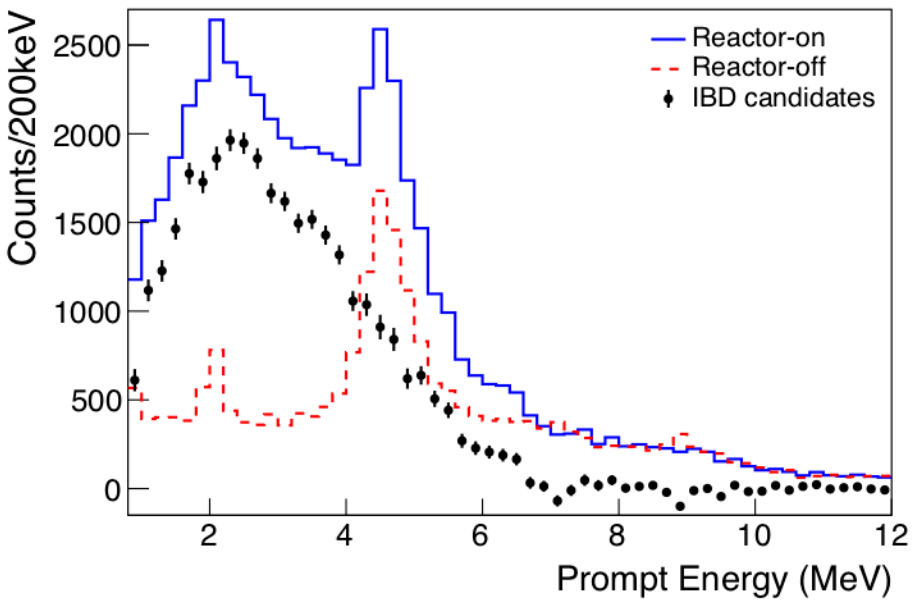

Figure 7.7: The measured prompt energy spectrum of IBD events (black) compared to reactor-on (blue) and reactor-off (red) correlated candidates with statistical errors included. The reactor-off correlated candidates have been scaled to match the reactor-on exposure [183].

Type	Value
Reactor-on (40.26 exposure days)	
Correlated+accidental	70811±267
Accidental (scaled)	20534±16
Correlated	50277±267
Reactor-off (37.80 exposure days, scaled)	
Correlated+accidental (scaled)	20036±145
Accidental (scaled)	1436±4
Correlated (scaled)	18600±145
Detection	
IBD candidates	31678±304 (678/day)
Correlated S:B	1.70:1
Accidental S:B	1.54:1

Table 7.2: Summary of IBD-like event statistics for the precision spectrum measurement in the region of interest [0.8,7.2] MeV. Uncertainties are statistical only. Reactor-off and accidental effective samples are scaled according to Equation 6.9. Signal-to-background is denoted by S:B.

7.5 Model generation and inputs

Predicted reactor $\overline{\nu}_e$ energy spectra are compared to the measured PROSPECT spectrum to explore the possible contributions of ^{235}U models to the local excess observed between 4-6 MeV in prompt energy by the LEU experiments. In this analysis, no attempt is made to unfold the detected prompt spectrum into the antineutrino energy distribution. It should be noted that the prompt energy scale measured by PROSPECT and other reactor experiments, including Daya Bay, are not identical. As the signal combines the deposited energy of IBD positron and annihilation γ-rays, the prompt scale is highly-dependent on the detector geometry and scintillator nonlinearity. Thus, input reactor predictions are converted from antineutrino energy into prompt energy via the detector response model produced by `PROSPECT-G4` Monte Carlo. With estimates for the systematic uncertainties, the predictions can then be qualitatively compared to the PROSPECT measurement.

7.5.1 Detector response

The energy response model, which includes the impact of the detector geometry and scintillator properties, is constrained by the same procedure as detailed in Chapter 5. Table 5.2 shows the best-fit parameters extracted for this analysis to describe the energy nonlinearity and scale. Using multiple γ-ray lines from the radioactive calibration sources, Figure 7.8**(top)** shows the ratio of the reconstructed energy to Monte Carlo for depositions throughout the full detector. The reconstruction is consistent within $\pm 1\%$ across the full data set and all segments. Additional figures demonstrating the agreement between data and the best-fit Monte Carlo from the spectrum analysis can been seen in Section 5.4.

With these parameters input into the simulation, the detector response matrix is built by generating a flat spectrum of $\overline{\nu}_e$ with binned energies 50 keV-wide, from

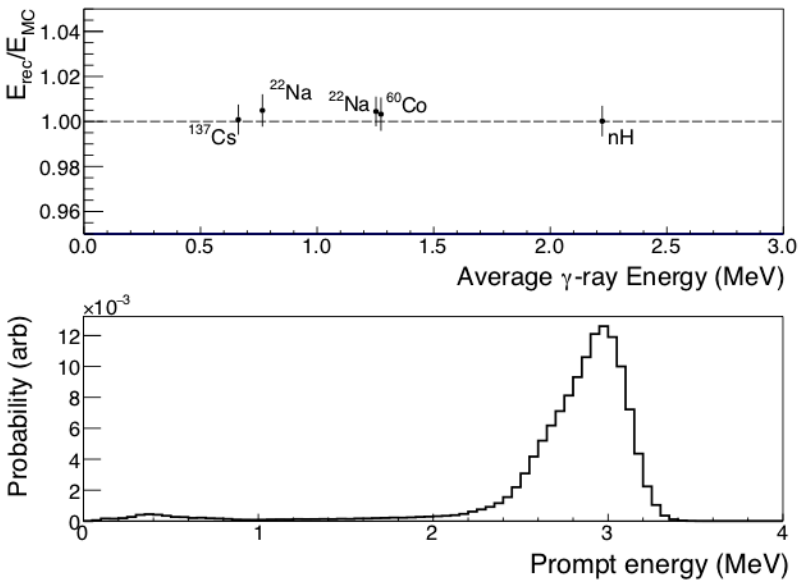

Figure 7.8: **(top)** Ratio of measured to MC E_{rec} versus average γ-ray energy, showing $\pm 1\%$ residual difference. **(bottom)** The simulated E_{rec} of a narrow band of [4.0, 4.05] MeV $\overline{\nu}_e$ energies. The distribution is shifted downwards due to scintillator nonlinearity and asymmetrically broadened by escaping annihilation γ-rays [183].

1.8 to 10.0 MeV. These events are run through the `PROSPECT2x_Analysis` pipeline and passed through the IBD selection criteria. Energy depositions in inactive segments are discarded. An example slice of reconstructed events with true antineutrino energy between [4.0,4.05] MeV is compared to the detected prompt energy in Figure 7.8**(bottom)**. It is clear that the prompt energy is not only shifted down from the IBD threshold, but the peak is broadened due to escaping annihilation γ-rays. Scintillator nonlinearity also contributes to the asymmetric nature of the tail. This response is notably different than that of large, homogenous scintillator detectors where a simple Gaussian is expected with only small corrections from detector effects. Figure 7.9 shows the total detector response matrix. Events with prompt energy around 0.5 MeV are caused by IBD interactions that originate in inactive segments but whose capture neutron and annihilation γ-rays are detected in the active material. These events are excluded from the analysis as they are outside the region of interest. The origin of the unphysical IBD events (100 out of $\sim$40 million detected) with prompt

energy above the true energy is not currently understood, but could be related to pile-up or accidental events in the Monte Carlo. The response matrix is rebinned into 200 keV-wide steps in order to convert reactor $\overline{\nu}_e$ models into PROSPECT prompt energy spectra.

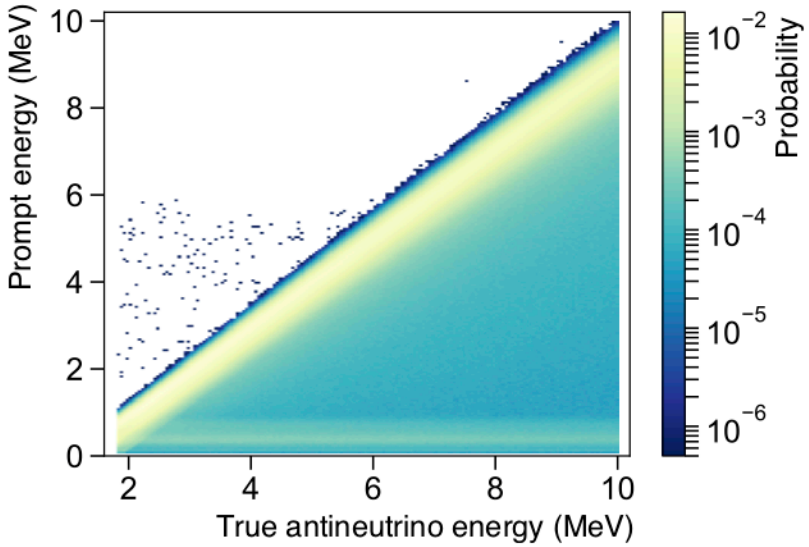

Figure 7.9: Total detector response matrix used in the spectrum analysis. Reconstructed events near ~0.5 MeV are produced by IBD interactions with vertices inside an inactive segment, and are outside of the region of interest. The unphysical events with prompt energy above the true antineutrino energy are suspected to be caused by unfiltered pile-up events in the Monte Carlo [183].

7.5.2 Reactor and detector model

Similar to the oscillation analysis (see Section 6.6), the predicted $\overline{\nu}_e$ spectrum is generated using the Huber ^{235}U flux model and the Vogel-Beacom IBD cross-section. The detector response is applied to this model, resulting in a predicted PROSPECT-like IBD prompt energy spectrum. This prediction assumes a 3ν model with no sterile neutrino oscillations.[2] Additional corrections are made to account for the non-^{235}U

[2]The existence of a sterile neutrino would create a distortion in the total energy spectrum at these baselines, dependent on the specific mixing parameters. However, since the PROSPECT oscillation measurements do not indicate the presence of a sterile, no correction is made here. Furthermore, a sterile neutrino cannot cause the local energy excess observed by the LEU reactor experiments, which is the primary focus of this analysis.

contributions to the $\overline{\nu}_e$ flux from ^{28}Al (0.68% total) and non-equilibrium isotopes (0.50%) for the reactor cycles used in this data set. An additional correction is made for the production of $\overline{\nu}_e$ from ^{9}Be in the neutron reflector:

$$n + {}^{9}Be \rightarrow \alpha + {}^{6}He \xrightarrow{t_{1/2}=0.80\,s} {}^{6}Li + \beta^{-} + \overline{\nu}_e, \tag{7.1}$$

where the β endpoint is Q=3.51 MeV. Again, this contribution (0.25% total) primarily impacts the spectrum at low energies and increases over time as control rods are withdrawn. The ^{28}Al and ^{6}He $\overline{\nu}_e$ fluxes are calculated using a detailed model of the reactor in SCALE (ORIGIN) [216–218]. Figure 7.10 illustrates the effect of these contributions compared to the Huber model in prompt energy, generated according to the ENDF and ENDSF data using the OKLO toolkit [219, 220]. No correction is applied to account for possible $\overline{\nu}_e$ from spent nuclear fuel.

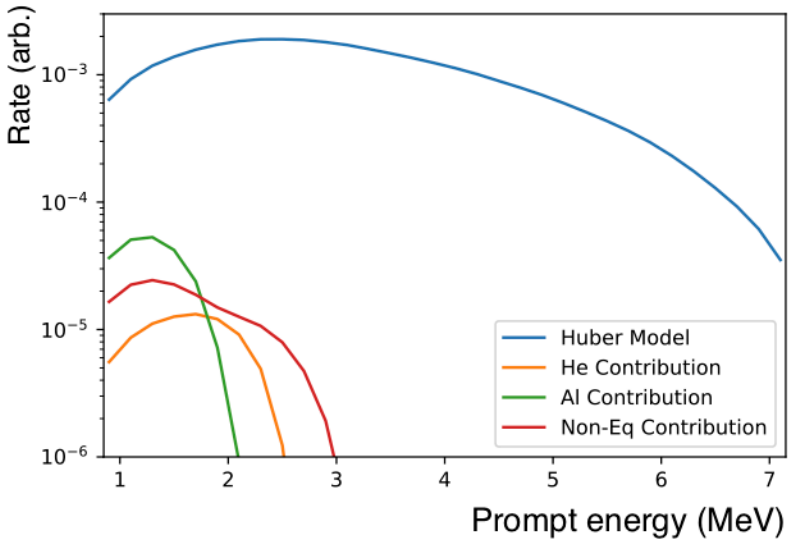

Figure 7.10: ^{28}Al, ^{6}He, and non-equilibrium contributions to total $\overline{\nu}_e$ spectrum, for the reactor cycles used in this analysis data set, as compared to the Huber model. From collaboration Ref. [221].

The Huber ^{235}U $\overline{\nu}_e$ spectrum, with the addition of non-^{235}U and non-equilibrium corrections, is multiplied by the detector response matrix and transformed into the

PROSPECT prompt energy basis. To match the data, the model is rebinned into 200 keV-wide bins via linear interpolation from the original 250 keV-wide bins. The spectrum is then normalized such that the integral in the region of interest from 0.8-7.2 MeV is equal to the statistics in the measured spectrum.

7.6 Uncertainty characterization

Covariance matrices for statistical and systematic uncertainties are summed together to create the full covariance matrix, V_{tot}. The uncorrelated statistical errors in each energy bin are calculated using Poisson statistics, accounting for the increased uncertainty due to the subtraction of reactor-on and reactor-off data (see Equation 6.10). `PROSPECT-G4` simulations, toy models, and calibration data are used estimate the systematic uncertainties.

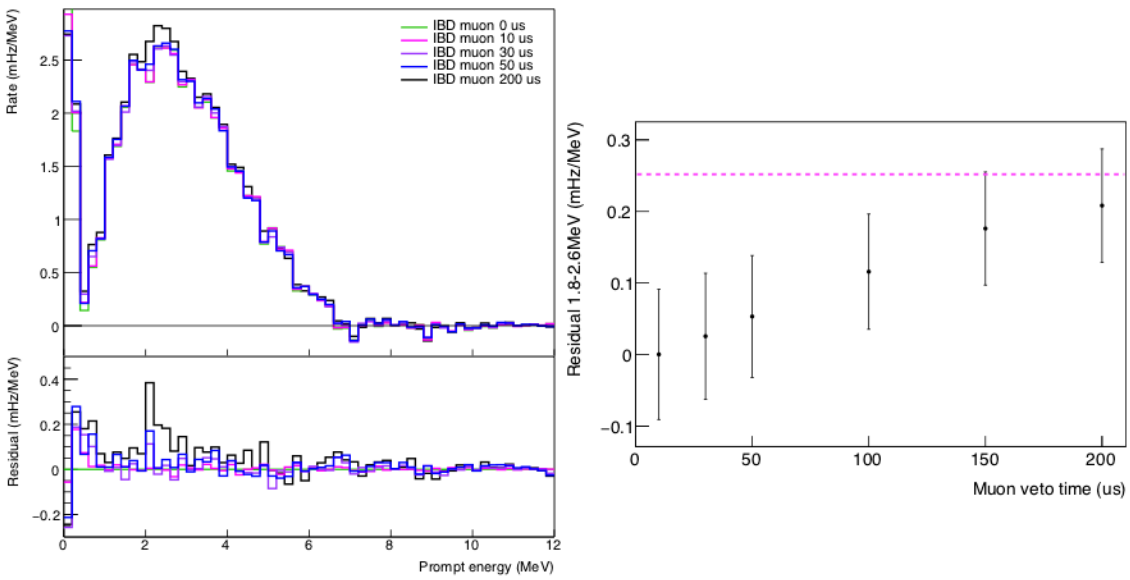

Figure 7.11: **(left)** IBD spectrum with various muon shower veto timing cuts, ranging from no cut (green) to the default value (black). The bottom panel shows the residual of each spectrum with respect to the no cut scenerio (green). **(right)** Integral of the residual from [1.8,2.6] MeV. The data approaches a rate of ∼0.25 mHz/MeV, where no contamination from neutron showers is expected. From collaboration Ref. [214].

The spectrum measurement is sensitive to the shape and rate of backgrounds due to the subtraction. A data-driven method is used to determine the background normalization uncertainty. Measurements of the variation between the two reactor-off periods (see Section 7.3) and the fast neutron correlation with atmospheric pressure indiciate a small systematic of 0.5%, which is significantly less than the conservative estimate used in the oscillation analysis. Toy models were generated by varying the atmospheric scale factor α between [0.95,1.02] to confirm the sensitivity of the bump region to the normalization. An additional systematic is included to account for any independent variation of muon and fast neutron induced background features. This is estimated by varying the muon shower veto window from 0μs, where no shower-induced events are vetoed, to the default cut value of 200μs. The region of the IBD spectrum around the background (n,H) peak is most sensitive to the veto, as illustrated in Figure 7.11**(left)**. The residual of each cut, relative to the 0μs scenerio, is integrated from [1.8,2.6] MeV. Figure 7.11**(right)** shows the residual approaching a rate plateauing near $\sim$0.25 mHz/MeV, representing the ideal scenerio where all cosmogenically-induced IBD events would vanish. The difference between this case and 200μs is $\sim$0.05 mHz/MeV, and when compared with the background rate in this region of 1.2 mHz/MeV (not shown), a 4% difference results. This number is taken as the muon veto (n,H) peak uncertainty, which has a small impact given the size of the statistical error.

Similar to the oscillation analysis, uncertainties in the energy response model are estimated by varying the best-fit parameters in the toy Monte Carlo. Additional systematics are added to account for the energy resolution smearing and threshold that is applied to the reconstructed data to ensure uniformity across all segments over time. Uncorrelated uncertainties for the optical separator thickness and the resolution of the z fidicualization cut are accounted for as they affect the total detected energy and IBD selection efficiency, respectively. Using the same procedure outlined

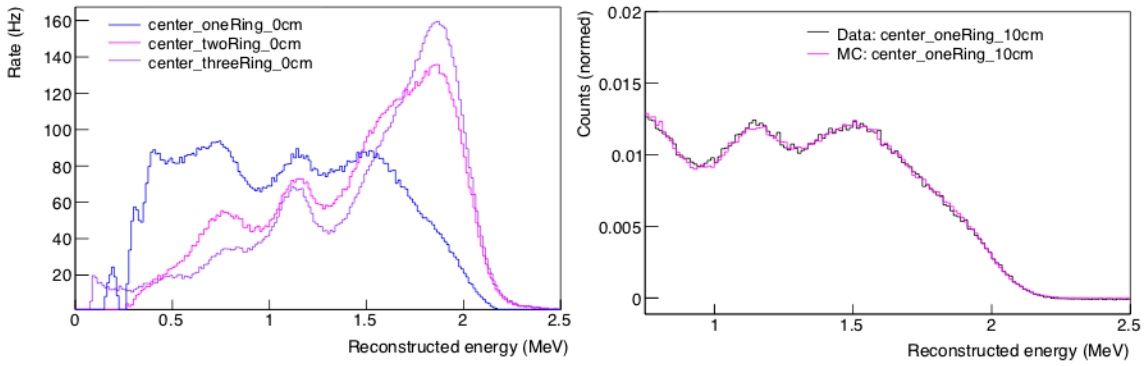

Figure 7.12: **(left)** ^{22}Na calibration spectra taken at the center of the detector in the center of the segments (z=0 cm). One ring (blue) sums the energy deposits from the segments adjacent to the source, two ring (pink) sums from two layers of segments (inclusive) around the source, and three ring (purple) integrates three layers of segments. The features differ due to the variation in γ-ray containment. **(right)** Data and Monte Carlo comparison of ^{22}Na one ring spectra from the center of the detector with a 10 cm offset from the segment center. Lower energy events have been removed due to contamination from the ^{137}Cs source deployed at the same time. The Monte Carlo is normalized to the data integral. From collaboration Ref. [222].

in Section 6.7, an energy loss systematic is calculated by comparing calibration data and Monte Carlo. Deployments of the ^{22}Na source near the center and edge of the detector at various z-positions can mimic the escaping energy of the IBD prompt annihilation γ-rays. Reconstructing the energy in layers around the source, in one, two, or three rings, allows for multiple features to compare with simulation, as illustrated in Figure 7.12. The energy loss error is taken from the largest shift observed between the fitted data and Monte Carlo from one ring reconstructions, the spectra shown in Figure 7.12. In this analysis, a shift of 8 keV was determined and used to generate PROSPECT-like toy Monte Carlo sample for obtaining the covariance matrix.

Reactor $\overline{\nu}_e$ model correlated uncertainties are included in the total covariance matrix V_{tot}. Bin-wise systematics for the Huber ^{235}U model are provided in Ref. [63]. Contributions from ^{28}Al, non-equilibrium isotopes, and ^{6}He are conservatively assumed to have 100% error. Table 7.3 summarizes the estimated systematic uncertainties for the spectrum analysis. The total covariance matrix, including statistical and

systematical uncertainties, is shown in Figure 7.13.

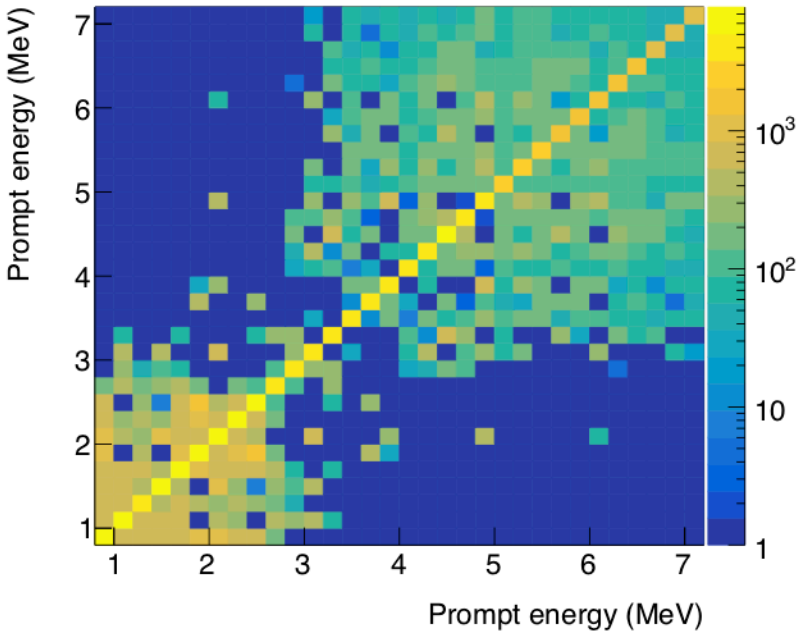

Figure 7.13: Total covariance matrix [183].

7.7 Comparison to ^{235}U $\overline{\nu}_e$ models

Following Equation 6.1, a χ^2 test is used to quantify the agreement between the PROSPECT measured spectrum and the model predictions. The total covariance matrix V_{tot} is multiplied by the 32-element vector Δ, which summarizes the difference between the measured and predicted spectra:

$$\Delta_i \equiv N_i^{obs} - N_i^{pred} \times (1 + \eta), \tag{7.2}$$

where N_i^{obs} and N_i^{pred} are the number of counts in each energy bin i. The prediction is normalized by the integral of the data in the region of interest, represented by the nuisance parameter η. The shape-only comparison of the PROSPECT detected prompt energy spectrum to the prediction based on the Huber ^{235}U model is shown in

Systematic parameter	Value	Uncertainty (σ)
Background		
Normalization	–	0.5%
Muon veto (n,H) peak	–	4% in [1.8,2.6] MeV
Detector effects		
Birks' coefficient k_{B1}	0.122 mm/MeV	0.002 mm/MeV
Birks' coefficient k_{B2}	0.032 mm/MeV	0.002 mm/MeV
Cherenkov nonlinearity k_C	41%	4%
Energy scale β_{rec}	1	0.06%
Energy loss	–	8 keV
Energy smearing	400 PE/MeV	8 PE/MeV
Uncorrelated separator thickness	1.18 mm	0.5 mm
Uncorrelated z fiducial cut	444 mm	25 mm
Energy threshold	85 keV	5 keV
Reactor $\overline{\nu}_e$ model		
^{28}Al spectrum correction	–	100%
Non-eq spectrum correction	–	100%
^{6}He spectrum correction	–	100%
Huber prediction [63]	–	per bin

Table 7.3: Summary of estimated systematics in the spectrum analysis. All uncertainties are correlated unless otherwise noted.

Figure 7.14. Statistical error bars are applied to the data, while the 1σ total systematic band is applied to the model. The top panel illustrates the spectral correction due to the $\overline{\nu}_e$ flux from ^{28}Al, ^{6}He, and non-equilibrium isotopes. When added to the Huber prediction, these events impact the low-energy region of the spectrum. A global minimum χ^2/ndf of 51.4/31 is observed between 0.8-7.2 MeV. This corresponds to a one-side p-value of 0.01, indicating poor overall agreement between the data and the model.

To quantify the impact of each bin on the overall fit, a signed χ^2 contribution per bin, $\widetilde{\chi}_i$, is calculated. Due to the large statistical fluctuations in the data, a free-floating nuisance parameter κ is multiplied by the prediction in every individual bin.

This allows each bin to vary completely, resulting in a change to the minimized χ^2,

$$\widetilde{\chi}_i = \frac{N_i^{obs} - N_i^{pred}}{\mid N_i^{obs} - N_i^{pred} \mid} \sqrt{\sum_j (\chi^2_{ij,original} - \chi^2_{ij,new})}, \tag{7.3}$$

where

$$\chi^2_{ij} = [N_i^{obs} - N_i^{pred}(1 + \eta + \kappa_i)] V_{ij}^{-1} [N_j^{obs} - N_j^{pred}(1 + \eta + \kappa_j)]. \tag{7.4}$$

The covariance matrix is adjusted for the new normalization to correctly handle the model uncertainties. Figure 7.14**(bottom)** displays the $\widetilde{\chi}_i$. Because of limited statistics, large variations between neighboring bins is observed. As expected, the bins above 5.5 MeV have the greatest contribution to the global χ^2.

As the statistical fluctuations dominate the uncertainties in each bin, it is advantageous to quantify the agreement on larger scales. Following a similar procedure used by Daya Bay [223], the significance of local deviations from the Huber prediction in 1 MeV-wide sliding windows is calculated. Here, the difference between data and prediction is modified as,

$$\Delta_i \equiv N_i^{obs} - N_i^{pred} \times (1 + \eta - \mu_{k=1,2,3,4,5}), \tag{7.5}$$

where the μ's are free-floating nuisance parameters allowed to vary for each of the five, 200 keV-wide bins in the window. The χ^2 is then re-minimized over the μ parameters and the global normalization η, which constrains the amount of bin-wise variation according to the integral of the total spectrum. With the covariance matrices scaled to account for the new normalization, the change in χ^2 (>0) is determined:

$$\Delta\chi^2 = \chi^2_{original} - \chi^2_{new}. \tag{7.6}$$

This $\Delta\chi^2$ represents the contribution of the particular window to the overall goodness-

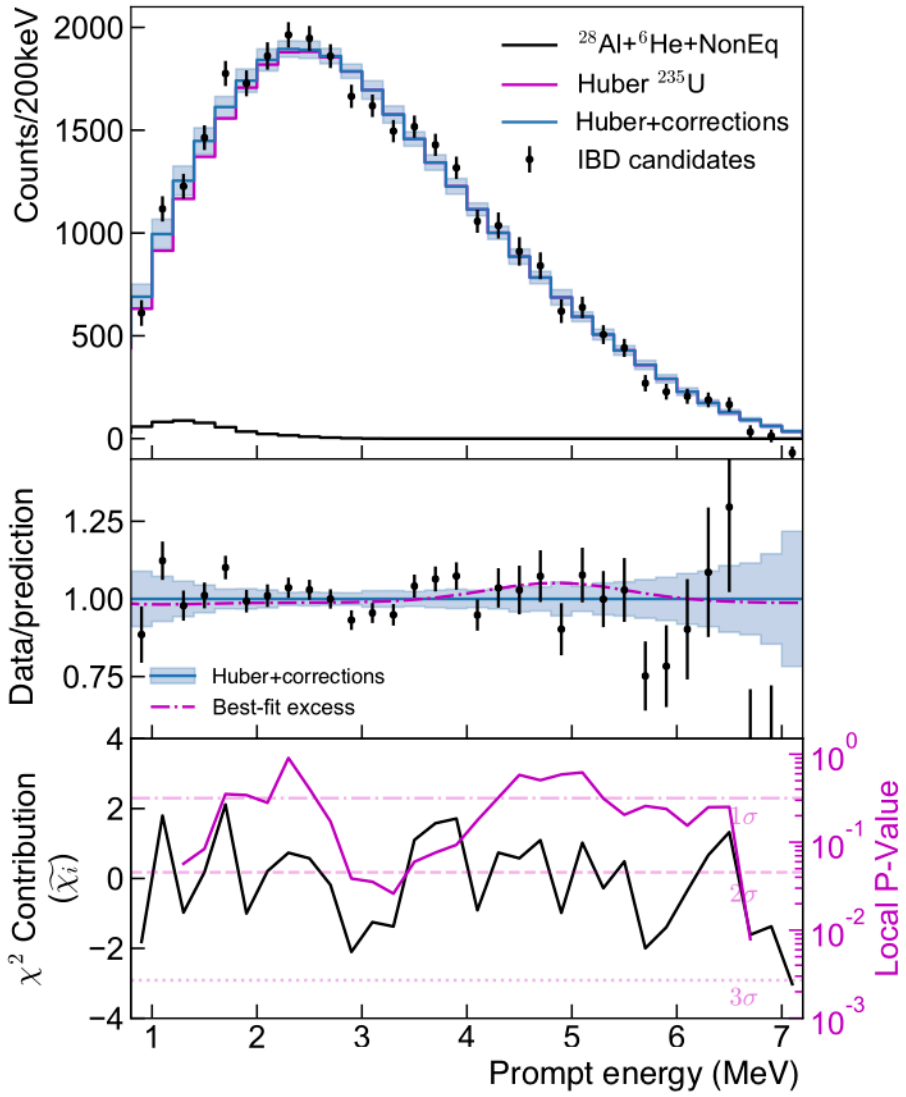

Figure 7.14: **(top)** The measured prompt energy spectrum of IBD events (black points) compared to prediction (blue line) based on the Huber ^{235}U model (purple line) with added $\overline{\nu}_e$ contributions from ^{28}Al, ^{6}He, and non-equilibrium isotopes (black line). The error bars are statistical only, while the shaded band includes detector and model uncertainties. This comparison is shape-only, as the normalization is left as a free parameter. **(middle)** Ratio of the corrected Huber model to the measured data and the best-fit excess represents the spectral discrepancy observed by experiments at LEU reactors. **(bottom)** The χ^2 contribution from each bin and the local p-value of a 1 MeV-wide sliding energy window for comparison to the corrected Huber prediction [183].

of-fit. Including the five degrees of freedom from each new nuisance parameter, the p-value is calculated. Figure 7.14**(bottom)** shows the local p-value for each successive,

overlapping 1 MeV window. With sensitivity to structure on the scale of ∼MeV, the regions of [2.8,3.5] MeV and >6.5 MeV show disagreements of 2-3σ significance between the PROSPECT data and the corrected Huber model prediction.

An additional ad-hoc model is created to compare PROSPECT's HEU spectrum to measurements from LEU reactors to address the possible contributions to the bump from ^{235}U. The model is generated by adding a Gaussian distribution with a fixed mean and width to the generic Huber prediction. These parameters (μ=5.6 MeV, σ=0.6 MeV) are found by comparing the Huber-Mueller prediction and the Gaussian distribution to the Daya Bay unfolded antineutrino energy spectrum [223], in the 5-7 MeV true energy region. The best-fit Gaussian distribution is then added to the corrected Huber prediction with the normalization n left as a free parameter (n=1 for Daya Bay). The normalization of the Gaussian distribution is varied in 500 steps from n = [-2.0,3.0], passed through the detector response matrix, rebinned, and normalized according to the data integral in the region of interest. Covariance matrices for each of the models are produced and the χ^2 between the data and prediction is calculated over the normalization. The minimum χ^2 is obtained at $n = 0.69 \pm 0.53$, where $n = 1$ corresponds to the Daya Bay excess. Although the correlated systematic uncertainties are included in the calculation through the total covariance matrix, statistics drive the sensitivity. The ratio of the best-fit model and the Huber prediction is shown in Figure 7.14**(middle)**. As Daya Bay's LEU measurement includes 50-60% fission-fraction from ^{235}U with the remainder from ^{238}U, ^{239}Pu, ^{241}Pu, PROSPECT's HEU measurement is compatible with the observed local energy excess. An excess of n = 1.78 would be required to match the size of the LEU spectrum distortion, which is disfavored at 2.1σ indicating that ^{235}U may not be the isotope responsible for the bump. With the current statstics, the PROSPECT $\overline{\nu}_e$ spectrum is consistent with the hypothesis that all of the LEU isotopes are incorrectly modelled in the 5-7 MeV antineutrino energy region.

Chapter 8

Conclusions and outlook

PROSPECT is a newly constructed, short-baseline neutrino oscillation experiment designed to search for eV-scale sterile neutrinos and precisely measure the ^{235}U antineutrino energy spectrum at the High Flux Isotope Reactor. With less than two months of reactor-on data, significant progress towards these goals has been achieved through the first oscillation search and spectrum measurement, which are detailed in this thesis. These results have made an early impact on the field, as PROSPECT currently provides the most competitive, model-independent limits on the existence of sterile neutrinos in the high Δm^2_{41} region based on $\overline{\nu}_e$ disappearance and the world-leading measurement of the ^{235}U $\overline{\nu}_e$ energy spectrum. Moreover, the instrumentation development program described here led to the construction of an innovative ^{6}Li-loaded liquid scintillator detector capable of observing neutrinos at Earth's surface with unparalleled signal-to-background.

Positioned >10 m from the 85 $\mathrm{MW_{th}}$ HEU High Flux Isotope Reactor, PROSPECT has measured the spectrum of $\overline{\nu}_e$ from ^{235}U fissions at multiple baselines. With a total of 25461±153(stat.) detected inverse beta decay interactions, prompt energy spectra measured at distances between 6.7 and 9.2 m are compared to the total spectrum. Through these ratios, a search for sterile neutrino oscillations was performed with

no reliance on reactor model predictions. Using the Feldman-Cousins prescription for determining confidence intervals, PROSPECT disfavors the Reactor Antineutrino Anomaly hypothesis at 2.2σ C.L. Reconstructing >31000 events across the full detector, PROSPECT has made the most precise measurement of the ^{235}U $\overline{\nu}_e$ energy spectrum to date. With an unprecedented signal-to-background of 1.7 at the near-surface and energy resolution of $5\%/\sqrt{E(\mathrm{MeV})}$, the measured spectrum is compared to reactor $\overline{\nu}_e$models to address the origin of the local excess observed by the LEU experiments. Tensions between the PROSPECT data and the Huber model result in a minimized global χ^2/ndf of 51.4/31, with 2-3σ local deviations in the regions of [2.8,3.5] MeV and >6.5 MeV prompt energy. Adding a Gaussian excess to this model informed by the Daya Bay measurements suggesting the data disfavors the hypothesis that the observed spectral deviations are caused by incorrect modelling of U^{235}-only. Further refinements and improvements to both analyses are underway with a larger data set containing more than twice the statistics presented in this thesis.

In the context of recent results from the other short-baseline oscillation experiments, PROSPECT is most sensitive to the high Δm^2_{41} region and has excluded a large region of the eV-scale sterile neutrino mixing parameter space with a small amount of data. With ~3 years of running and increased statistics, PROSPECT will be sensitive to most of the suggested (Δm^2_{41}, $\sin^2 2\theta_{14}$) mixing parameters. In particular, it will cover the favored region near $|U_{e4}|^2 = |\sin\theta_{14} e^{-i\delta_{14}}|^2 \approx 0.01$ and $\Delta m^2_{41} \approx 1.3\,\mathrm{eV}^2$ reported by the global fit in Ref. [224], which includes $\overline{\nu}_e$ disappearance data from NEOS [106] and DANSS [105]. It should be noted that neither experiment claims an observation of a sterile neutrino. They report best-fit values from their oscillation analyses, and those numbers have been interpreted and combined at a high-level. Additionally, the Neutrino-4 experiment reports an observation of active-sterile mixing with $\Delta m^2_{41} \approx 7.34\,\mathrm{eV}^2$ and $\sin^2 2\theta_{14} \approx 0.39$ [107]. This analysis does not use the suggested Feldman-Cousins method to define confidence intervals and

does not account for systematics. This observation is in conflict with the NEOS and DANSS results, as well as PROSPECT, which excludes the postive claim best-fit at >95% C.L.

The disagreement between the PROSPECT measured spectrum and Huber prediction adds more evidence pointing towards insufficiencies with the β conversion models. At the very least, the reported uncertainties are not representative of the imposed methods. In addition, *ab initio* calculations are steadily improving with the inclusion of new fission fragment data from total absorption γ-ray spectroscopy experiments, reducing the pandemonium effect. Ref. [225] reports the comparison of Daya Bay data to a new summation model and reports better agreement through the 2-5 MeV spectral range, resulting in a reduction of the flux deficit. The bump around 5-7 MeV is still observed, but with reduced amplitude. Works is underway to combine data from PROSPECT, STEREO [226] and Daya Bay to disentangle the isotopic contributions to the bump. With more statistics, PROSPECT could reveal fine structures from pronounced β endpoints, predicted by some *ab initio* models [227]. Furthermore, the $\overline{\nu}_e$ experimental data can be used to constrain the fission fragment nuclear data and improve the nuclear databases.

PROSPECT's power lies in unique ability to surpress large amounts of cosmogenic and reactor-related backgrounds that mimic inverse beta decay events. This is possible through the efficient use of optical segmentation, pulse shape discrimination, and neutron tagging within a compact, ^{6}Li-loaded liquid scintillator detector. PROSPECT's signal-to-background ratio is the best achieved by a detector operating on the Earth's surface. The development of this technology will not only benefit future neutrino experiments, but can also be leveraged in applied neutrino physics [228,229]. In non-proliferation scenerios where reactors can only be monitored at a distance, the unattenuated neutrino flux is an ideal signal. Precise measurements of the spectrum could provide further isotopic breeding information. As the PROSPECT detector

was shipped to Oak Ridge in a truck, the construction of mobile detectors can be imagined, using the developed scintillator technology that would allow for operation on the surface to monitor various reactors. For increased robustness with directionality, highly-segmented, plastic ^{6}Li-loaded scintillators with pulse-shape discrimination are now being developed [230], using the PROSPECT detector as an example.

Appendix A

TACO: The Awesome Compton Observatory

A.1 Motivation and methodology

The precise characterization of PROSPECT ^{6}Li-loaded organic scintillator energy response is essential for future, high-statistics $\overline{\nu}_e$ spectrum measurements. Specifically, to take advantage of the exceptional energy resolution, the systematic uncertainty associated with the nonlinear response to energy depositions from low energy ($<$2 MeV), electronic recoils. As described in Chapter 5, this effect is currently modelled using Birks' parameters k_{B1}, k_{B2} and the Cherenkov parameter k_C, where the best-fit values are obtained by comparing calibration measurements *in situ* to `PROSPECT-G4` Monte Carlo. However, the overall energy scale is coupled to the other response effects. Furthermore, the Birks' model has known imperfections, including quenching factors that are independent of particle type. Thus, it is necessary to directly and precisely measure this nonlinearity, thereby reducing one of the dominant systematics in PROSPECT.

As detailed previously, the emission of scintillation light from organic scintillators

depends on the particle type and is strongly energy dependent, especially below a few MeV. This sizable nonlinearity of ∼10% is usually attributed to ionization quenching and Cherenkov light emissions. Ionization quenching, which is the result of two excited scintillation molecules interacting, reduces the light output as the deexcitation is combined. Electrons, positrons, and γ-rays with low energies can produce blue and UV Cherenkov radiation, which is readily absorbed by the scintillator and can produce additional scintillation light. Although these processes have different consequences and can be modelled independently (see Equations 5.14 and 5.15), it is often difficult to disentangle the effects in laboratory experiments. Therefore, this initial work focuses on measuring bulk light output per given input energy. In the future, explicit comparisons between these data and Monte Carlo, along with precise measurements of the scintillator refractive index and absorption/reemission spectra, can be used to determine k_{B1}, k_{B2}, and k_C.

To measure the scintillator nonlinearity to percent-levels, we use the Compton coincidence technique. In this method, the signal from a Compton scattered electron is coupled to the signal of the deflected γ-ray, in order to tag each single-Compton event and to eliminate backgrounds and other irrelevant processes. The advantage of using electrons from a γ-ray source is the monoenergetic energy depositions, as compared to dissolving a β source in the scintillator resulting in a smeared energy spectrum.[1] This requires a collimated, low energy γ-ray source with known energy to impinge on a small scintillator target coupled to PMTs and a detector with sufficient energy resolution, typically a high-purity germanium (HPGe) crystal, to collect the deflected γ-rays.

The γ-rays emitted through the collimator with energy $h\nu$ travel perpendicular to the target and interact with the liquid scintillator. For the Compton scattered events,

[1]It should be noted that, although the Birks' model lacks dependence on particle type, positrons, electrons, and γ-rays have slightly different nonlinear behaviors. As it is unfeasible at this stage to have a positron source, Compton scattered γ-rays are used as a proxy given the size of the systematic required.

the recoil electron with energy E_e will produce scintillation light that is captured by the PMTs. Some of the Compton-scattered γ-rays will exit the scintillator at some angle θ and deposit energy $h\nu'$ in the γ-ray detector, as pictured in Figure A.1. The time coincidence between the PMTs and HPGe will indicate a Compton scattering event. The HPGe will give a high-precision measurement of the deflected γ-ray energy $h\nu'$. Comparing to the known incident energy of the γ-ray from the source $h\nu$, the monoenergetic electron energy can be recovered as,

$$E_e = h\nu - h\nu', \tag{A.1}$$

with high resolution. Such a technique can be carried out for a range of $h\nu'$ values by changing θ via the Compton scattering equation,

$$h\nu' = \frac{h\nu}{1 + h\nu/m_e c^2(1 - cos\theta)} \tag{A.2}$$

and thus different values of E_e can be measured with varying angles. The challenges associated with this measurement include optimizing the geometry of the spectrometer components for event rate and understanding systematics from multiple scatters, energy loss, and electronics nonlinearities to sub-percent levels.

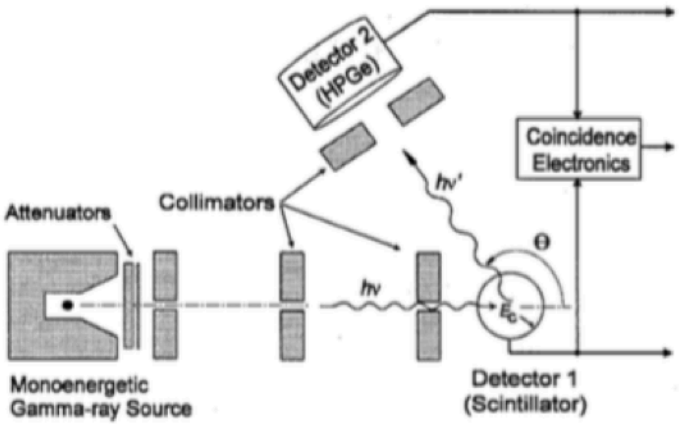

Figure A.1: Schematic of Compton spectrometer from the original paper by Rooney and Valentine proposing this technique [231].

A.2 Proof-of-concept

Previous experiments have used this technique to measure the nonlinearity of a variety of scintillators, both organic and inorganic, used for multiple applications [231–233]. Recently, groups within Daya Bay have also performed measurements using Compton coincidence to understand the behavior of linear alkylbenzene with different γ-ray detector types and sources [234, 235]. As a proof-of-concept, a basic Compton setup was built with materials and detectors available from the Yale Wright Laboratory and Department of Physics. Figure A.2 shows a photograph of the apparatus mounted to an aluminum table with adjustable arms in three dimensions. Various sources are roughly collimated by a 5.7 cm thick, 15.2 cm long brass-covered lead cylinder with a 2.54 cm borehole through the center. Mounted to the table center on axis with the source is the target coupled to a single, 51 mm diameter Philips XP2262 PMT. For this test, EJ-299 plastic scintillator [236] was used. On the opposite end is an Ortec GMX 28190-PS poptop HPGe detector [237] with a coaxial, n-type 52.0 mm diameter crystal surrounded by a 6.35 mm lead shield. The HPGe is cooled to 77 K with liquid nitrogen housed in a 13 L dewar. The source and HPGe are positioned 33 cm and 23 cm, respectively, away from the target on-axis.

To simplify the off-line analysis, pulses from the HPGe preamplifier are passed through a spectroscopy amplifier to integrate the signal and control the shape. A 6μs amplifier time constant was shown to optimize the resolution of the detector between 3.23-3.57 keV FWHM at voltages from 2000-3000 V. Events are recorded if both the PMT and HPGe are triggered within a certain time window. Due to the timing difference between the detectors, with the scintillator-PMT setup operating on nanosecond timescales versus the tens of microsecond HPGe signals, logic is required. The trigger scheme is illustrated in Figure A.3. Analog signals from the PMT and HPGe spectroscopy amplifier are copied via linear fan in/out units, with one copy directly routed to the CAEN 1720 (12-bit, 250 MS/s) digitizer [155]. A second copy

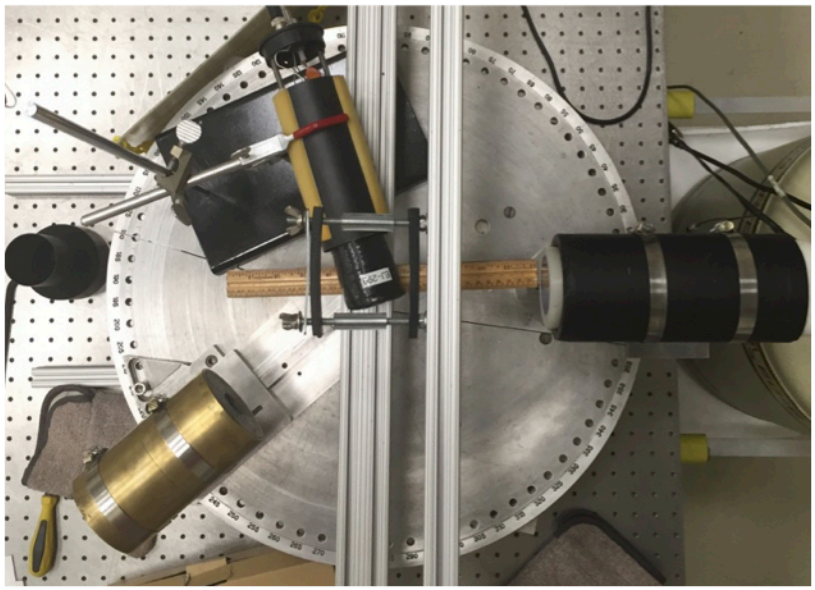

Figure A.2: Bird's eye photograph of the proof-of-concept Compton setup. A brass-covered lead collimator funnels γ-rays from a ^{137}Cs source towards the EJ-299 plastic scintillator target coupled to one PMT. The deflected γ-rays are captured by the HPGe detector housed in a thin lead shield. The source angle can be changed to vary the Compton scattered γ-ray energy.

of each signal is sent through the logic chain, first encountering a discriminator with predetermined threshold. The width of the outgoing NIM signal is adjusted according to the time scales of the detector pulses to reduce deadtime and pileup effects. The PMT NIM signal is then stretched to match the time delay of the HPGe detector through a gate module. Both logic paths meet at a coincidence unit, and if both return true, the digitizer is triggered and the events are written to disk.

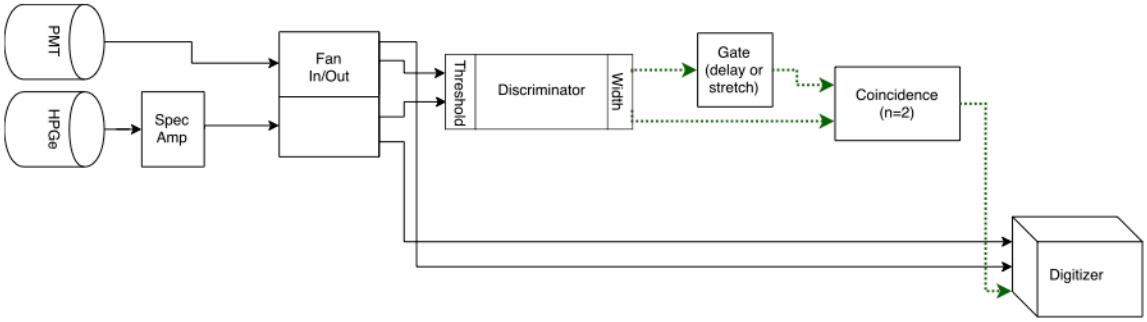

Figure A.3: Block diagram for proof-of-concept trigger scheme.

Preliminary data was taken using a ^{137}Cs source with a trigger rate on the order

of 10 Hz. Figure A.4 shows the coincidence between the PMT and HPGe signals with the source at multiple angles with respect to the HPGe center position. Each data run lasted 24 hours and 600,000 to 1.7 million events were recorded per angle. The oblong oval-shaped features mark the region of interest where both detectors observe a single, Compton scattered event, smeared by the large acceptance of scattering angle due to the large collimator hole size. As the angle changes, the energy detected by the PMT and HPGe are inversely proportional as expected. The Compton continuum is observed below this region and is a result of multiple scatters or other energy loss mechanisms. Distinct γ-ray lines from non-scattered ^{137}Cs events are randomly triggered and directly detected by the HPGe. Due to the large uncertainties from statistics and systematics from the collimator, a reliable measurement cannot be made from this data set.

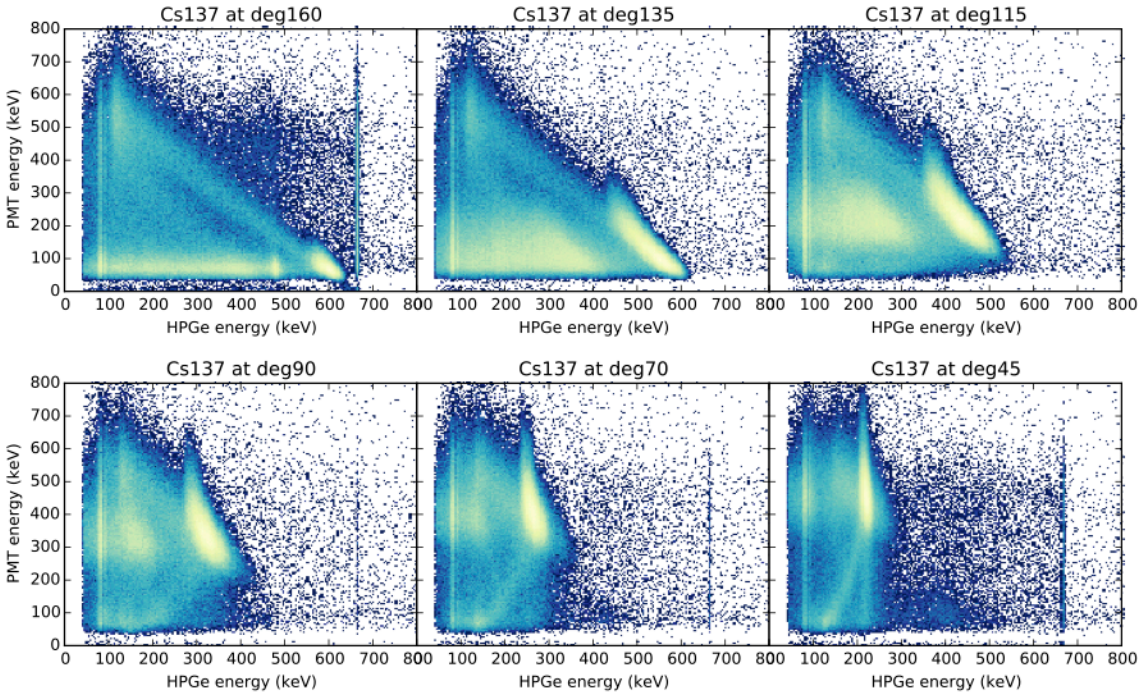

Figure A.4: Energy collected from scintillator-PMT target versus deflected γ-ray deposition in the HPGe detector. Data were taken with a ^{137}Cs source at multiple angles with respect to the HPGe perpendicular. The coincidence region appears as oblong ovals, smeared by the large scattering angle acceptance. The continuum region below is a side-effect of multiple scattering. Lines around 662 keV from non-scattered γ-rays are observed as direct hits in the HPGe detector.

A.3 Experimental setup

The final TACO apparatus is designed to be flexible, enabling the position adjustment of each instrument and easy replacement of the target volume. A variety of γ-ray sources can be deployed to scan multiple energy ranges. For the PROSPECT non-linearity measurements, ^{22}Na is the candidate emitter because of the two associated lines (see Table 3.3) and the position-correlated emission of the annihilation γ-rays. Efficient tagging is required to take advantage of these features in the data. As the scheme is similar to the proof-of-concept design, a similar trigger and DAQ system is used with increased channels. A simulation package was built to inform the geometry of the scintillator target cell, collimator, and required source activity. Careful Monte Carlo studies will be necessary to compare to data to understand the systematics of each data run.

A.3.1 Design

The major components of TACO include the collimation system, scintillator target and PMT detector, HPGe detector, and the adjustable mechanical structure, as seen in Figure A.5. The collimator is made from 10, 1 cm thick tungsten plates with a $10\times10\,\mathrm{cm}^2$ cross section, providing >90% γ-ray attenuation to the surrounding environment. Holes of sizes 6.0, 10.0, 12.0, 15.0 cm were drilled equidistant to the center of each plate using a water jet cutter. Multiple sized holes give the ability to change the beam size to increase statistics or reduce the acceptance angle. Furthermore, the stacked plates allow for straight or stepped collimation designs, which can help eliminate small angle scattering. Preliminary simulations have shown that there is no substantive effect on the scintillator Compton spectrum due to γ-rays scattering from the holes not in use. The source will be mounted to the back of the collimator away from the target in an acrylic holder to allow for reproducibility of the source

location.

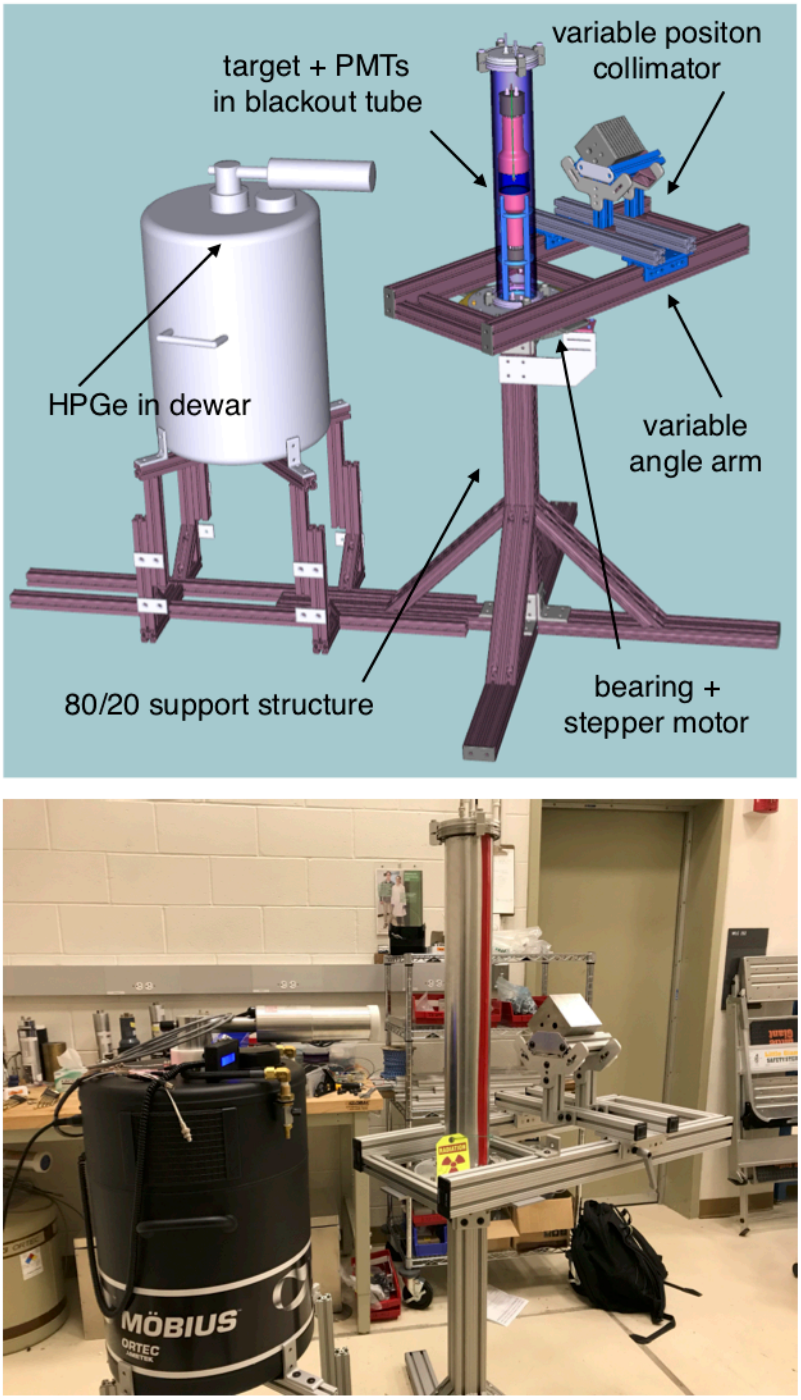

Figure A.5: **(top)** 3D rendering of TACO setup. **(bottom)** Photograph of TACO setup. BGO detectors have not yet been installed.

PROSPECT production ^{6}LiLS is used as the target. It is housed in a 5 cm tall annealed acrylic cylinder with a 5 cm diameter made gas-tight through Acrifix [124]

joint seals. The outside of the cell is coated with EJ-510 [153] diffuse reflective paint. Two small nylon fittings are screwed into the top of the cell as liquid filling ports. The scintillator was pumped into the cell using a small peristaltic pump outfit with Viton tubing inside a nitrogen glove box to reduce exposure to oxygen. After eliminating all air bubbles, the Viton tubing was plugged to act as an expansion volume. The cell is coupled to 2, 3 in Hamamatsu R6091 [238] PMTs via EJ-550 [154] silicone optical grease. The system is mounted vertically on top of a water-jet cut aluminum stand inside of a 1 mm thick aluminum blackout tube. The ends are sealed with vacuum flanges with feedthroughs to accommodate the signal and high voltage cables.

The deflected γ-rays are detected with a GMX20P4-70 Ortec coaxial N-type HPGe poptop detector [237]. The crystal is surrounded by a 70 mm diameter endcap with the face covered by a 0.51 mm thin beryllium window. A CFG-PH4 horizontal dipstick cryostat is used in combination with a MÖBIUS recycler condensing liquid nitrogen cooling system [239]. This dewar only requires filling every one to two years, allowing for continuous cooling with low maintenance. At base temperature, the energy resolution of the HPGe system is $\sim$2 keV FHWM at 1.33 MeV.

All systems are mounted to an 80/20 aluminum T-slotted frame. The vertical stand support is made from an 3$\times$3 in 80/20 quad piece supported on the sides and bottom by 3$\times$1 in double rails. The load of the source arm is also supported by 3$\times$1 in double rails mounted on linear slides for position adjustments. This structure is bolted to an anodized aluminum round turntable with a PTFE sleeve bearing [240] to allow $>180^{\circ}$ rotation around the target. The 38 mm thick turntable has an outer diameter of 300 mm with a 2 ton capacity. A water jet cut 300 mm major diameter aluminum, 1.5 module (200 teeth) gear is mounted to the bearing and connected to a NEMA 23 stepper motor [135] via a small system of gears. The motor is held below the bearing by a custom aluminum support box. Position steps of the arm are read out with a 1024 pulse/revolution optical encoder. The blackout tube is mounted

on a custom aluminum plate bolted to the top of the turntable. The remaining structures, including the HPGe dewar platform, are constructed from 1.5×1.5 in single rails bolted together with 80/20 accessories. In this configuration, the height of the turntable is 91 cm from the ground and is 34 cm below the target volume. The collimator hole and HPGe crystal center were aligned with the center of the target by a laser ranger to ∼1 mm. The front of the collimator and HPGe face can be varied from 9 to 70 cm and 29 to 70 cm, respectively, away from the target volume center. Two, 50.8 cm diameter Saint Gobain SCINTBLOC bismuth germanate (BGO) scintillator detectors [241] were acquired to accommodate different tagging schemes using ^{22}Na. At the time of writing, these assemblies were not yet installed on the setup.

A.3.2 Data acquisition and systems control

A similar NIM-based trigger scheme as shown in Figure A.3 will be used, with additional logic for the BGO tagging detectors. Data is digitized by a CAEN DT5730 8 channel (14 bit, 500 MS/s) desktop digitizer [242]. For acquisition control and data visualization, the open-source `ADAQ` [243] software has been adapted for TACO. Written in `ROOT`, this system allows for interactive data taking with a graphical user interface. Waveform binary data is unpacked and stored in `TTrees` with parameters defined by the user. Simple integration and analysis can also be performed in the program.

High voltage is supplied to all detectors via two, DT1470ET 4 channel, 8 kV desktop power supply modules. These units are controlled remotely by the TACO slow control system [137] via ethernet connection. The slow control also handles the communication with the stepper motor through an Ardiuno microcontroller [136]. Environmental monitoring, such as temperature, pressure, and humidity conditions, will soon be added to the system.

A.3.3 Simulation package

A TACO simulation package [244] was developed using RAT [245], a `ROOT`-based wrapper built around `GEANT-4`. The framework is used by multiple neutrino and dark matter experiments to model scintillation and PMT interactions in detail, along with the corresponding DAQ and reconstruction processes. For TACO, the Monte Carlo has been used to inform the geometry of the scintillator target volume and collimator bore hole sizes to increase the number of of single-scatter events, while providing an adequate coincidence rate for various configurations of the apparatus. Similarly, the simulations have shown that a few μCi activity source collimated <10 mm is required to collect sufficient statistics in a few days of running at each angle. Figure A.6**(right)** shows the default TACO geometry, where only the main components of the setup are modelled.

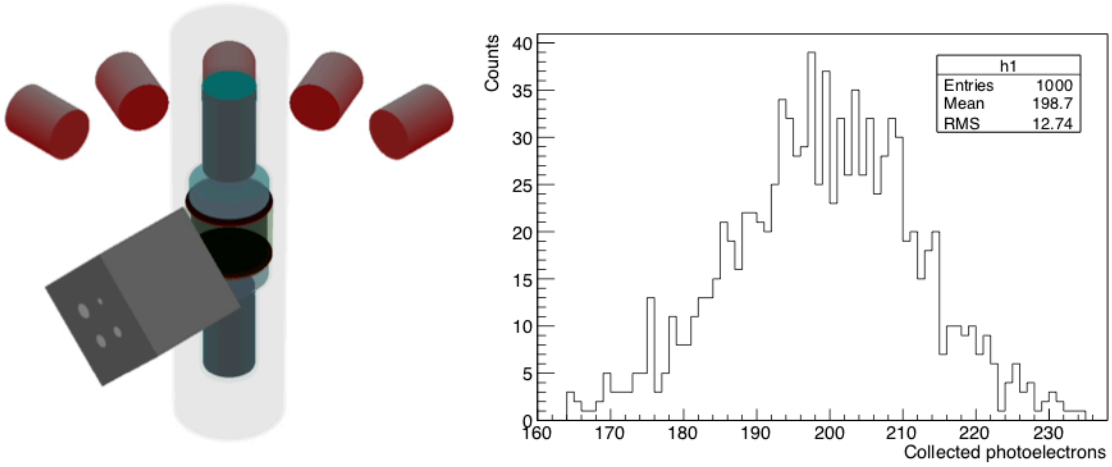

Figure A.6: **(left)** Rendering of TACO simulation geometry. Each material and their reflective properties are modelled to the best of knowledge. Scintillator parameters, including light yield, density, wavelength-dependent absorption and emission are represented. The PMT photocathode conversion of photons to photoelectrons is also modelled with 25% quantum efficiency. Multiple germanium crystals are used to run simulations with multiple angles simultaneously. **(right)** Simulated collected photoelectrons after deploying a 1000 event, 1 MeV photon bomb in the center of the scintillator cell. This results in an expected geometric collection efficiency of 79%.

The PROSPECT ^{6}LiLS material and optical properties are input into the simu-

lation, along with the reflective surfaces of the acrylic cell and diffuser paint. The photocathode material and structure of the PMTs are accurately modelled and set to quantum efficiency of 25%. Multiple germanium crystal volumes are used to scan multiple angles (energies) with a single simulation run. The geometry was verified by comparing light collection measurements between Monte Carlo and data. Figure A.6**(right)** shows the number of photoelectrons collected by the combined PMT system after deploying a 1000 event, 1 MeV photon bomb in the center of the scintillator cell in simulation. Accounting for the quantum efficiency of the PMTs, the expected geometric collection efficiency is 79±2.5% (1620±51 PE/MeV). Taking into account the gain of each PMT, measurements with the TACO setup using a ^{137}Cs result in a collection of 1500±140 PE/MeV, or 73±7%, where a conservative uncertainty is added due to the fit of the Compton edge. A few percent difference is expected as the simulation currently does not account for nonlinearity effects. Further tests will be performed to show the good agreement between the data and Monte Carlo. The scattering dynamics of the collimator system and the associated systematics will also be studied when first production data is taken.

A.4 Future work

At present, the TACO setup is fully functional. First data will be taken once the appropriate activity ^{22}Na source has been obtained and the BGO tagging detectors have been installed. The trigger and analysis scheme will be developed in the interim. For a precision measure of the nonlinearity across a sizable range of energies below 1.2 MeV, data will be to be taken at ∼10 different angles. Each run will require a few days of data taking, dependent on the collimator configuration, to acquire enough statistics. In this case, systematics from multiple scattering and other forms of energy loss will dominate the measurement. These will need to be studied in extreme detail

to reach a total systematic uncertainty of ∼1%. Future, high-statistics PROSPECT $\overline{\nu}_e$ spectrum analyses can use this measurement to better constrain the nonlinearity model in `PROSPECT-G4` to reduce the contribution of the energy response to the overall systematics.

Although nonlinearity is expected to be very small at high energies, ideally measurements could be made to map the full IBD energy range up to ∼8 MeV. Standard laboratory γ-ray sources cannot provide energies above a few MeV. One way to circumvent this constraint would be to use the TACO spectrometer at a thermal or cold neutron beam facility, such as the NIST Center for Neutron Research and Physical Measurement Laboratory, where high energy γ-rays can be produced. Neutrons impinging on a target with a high neutron capture cross-section, for example ^{51}V and ^{48}Ti, can produce high intensity, high-energy γ-excitations in the IBD range. Parts of the apparatus may need to be altered or completely changed, including the collimation scheme and scintillator cell volume. The TACO simulation package could easily be adapted to understand the geometry, as well as study the associated systematics. Such a measurement has yet to be performed in the context of reactor $\overline{\nu}_e$ experiments.

In the future, TACO will be adapted to replace the existing advanced physics laboratory Compton scattering experiment at Yale University. This will allow students a unique opportunity to work with variety of research-grade equipment and become familiar with sophisticated instrumentation and data analysis techniques. Multiple goals can be achieved using the TACO infrastructure:

- explore particle-like nature of light
- confirm Compton scattering and differential cross section formulas
- measure nonlinearity of scintillator target
- learn to design a hardware trigger and pulse shaping system

- understand how to work with and operate cryogenic semiconductor detectors, PMTs, and scintillators
- gain experience with digital readout systems
- measure the position correlation of ^{22}Na annihilation γ-rays

In addition, the target volume can be easily changed to allow study of inorganic, organic, liquid, plastic, and crystal scintillators or other materials. The entire TACO system was designed to be user-friendly and low maintenance to reduce instructor setup time.

Bibliography

[1] H. Becquerel. Sur les radiations émises par phosphorescence. *Compt. Rend. Acad. Sci.* **122**, 420–421 (1896).

[2] E. Rutherford. Uranium Radiation and the Electrical Conduction produced by it. *Phil. Mag.* **47**, 109–162 (1899).

[3] J. J. Thomson. Cathode rays. *Phil. Mag.* **44**, 293–316 (1897).

[4] O. v. Baeyer, O. Hahn, and L. Meitner. Über die β-Strahlen des aktiven Niederschlags des Thoriums. *Phys. Z* **12**, 273–279 (1911).

[5] J. Chadwick. Intensitätsverteilung im magnetischen Spektrum von β-Strahlen von Radium B+C. *Verh. Phys. Gesell.* **16**, 383–391 (1914).

[6] C. D. Ellis and W. A. Wooster. The Average Energy of Disintegration of Radium E. *Proc. Roy. Soc.* **A117**, 109–123 (1927).

[7] W. Pauli. Dear radioactive ladies and gentlemen. *Phys. Today* **31N9**, 1 (1978).

[8] J. Chadwick. The Existence of a Neutron. *Proc. Roy. Soc.* **A136**, 692–708 (1932).

[9] E. Fermi. Trends to a Theory of beta Radiation. *Nuovo Cim.* **11**, 1–19 (1934). [,535(1934)].

[10] H. Bethe and R. Peierls. The 'neutrino'. *Nature* **133**, 532 (1934).

[11] F. Reines and C. L. Cowan. Detection of the Free Neutrino. *Phys. Rev.* **92**, 830–831 (1953).

[12] F. Reines, C. L. Cowan, F. B. Harrison, A. D. McGuire, and H. W. Kruse. Detection of the free anti-neutrino. *Phys. Rev.* **117**, 159–173 (1960).

[13] B. Pontecorvo. Electron and Muon Neutrinos. *Sov. Phys. JETP* **10**, 1236–1240 (1960). [Zh. Eksp. Teor. Fiz.37,1751(1959)].

[14] G. Danby, J. M. Gaillard, K. A. Goulianos, L. M. Lederman, N. B. Mistry, M. Schwartz, and J. Steinberger. Observation of High-Energy Neutrino Reactions and the Existence of Two Kinds of Neutrinos. *Phys. Rev. Lett.* **9**, 36–44 (1962).

[15] K. Kodama *et al.* (DONUT). Observation of tau neutrino interactions. *Phys. Lett.* **B504**, 218–224 (2001). arXiv:hep-ex/0012035.

[16] S. L. Glashow. Partial Symmetries of Weak Interactions. *Nucl. Phys.* **22**, 579–588 (1961).

[17] S. Weinberg. A Model of Leptons. *Phys. Rev. Lett.* **19**, 1264–1266 (1967).

[18] A. Salam and J. C. Ward. Weak and electromagnetic interactions. *Nuovo Cim.* **11**, 568–577 (1959).

[19] C. S. Wu, E. Ambler, R. W. Hayward, D. D. Hoppes, and R. P. Hudson. Experimental Test of Parity Conservation in Beta Decay. *Phys. Rev.* **105**, 1413–1414 (1957).

[20] T. D. Lee and C.-N. Yang. Parity Nonconservation and a Two Component Theory of the Neutrino. *Phys. Rev.* **105**, 1671–1675 (1957). [,245(1957)].

[21] M. Tanabashi *et al.* (Particle Data Group). Review of Particle Physics. *Phys. Rev.* **D98**, 030001 (2018).

[22] G. Aad *et al.* (ATLAS). Observation of a new particle in the search for the Standard Model Higgs boson with the ATLAS detector at the LHC. *Phys. Lett.* **B716**, 1–29 (2012). arXiv:1207.7214.

[23] S. Chatrchyan *et al.* (CMS). Observation of a new boson at a mass of 125 GeV with the CMS experiment at the LHC. *Phys. Lett.* **B716**, 30–61 (2012). arXiv:1207.7235.

[24] S. Schael *et al.* (ALEPH, DELPHI, L3, OPAL, SLD, LEP Electroweak Working Group, SLD Electroweak Group, SLD Heavy Flavour Group). Precision electroweak measurements on the Z resonance. *Phys. Rept.* **427**, 257–454 (2006). arXiv:hep-ex/0509008.

[25] B. Pontecorvo. On a method for detecting free neutrinos. *National Research Council of Canada Report No. PD 141* **AB 2 675** (1945).

[26] R. Davis, Jr., D. S. Harmer, and K. C. Hoffman. Search for neutrinos from the sun. *Phys. Rev. Lett.* **20**, 1205–1209 (1968).

[27] J. N. Bahcall, N. A. Bahcall, and G. Shaviv. Present status of the theoretical predictions for the Cl-36 solar neutrino experiment. *Phys. Rev. Lett.* **20**, 1209–1212 (1968).

[28] B. T. Cleveland, T. Daily, R. Davis, Jr., J. R. Distel, K. Lande, C. K. Lee, P. S. Wildenhain, and J. Ullman. Measurement of the solar electron neutrino flux with the Homestake chlorine detector. *Astrophys. J.* **496**, 505–526 (1998).

[29] J. N. Bahcall and M. H. Pinsonneault. What do we (not) know theoretically about solar neutrino fluxes? *Phys. Rev. Lett.* **92**, 121301 (2004). arXiv:astro-ph/0402114.

[30] K. S. Hirata *et al.* (Kamiokande-II). Observation of B-8 Solar Neutrinos in the Kamiokande-II Detector. *Phys. Rev. Lett.* **63**, 16 (1989).

[31] K. S. Hirata *et al.* (Kamiokande-II). Experimental Study of the Atmospheric Neutrino Flux. *Phys. Lett.* **B205**, 416 (1988). [,447(1988)].

[32] D. Casper *et al.* Measurement of atmospheric neutrino composition with IMB-3. *Phys. Rev. Lett.* **66**, 2561–2564 (1991).

[33] W. W. M. Allison *et al.* Measurement of the atmospheric neutrino flavor composition in Soudan-2. *Phys. Lett.* **B391**, 491–500 (1997). arXiv:hep-ex/9611007.

[34] C. Longuemare (FREJUS). Study of neutrino oscillations in the FREJUS experiment. *Nucl. Phys. Proc. Suppl.* **16**, 490–492 (1990).

[35] M. Aglietta *et al.* (NUSEX). Experimental study of atmospheric neutrino flux in the NUSEX experiment. *Europhys. Lett.* **8**, 611–614 (1989).

[36] M. Kobayashi and T. Maskawa. CP Violation in the Renormalizable Theory of Weak Interaction. *Prog. Theor. Phys.* **49**, 652–657 (1973).

[37] Y. Fukuda *et al.* (Super-Kamiokande). Evidence for oscillation of atmospheric neutrinos. *Phys. Rev. Lett.* **81**, 1562–1567 (1998). arXiv:hep-ex/9807003.

[38] Q. R. Ahmad *et al.* (SNO). Measurement of the rate of $\nu_e + d \rightarrow p + p + e^-$ interactions produced by ^8B solar neutrinos at the Sudbury Neutrino Observatory. *Phys. Rev. Lett.* **87**, 071301 (2001). arXiv:nucl-ex/0106015.

[39] T. Araki *et al.* (KamLAND). Measurement of neutrino oscillation with KamLAND: Evidence of spectral distortion. *Phys. Rev. Lett.* **94**, 081801 (2005). arXiv:hep-ex/0406035.

[40] T. Araki *et al.* Experimental investigation of geologically produced antineutrinos with KamLAND. *Nature* **436**, 499–503 (2005).

[41] S. Abe *et al.* (KamLAND). Precision Measurement of Neutrino Oscillation Parameters with KamLAND. *Phys. Rev. Lett.* **100**, 221803 (2008). arXiv:0801.4589.

[42] A. Gando *et al.* (KamLAND). Reactor On-Off Antineutrino Measurement with KamLAND. *Phys. Rev.* **D88**, 033001 (2013). arXiv:1303.4667.

[43] E. Majorana. Teoria simmetrica dell'elettrone e del positrone. *Nuovo Cim.* **14**, 171–184 (1937).

[44] M. Gell-Mann, P. Ramond, and R. Slansky. Complex Spinors and Unified Theories. *Conf. Proc.* **C790927**, 315–321 (1979). arXiv:1306.4669.

[45] R. N. Mohapatra and G. Senjanovic. Neutrino Mass and Spontaneous Parity Nonconservation. *Phys. Rev. Lett.* **44**, 912 (1980). [,231(1979)].

[46] F. P. An *et al.* (Daya Bay). Observation of electron-antineutrino disappearance at Daya Bay. *Phys. Rev. Lett.* **108**, 171803 (2012). arXiv:1203.1669.

[47] J. K. Ahn *et al.* (RENO). Observation of Reactor Electron Antineutrino Disappearance in the RENO Experiment. *Phys. Rev. Lett.* **108**, 191802 (2012). arXiv:1204.0626.

[48] Y. Abe *et al.* (Double Chooz). Background-independent measurement of θ_{13} in Double Chooz. *Phys. Lett.* **B735**, 51–56 (2014). arXiv:1401.5981.

[49] A. C. Hayes and P. Vogel. Reactor Neutrino Spectra. *Ann. Rev. Nucl. Part. Sci.* **66**, 219–244 (2016). arXiv:1605.02047.

[50] X. Qian and J.-C. Peng. Physics with Reactor Neutrinos (2018). arXiv:1801.05386.

[51] P. Vogel, G. K. Schenter, F. M. Mann, and R. E. Schenter. Reactor Antineutrino Spectra and Their Application to Anti-neutrino Induced Reactions. 2. *Phys. Rev.* **C24**, 1543–1553 (1981).

[52] T. A. Mueller *et al.* Improved Predictions of Reactor Antineutrino Spectra. *Phys. Rev.* **C83**, 054615 (2011). arXiv:1101.2663.

[53] A. A. Sonzogni, T. D. Johnson, and E. A. McCutchan. Nuclear structure insights into reactor antineutrino spectra. *Phys. Rev.* **C91**, 011301 (2015).

[54] D. A. Brown *et al.* ENDF/B-VIII.0: The 8th Major Release of the Nuclear Reaction Data Library with CIELO-project Cross Sections, New Standards and Thermal Scattering Data. *Nucl. Data Sheets* **148**, 1–142 (2018).

[55] J. Tuli. Evaluated nuclear structure data file .

[56] A. C. Hayes, J. L. Friar, G. T. Garvey, G. Jungman, and G. Jonkmans. Systematic Uncertainties in the Analysis of the Reactor Neutrino Anomaly. *Phys. Rev. Lett.* **112**, 202501 (2014). arXiv:1309.4146.

[57] A. Fijałkowska *et al.* Impact of Modular Total Absorption Spectrometer measurements of β decay of fission products on the decay heat and reactor $\overline{\nu}_e$ flux calculation. *Phys. Rev. Lett.* **119**, 052503 (2017).

[58] V. Guadilla *et al.* Large Impact of the Decay of Niobium Isomers on the Reactor $\overline{\nu}_e$ Summation Calculations. *Phys. Rev. Lett.* **122**, 042502 (2019).

[59] F. Von Feilitzsch, A. A. Hahn, and K. Schreckenbach. Experimental beta spectra from Pu-239 and U-235 thermal neutron fission products and their correlated anti-neutrinos spectra. *Phys. Lett.* **B118**, 162–166 (1982).

[60] K. Schreckenbach, G. Colvin, W. Gelletly, and F. Von Feilitzsch. Determination of the anti-neutrino spectrum from U-235 thermal neutron fission products up to 9.5-MeV. *Phys. Lett.* **B160**, 325–330 (1985).

[61] A. A. Hahn, K. Schreckenbach, G. Colvin, B. Krusche, W. Gelletly, and F. Von Feilitzsch. Anti-neutrino Spectra From ^{241}Pu and ^{239}Pu Thermal Neutron Fission Products. *Phys. Lett.* **B218**, 365–368 (1989).

[62] N. Haag, A. Gütlein, M. Hofmann, L. Oberauer, W. Potzel, K. Schreckenbach, and F. M. Wagner. Experimental Determination of the Antineutrino Spectrum of the Fission Products of ^{238}U. *Phys. Rev. Lett.* **112**, 122501 (2014). arXiv:1312.5601.

[63] P. Huber. On the determination of anti-neutrino spectra from nuclear reactors. *Phys. Rev.* **C84**, 024617 (2011). [Erratum: Phys. Rev.C85,029901(2012)], arXiv:1106.0687.

[64] P. Vogel and J. Engel. Neutrino Electromagnetic Form-Factors. *Phys. Rev.* **D39**, 3378 (1989).

[65] P. Vogel and J. F. Beacom. Angular distribution of neutron inverse beta decay, $\overline{\nu}_e + p \to e^+ + n$. *Phys. Rev.* **D60**, 053003 (1999). arXiv:hep-ph/9903554.

[66] F. Reines, H. W. Sobel, and E. Pasierb. Evidence for Neutrino Instability. *Phys. Rev. Lett.* **45**, 1307 (1980).

[67] H. Kwon, F. Boehm, A. A. Hahn, H. E. Henrikson, J. L. Vuilleumier, J. F. Cavaignac, D. H. Koang, B. Vignon, F. Von Feilitzsch, and R. L. Mossbauer. Search for Neutrino Oscillations at a Fission Reactor. *Phys. Rev.* **D24**, 1097–1111 (1981).

[68] J. F. Cavaignac, A. Hoummada, D. H. Koang, B. Vignon, Y. Declais, H. de Kerret, H. Pessard, and J. M. Thenard. Indication for Neutrino Oscillation From a High Statistics Experiment at the Bugey Reactor. *Phys. Lett.* **148B**, 387–394 (1984).

[69] J. L. Vuilleumier *et al.* (Cal Tech-SIN-TUM). New Limits on Oscillation Parameters for Electron Anti-neutrinos. *Phys. Lett.* **114B**, 298 (1982).

[70] K. Gabathuler, F. Boehm, F. von Feilitzsch, J. L. Gimlett, H. Kwon, R. L. Mossbauer, J. L. Vuilleumier, G. Zacek, and V. Zacek (Cal Tech-SIN-TUM). A Search for Neutrino Oscillations by Measurement of the $\bar{\nu}_e$ Spectra at Two Distances From a Nuclear Reactor. *Phys. Lett.* **138B**, 449–453 (1984).

[71] G. Zacek *et al.* (CALTECH-SIN-TUM). Neutrino Oscillation Experiments at the Gosgen Nuclear Power Reactor. *Phys. Rev.* **D34**, 2621–2636 (1986).

[72] A. I. Afonin, A. A. Borovoi, Yu. L. Dobrynin, S. N. Ketov, V. I. Kopeikin, L. A. Mikaelyan, M. D. Skorokhvatov, S. V. Tolokonnikov, and A. N. Kheruvimov. Neutrino experiment in the reactor of the Rovno atomic power plant: cross-section for inverse beta decay. *JETP Lett.* **41**, 435–438 (1985). [Pisma Zh. Eksp. Teor. Fiz.41,355(1985)].

[73] A. I. Afonin *et al.* $\bar{\nu}_e$ Spectra at Two Distances From the Reactor of the Rovno Nuclear Power Plant: Search for Oscillations. *JETP Lett.* **45**, 247–251 (1987). [Pisma Zh. Eksp. Teor. Fiz.45,201(1987)].

[74] A. A. Kuvshinnikov, L. A. Mikaelyan, S. V. Nikolaev, M. D. Skorokhvatov, and A. V. Etenko. Measuring the anti-electron-neutrino + p —¿ n + e+ cross-section and beta decay axial constant in a new experiment at Rovno NPP reactor. (In Russian). *JETP Lett.* **54**, 253–257 (1991). [Sov. J. Nucl. Phys.52,300(1990)].

[75] Y. Declais *et al.* Search for neutrino oscillations at 15-meters, 40-meters, and 95-meters from a nuclear power reactor at Bugey. *Nucl. Phys.* **B434**, 503–534 (1995).

[76] M. Abbes *et al.* The Bugey-3 neutrino detector. *Nucl. Instrum. Meth.* **A374**, 164–187 (1996).

[77] M. Apollonio *et al.* (CHOOZ). Initial results from the CHOOZ long baseline reactor neutrino oscillation experiment. *Phys. Lett.* **B420**, 397–404 (1998). arXiv:hep-ex/9711002.

[78] M. Apollonio *et al.* (CHOOZ). Limits on neutrino oscillations from the CHOOZ experiment. *Phys. Lett.* **B466**, 415–430 (1999). arXiv:hep-ex/9907037.

[79] M. Apollonio *et al.* (CHOOZ). Search for neutrino oscillations on a long baseline at the CHOOZ nuclear power station. *Eur. Phys. J.* **C27**, 331–374 (2003). arXiv:hep-ex/0301017.

[80] F. Boehm *et al.* Final results from the Palo Verde neutrino oscillation experiment. *Phys. Rev.* **D64**, 112001 (2001). arXiv:hep-ex/0107009.

[81] F. Boehm *et al.* Results from the Palo Verde neutrino oscillation experiment. *Phys. Rev.* **D62**, 072002 (2000). arXiv:hep-ex/0003022.

[82] X. Qian and W. Wang. Reactor neutrino experiments: θ_{13} and beyond. *Mod. Phys. Lett.* **A29**, 1430016 (2014). arXiv:1405.7217.

[83] F. P. An *et al.* (Daya Bay). Measurement of electron antineutrino oscillation based on 1230 days of operation of the Daya Bay experiment. *Phys. Rev.* **D95**, 072006 (2017). arXiv:1610.04802.

[84] F. An *et al.* (JUNO). Neutrino Physics with JUNO. *J. Phys.* **G43**, 030401 (2016). arXiv:1507.05613.

[85] G. Mention, M. Fechner, T. Lasserre, T. A. Mueller, D. Lhuillier, M. Cribier, and A. Letourneau. The Reactor Antineutrino Anomaly. *Phys. Rev.* **D83**, 073006 (2011). arXiv:1101.2755.

[86] K. N. Abazajian *et al.* Light Sterile Neutrinos: A White Paper (2012). arXiv:1204.5379.

[87] A. Aguilar-Arevalo *et al.* (LSND). Evidence for neutrino oscillations from the observation of anti-neutrino(electron) appearance in a anti-neutrino(muon) beam. *Phys. Rev.* **D64**, 112007 (2001). arXiv:hep-ex/0104049.

[88] A. A. Aguilar-Arevalo *et al.* (MiniBooNE). A Search for electron neutrino appearance at the $\Delta m^2 \sim 1\text{eV}^2$ scale. *Phys. Rev. Lett.* **98**, 231801 (2007). arXiv:0704.1500.

[89] W. Hampel *et al.* (GALLEX). Final results of the Cr-51 neutrino source experiments in GALLEX. *Phys. Lett.* **B420**, 114–126 (1998).

[90] J. N. Abdurashitov *et al.* Measurement of the response of a Ga solar neutrino experiment to neutrinos from an Ar-37 source. *Phys. Rev.* **C73**, 045805 (2006). arXiv:nucl-ex/0512041.

[91] J. Kopp, P. A. N. Machado, M. Maltoni, and T. Schwetz. Sterile Neutrino Oscillations: The Global Picture. *JHEP* **05**, 050 (2013). arXiv:1303.3011.

[92] Y. Abe *et al.* (Double Chooz). Improved measurements of the neutrino mixing angle θ_{13} with the Double Chooz detector. *JHEP* **10**, 086 (2014). [Erratum: JHEP02,074(2015)], arXiv:1406.7763.

[93] S.-B. Kim. New results from RENO and prospects with RENO-50. *Nucl. Part. Phys. Proc.* **265-266**, 93–98 (2015). arXiv:1412.2199.

[94] R. Gandhi, B. Kayser, M. Masud, and S. Prakash. The impact of sterile neutrinos on CP measurements at long baselines. *JHEP* **11**, 039 (2015). arXiv:1508.06275.

[95] P. A. R. Ade *et al.* (Planck). Planck 2015 results. XIII. Cosmological parameters. *Astron. Astrophys.* **594**, A13 (2016). arXiv:1502.01589.

[96] C. Giunti and T. Lasserre. eV-scale Sterile Neutrinos (2019). arXiv:1901.08330.

[97] M. G. Aartsen *et al.* (IceCube). Searches for Sterile Neutrinos with the IceCube Detector. *Phys. Rev. Lett.* **117**, 071801 (2016). arXiv:1605.01990.

[98] F. P. An *et al.* (Daya Bay). Evolution of the Reactor Antineutrino Flux and Spectrum at Daya Bay. *Phys. Rev. Lett.* **118**, 251801 (2017). arXiv:1704.01082.

[99] C. Buck *et al.* (Double Chooz). New Results from the Double Chooz Experiment. *XXVIII International Conference on Neutrino Physics and Astrophysics (Neutrino 2018)* (2018).

[100] S. H. Seo *et al.* (RENO). Spectral Measurement of the Electron Antineutrino Oscillation Amplitude and Frequency using 500 Live Days of RENO Data. *Phys. Rev.* **D98**, 012002 (2018). arXiv:1610.04326.

[101] A. C. Hayes, J. L. Friar, G. T. Garvey, D. Ibeling, G. Jungman, T. Kawano, and R. W. Mills. Possible origins and implications of the shoulder in reactor neutrino spectra. *Phys. Rev.* **D92**, 033015 (2015). arXiv:1506.00583.

[102] D. A. Dwyer and T. J. Langford. Spectral Structure of Electron Antineutrinos from Nuclear Reactors. *Phys. Rev. Lett.* **114**, 012502 (2015). arXiv:1407.1281.

[103] A. Sonzogni, E. McCutchan, and A. Hayes. Dissecting Reactor Antineutrino Flux Calculations. *Phys. Rev. Lett.* **119**, 112501 (2017).

[104] I. Alekseev *et al.* DANSS: Detector of the reactor AntiNeutrino based on Solid Scintillator. *JINST* **11**, P11011 (2016). arXiv:1606.02896.

[105] I. Alekseev *et al.* (DANSS). Search for sterile neutrinos at the DANSS experiment. *Phys. Lett.* **B787**, 56–63 (2018). arXiv:1804.04046.

[106] Y. Ko *et al.* (NEOS). Sterile Neutrino Search at the NEOS Experiment. *Phys. Rev. Lett.* **118**, 121802 (2017). arXiv:1610.05134.

[107] Serebrov *et al.* (NEUTRINO-4). The first observation of effect of oscillation in Neutrino-4 experiment on search for sterile neutrino (2018). arXiv:1809.10561.

[108] J. Ashenfelter *et al.* (PROSPECT). The PROSPECT Reactor Antineutrino Experiment. *Nucl. Instrum. Meth.* **A922**, 287–309 (2019). arXiv:1808.00097.

[109] J. Ashenfelter *et al.* (PROSPECT). The PROSPECT Physics Program. *J. Phys.* **G43**, 113001 (2016). arXiv:1512.02202.

[110] Y. Abreu *et al.* (SoLid). A novel segmented-scintillator antineutrino detector. *JINST* **12**, P04024 (2017). arXiv:1703.01683.

[111] Y. Abreu *et al.* (SoLid). Performance of a full scale prototype detector at the BR2 reactor for the SoLid experiment. *JINST* **13**, P05005 (2018). arXiv:1802.02884.

[112] N. Allemandou *et al.* (STEREO). The STEREO Experiment. *JINST* **13**, P07009 (2018). arXiv:1804.09052.

[113] J. Ashenfelter *et al.* (PROSPECT). Background Radiation Measurements at High Power Research Reactors. *Nucl. Instrum. Meth.* **A806**, 401–419 (2016).

[114] J. Ashenfelter *et al.* (PROSPECT). Performance of a segmented ^{6}Li-loaded liquid scintillator detector for the PROSPECT experiment. *JINST* **13**, P06023 (2018). arXiv:1805.09245.

[115] K. M. Heeger, B. R. Littlejohn, H. P. Mumm, and M. N. Tobin. Experimental Parameters for a Reactor Antineutrino Experiment at Very Short Baselines. *Phys. Rev.* **D87**, 073008 (2013). arXiv:1212.2182.

[116] WaterBrick International URL `https://www.waterbrick.org`.

[117] J. B. Birks. The Theory and practice of scintillation counting. *International series of Monographs on Electronics and Instrumentation, v. 27 Macmillan, New York* (1964). URL `http://www.slac.stanford.edu/spires/find/books/www?cl=QCD928:B52`.

[118] F. D. Brooks. Development of organic scintillators. *Nucl. Instrum. Meth.* **162**, 477–505 (1979).

[119] Eljen Technology URL `https://eljentechnology.com/products/liquid-scintillators/ej-301-ej-309`.

[120] D. E. Bergeron, H. P. Mumm, and M. A. Tyra. Phase stability and lithium loading capacity in a liquid scintillation cocktail. *J. Radioanal. and Nuc. Chem.* **314**, 767–771 (2017). ISSN 1588-2780. URL `https://doi.org/10.1007/s10967-017-5341-8`.

[121] J. Ashenfelter *et al.* (PROSPECT). Lithium-loaded Liquid Scintillator Production for the PROSPECT experiment. *JINST* **14**, P03026 (2019). arXiv:1901.05569.

[122] J. Ashenfelter *et al.* (PROSPECT). A low mass optical grid for the PROSPECT reactor antineutrino detector. *Journal of Instrumentation* **14**, P04014–P04014 (2019). arXiv:1902.06430.

[123] Chemours Viton URL `https://www.chemours.com/Viton/en_US/`.

[124] Acrifix 2R URL https://www.acrifix.com/product/acrifix/en/products/reaction-adhesives/acrifix-2r-0190/.

[125] 3M DF2000MA URL https://www.3m.com/3M/en_US/company-us/all-3m-products/~/3M-Specular-Film-DF2000MA-49-in-x-50-yds/?N=5002385+3294794207&preselect=8710037+8710647+8710827+8735787+8735836&rt=rud.

[126] Chemours Krytox URL https://www.chemours.com/Lubricants/en_US/index.html.

[127] Pasternack RG188 URL https://www.pasternack.com/flexible-0.122-rg188-ds-50-ohm-coax-cable-ptfe-jacket-rg188-ds-p.aspx.

[128] Hitachi Metals Finemet URL https://www.hitachi-metals.co.jp/products/elec/tel/pdf/hl-fm9-h.pdf.

[129] All Leak Repair Tape BU-R8520 URL https://shop.echotape.com/tape/bu-r8520-all-leak-repair-tape-76mm-x-8m-3-in-x-25-ft/.

[130] Icotek Cable Grommets URL https://www.icotek.com/us/product-catalog/cable-entry-systems/cable-grommets/.

[131] Silicone RTV615 URL http://www.farnell.com/datasheets/2335231.pdf?_ga=2.194755364.821168864.1567542899-387864698.1567542899.

[132] Powdered graphite URL https://www.michaels.com/generals-graphite-powder/D219061S.html.

[133] Silica Thickener URL http://www.totalboat.com/product/silica-thickener/.

[134] AeroGo Air Casters URL https://www.aerogo.com/products/aero-casters/.

[135] Stepper Online NEMA23 URL http://us.stepperonline.com/nema-23-stepper-motor-54v-15a-116nm1643ozin-23hs221504s-p-68.html.

[136] Arduino URL https://www.arduino.cc.

[137] J. Nikkel. astro-slow-control URL https://bitbucket.org/jnikkel/astro-slow-control/src/master/.

[138] A. Hansell. Cf-252 Homed position IBD-like analysis. *PROSPECT DocDB* **2485-v1** (2018).

[139] Thorlabs LP450-SF15 URL https://www.thorlabs.com/thorproduct.cfm?partnumber=LP450-SF15.

[140] AVTECH model AVO-9A4-B-P0-N-DRXA-VXI-R5 URL https://www.avtechpulse.com/manuals/AVO-9A4-B-P0-N-DRXA-VXI-R5%2Ced1.pdf.

[141] Thorlabs PDA10A and PDA8 URL https://www.thorlabs.com/thorproduct.cfm?partnumber=PDA10A.

[142] Industrial Fiber Optics IF 181L-3-0 URL http://i-fiberoptics.com/patchcord-detail.php?summaryrow=&series=181L&stock_number=IF%20181L-3-0.

[143] ISEG EH161030n URL https://iseg-hv.com/en/products/detail/EHS.

[144] Weiner MPOD crate URL http://www.wiener-d.com/sc/power-supplies/mpod--lvhv/mpod-crate.html.

[145] Advantech ADAM 6015 URL http://advdownload.advantech.com/productfile/PIS/ADAM-6017/Product%20-%20Datasheet/ADAM-6015_6017_6018_DS(10.18.17)20171102161244.pdf.

[146] ToughSonic 14, TSPC-30S1-485 URL https://senix.com/wp-content/uploads/ToughSonic-14-Data-Sheet.pdf.

[147] CAEN V1725 URL https://www.caen.it/products/v1725/.

[148] Weiner 6023 VME crate URL http://www.wiener-d.com/sc/powered-crates/vme/6u-vme-6023.html.

[149] CAEN A3818 Optical Controller PCI Express Cards .

[150] 757 NIM Logic Fan-In/Fan-Out URL http://www.phillipsscientific.com/pdf/757ds.pdf.

[151] PerkinElmer UltimaGold AB LiquiC Scintillator URL http://perkinelmer.com/catalog/family/id/ultima+gold+ab.

[152] D. Norcini. Development of lithium-loaded liquid scintillator for PROSPECT. In *APS Meeting Abstracts*, U16.001 (2015).

[153] Eljen Technology EJ-510 Reflective Paint URL https://eljentechnology.com/products/accessories/ej-510-ej-520.

[154] Eljen Technology EJ-550 Optical Grease URL https://eljentechnology.com/products/accessories/ej-550-ej-552.

[155] CAEN V1720 URL https://www.caen.it/products/v1720/.

[156] 3M Enhanced Specular Reflector URL https://multimedia.3m.com/mws/media/12450890/.

[157] WhiteOptics White98 film URL http://www.whiteoptics.com/wp-content/uploads/2018/05/F16-Product-Data-Sheet.pdf.

[158] CAEN V1725 URL https://www.caen.it/products/v1730/.

[159] D. Norcini. Development of PROSPECT detectors for precision antineutrino studies. In *Proceedings, Meeting of the APS Division of Particles and Fields (DPF 2015): Ann Arbor, Michigan, USA, 4-8 Aug 2015* (2015). arXiv:1510.09082.

[160] J. Ashenfelter *et al.* (PROSPECT). Light Collection and Pulse-Shape Discrimination in Elongated Scintillator Cells for the PROSPECT Reactor Antineutrino Experiment. *JINST* **10**, P11004 (2015).

[161] CAEN SP5601 LED driver URL `https://www.caen.it/products/sp5601/`.

[162] D. Norcini. P50D issue 6, 7 update. *PROSPECT DocDB* **1509-v3** (2016).

[163] PolyFab URL `http://www.polyfab.com`.

[164] Alconox detergent URL `http://www.alconox.com`.

[165] Weld-On 16 URL `https://weldon.com`.

[166] Ingeniven URL `https://ingeniven.com`.

[167] Autotiv Manufactoring URL `https://autotiv.com`.

[168] Hilman rollers URL `https://www.hilmanrollers.com`.

[169] 80/20 URL `https://8020.net`.

[170] PROSPECT. PROSPECT2x Analysis (Accessed 2019). URL `https://github.com/PROSPECT-collaboration/PROSPECT2x_Analysis`.

[171] GEANT4 URL `https://geant4.web.cern.ch`.

[172] PROSPECT. PROSPECT-G4 (Accessed 2019). URL `https://github.com/PROSPECT-collaboration/PROSPECT-G4`.

[173] ROOT URL `https://root.cern.ch`.

[174] M. Mendenhall. Pulse shape analysis components. *PROSPECT DocDB* **497-v1** (2015).

[175] M. Mendenhall. Segment-by-segment calibration. *PROSPECT DocDB* **2314-v2** (2018).

[176] M. Mendenhall. Calibrations overview. *PROSPECT DocDB* **2254-v1** (2018).

[177] M. Mendenhall. 2018C Calibrations tracking. *PROSPECT DocDB* **2614-v1** (2018).

[178] ^{12}B β^- decay: XUNDL-37. *ENSDF: Evaluated Nuclear Structure Data File Search and Retrieval* (2016). URL `https://www.nndc.bnl.gov/ensdf/EnsdfDispatcherServlet`.

[179] X. Zhang. Energy scale study for PROSPECT 2018A data release. *PROSPECT DocDB* **2315-v6** (2018).

[180] J. Ashenfelter *et al.* (PROSPECT). The Radioactive Source Calibration System of the PROSPECT Reactor Antineutrino Detector. *Nucl. Instrum. Meth.* **A944**, 2019 (2019). arXiv:1906.07244.

[181] C. N. Chou. The Nature of the Saturation Effect of Fluorescent Scintillators. *Phys. Rev.* **87**, 904–905 (1952).

[182] A. Formozov. On the role of radiative losses in energy scale of large liquid scintillator and water Cerenkov detectors (2018). arXiv:1808.07458.

[183] J. Ashenfelter *et al.* (PROSPECT). Measurement of the Antineutrino Spectrum from ^{235}U Fission at HFIR with PROSPECT. *Phys. Rev. Lett.* **122**, 251801 (2019). arXiv:1812.10877.

[184] X. Zhang. Energy Scale Update and Quoting Key Parameters. *PROSPECT DocDB* **2363-v2** (2018).

[185] D. Norcini. Wet Commissioning: PMT ingress P50X vs AD. *PROSPECT DocDB* **2245-v4** (2018).

[186] D. Berish. Data Analysis Plots RnPo Coincidences in AD. *PROSPECT DocDB* **2363-v2** (2018).

[187] D. Jones. BiPo Analysis and Plots. *PROSPECT DocDB* **2571-v1** (2018).

[188] J. Ashenfelter *et al.* (PROSPECT). First search for short-baseline neutrino oscillations at HFIR with PROSPECT. *Phys. Rev. Lett.* **121**, 251802 (2018). arXiv:1806.02784.

[189] D. Berish. Analysis of 227Ac in the PROSPECT AD. *PROSPECT DocDB* **2424-v11** (2019).

[190] G. J. Feldman and R. D. Cousins. A Unified approach to the classical statistical analysis of small signals. *Phys. Rev.* **D57**, 3873–3889 (1998). arXiv:physics/9711021.

[191] M. Mendenhall. Preliminary IBD selection cuts overview. *PROSPECT DocDB* **2172-v1** (2018).

[192] D. Norcini. IBD baseline analysis. *PROSPECT DocDB* **2438-v1** (2018).

[193] B. B. Kinsey and G. A. Bartholomew. Neutron Capture γ-Rays from Titanium, Chromium, Iron, Nickel, and Zinc. *Phys. Rev.* **89**, 375–385 (1953). URL `https://link.aps.org/doi/10.1103/PhysRev.89.375`.

[194] J. Clem and L. Dorman. Neutron Monitor Response Functions. *Space Science Reviews* **93**, 335 (2000).

[195] Oak Ridge Reservation Meterology URL `https://metweb.ornl.gov/`.

[196] Weather Underground URL `http://wunderground.com`.

[197] O. Kyzylova. IBD-like rate and FN+nLi plots. *PROSPECT DocDB* **2370-v8** (2018).

[198] D. Norcini. NuFact v1: a look at IBDs. *PROSPECT DocDB* **2414-v7** (2018).

[199] P. T. Surukuchi. PROSPECT Oscillation Fitting. *PROSPECT DocDB* **2324-v2** (2018).

[200] P. T. Surukuchi. Detector Response Matrices. *PROSPECT DocDB* **2233-v3** (2018).

[201] D. Norcini. Neutrino v2: a look at IBDs. *PROSPECT DocDB* **2372-v6** (2018).

[202] PROSPECT. OscSens CovMatrix (Accessed 2019). URL `https://github.com/PROSPECT-collaboration/OscSens_CovMatrix`.

[203] A. Detweiler and B. Littlejohn. Ratio of Spent Nuclear Fuel (SNF) Events to Total IBD Events in HFIR's HEU core. *PROSPECT DocDB* **2316-v1** (2018).

[204] P. Huber *et al.* Impact of isotope production on neutrino fluxes at HFIR. *PROSPECT DocDB* **207-v1** (2014).

[205] A. Conant. HFIR Aluminum Activation Update. *PROSPECT DocDB* **2160-v2** (2018).

[206] P. T. Surukuchi. Al28 contribution. *PROSPECT DocDB* **2338-v2** (2018).

[207] P. T. Surukuchi. Non-equilibrium isotope correction. *PROSPECT DocDB* **2346-v1** (2018).

[208] D. Norcini. Na22 peak shifts: input for osc. *PROSPECT DocDB* **2349-v2** (2018).

[209] D. Norcini. Missing energy - Na22 calibration. *PROSPECT DocDB* **2503-v5** (2018).

[210] P. T. Surukuchi. Thesis: Sterile Neutrino Search with the PROSPECT Experiment. *PROSPECT DocDB* **2733-v1** (2018).

[211] D. Norcini *et al.* Optimizing IBD event selection for spectrum. *PROSPECT DocDB* **2404-v1** (2018).

[212] D. Norcini *et al.* IBD spectrum cuts summary. *PROSPECT DocDB* **2427-v1** (2018).

[213] D. Norcini. Muon veto variation. *PROSPECT DocDB* **2431-v1** (2018).

[214] D. Norcini. Spectrum Checks: 2018A data release. *PROSPECT DocDB* **2504-v9** (2018).

[215] I. Mitchell. Segment-by-Segment Efficiency Update. *PROSPECT DocDB* **2518-v1** (2018).

[216] N. Xoubi and R. Primm III. Modeling of the high flux isotope reactor cycle 400. *ORNL/TM-2004/251, Oak Ridge National Laboratory* (2005).

[217] Oak Ridge National Laboratory. SCALE: A Comprehensive Modeling and Simulation Suite for Nuclear Safety Analysis and Design. Technical report (2011). ORNL/TM-2005/39.

[218] X-5 Monte Carlo Team. MCNP - A General Monte Carlo N-Particle Transport Code, Version 5. Technical report, Los Alamos National Laboratory (2005). LA-UR-03-1987.

[219] H. H. Schmidt, P. Hungerford, H. Daniel, T. von Egidy, S. A. Kerr, R. Brissot, G. Barreau, H. G. Borner, C. Hofmeyr, and K. P. Lieb. Levels and gamma energies of Al-28 studied by thermal neutron capture. *Phys. Rev.* **C25**, 2888–2901 (1982).

[220] D. Dwyer. Oklo. `https://github.com/dadwyer/oklo` (2015).

[221] A. Conant *et al.* Al-28 and He-6 Contribution. *PROSPECT DocDB* **2709-v3** (2018).

[222] D. Norcini. Missing energy - Na22 calibration: 2018A data release. *PROSPECT DocDB* **2503-v5** (2018).

[223] F. P. An *et al.* (Daya Bay). Improved Measurement of the Reactor Antineutrino Flux and Spectrum at Daya Bay. *Chin. Phys.* **C41**, 013002 (2017). arXiv:1607.05378.

[224] C. Giunti and T. Lasserre. eV-scale Sterile Neutrinos (2019). arXiv:1901.08330.

[225] M. Estienne *et al.* Updated Summation Model: An Improved Agreement with the Daya Bay Antineutrino Fluxes (2019). arXiv:1904.09358.

[226] L. Bernard. New Results from STEREO: a Search for a Sterile Neutrino ∼1eV at Short Baseline. In *Rencontres de Moriond* (2019).

[227] A. A. Sonzogni, M. Nino, and E. A. McCutchan. Revealing Fine Structure in the Antineutrino Spectra From a Nuclear Reactor. *Phys. Rev.* **C98**, 014323 (2018). arXiv:1710.00092.

[228] R. Carr *et al.* Neutrino-based tools for nuclear verification and diplomacy in North Korea (2018). arXiv:1811.04737.

[229] R. Carr *et al.* Neutrino physics for Korean diplomacy. *Science* **362**, 649–650 (2018). ISSN 0036-8075.

[230] V. A. Li *et al.* SANDD: A highly-segmented pulse-shape-sensitive plastic scintillator detector incorporating silicon photomultiplier arrays (2019). arXiv:1903.11668.

[231] B. D. Rooney and J. D. Valentine. Benchmarking the Compton coincidence technique for measuring electron response non-proportionality in inorganic scintillators. In *1995 IEEE Nuclear Science Symposium and Medical Imaging Conference Record*, volume 1, 404–408 vol.1 (1995).

[232] S. Wagner. *Energy non-linearity studies and pulse shape analysis of liquid scintillator signals in the Double Chooz experiment*. Ph.D. thesis, Heidelberg U. (2014).

[233] E. L. Flumerfelt. A Compton Spectrometer Experiment in Support of the NOvA Experiment Calibration Effort. *Phys. Procedia* **61**, 683–688 (2015).

[234] F.-H. Zhang, B.-X. Yu, W. Hu, M.-S. Yang, G.-F. Cao, J. Cao, and L. Zhou. Measurement of the liquid scintillator nonlinear energy response to electron. *Chin. Phys.* **C39**, 016003 (2015). arXiv:1403.3257.

[235] C. Dorfer. *Characterization of the Nonlinear Light Emission by the Liquid Scintillator Used in the Daya Bay Experiment*. Ph.D. thesis, Technischen Universitat Wien (2015).

[236] Eljen Technology URL `https://eljentechnology.com/products/plastic-scintillators/ej-299-33a-ej-299-34`.

[237] Ortec Gamma-X (GMX) N-type High Purity Germanium (HPGe) Coaxial Radiation Detectors URL `https://www.ortec-online.com/products/radiation-detectors/germanium-hpge-radiation-detectors/hpge-radiation-detector-types-how-choose/gmx-n-type-coaxial-hpge-radiation-detectors`.

[238] Hamamatsu R6091 HA URL `https://www.hamamatsu.com/us/en/product/optical-sensors/pmt/index.html`.

[239] Ortec Mobius Recyclyer Condensing Liquid Nitrogen Cooling System URL https://www.ortec-online.com/products/radiation-detectors/germanium-hpge-radiation-detectors/detector-cooling/mobius.

[240] Round Maintenance-Free Turntable URL https://www.mcmaster.com/turntables.

[241] Saint Gobain BGO Bismuth Germanate URL https://www.crystals.saint-gobain.com/products/bgo.

[242] CAEN DT5730 URL https://www.caen.it/products/dt5730/.

[243] Z. Hartwig. ADAQ URL https://github.com/zach-hartwig/ADAQ.

[244] rat-pac-taco URL https://github.com/dnorcini/rat-pac-taco.

[245] rat-pac URL https://github.com/rat-pac/rat-pac.